3.3.2 Number of research papers per teachers in the Journals notified on UGC website during the year

List of research papers per teachers in the Journals notified on UGC website during the year

RAMANANDA COLLEGE

BISHNUPUR * BANKURA
Pin - 722122, West Bengal

Mob:- 6297976619
e-mail : principalramananda@gmail.com
Website : www.ramanandacollege.org

Estd.: 1945

UGC Recognized & State Government Aided Constituent College
Under the Bankura University (dt.-01.01.2017)
(Re-Accredited by NAAC 3rd Cycle at B ++ Level)

Ref. No..... Date.....

From : Principal
Secretary, G.B.

Number of research papers per teachers in the Journals notified on UGC website during the year

Title of paper	Name of the author/s	Department of the teacher	Name of journal	Year of publication	ISSN number	Link to the recognition in UGC enlistment of the Journal
Comprehensive review of Mycobacterium ulcerans and Buruli ulcer from a bioinformatics perspective – what have we learnt?	**S Sur** &B Pal	Botany	Acta Biologica Szegediensis	2021	1588-4082	https://www.scopus.com/sourceid/87723
A Genetic Variation of LPS Binding Protein (LBP) Affects the Inflammatory Response and is Associated with Improved Outcome during Sepsis	O Kumpf, K Gürtler, **S Sur**, M Parvin, LK Zerbe, J Eckert, ANR Weber, DY Oh, L Lundvall, L Hamann & RR Schumann	Botany	Immunohorizons	2021	2573-7732	https://pubmed.ncbi.nlm.nih.gov/34921059/
Mycobacterium abscessus: insights from a bioinformatic perspective.	**S Sur***, T Patra, M Karmakar & A Banerjee	Botany	Critical Reviews in Microbiology	2022	1549-7828	https://www.scopus.com/sourceid/19662
Traditional fishing gears of Bankura District, WB, India: Some uniqueness in fish catching	Arindam GANGULY, Ujjal KONAR, Animesh KUNDU, Sandeep CHATTERJEE, Sristishil NANDI, **Rajesh K. GUIN**, Madhuchhanda DUARI3, **Asish**	Botany	Notulae Scientia Biologicae	2022	2067-3264	https://www.notulaebiologicae.ro/index.php/nsb

RAMANANDA COLLEGE ESTD.-1945 (BANKURA) BISHNUPUR

16/5/2022
Principal
Ramananda College,
Bishnupur, Bankura

RAMANANDA COLLEGE

BISHNUPUR * BANKURA
Pin - 722122, West Bengal

Mob:- 6297976619
e-mail : principalramananda@gmail.com
Website : www.ramanandacollege.org

Estd.:1945

UGC Recognized & State Government Aided Constituent College
Under the Bankura University (dt.-01.01.2017)
(Re-Accredited by NAAC 3rd Cycle at B ++ Level)

Ref. No..... Date.....

From : Principal
Secretary, G.B.

	MANDAL, Pradeep K. DAS MOHAPATRA5*					
Diversity and distribution of wild mushrooms in diff erent forest areas of Bankura district, WB, India	Arindam Ganguly, Susmita Nad, Krishanu Singha, Rituparna Pathak, Palash Hazra, Pritha Singha, Priti Dhua, Pradeep Kumar Das Mohapatra3, **Asish Mandal**	Bota ny	Acta Biologica Szegediensi s	2021	1588 - 4082	http://abs.bibl .u-szeged.hu/ind ex.php/abs
Effect of Arsenic on Growth and Cell Division in Root Tip Cells of (*Allium sativum* L.)	Soumik Chatterjee & **Sabyasachi Chatterjee**	Bota ny	Asian Journal of Emerging Research	2021	2663 - 4988 / 2664 - 5211	https://ajer.sci one.com
In Vitro regeneration of *Piper Longum* L. and comparative RP-HPLC analysis of Piperine production of *In Vitro* and *In Vivo* grown plants	Mousumi Chatterjee, **Sabyasachi Chatterjee** and Indrani Chandra	Bota ny	Plant cell, Tissue and Organ culture	2022	Print ISSN 0167 -685, Elect ronic ISSN 1573 5044	https://doi.org /10.1007/s112 40-022-02237-0
Molecular selectivity of indenopyridines for fullerenes: A comparative study	Dr. Chiranjit Pal	Che mistr y	Journal of the Indian Chemical Society	2021	0019 - 4522	https://doi.org /10.1016/j.jics .2021.100145
Out-of-equilibrium chemical logic systems: Light and sound controlled programmable	Rahul Dev Mukhopadhyay	Che mistr y	Chem, Cellpress, I.F. 25.832	2022	2451 - 9294	https://doi.org /10.1016/j.che mpr.2022.04.0 20

RAMANANDA COLLEGE ESTD.-1945 (BANKURA) * BISHNUPUR *

16/5/2022
Principal
Ramananda College,
Bishnupur, Bankura

RAMANANDA COLLEGE

BISHNUPUR * BANKURA
Pin - 722122, West Bengal
Mob:- 6297976619
e-mail : principalramananda@gmail.com
Website : www.ramanandacollege.org

Estd.:1945

UGC Recognized & State Government Aided Constituent College
Under the Bankura University (dt.-01.01.2017)
(Re-Accredited by NAAC 3rd Cycle at B ++ Level)

Ref. No..... Date.....

From : Principal
Secretary, G.B.

spatiotemporal patterns and mechanical functions						
Cascade reaction networks within audible sound induced transient domains in a solution	Rahul Dev Mukhopadhyay	Chemistry	Nature Communications, Nature Publishing Group, I.F. 17.69	2022	2041 - 1723	https://doi.org/10.1038/s41467-022-30124-x
Remotely controllable supramolecular rotor mounted inside a porphyrinic cage	Rahul Dev Mukhopadhyay	Chemistry	Chem, Cellpress, I.F. 25.832	2022	2451 - 9294	https://doi.org/10.1016/j.chempr.2021.12.008
Audible Sound Controlled Blue Bottle Experiment	Rahul Dev Mukhopadhyay	Chemistry	Journal of Chemical Education American Chemical Society and Division of Chemical Education, I. F. 3.208	2022	0021 - 9584	https://doi.org/10.1021/acs.jchemed.1c01146
Structural and Electronic Effects from Mn and Nb Co-doping for Low Band Gap BaTiO3 Ferroelectrics	Shyamasish Das	Chemistry	The Journal of Physical Chemistry C	2021	1932 - 7447	https://doi.org/10.1021/acs.jpcc.1c02539
The COVID-19 and the Influence of Sigma	Ajit Debnath	History	Journal of Critical review	2021	2394 - 5125	https://www.jcreview.com/
Mahatma Gandhi & his Alternative theory of Economic Sustainability	Ajit Debnath	History	Dogo-Rangsang	2022	2347 - 7180	https://www.jcreview.com/
The Administrative Aspects of Kautilya's Arthashastra	Ajit Debnath	History	Bharatiya Shiksha	2022	0970 - 7630	https://www.jcreview.com/

RAMANANDA COLLEGE ESTD.-1945 (BANKURA) BISHNUPUR

16/5/2022

Principal
Ramananda College,
Bishnupur, Bankura

RAMANANDA COLLEGE

BISHNUPUR * BANKURA
Pin - 722122, West Bengal
Estd.: 1945

Mob:- 6297976619
e-mail : principalramananda@gmail.com
Website : www.ramanandacollege.org

UGC Recognized & State Government Aided Constituent College
Under the Bankura University (dt.-01.01.2017)
(Re-Accredited by NAAC 3rd Cycle at B ++ Level)

Ref. No..... Date.....

From : Principal
Secretary, G.B.

			Shodh Patrika			
Anti-synchronization Phenomenon of discrete chaotic maps using linear transformations	**MA Khan**, HP Mazumdar and SD Jabeen	Mathamatics	Journal of Information and Optimization Sciences	2022	2169-0103	https://www.tandfonline.com/doi/abs/10.1080/02522667.2017.1321766?journalCode=tios20
Spatiotemporal Synchronization of Diffusively Coupled Modified Logistic Map Under Complex Network	**MA Khan**, D Maity and SD Jabeen	Mathamatics	Proceedings of the National Academy of Sciences, India Section A: Physical Sciences	2022	0369-8203	https://link.springer.com/article/10.1007/s40010-020-00726-5
Design of multistability of chaotic systems via self and cross coupling	**MA Khan**, G Mahapatra, J Sarkar and SD Jabeen	Mathamatics	The European Physical Journal Plus	2021	2190-5444	https://link.springer.com/article/10.1140/epjp/s13360-021-01884-0
Design of multistable system of coupled different Lorenz and Nuclear Spin Generator System	Jayanta Kumar Sarkar, Mohammad Ali Khan, Gour Chandra Mahata.	Mathamatics	Advances in Mathematics Scientific Journal	2022	ISSN : 1857-8365 (printed); 1857-8438 (electronic)	https://www.researchgate.net/publication/361493543_DESIGN_OF_MULTISTABLE_SYSTEM_OF_COUPLED_DIFFERENT_LORENZ_AND_NUCLEAR_SPIN_GENERATOR_SYSTEMS

RAMANANDA COLLEGE ESTD.-1945 (BANKURA) BISHNUPUR

16/5/2023

Principal
Ramananda College,
Bishnupur, Bankura

RAMANANDA COLLEGE

BISHNUPUR * BANKURA
Pin - 722122, West Bengal

Mob:- 6297976619
e-mail : principalramananda@gmail.com
Website : www.ramanandacollege.org

Estd. :1945

UGC Recognized & State Government Aided Constituent College
Under the Bankura University (dt.-01.01.2017)
(Re-Accredited by NAAC 3rd Cycle at B ++ Level)

Ref. No..... Date.....

From : Principal
Secretary, G.B.

A mathematical model for fluxes associated with internal gravit waves excited by a corner mountain	**Prasanta Das** & Somenath Dutta	Math amati cs	MAUSAM	2022	2529 - 9416	https://mausamjournal.imd.gov.in/index.php/MAUSAM/article/view/5091
Laminar Forced Convection MHD Couette-Poiseuille Flow with Viscus and Joule Dissipation	**Dr. Bhaskar Chandra Sarkar**	Math amati cs	Journal of Scientific Research	2022	2070 - 0245	https://www.banglajol.info/index.php/JSR/article/view/58945
A novel approach of developing all-optical frequency encoded dibit-based Peres gate using reflective semiconductor optical amplifier	**Baibaswata Bhattacharjee,** Surajit Bosu	Physi cs	Journal of Nonlinear Optical Physics & Materials, World Scientific,	2022	ISSN (print): 021-8635 ISSN (online): 179-6624	https://www.worldscientific.com/doi/10.1142/S0218863523500224
A design of all-optical read-only memory using reflective semiconductor optical amplifier	Surajit Bosu, **Baibaswata Bhattacharjee**	Physi cs	Journal of Optics, Springer, (Scopus), (ESCI)	2022	Electronic ISS-097-6900 Print ISS-097-8821	https://link.springer.com/article/10.1007/s12596-022-00943-8
All-optical dibitbased Feynman gate using reflective semiconductor optical amplifier with frequency encoding scheme	Surajit Bosu, **Baibaswata Bhattacharjee**	Physi cs	Journal of Optics, Springer, (Scopus), (ESCI)	2022	Electronic ISS-097-6900 Print ISS-097-8821	https://link.springer.com/article/10.1007/s12596-022-00875-3

RAMANANDA COLLEGE ESTD.-1945 (BANKURA) BISHNUPUR

16/5/2023

Principal
Ramananda College,
Bishnupur, Bankura

RAMANANDA COLLEGE

BISHNUPUR * BANKURA
Pin - 722122, West Bengal

Mob:- 6297976619
e-mail : principalramananda@gmail.com
Website : www.ramanandacollege.org

Estd. : 1945

UGC Recognized & State Government Aided Constituent College
Under the Bankura University (dt.-01.01.2017)
(Re-Accredited by NAAC 3rd Cycle at B ++ Level)

Ref. No..... Date.....

From : Principal
Secretary, G.B.

All-Optical Frequency Encoded 2-bit Comparator using Dibit-based logic and Reflective Semiconductor Optical Amplifier	Surajit Bosu, **Baibaswata Bhattacharjee**	Physics	International Journal of Nanoparticles, Inderscience, (Scopus)	2022	ISSN online 175-2515 ISSN print 175-2507	https://www.inderscience.com/info/ingeneral/forthcoming.php?jcode=ijnp
All-optical frequency encoded dibit-based parity generator using reflective semiconductor optical amplifier with simulative verification	Surajit Bosu, **Baibaswata Bhattacharjee**	Physics	Facta Universitatis. Series: Electronics and Energetics , (Web of Science) (ESCI)	2022	Print ISS: 035-3670 Online ISS: 221-5997	http://www.doiserbia.nb.rs/Article.aspx?id=0353-36702201029B#.Y0jMlv1BzIU
A novel design of frequency encoded multiplexer and demultiplexer systems using reflected semiconductor optical amplifier with simulative verification	Surajit Bosu, **Baibaswata Bhattacharjee**	Physics	Journal of Optics, Springer (Scopus) (ESCI)	2021	Electronic ISSN-097-6900 Print ISSN-097-8821	https://link.springer.com/article/10.1007/s12596-021-00711-0
Localization and delocalization in networks with varied connectivity	Tamoghna Ray, **Amit Dey**, Manas Kulkarni	Physics	Physical Review A	2022	246-9934 (online)	https://journals.aps.org/pra/abstract/10.1103/PhysRevA.106.042610
Environmental ethics in the Abhijnanasakuntalam	Dr. Gour Baran De	Sanskrit	Sodhsamhita	2022	277-7067	https://ugccare.unipune.ac.in/Apps1/User/WebA/ViewDetails?Journall

RAMANANDA COLLEGE ESTD.-1945 (BANKURA) BISHNUPUR

16/5/2023

Principal
Ramananda College,
Bishnupur, Bankura

RAMANANDA COLLEGE

BISHNUPUR * BANKURA
Pin - 722122, West Bengal

Mob:- 6297976619
e-mail : principalramananda@gmail.com
Website : www.ramanandacollege.org

Estd. : 1945

UGC Recognized & State Government Aided Constituent College
Under the Bankura University (dt.-01.01.2017)
(Re-Accredited by NAAC 3rd Cycle at B ++ Level)

Ref. No..... Date.....

From : Principal
Secretary, G.B.

						d=101051174&flag=Search
Vivekananda: A life to be Revisited	Dr. Gour Baran De	Sanskrit	Vyasasrih	2022	2320 - 2025	https://ugccare.unipune.ac.in/Apps1/User/WebA/SearchList
An Analytical Approach for Implementing an All-Optical NOR Operation Using Amplitude Squeezed Light	Dr. Saibal Mitra	Physics	Brazilian Journal of Physics	2021	010-9733 (print)167-4448 (web)	https://doi.org/10.1007/s13538-021-01034-y

RAMANANDA COLLEGE ESTD.-1945 (BANKURA) BISHNUPUR

16/5/2023

Principal
Ramananda College,
Bishnupur, Bankura

Supporting Document

Dr. Saubashya Sur

Acta Biologica Szegediensis

Volume 65(2):233-245, 2021
Acta Biologica Szegediensis
http://abs.bibl.u-szeged.hu/index.php/abs

DOI:10.14232/abs.2021.2.233-245

ARTICLE

Comprehensive review of *Mycobacterium ulcerans* and Buruli ulcer from a bioinformatics perspective – what have we learnt?

Saubashya Sur* and Biswajit Pal

Postgraduate Department of Botany, Life Sciences Block, Ramananda College, Bishnupur-722122, West Bengal, India

ABSTRACT *Mycobacterium ulcerans* is a non-tuberculous mycobacterium responsible for causing Buruli ulcer. This is a neglected tropical disease characterized by ulceration, necrotization and scarring of the soft tissues in human limbs. Pathogenesis of *M. ulcerans* is mediated by a cytotoxic and immunosuppressive compound called mycolactone. This steadily evolving mycobacteria has adapted itself with the aquatic insect ecosystem. Human communities in wetland ecosystems are prone to Buruli ulcer and several endemic regions have been identified. So far, there is no vaccine and surgery or prolonged treatment with antibiotic cocktail has been mandated to overcome resistance patterns. Application of bioinformatics tools in *M. ulcerans* and Buruli ulcer research during the post genomic era, has provided immense opportunities. In this review, we summarize the outcome of genome studies, comparative genomics, population genomics, genetic diversity analysis, phylogenetic studies and proteomics research pertaining to this disease. We also highlight the implications of in silico vaccine design and computational studies on natural products. Resultant findings are conducive for interpreting genome architecture, pathogenomic evolution and intraspecific divergence due to phylogeographic and virulence factors of *M. ulcerans*. Moreover, the outcome of population genomics studies in disease management, coupled with the efforts in discovering vaccine candidates and novel lead compounds, will enrich our understanding of Buruli ulcer.
Acta Biol Szeged 65(2):233-245 (2021)

KEY WORDS
bioinformatics
Buruli ulcer
infectious disease
Mycobacterium ulcerans
non-tuberculous mycobacteria

ARTICLE INFORMATION
Submitted
27 September 2021
Accepted
22 October 2021
***Corresponding author**
E-mail: saubashya@gmail.com

Introduction

The broadly diverse mycobacteria are known to exist in wide ranging environments like soil, water, dust etc. (Eddyani et al. 2008; Johansen et al. 2020). They have been divided into tuberculous and non-tuberculous mycobacteria (NTM) (Wolinsky 1992). Non-tuberculous mycobacteria (NTM) consist of more than 170 different species (Baldwin et al. 2019). While majority of them have a worldwide presence, some are endemic to certain geographical locations (Hoefsloot et al. 2013). NTM are responsible for a wide array of pulmonary, extrapulmonary and disseminated diseases affecting all organs (Baldwin et al. 2019; Johansen et al. 2020). NTM infections are increasing globally owing to a multitude of factors (Collins 1989; Faverio et al. 2016). Constrained diagnostic capabilities, coupled with high degree of antibiotic resistance and lack of vaccines has aggravated the problem (Ahmed et al. 2020).

First identified in 1947, *Mycobacterium ulcerans* is a pathogenic NTM responsible for causing Buruli ulcer (Yotsu et al. 2015). *M. ulcerans* is a fragile (Eddyani et al. 2008) environmental bacterial pathogen (Ohtsuka et al. 2014), that has an optimal growth temperature of 30-33°C (Hoxmeier 2014). It has been known to adapt to certain ecological niches (Stinear et al. 2007) and are transmitted by some aquatic insects, mosquitoes, mammals etc. (Stinear et al. 2004; Einarsdottir and Huygen 2011). Evidences show that *M. ulcerans* evolved one million years ago by diverging from the common ancestor shared by *Mycobacterium marinum* (Stinear et al. 2005). This was made possible by acquisition of a plasmid encoding mycolactone and reductive evolution (Demangel et al. 2009; Hoxmeier 2014). Mycolactone is responsible for the virulence of *M. ulcerans* (Liu et al. 2019). *M. ulcerans* infection results in tissue destruction of limbs owing to necrosis of the skin and soft tissues (Einarsdottir and Huygen 2011; O'Brien et al. 2019).

The World Health Organization (WHO) considers Buruli ulcer as a neglected tropical disease. It has been reported from 34 countries (Fig. 1), especially Ghana, Benin, Democratic Republic of Congo, Ivory Coast, Togo, French Guiana, Australia, China, Papua New Guinea, and Japan (Yotsu et al. 2015; Röltgen and Pluschke 2015, Simpson et al. 2019). People living near swamps, lakes

Figure 1. World map depicting countries with reported Buruli ulcer cases.

and rivers are more prone to infection (Brou et al. 2008; Einarsdottir and Huygen 2011). Changes in the ecosystem has been cited as a reason behind incidence of Buruli ulcer (Morris et al. 2014). Multiple lines of evidence have pointed out that amongst mycobacterial diseases, Buruli ulcer is the third common one after tuberculosis and leprosy (Van der Werf et al. 1999; Etuaful et al. 2005; Walsh et al. 2011). What starts as a painless nodule in the limbs, when left untreated progresses into severe ulceration and necrosis (Fig. 2) owing to the immunosuppression triggered by mycolactone (de Souza et al. 2012; Hall et al. 2014). Age, late diagnosis, and joint infections are some of the risk factors for Buruli ulcer severity (Tai et al. 2018). Immunization with BCG in a controlled setting offered small degree of protection (Smith et al. 1977). However, in the absence of suitable vaccine (Philips et al. 2014), surgery and combinatorial antibiotic treatment with rifampicin and streptomycin was recommended (Yotsu et al., 2015). In Japan, a regimen of rifampicin, levofloxacin and clarithromycin was followed (Sugawara et al. 2015). But numerous side-effects have been reported. Repurposed anti tuberculosis drugs proved to be ineffective against Buruli ulcer (Liu et al. 2018).

Explosion of genome projects in the last two decades, coupled with development of high-performance computational facilities and software have resulted in a wealth of information (Sur et al. 2010). This includes

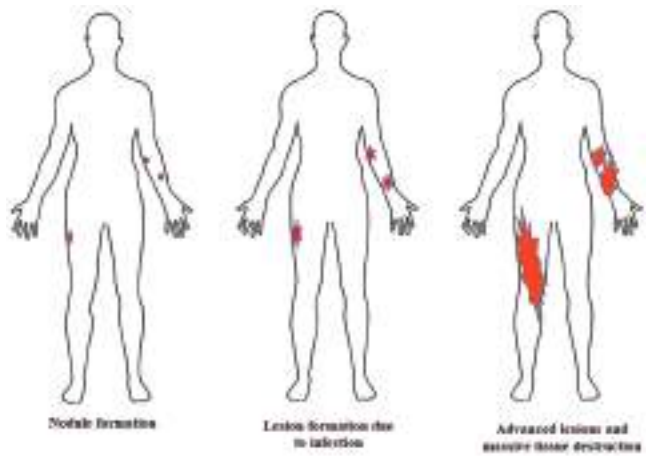

Figure 2. Buruli ulcer disease progression.

M. ulcerans as well. Here, we present a comprehensive review of the knowledge based on various bioinformatic analyses concerning *M. ulcerans* and Buruli ulcer. This is from the perspective of genomics and or comparative genomics, diversity, phylogenetic analyses, proteomics, vaccinomics, resistomics, etc. Additionally, we also comment on the opportunities of utilizing computational studies for controlling this pathogen.

Whole genome, comparative and population genomics research

Advances in molecular biology and genomics coupled with the publication of human genome in the early 21st century accelerated studies on whole genome. A necessity was felt to decode the huge deluge of information coming out from genome projects, aimed at enriching comparative genomics that could be applied to research on mycobacterial diseases (Zakham et al. 2011). While earlier genomic studies on identification of *M. ulcerans* concentrated on the use of 16SrRNA gene sequencing technology (Nakanaga et al. 2007), the whole genome sequencing of *M. ulcerans* Agy99 (Stinear et al. 2007) offered a new outlook into the biology of the pathogen. This was the first ever whole genome sequence of a *M. ulcerans* strain. It established the implication of reductive evolution and adaptation of the pathogen to specific niche (Stinear et al. 2007). Since 2007, several whole genome sequences of human pathogenic *M. ulcerans* strain Harvey, *M. ulcerans* subsp. *shinshuense* ATCC33728, *M. ulcerans* strain S4018, *M. ulcerans* strain CSURP7741, *M. ulcerans* strain SGL03, *M. ulcerans* strain P7741 etc. became available in the public domain. The genome sequence of *M. ulcerans* subsp. *shinshuense* ATCC33728 isolated from Japan and determined by 454 GS FLX Titanium technology, is made up of a 5.9 mb chromosome and a 166 kb plasmid (Yoshida et al. 2016). *M. ulcerans* strain S4018 isolated from a Buruli ulcer patient in Benin was sequenced on a MiSeq sequencer platform (Kambarev et al. 2017). *M. ulcerans* strain CSURP7741 isolated from French Guiana, was sequenced using a combinatorial approach of Nanopore and Illumina methods. It had some affinities with the frog pathogen *M. ulcerans* subsp. *lifandii* (Saad et al. 2019). Most of these genomes had a high GC content. *M. ulcerans* strain Harvey is the largest among human pathogenic *M. ulcerans,* having coding sequences more than 9000 coding sequences ((https://patricbrc.org/view/Taxonomy/2#view_tab=genomes&filter=and(keyword(Mycobacterium),keyword(ulcerans)). These genome sequences house valuable information that are crucial for understanding the phylogeny, pathophysiology, and lifestyle of this bacteria.

Over the years, comparative genomics research on different mycobacterial species have been the successful in providing valuable insights (Zakham et al. 2011). One such work focused on genes located within regions of difference accounting for 7% of *M. ulcerans* genome. The work demonstrated that gain of virulence plasmid along with deficiency of recognizable anti-virulence genes, catalyzed by IS2606 expansion. This armed the classical lineage with better capability with respect to virulence and transmissibility (Käser and Pluschke 2008). An extensive comparative genomics analyses from Benin using bioinformatic methods, resulted in the detection of 45 *M. ulcerans* specific proteins that could assist in the serodiagnosis of Buruli ulcer. This study underscored the importance of further research in generating antigenic repertoire of *M. ulcerans* (Pidot et al. 2010). That, *M. ulcerans* Agy99 showed affinity with *Mycobacterium leprae* Br4923, *Mycobacterium* sp. KMS and *Mycobacterium* sp. MCS was illustrated by a study with 14 mycobacterial genomes (Zakham et al. 2011). A comparison of whole genome sequences of thirty mycolactone producing mycobacteria and *M. marinum,* highlighted that *M. ulcerans* does not behave as a normal saprophyte. In all probability it had adapted itself to an aerobic and osmotically stable ecological niche that also protects it from light (Doig et al. 2012). Comparison of the *M. ulcerans* and *M. marinum* complex portrayed some fascinating aspects. The work highlighted mycolactone producing mycobacteria as a monophyletic group and stressed the importance to consider these bacteria as a single species i.e., *M. ulcerans* (Doig 2012). Moreover, the work also demonstrated the role of selective pressure and purifying selection in protein coding genes of *M. ulcerans.* Besides, the outcome also accentuated that speciation of *M. ulcerans* had no effect on codon translation (Doig 2012). Investigation of 21 mycobacterial genomes including *M. ulcerans* Agy99 divulged that although they differed in size, yet they had comparable high GC and low tRNA content. Besides, the ES1 locus extant in *Mycobacterium tuberculosis* and *M. marinum* was missing in *M. ulcerans* Agy99 (Zakham et al. 2012). A robust comparative genomics methodology was successful in detecting 424 essential genes from the genomes of *M. ulcerans* linked to carbohydrate and amino acid metabolism. Out of them, 236 were possible candidates for vaccine development. Furthermore, a number of enzymes associated with the cell wall, thiamine, histidine and protein biosynthesis pathways were also predicted to be prospective drug targets (Butt et al. 2012).

Increasing interest in mycobacterial comparative genomics prompted development of a user-friendly analysis platform named MycoCAP (Choo et al. 2015). This served as a suite for analyzing genomes from 55 *Mycobacterium* species including *M. ulcerans.* MycoCAP houses an assortment of web-based tools for searching, genome annotation, comparing genomes and virulence genes, determining phylogenetic relationships between mycobacterial strains and super classification. The developers of this trailblazing platform contemplate that, addition of newer genomes and their analysis will provide significant evolutionary insights (Choo et al. 2015).

The last decade also witnessed the use of whole genomes studies to figure out transmission and outbreak

of *M. ulcerans* in different countries. Research on whole genomes of *M. ulcerans* in clinical isolates from Ghana, Ivory Coast, Togo, Benin, and Nigeria, revealed widespread presence of the bacterium coupled with the existence of multiple genotypes in certain areas (Ablordey et al. 2015). The researchers opined that mobility of Buruli ulcer infected humans and livestock, from neighboring countries might have had contaminated the water bodies in different parts of Ghana. As a result, certain genotypes were introduced which later on transmitted among the population. This work stressed the need to undertake more whole genome surveys to understand the mechanism of genotype admixtures (Ablordey et al. 2015). Whole genome sequencing of isolates using NGS technologies from Benin and their comparison revealed incidence of exogenous Buruli ulcer reinfection (Eddyani et al. 2015). This incident demonstrated the importance of understanding transmission routes by targeted genome sequencing in Ouémé river valley. Another work based on whole genome amplification of crayfish samples in water bodies from Japan, illustrated seasonal emergence of *M. ulcerans* subsp. *shinshuense* (Luo et al. 2015). This study specified the link between contaminated water and incidence of Buruli ulcer.

Ever increasing number of mycobacterial genomes resulted in a plethora of information regarding cytochrome P450 monooxygenases (CYPs), a crucial enzyme for metabolic processes. Computational analysis of mycobacterial CYPs including those from *M. ulcerans* Agy99 demonstrated high diversity and their association with oxidation of steroids, fatty acids and terpenoids (Parvez et al. 2016). Human pathogenic mycobacteria have low count of CYPs which are crucial for lipid synthesis (Senate et al. 2019). Recently, a comparative study of CYPs from complete genomes of seven *M. ulcerans* strains provided insights into their lifestyle. Using CYPMiner software (Kweon et al. 2020) the study predicted 261 CYPs in the strains, classified into 35 and 38 families and subfamilies (Sur 2021). Although a few of them were diagnostic markers for some strains, there were 20 conserved families and subfamilies. While the flourishing family CYP140 was linked to mycolactone synthesis and pathogenesis, others were destined for lipid utilization. Interestingly, African strains showed similarities in their CYP profile (Sur 2021). Furthermore, the work revealed mutual association between CYP families and subfamilies.

Scientists have conducted population genomics studies applying bioinformatics methodologies, to ascertain the population structure and evolution of *M. ulcerans* in Africa. One such study using evolutionary trajectory and dynamics of *M. ulcerans* from Democratic Republic of Congo, Republic of Congo and Angola detected distinct sequence types. The research highlighted that a superior sublineage of *M. ulcerans* evolved in these countries and became endemic to hotspots in certain transmitted regions (Vandelannoote et al. 2019). This outcome once again pointed out the necessity for novel intervention-based health strategies, to disrupt transmission from localized outbreaks. Another study with whole genome sequences from clinical isolates in Melbourne, applying phylogeographic and Bayesian phylogenetic techniques divulged an interesting outcome. The investigation portrayed that *M. ulcerans* started migrating in eastern portion of Southeast Australia in the 1980's and gradually expanded to the western regions by increasing its population to a great extent (Buultjens et al. 2018). It once again emphasized the urgency to conduct environmental surveillance of pathogen mobility and have suitable interventional strategies in place to prevent migration and growth of endemic cases. It is clear from these sorts of research in Africa and Australia, that assessment of population structure and disease management based on comparative genomics data, is pivotal for controlling Buruli ulcer. In African countries and Australia with high burden of the disease, a localized assessment of *M. ulcerans* population using genomics (Vandelannoote et al. 2019a) can go a long way in treating Buruli ulcer.

Genomic diversity research based on computational techniques

Last decade of the 20th century witnessed a growing clamor for molecular typing of different strains of *M. ulcerans* from various parts of the globe (Jackson et al. 1995). Scientists were of the opinion that diversity studies would usher a new chapter for better understanding of Buruli ulcer epidemiology. Accessibility of genome sequence data of mycobacterial pathogens including *M. ulcerans,* signified the importance of studying genome polymorphisms to recognize pathogenic characteristics (Zhu et al. 2009). The necessity to have a database for mycobacterial genome polymorphisms gave birth to MyBASE. This user-friendly database accommodates information on genomic polymorphisms of different mycobacteria including *M. ulcerans*. It facilitates interpretation of diversity in pathogenicity, genome structure, evolution etc. (Zhu et al. 2009).

A single nucleotide polymorphism (SNP) profiling, using next-generation sequencing methodology from three strains of *M. ulcerans* demonstrated certain features (Qi et al. 2009). The Ghanaian isolate of *M. ulcerans* Agy99, when compared to a Japanese strain indicated 26564 SNPs in the latter. However, juxtaposition of *M. ulcerans* Agy99 with two other strains from Ghana revealed only 173 SNPs. This study illustrated that the Ghanaian clade

diverged from the Japanese strain 394-529 thousand years back, while two other Ghanaian subtypes diverged only 1000-3000 years back (Qi et al. 2009). One more study using high-throughput DNA sequencing data, of *M. ulcerans* genome isolates from Densu river basin of Ghana indicated sparse SNPs. Additional phylogenetic reconstruction analysis using SNP genotyping data divulged the ascendancy of a clonal complex and variants within it (Röltgen et al. 2010).

It was reported that multilocus sequence typing (MLST) based on housekeeping genes, of *M. ulcerans* isolates resulted in six contrasting genotypes from wide-ranging biogeographical regions of the world (Narh et al. 2014). Comparative DNA analysis between samples from water, soil, biofilms, and clinical samples, from Buruli ulcer patients in South Togo revealed similar *M. ulcerans* genetic profile (Maman et al. 2018). This study demonstrated riverine source of *M. ulcerans* infection in regions through which Haho and Zio rivers flow. MLST, short read DNA sequencing and SNP calling in a Japanese study, illustrated the difference between pigmented and non-pigmented colonies of *M. ulcerans* subsp. *shinshuense.* The pigmented and non-pigmented isolates differed only in 8 SNPs and 20 indels (Nakanaga et al. 2018). The latter was devoid of a large plasmid encoding regions for mycolatone biosynthesis, rendering it non-pathogenic in contrast to the former. Genome-wide association analysis of Buruli ulcer patients from Ouémé and plateau regions of Benin, revealed the role of lncRNAs and pathways linked to autophagy in the disease (Manry et al. 2019). These sort of genomic diversity studies using an assortment of computational techniques, enhanced our understanding of *M. ulcerans* regarding intraspecific divergence, geographical dissimilarities, virulence etc.

Research from Benin assessed bacterial diversity in skin lesions from individuals with Buruli ulcer. They performed a small-scale microbiome analysis using 16SrRNA sequencing, to gauge the composition of microbes from Buruli ulcer lesions, non Buruli ulcer lesions and skin samples of healthy persons (Leuvenhaege et al. 2017). The samples from Buruli ulcer lesions exhibited higher proportion of unassociated bacteria like *Bacteroides* and obligate anaerobes, in contrast to non Buruli ulcer lesions (Van Leuvenhaege et al. 2017). Since, skin microbiome is influenced by geography, genetics, climatic condition etc., its comparative study on a large scale should be used for estimating diversity in different populations (Nuhamunada et al. 2018). This work on Buruli ulcer lesions from Benin underlined that, additional microbiome-based analysis should be accompanied with standard microbiological studies.

In silico phylogenetics studies

Rapid improvement in "omics" data analysis and mycobacterial genomics research, has contributed to the understanding of evolutionary mechanisms (Bottai et al. 2014). One of the earliest works based on whole genome of *M. ulcerans* Agy99, indicated its evolution by lateral gene transfer and reductive evolution from *M. marinum* (Stinear et al. 2007). In fact, a number of factors viz., amassing 304 insertion sequence elements like IS2404 and IS2606, presence of 771 pseudogenes, genomic rearrangements, genome reduction, inability to tolerate sunlight, plasmid acquisition, mycolactone selective pressure and occurrence of foreign genes, contributed to its evolution and allowed it to colonize insects (Fig. 3a) by adapting to an arthropod ecosystem (Stinear et al. 2007). Moreover, the loss of ESX1 locus was also regarded as a survival strategy. Extensive comparative genomics analysis of insertions, deletions and genomic rearrangements from clinical isolates of *M. ulcerans* revealed that the microorganism evolved into five haplotypes (Käser et al. 2007). Two phylogeographically well-defined lineages were observed (Fig. 3a). The classical lineage underwent substantial genomic rearrangements and comprised of highly pathogenic genotypes concentrated mainly in Africa, Australia and Southeast Asia. They were over-represented by genes belonging to the PPE/PE families. On the other hand, the less pathogenic ancestral lineage housed environmental genotypes from China, South America and Mexico which showed similarity with *M. marinum* (Käser et al. 2007). There is strong evidence that, the classical and ancestral lineages diverged during the arrival of modern humans (Qi et al. 2009). However, the African isolates were not quite archaic and came into existence in the last 18,000 years (Stinear et al. 2000).

Some *in silico* analysis pointed out that, reductive evolution increased the pathogenic capacity of *M. ulcerans* by gaining a virulence plasmid pMUM001 (Demangel et al. 2009). Further comparative evolutionary genomic studies with two Ghanaian strains and one Japanese strain, demonstrated that the latter had an unstable genome compared to the former. Additionally, reductive evolutionary pressure was less among the Ghanaian strains (Qi et al. 2009). These were attributed to chromosomal rearrangements. Phylogenetic analysis of different mycobacterial species using 16SrRNA sequences, divulged the placement of *M. ulcerans* in a separate clade along with *M. marinum* (Zakham et al. 2012). A vast phylogenetic study with mycolactone producing mycobacteria including *M. ulcerans,* specified the role of pMUM plasmid housing genes for mycolactone biosynthesis to their advent (Doig et al. 2012). Add to this was the gain of cell wall associated genes and loss of cell wall antigens. This set

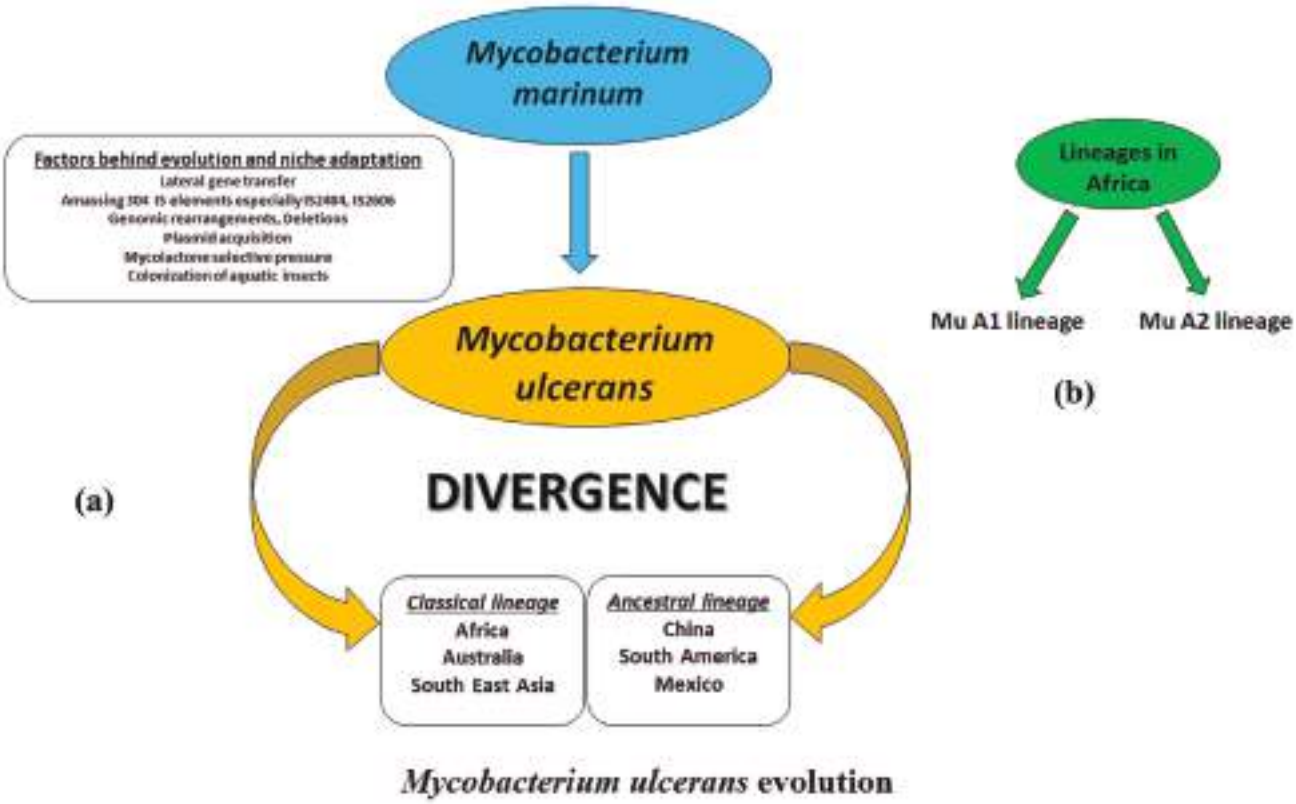

Figure 3. (a) Schematic depiction of the evolution of *Mycobacterium ulcerans* and its divergence into two major lineages (Stinear et al. 2007; Käser et al. 2007; Käser and Pluschke 2008). Note the factors responsible for evolution from *M. marinum* and niche adaptation. (b) Specific *M. ulcerans* lineages from Africa (Vandelannoote et al. 2017; Zingue et al. 2018).

off the process of cell wall remodeling that was crucial for the lifestyle of *M. ulcerans,* especially in its potential to form biofilms. Additional analysis of the mycolactone producing mycobacterial complex showed that, *M. ulcerans* were in all probability transferred between Africa and Australia not long ago. This was ascribed to genetic drift and deletion of some genes, linked to metabolism and respiration that were futile for adaptation to distinct ecological niches (Doig et al. 2012).

Phylogenetic analysis based on complete mycobacterial genomes, hypothesized occurrence of shared common mobile elements between *M. ulcerans* and *M. marinum* (Reva et al. 2015). Moreover, reticulate network analysis also supported the close relationship between these bacteria. Evolutionary reconstruction studies and Bayesian analysis of *M. ulcerans* from 11 endemic regions of Africa, identified two specific *M. ulcerans* lineages (Fig. 3b) housed in the continent (Vandelannoote et al. 2017). While the Mu_A1 lineage was from 68 BC, the Mu_A2 lineage was introduced by humans in 1800 AD (Zingue et al. 2018). The close relation of the latter with isolates from Papua New Guinea was attributed to anthropogenic activities.

One recent phylogenetic study with *M. ulcerans* from French Guiana and its comparison with global strains, utilizing core and accessory genomes threw up interesting facts. Five distinct lineages were identified by maximum likelihood phylogeny (Reynoud et al. 2019). Out of these, the L1.2 lineage was completely independent. The French Guinean strains were clustered together (Reynoud et al. 2019). Research using complex whole genome sequences of *M. ulcerans* from Australian counties, underscored the impact of microevolution. It was found that three *M. ulcerans* complex clones, were the reason behind uptick of cases in Southern Australian counties compared to non-endemic counties in rest of Australia (Saad et al. 2020).

The outcome of *M. ulcerans* phylogenetic studies accentuated the interplay of myriad factors including phylogeography and human activities, which were responsible for variation amongst lineages, pathogenic lifestyle, and adaptation to specific niches.

Proteomics of *M. ulcerans* and Buruli ulcer

Prokaryote research has reaped the benefit of rapid advances in the field of proteomics (Burley and Bonnano 2002). One of the pioneering computational proteome-based studies concerning *M. ulcerans,* was a comparative analysis of *Mycobacterium tuberculosis* strains and NTMs that included *M. ulcerans* Agy99 (Zakham et al. 2012). It used a BLAST matrix to perform genomic analysis of the predicted proteomes (Zakham et al. 2012). The work revealed low similarity between *M. tuberculosis* strains, *M. ulcerans* Agy99 and MAV complex. A classic investigation involving quantitative proteomics and transcript level analysis, highlighted the implication of culture conditions on the regulation of mycolactone toxin in *M. ulcerans* (Deshayes et al. 2013). Data from 2D gel electrophoresis and mass spectrometry analysis demonstrated that during pathogenesis and lesion formation, mycolactone altered the cytoskeleton and hindered collagen biosynthesis (Gama et al. 2014). It reiterated that mycolactone toxin was associated with reduction in collagen content in Buruli ulcer lesions. Another worker (Sarpong 2018) used high throughput mass spectrometry data to explore differentially expressed proteins from fast and slow healing Buruli ulcers. Highly expressed proteins viz., IFI30, PSME3, CD74, C4A linked to MHC class I, MHC class II and complement pathways showed better promise in healing Buruli ulcer (Sarpong 2018).

Vaccinomics research

The genome sequencing of a number of *M. ulcerans* strains opened up numerous possibilities for identifying potential vaccine candidates. Currently, there is no vaccine preventing Buruli ulcer (Mangas et al. 2020). A limited transient protection lasting for a year or so has been reported in individuals administered with *Mycobacterium bovis* BCG vaccine (Einarsdottir and Huygen 2011). Thus, development of a suitable vaccine is important for preventing *M. ulcerans* infections and Buruli ulcer severity. In the post genomic era, a study on mice revealed the efficacy of priming species specific Ag85A-DNA and homologous protein boosting, in eliciting strong Th1 immune responses against *M. ulcerans* infection (Tanghe et al. 2008). Efforts to develop inactivated vaccines, DNA/protein vaccines by targeting the mycolactone toxin, enzymes synthesizing mycolactones, mycobacterial proteins and *M. ulcerans* specific proteins demonstrated some degree of humoral and cellular responses (Huygen et al. 2009; Pidot et al. 2010; Einarsdottir and Huygen 2011). Comparative genomics methods were used for serological assessment of the antigens (Pidot et al. 2010). However, none of them were tested in clinical trials. The last decade saw increased interest in *in silico* identification of potential antigens and peptides for designing new vaccine candidates. Development of mycobacrvR package using reverse vaccinology and integrative immunoinformatic approach, served as a means for designing epitope-based vaccine candidates against mycobacterial diseases (Chaudhuri et al. 2014). This package used an assortment of 20 algorithms for determining adhesins with extracellular and surface localized characteristics (Chaudhuri et al. 2014). Analysis of the whole proteome of *M. ulcerans* Agy99 identified 36 adhesin and adhesin like proteins. Out of these, 26 potential vaccine candidates were identified by the enhanced reverse vaccinology method (Chaudhuri et al. 2014). Others attempted to develop a recombinant vaccine from *Mycobacterium marinum* against Buruli ulcer (Hart et al. 2016).

Mycobacterial secretory proteins have been the target of vaccine researchers since they are known to induce immune responses (Gcebe et al. 2016). There is evidence that the PE/PPE family of genes possess the capability to elicit Th1 response against tuberculosis (Bennan et al. 2017). Some workers studied the highly antigenic PE-PGRS family proteins from the whole proteome of *M. ulcerans* Agy99, to predict multi-epitope vaccine against it (Nain et al. 2020). They applied a robust integrated vaccinomics methodology (Fig. 4) by utilizing a wide array of algorithms. Initially, they selected 15 suitable epitopes which interacted with HLA binding alleles and demonstrated significant population coverage on a global coverage. This was followed by designing the vaccine chimera. The designed construct revealed antigenic, immunogenic, and non-allergenic characteristics. Docking and MD simulation studies demonstrated binding affinity with TLR2 receptor (Nain et al. 2020). Furthermore, *in silico* cloning, codon optimization and *in silico* immune response simulation analysis postulated that the vaccine construct is a suitable candidate for generating immune response against *M. ulcerans* Agy99 (Nain et al. 2020). Although, experimental studies are necessary to substantiate the findings.

In silico studies on antibiotic resistance and exploration of natural products as anti Buruli ulcer drugs

The World Health Organization (WHO) has approved the use of antibiotics for primary treatment of Buruli ulcer lesions (Omansen et al. 2019). Although there are some uncertainties surrounding antibiotic therapy, further treatments using surgery, physical therapy, analgesia, and community therapy are followed in many countries

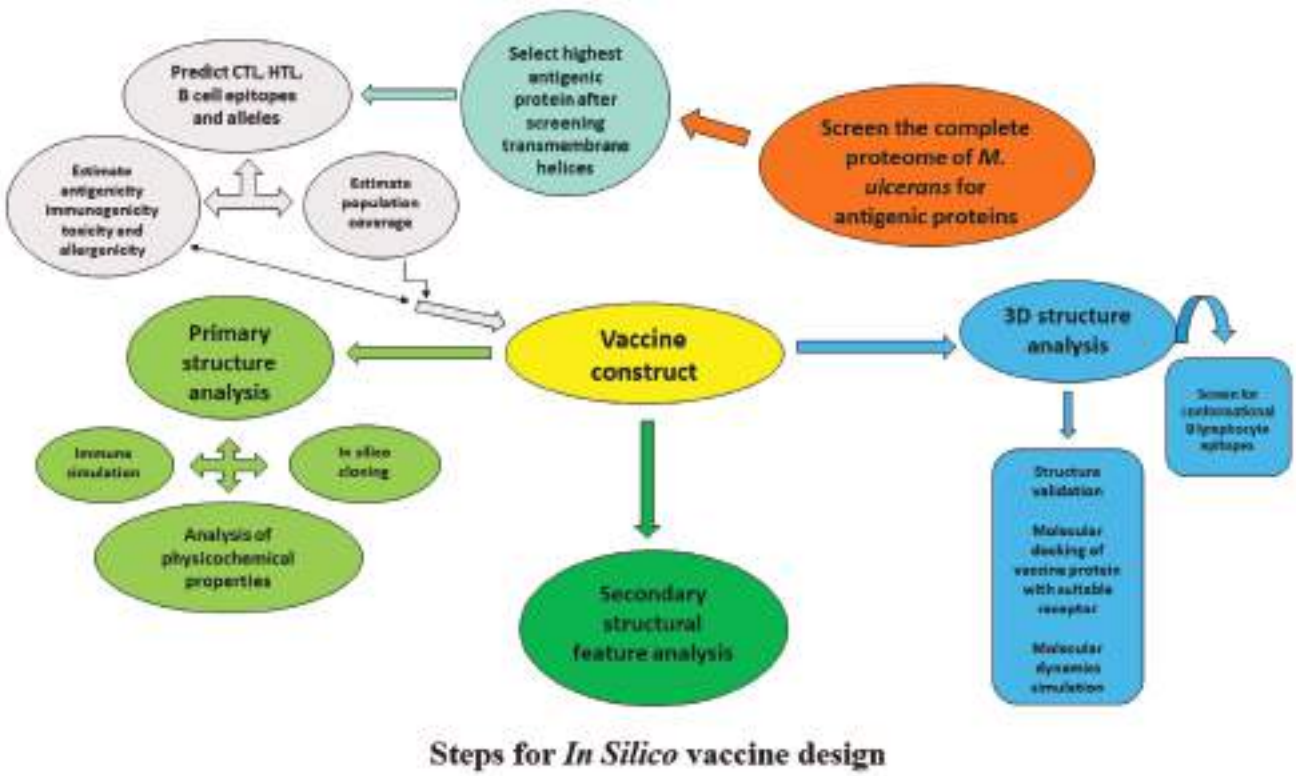

Figure 4. Schematic representation of the *in silico* vaccine design methodology (Nain et al. 2020). CTL = cytotoxic T-lymphocyte, HTL = helper T-lymphocyte.

(Omansen et al. 2019). In recent years, development of a number of bioinformatics tools and databases, opened up the possibility of exploring microbial whole genome sequencing data for investigating antibiotic resistance (Hendriksen et al. 2019). An *in silico* study highlighted the occurrence of 14 antibiotic resistance genes in *M. ulcerans* Agy99. Single mutation in *katG* and *pncA* genes were responsible for resistance to isoniazid and pyrazinamide drugs (Gupta et al. 2017). This rendered them useless against *M. ulcerans* Agy99. Additionally, this study predicted that, using a cocktail of antibiotics like rifampin, streptomycin, azithromycin, clarithromycin etc., probably assisted in overcoming the impact of mutation and may control Buruli ulcer (Gupta et al. 2017). Nonetheless, these sorts of studies should be expanded to other *M. ulcerans* strains as well.

The growing concern of antibiotic resistance, coupled with the lack of potent antibiotics against late stage Buruli ulcer has troubled the clinicians. Despite this, identification of suitable lead compounds that could act as anti Buruli ulcer drug in an *in silico* study from Ghana (Kwofie et al. 2018) showed promise. They screened isocitrate lyase from *M. ulcerans and* generated its three-dimensional structure using molecular modeling. After refinement, molecular dynamics simulation, and active site prediction, the structure was used for molecular docking with AutoDock (Kwofie et al. 2018). Virtual screening of the AfroDb for natural compounds, followed by docking resulted in 20 compounds showing reasonable affinity for isocitrate lyase. Further physicochemical analysis and ADMET testing narrowed upon ZINC38143792, ZINC95485880, and ZINC95486305 as best leads that could be suitable for experimental validation (Kwofie et al. 2018). These lead compounds known to possess inhibitory (Mujovo et al. 2008) and anti-bacterial properties (Kwofie et al. 2018) possibly restricted disease progression by neutralising isocitrate lyase.

Conclusion and future perspectives

Buruli ulcer caused by *M. ulcerans* is a neglected tropical disease. *M. ulcerans* has been understudied in comparison to other mycobacterial pathogens. The major burden of Buruli ulcer is often borne by the poor. This has resulted in socioeconomic problems. In the recent years, a deluge of information from *M. ulcerans* genome projects, coupled with state-of-the art research in comparative genomics,

population genomics, pathogen mobility/transmissibility, pathogen phylogeny, proteomics and designing vaccine candidates using *in silico* tools, has provided fantastic insights. This has revolutionized our understanding of Buruli ulcer. Phylogenetic and population genomics studies have illustrated the significance of incorporating microbial phylogeographic data in the analysis, since it highlighted information about strain origin, spread of the bacterium and migration of hosts. This has met with success in some regions of Africa and Australia wherein, early detection of active cases, surveillance and treatment resulted in reduced transmission and disease incidence (Vandelannoote et al. 2017, 2019). However, lot more needs to be done. Governments and international organizations should understand the necessity to finance Buruli ulcer research so as to improve disease control measures and minimize the burden. There is a need to have an international network of researchers with diverse expertise to foster technological innovations. This should be aimed at expanding high precision cost effective sequencing methodologies, advancing development of new tools/software, large scale targeted studies on genome variability/diversity in countries/regions with high prevalence, investigating the pattern of host microbiomes and identification of new vaccine candidates. Information from genomes could also be used to develop potent diagnostic and treatment regimens. Moreover, genome-based investigations should be increasingly conducted to understand insect vector-based transmission of Buruli ulcer. This is important since, *M. ulcerans* has crafted an ecological niche for itself in aquatic insects. Furthermore, there is a need to broaden newer genotyping strategies and boosting genomic diversity studies. Sequencing more genomes from different locations could aid such studies. Additionally, *in silico* techniques should be applied to understand the nature of pMUM plasmid and mechanism of mycolactone toxin immunosuppression (Einarsdottir and Huygen 2011). The information from such studies can aid in the development of effective vaccines and therapeutic drugs against *M. ulcerans,* using immunoinformatics and immunogenomics approaches. Pharmaceutical companies and biomedical industries should take initiatives to validate the vaccine constructs designed by robust *in silico* techniques. Computational studies on antimicrobial inhibitors and drug compounds from indigenous plants should be encouraged. This aspect of research is lacking. Clinicians and pharmaceutical scientists should assist bioinformaticians in this regard to combat the pathogen. The bottom line is to have a multidisciplinary effort in place, to better understand the epidemiological and transmission factors of this challenging and steadily evolving bacterium.

Acknowledgements

The authors express gratitude to Ramananda College, India. This work was partially carried out utilizing the grant support (Ref. No: 826/B/2020) to SS by Ramananda College. The authors also thank anonymous reviewers for their constructive comments.

References

Ablordey AS, Vandelannoote K, Frimpong IA, Ahortor EK, Amissah NA, Eddyani M, Durnez L, Portaels F, de Jong BC, Leirs H, Porter JL, Mangas KM, Lam MMC, Buultjens A, Seemann T, Tobias NJ, Stinear TP (2015) Whole genome comparisons suggest random distribution of *Mycobacterium ulcerans* genotypes in a Buruli ulcer endemic region of Ghana. PLoS Negl Trop Dis 9:e0003681.

Ahmed I, Tiberi S, Farooqi J, Jabeen K, Yeboah-Manu D, Migliori GB, Hasan R (2020) Non-tuberculous mycobacterial infections—a neglected and emerging problem. Int J Infect Dis 92S:S46-S50.

Baldwin SL, Larsen SE, Ordway D, Cassell G, Coler RN (2019) The complexities and challenges of preventing and treating nontuberculous mycobacterial diseases. PLoS Negl Trop Dis 13:e0007083.

Bottai D, Stinear TP, Supply P, Brosch R (2014) Mycobacterial pathogenomics and evolution. Microbiol Spectr 2:MGM2-0025-2013.

Brennan MJ (2017) The enigmatic PE/PPE multigene family of mycobacteria and tuberculosis vaccination. Infect Immun 85:e00969-16.

Brou T, Broutin H, Elguero E, Asse H, Guegan JF (2008) Landscape diversity related to Buruli ulcer disease in Côte d'Ivoire. PLoS Negl Trop Dis 2:e271.

Buultjens AH, Vandelannoote K, Meehan CJ, Eddyani M, de Jong BC, Fyfe JAM, Globan M, Tobias NJ, Porter JL, Tomita T, Tay EL, Seemann T, Howden BP, Johnson PDR, Stinear TP (2018) Comparative genomics shows that *Mycobacterium ulcerans* migration and expansion preceded the rise of Buruli ulcer in southeastern Australia. Appl Environ Microbiol 84:e02612-17.

Burley SK, Bonnano JB (2002) Structuring the universe of proteins. Ann Rev Genomics Hum Genet 3:243-262.

Butt AM, Nasrullah I, Tahir S, Tong Y (2012) Comparative genomics analysis of *Mycobacterium ulcerans* for the identification of putative essential genes and therapeutic candidates. PLoS ONE 7:e43080.

Chaudhuri R, Kulshrestha D, Raghunandan MV, Ramachandran S (2014) Integrative immunoinformatics for mycobacterial diseases in R platform. Syst Synth Biol

8:27-39.
Choo SW, Ang MY, Dutta A, Tan SY, Siow CC, Heydari H, Mutha NVR, Wee WY, Wong GH (2015) MycoCAP-*Mycobacterium* comparative analysis platform. Sci Rep 5:18227.
Collins FM (1989) Mycobacterial disease, immunosuppression, and acquired immunodeficiency syndrome. Clin Microbiol Rev 2:360–377.
Demangel C, Stinear T, Cole S (2009) Buruli ulcer: reductive evolution enhances pathogenicity of *Mycobacterium ulcerans*. Nat Rev Microbiol 7:50–60.
Deshayes C, Angala SK, Marion E, Brandli I, Babonneau J, Preisser L, Eyangoh S, Delneste Y, Legras P, De Chastellier C, Stinear TP, Jackson M, Marsollier L (2013) Regulation of mycolactone, the *Mycobacterium ulcerans* toxin, depends on nutrient source. PLoS Negl Trop Dis 7:e2502.
de Souza KD, Quaye C, Mosi L, Addo P, Boakye DA (2012) A quick and cost-effective method for the diagnosis of *Mycobacterium ulcerans* infection. BMC Infect 12:8.
Doig KD (2012) Comparative genomics of the *Mycobacterium ulcerans* and *Mycobacterium marinum* complex. MPhil Thesis, Melbourne University, Melbourne, Australia.
Doig KD, Holt KE, Fyfe JAM, Lavender CJ, Eddyani M, Portaels F, Yeboash-Manu D, Pluschke G, Seemann T, Stinear TP (2012) On the origin of *Mycobacterium ulcerans*, the causative agent of Buruli ulcer. BMC Genomics 13:258.
Eddyani M, De Jonckheere JF, Durnes L, Suykerbuyk P, Leirs H, Portaels F (2008) Occurrence of fee-living amoebae in communities of low and high endemicity for Buruli Ulcer in southern Benin. Appl Environ Microbiol 74:6547-6553.
Eddyani M, Vandelannoote K, Meehan CJ, Bhuju S, Porter JL, Aguiar J, Seemann T, Jarek M, Singh M, Portaels F, Stinear TP, de Jong BC (2015) A genomic approach to resolving relapse versus reinfection among four cases of Buruli Ulcer. PLoS Negl Trop Dis 9:e0004158.
Einarsdottir T, Huygen K (2011) Buruli ulcer. Human Vaccines 7:1198-1203.
Etuaful S, Carbonnelle B, Grosset J, Lucas S, Horsfield C, Phillips R, Evans M, Ofori-Adjei D, Klustse E, Owusu-Boateng J, Amedofu GK, Awuah P, Ampadu E, Amofah G, Asiedu K, Wansbrough-Jones M (2005) Efficacy of the combination rifampin-streptomycin in preventing growth of *Mycobacterium ulcerans* in early lesions of Buruli ulcer in humans. Antimicrob Agents Chemother 49:3182–3186.
Faverio P, Stainer A, Bonaiti G, Zucchetti SC, Simonetta E, Lapadula G, Marruchella A, Gori A, Blasi F, Codecasa L, Pesci A, Chalmers JD, Loebinger MR, Aliberti S (2016) Characterizing non-tuberculous mycobacteria infection in bronchiectasis. Int J Mol Sci 17:1913.
Gama JB, Ohlmeier S, Martins TG, Fraga AG, Sampaio-Marques B, Carvalho MA, Proença F, Silva MT, Pedrosa J, Ludovico P (2014) Proteomic analysis of the action of the *Mycobacterium ulcerans* toxin mycolactone: targeting host cells cytoskeleton and collagen. PLoS Negl Trop Dis 8:e3066.
Gcebe N, Michel A, Gey van Pittius NC and Rutten V (2016) Comparative genomics and proteomic analysis of four non-tuberculous *Mycobacterium* species and *Mycobacterium tuberculosis* complex: occurrence of shared immunogenic proteins. Front Microbiol 7:795.
Gupta SK, Drancourt M, Rolain JM (2017) In silico prediction of antibiotic resistance in *Mycobacterium ulcerans* Agy99 through whole genome sequence analysis. Am J Trop Med Hyg 97:810–814.
Hall BS, Hill K, McKenna M, Ogbechi J, High S, Willis AE, Simmonds RE (2014) The pathogenic mechanism of the *Mycobacterium ulcerans* virulence factor, mycolactone, depends on blockade of protein translocation into the ER. PLoS Pathog 10:e1004061.
Hart BE, Laura PH, Sunhee L (2016) Immunogenicity and protection conferred by a recombinant *Mycobacterium marinum v*accine against Buruli Ulcer. Trials Vaccinol 5:88–91.
Hendriksen RS, Bortolaia V, Tate H, Tyson GH, Aarestrup FM, McDermott PF (2019) Using genomics to track global antimicrobial resistance. Front Public Health 7:242.
Hoefsloot W, van Ingen J, Andrejak C, Angeby K, Bauriaud R, Bemer P, Beylis N, Boeree MJ, Cacho J, Chihota V, Chimara E, Churchyard G, Cias R, Daza R, Daley CL, Dekhuijzen PN, Domingo D, Drobniewski F, Esteban J, Fauville-Dufaux M, Folkvardsen DB, Gibbons N, Gómez-Mampaso E, Gonzalez R, Hoffmann H, Hsueh PR, Indra A, Jagielski T, Jamieson F, Jankovic M, Jong E, Keane J, Koh WJ, Lange B, Leao S, Macedo R, Mannsåker T, Marras TK, Maugein J, Milburn HJ, Mlinkó T, Morcillo N, Morimoto K, Papaventsis D, Palenque E, Paez-Peña M, Piersimoni C, Polanová M, Rastogi N, Richter E, Ruiz-Serrano MJ, Silva A, da Silva MP, Simsek H, van Soolingen D, Szabó N, Thomson R, Tórtola Fernandez T, Tortoli E, Totten SE, Tyrrell G, Vasankari T, Villar M, Walkiewicz R, Winthrop KL, Wagner D (2013) Nontuberculous Mycobacteria Network European Trials Group. The geographic diversity of nontuberculous mycobacteria isolated from pulmonary samples: an NTM-NET collaborative study. Eur Respir J 42:1604-13.
Hoxmeier JC (2014) The pathogenesis and environmental maintenance of *Mycobacterium ulcerans*. PhD thesis. Colorado State University, Colorado, USA.
Huygen K, Adjei O, Affolabi D, Bretzel G, Demangel C, Fleischer B, Johnson RC, Pedrosa G, Phanzu DM, Phillips RO, Pluschke G, Siegmund F, Singh M, van der Werf TS, Wansbrough-Jones M, Portaels F (2009) Buruli ulcer disease: prospects for a vaccine. Med Microbiol Immunol

(Berl) 198:69-77.

Jackson K, Edwards R, Leslie DE, Hayman J (1995) Molecular method for typing *Mycobacterium ulcerans*. J Clin Microbiol 33:2250-3.

Johansen MD, Herrmann JL, Kremer L (2020) Non-tuberculous mycobacteria and the rise of *Mycobacterium abscessus*. Nat Rev Microbiol 18:392-407.

Kambarev S, Corvec S, Chauty A, Marion E, Marsollier L, Pecorari F (2017) Draft genome sequence of *Mycobacterium ulcerans* S4018 isolated from a patient with an active Buruli ulcer in Benin, Africa. Genome Announc 5:e00248-17.

Käser M, Rondini S, Naegeli M, Stinear T, Portaels F, Certa U, Pluschke G (2007) Evolution of two distinct phylogenetic lineages of the emerging human pathogen *Mycobacterium ulcerans*. BMC Evol Biol 7:177.

Käser M, Pluschke G (2008) Differential gene repertoire in *Mycobacterium ulcerans* identifies candidate genes for patho-adaptation. PLoS Negl Trop Dis 2:e353.

Kweon K, Kim SJ, Kim JH, Nho SW, Bae D, Chon J, Hart M, Baek DH, Kim YC, Wang W, Kim SK, Sutherland JB, Cerniglia CE (2020) CYPminer: an automated cytochrome P450 identification, classification, and data analysis tool for genome data sets across kingdoms. BMC Bioinformatics 21:160.

Kwofie SK, Dankwa B, Odame EA, Agamah FE, Doe LPA, Teye J, Agyapong O, Miller 3rd WA, Mosi L, Wilson MD (2018) *In silico* screening of isocitrate lyase for novel anti-Buruli ulcer natural products originating from Africa. Molecules 23:1550.

Liu Y, Gao Y, Liu J, Tan Y, Liu Z, Chhotaray C, Jiang H, Lu Z, Chiwala G, Wang S, Makafe G, Islam MM, Hameed HMA, Cai X, Wang C, Li X, Tan S, Zhang T (2019) The compound TB47 is highly bactericidal against *Mycobacterium ulcerans* in a Buruli ulcer mouse model. Nat Commun 10:524.

Luo Y, Degang Y, Ohtsuka M, Ishido Y, Ishii N, Suzuki K (2015) Detection of *Mycobacterium ulcerans* subsp. *shinshuense* DNA from a water channel in familial Buruli ulcer cases in Japan. Future Microbiol 10:461-469.

Maman I, Tchacondo T, Kere AB, Beissner M, Badziklou K, Tedihou E, Nyaku E, Amekuse K, Wiedemann FX, Karou DS, Bretzel G (2018) Molecular detection of *Mycobacterium ulcerans* in the environment and its relationship with Buruli ulcer occurrence in Zio and Yoto districts of maritime region in Togo. PLoS Negl Trop Dis 12:e0006455.

Mangas KM, Tobias NJ, Marion E, Babonneau J, Marsollier L, Porter JL, Pidot SJ, Wong CY, Jackson DC, Chua BY, Stinear TP (2020) High antibody titres induced by protein subunit vaccines using *Mycobacterium ulcerans* antigens Hsp18 and MUL_3720 with a TLR-2 agonist fail to protect against Buruli ulcer in mice. Peer J 8:e9659.

Manry J, Vincent QB, Johnson C, Chrabieh M, Lorenzo L, Theodorou I, Ardant MF, Marion E, Chauty A, Marsollier L, Abel L, Alcais A (2020) Genome-wide association study of Buruli ulcer in rural Benin highlight's role of two LncRNAs and the autophagy pathway. Commun Biol 3:177.

Morris A, Gozlan R, Marion E, Marsollier L, Andreou D, Sanhueza D, Ruffine R, Couppie P, Guegan JF (2014) First Detection of *Mycobacterium ulcerans* DNA in environmental samples from South America. PLoS Negl Trop Dis 8:e2660.

Mujovo SF, Hussein AA, Meyer JJM, Fourie B, Muthivhi T, Lall N (2008) Bioactive compounds from *Lippia javanica* and *Hoslundia opposita*. Nat Prod Res 22:1047-1054.

Nakanaga K, Ishii N, Suzuki K, Tanigawa K, Goto M, Okabe T, Imada H, Kodama A, Iwamoto T, Takahashi H, Saito H (2007) "*Mycobacterium ulcerans* subsp. *shinshuense*" isolated from a skin ulcer lesion: identification based on 16S rRNA gene sequencing. J Clin Microbiol 45:3840-3843.

Nakanaga K, Ogura Y, Toyoda A, Yoshida M, Fukano H, Fujiwara N, Miyamoto Y, Nakata N, Kazumi Y, Maeda S, Ooka T, Goto M, Tanigawa K, Mitarai S, Suzuki K, Ishii N, Ato M, Hayashi T, Hoshino Y (2018) Naturally occurring a loss of a giant plasmid from *Mycobacterium ulcerans* subsp. *shinshuense* makes it non-pathogenic. Sci Rep 8:8218.

Nain Z, Karim MM, Sen MK, Adhikari UK (2020) Structural basis and designing of peptide vaccine using PE-PGRS family protein of *Mycobacterium ulceran*s - An integrated vaccinomics approach. Mol Immunol 120:146-163.

Narh CA, Mosi L, Quaye C, Tay SCK, Bonfoh B, deSouza DK (2014) Genotyping tools for *Mycobacterium ulcerans* drawbacks and future prospects. J Mycobac Dis 4:149.

Nuhamunada M, Pratama GA, Wikanthi S, Anam MK, Rizki RLP, Wijayanti N (2018) Data mining and comparative analysis of human skin microbiome from EBI metagenomics database. In 1st International Conference on Bioinformatics, Biotechnology, and Biomedical Engineering-Bioinformatics and Biomedical Engineering, 1-6, doi:10.1109/BIOMIC.2018.8610588.

O'Brien DP, Murrie A, Meggyesy P, Priestley J, Rajcoomar A, Athan E (2019) Spontaneous healing of *Mycobacterium ulcerans* disease in Australian patients. PLoS Negl Trop Dis 13:e0007178.

Ohtsuka M, Kikuchi N, Yamamoto T, Suzutani T, Nakanaga K, Suzuki K, Ishii N (2014) Buruli ulcer caused by *Mycobacterium ulcerans* subsp. *shinshuense*: a rare case of familial concurrent occurrence and detection of insertion sequence 2404 in Japan. JAMA Dermatol 150:64-67.

Omansen TF, van der Werf TS, Phillips RO (2019) Antimicobial treatment of *Mycobacterium ulcerans* infection. In Pluschke G, Röltgen K, Eds, Buruli Ulcer, Springer, Switzerland, 203-220.

Parvez M, Qhanya LB, Mthakathi NT, Kgosiemang IK, Bamal HD, Pagadala NS, Xie T, Yang H, Chen H, Theron CW, Monyaki R, Raselemane SC, Salewe V, Mongale BL, Matowane RG, Abdalla SM, Booi WI, van Wyk M, Olivier D, Boucher CE, Nelson DR, Tuszynski JA, Blackburn JM, Yu JH, Mashele SS, Chen W, Syed K (2016) Molecular evolutionary dynamics of cytochrome P450 monooxygenases across kingdoms: Special focus on mycobacterial P450s. Sci Rep 6:33099.

Phillips R, Horsfield C, Laing MK, Awuah EP, Nyarko K, Osei-Sarpong F, Butcher P, Lucas S, Wansbrough-Jones M (2006) Cytokine mRNA expression in *Mycobacterium ulcerans*-Infected human skin and correlation with local inflammatory response. Infect Immun 74:2917-2924.

Pidot SJ, Porter JL, Marsollier L, Chauty A, Migot-Nabias F, Badaut C, Benard A, Ruf MT, Seemann T, Johnson PDR, Davies JK, Jenkin GA, Pluschke G, Stinear TP (2010) Serological evaluation of *Mycobacterium ulcerans* antigens identified by comparative genomics. PLoS Negl Trop Dis 4:872.

Qi W, Käser M, Röltgen K, Yeboah-Manu D, Pluschke G (2009) Genomic diversity and evolution of *Mycobacterium ulcerans* revealed by next-generation sequencing. PLoS Pathog 5:e1000580.

Reva O, Koroteitskiy I, Ilin A (2015) Role of the horizontal gene exchange in evolution of pathogenic Mycobacteria. BMC Evol Biol 15:S2.

Reynaud Y, Fresia P, Iraola G (2019) Phylogenetic analyses of *Mycobacterium ulcerans* from French Guiana using combination of core and accessory genomes. Caribbean Science and Innovation Meeting 2019, Pointe-à-Pitre (Guadeloupe), France. (hal-02453184). https://hal.univ-antilles.fr/hal-02453184.

Röltgen K, Qi W, Ruf MT, Mensah-Quainoo E, Pidot SJ, Seemann T, Stinear TP, Käser M, Yeboah-Manu D, Pluschke G (2010) Single nucleotide polymorphism typing of *Mycobacterium ulcerans* reveals focal transmission of Buruli ulcer in a highly endemic region of Ghana. PLoS Negl Trop Dis 4:e751.

Röltgen K, Pluschke G (2015) Epidemiology and disease burden of Buruli ulcer: a review. Res Rep Trop Med 6:59-73.

Saad J, Combe M, Hammoudi N, Couppié P, Blaizot R, Jedir F, Gozlan RE, Drancourt M, Bouam A (2019) Whole-genome sequence of *Mycobacterium ulcerans* CSURP7741, a French Guianan clinical isolate. Microbiol Resour Announc 8:e00215-19.

Saad J, Hammoudi N, Zghieb H, Anani H, Drancourt M (2020) Geographic microevolution of *Mycobacterium ulcerans* sustains Buruli ulcer extension, Australia. bioRxiv doi: https://doi.org/10.1101/2020.11.03.366435.

Sarpong FN (2018) Proteomics of Buruli Ulcer Disease Healing. Master's Thesis. Kwame Nkrumah University of Science and Technology, Kumasi, Ghana.

Senate LM, Tjatji MP, Pillay K, Chen W, Zondo NM, Syed PR, Mnguni FC, Chiliza ZE, Bamal HD, Karpoormath R, Khoza T, Mashele SS, Blackburn JM, Yu JH, Nelson DR, Syed K (2019) Similarities, variations, and evolution of cytochrome P450s in *Streptomyces* versus *Mycobacterium*. Sci Rep 9:3962.

Simpson H, Deribe K, Tabah EN, Peters A, Maman I, Frimpong M, Ampadu E, Phillips R, Saunderson P, Pullan RL, Cano J (2019) Mapping the global distribution of Buruli ulcer: a systematic review with evidence consensus. Lancet Glob Health 7:e912-e922.

Smith PG, Revill WD, Lukwago E, Rykushin YP (1977) The protective effect of BCG against *Mycobacterium ulcerans* disease:a controlled trial in an endemic area of Uganda. Trans R Soc Trop Med Hyg 70:449-457.

Stinear TP, Jenkin GA, Johnson PDR, Davies JK (2000) Comparative genetic analysis of *Mycobacterium ulcerans* and *Mycobacterium marinum* reveals evidence of recent divergence. J Bacteriol 182:6322-6330.

Stinear TP, Mve-Obiang A, Small PLC, Frigui W, Pryor MJ, Brosch R, Jenkin GA, Johnson PDR, Davies JK, Lee RE, Adusumilli S, Garnier T, Haydock SF, Leadlay PF, Cole ST (2004) Giant plasmid-encoded polyketide synthases produce the macrolide toxin of *Mycobacterium ulcerans.* Proc Natl Acad Sci USA 101:1345-1349.

Stinear TP, Pryor MJ, Porter JL, Cole ST (2005) Functional analysis and annotation of the virulence plasmid pMUM001 from *Mycobacterium ulcerans*. Microbiology 151:683-692.

Stinear TP, Seemann T, Pidot S, Frigui W, Reysset G, Garnier T, Meurice G, Simon D, Bouchier C, Ma L, Tichit M, Porter JL, Ryan J, Johnson PDR, Davies JK, Jenkin GA, Small PLC, Jones LM, Tekaia F, Laval F, Daffe M, Parkhill J, Cole ST (2007) Reductive evolution and niche adaptation inferred from the genome of *Mycobacterium ulcerans*, the causative agent of Buruli ulcer. Genome Res 17:192-200.

Sugawara M, Ishii N, Nakanaa K, Suzuki K, Umebayashi Y, Makigami K, Aihara M (2015) Exploration of a standard treatment for Buruli ulcer through a comprehensive analysis of all cases diagnosed in Japan. J Dermatol 42:581-595.

Sur S, Bothra AK, Sen A (2010) Symbiotic nitrogen fixation-a bioinformatics perspective. Biotechnology 9:257-273.

Sur S (2021) Understanding the nature and dynamics of *Mycobacterium ulcerans* cytochrome P450 monooxygenases (CYPs)–a bioinformatics approach. Acta Biol Szeged 65:93-103.

Tai AYC, Athan E, Friedman ND, Hughes A, Walton A, O'Brien DP (2018) Increased Severity and Spread of *Mycobacterium ulcerans*, Southeastern Australia. Emerg Infect Dis 24:58-64.

Tanghe A, Dangy JP, Pluschke G, Huygen K (2008) Improved

protective efficacy of a species-specific DNA vaccine encoding mycolyl-transferase Ag85A from *Mycobacterium ulcerans* by homologous protein boosting. PLoS Negl Trop Dis 2:e199.

Vandelannoote K, Meehan CJ, Eddyani M, Affolabi D, Phanzu DM, Eyangoh S, Jordaens K, Portaels F, Mangas K, Seemann T, Marsollier L, Marion E, Chauty A, Landier J, Fontanet A, Leirs H, Stinear TP, de Jong BC (2017) Multiple introductions and recent spread of the emerging human pathogen *Mycobacterium ulcerans* across Africa. Genome Biol Evol 9:414-426.

Vandelannoote K, Phanzu DM, Kibadi K, Eddyani M, Meehan CJ, Jordaens K, Leirs H, Portaels F, Stinear TP, Harris SR, de Jong BC (2019) *Mycobacterium ulcerans* population genomics to inform on the spread of Buruli ulcer across Central Africa. mSphere 4:e00472-18.

Vandelannoote K, Eddyani M, Buultjens A, Stinear TP (2019a) Population genomics and molecular epidemiology of *Mycobacterium ulcerans.* In Pluschke G, Röltgen K, Eds, Buruli Ulcer, Springer, Switzerland, 107-115.

Van Leuvenhaege C, Vandelannoote K, Affolabi D, Portaels F, Sopoh G, de Jong BC, Eddyani M, Meehan CJ (2017) Bacterial diversity in Buruli ulcer skin lesions: challenges in the clinical microbiome analysis of a skin disease. PLoS ONE 12:e0181994.

Van der Werf TS, Van der Graaf WT, Tappero JW, Asiedu K (1999) *Mycobacterium ulcerans* infection. Lancet 354:1013-1018.

Walsh DS, Portaels F, Meyers WM (2011) Buruli ulcer: Advances in understanding *Mycobacterium ulcerans* infection. Dermatol Clin 29:1-8.

Wolinsky E (1992) Mycobacterial diseases other than tuberculosis. Clin Infect Dis 15:1-10.

Yoshida M, Nakanaga K, Ogura Y, Toyoda A, Ooka T, Kazumi Y, Mitarai S, Ishii N, Hayashi T, Hoshino Y (2016) Complete genome sequence of *Mycobacterium ulcerans* subsp. *shinshuense*. Genome Announc 4:e01050-16.

Yotsu RR, Murase C, Sugawara M, Suzuki K, Nakanaga K, Ishii N, Asiedu K (2015) Revisiting Buruli ulcer. J Dermatol 42:1033-1041.

Zakham F, Belayachi L, Ussery D, Akrim M, Benjouad A, Aouad RE, Ennaji MM (2011) Mycobacterial species as a case-study of comparative genome analysis. Cell Mol Biol 57(Supp):OL1462-OL1469.

Zakham F, Aounae O, Ussery D, Benjouad A, Ennaji MM (2012) Computational genomics-proteomics and phylogeny analysis of twenty-one mycobacterial genomes (Tuberculosis & non Tuberculosis strains). Microb Inform Exp 2:7.

Zhu X, Chang S, Fang K, Cui S, Liu J et al. (2009) MyBASE: a database for genome polymorphism and gene function studies of *Mycobacterium*. BMC Microbiol 9:40.

Zingue D, Bouam A, Tian RBD, Drancourt M (2018) Buruli ulcer, a prototype for ecosystem-related infection, caused by *Mycobacterium ulcerans*. Clin Microbiol Rev 31:e00045-17.

A Genetic Variation of Lipopolysaccharide Binding Protein Affects the Inflammatory Response and Is Associated with Improved Outcome during Sepsis

Oliver Kumpf, Kathleen Gürtler, Saubashya Sur, Monalisa Parvin, Lena-Karoline Zerbe, Jana K. Eckert, Alexander N. R. Weber, Djin-Ye Oh, Linn Lundvall, Lutz Hamann and Ralf R. Schumann

ImmunoHorizons 2021, 5 (12) 972-982
doi: https://doi.org/10.4049/immunohorizons.2100095
http://www.immunohorizons.org/content/5/12/972

ImmunoHorizons is an open access journal published by
The American Association of Immunologists, Inc.,
1451 Rockville Pike, Suite 650, Rockville, MD 20852

ISSN 2573-7732.

ImmunoHorizons

RESEARCH ARTICLE

Innate Immunity

A Genetic Variation of Lipopolysaccharide Binding Protein Affects the Inflammatory Response and Is Associated with Improved Outcome during Sepsis

Oliver Kumpf,[*,1] Kathleen Gürtler,[†,‡,1] Saubashya Sur,[§] Monalisa Parvin,[§] Lena-Karoline Zerbe,[†,¶] Jana K. Eckert,[†,‖] Alexander N. R. Weber,[#] Djin-Ye Oh,[†,,††] Linn Lundvall,[†] Lutz Hamann,[†] and Ralf R. Schumann[†]**

*Charité — Universitätsmedizin Berlin, Corporate Member of Freie Universität Berlin and Humboldt-Universität zu Berlin, Department of Anesthesiology and Intensive Care Medicine, Berlin, Germany; [†]Charité — Universitätsmedizin Berlin, Corporate Member of Freie Universität Berlin and Humboldt-Universität zu Berlin, Institute of Microbiology, Infectious Diseases and Immunology, Berlin, Germany; [‡]Klinik für Gynäkologie, DRK-Kliniken Berlin Westend, Berlin, Germany; [§]Department of Botany, Ramananda College, Bishnupur, West Bengal, India; [¶]Psychiatrische Universitätsklinik der Charité im St. Hedwig-Krankenhaus, Berlin, Germany; [‖]Division of Pediatric Allergy, Department of Pediatrics, Dr. von Hauner Children's Hospital, University Hospital, Ludwig Maximilian University of Munich, Munich, Germany; [#]Department of Immunology, Interfaculty Institute for Cell Biology, University of Tübingen, Germany; **Aaron Diamond AIDS Research Center, The Rockefeller University, New York, NY; and [††]Department of Infectious Diseases, Robert-Koch-Institute, Berlin, Germany

ABSTRACT

LPS binding protein (LBP) is an important innate sensor of microbial cell wall structures. Frequent functionally relevant mutations exist and have been linked to influence susceptibility to and course of bacterial infections. We examined functional properties of a single nucleotide polymorphism resulting in an exchange of phenylalanine to leucine at position 436 of LBP (rs2232618) and compared the frequent variant of the molecule with the rare one in ligand binding experiments. We then stimulated RAW cells with bacterial ligands in the presence of serum obtained from individuals with different LBP genotypes. We, furthermore, determined the potential effects of structural changes in the molecule by in silico modeling. Finally, we analyzed 363 surgical patients for this genetic variant and examined incidence and course of sepsis following surgery. We found that binding of LBP to bacterial ligands was reduced, and stimulation of RAW cells resulted in an increased release of TNF when adding serum from individuals carrying the F436L variant as compared with normal LBP. In silico analysis revealed structural changes of LBP, potentially explaining some of the effects observed for the LBP variant. Finally, patients carrying the F436L variant were found to be similarly susceptible for sepsis. However, we observed a more favorable course of severe infections in this cohort. Our findings reveal new insights into LPS recognition and the subsequent activation of the innate immune system brought about by LBP. The identification of a genetic variant of LBP influencing the course of sepsis may help to stratify individuals at risk and thus reduce clinical complications of patients. *ImmunoHorizons*, 2021, 5: 972–982.

Received for publication November 1, 2021. Accepted for publication November 2, 2021.

Address correspondence and reprint requests to: Dr. Oliver Kumpf, Charité - Universitätsmedizin Berlin, corporate member of Freie Universität Berlin and Humboldt-Universität zu Berlin, Department of Anesthesiology and Intensive Care Medicine, Charitéplatz 1, 10117 Berlin, Germany. E-mail address: oliver.kumpf@charite.de

ORCIDs: 0000-0001-7891-8872 (O.K.); 0000-0001-7002-628X (S.S.); 0000-0002-3339-4910 (L.-K.Z.); 0000-0003-1616-7430 (J.K.E.); 0000-0002-8627-7056 (A.N.R.W.); 0000-0001-8332-0293 (L.L.).

This work was supported by different grants from the Deutsche Forschungsgemeinschaft, some of them as part of the priority program "Innate Immunity" to R.R.S. Ramananda College provided financial assistance for S.S. (826/B/2020).

R.R.S and O.K. designed and supervised the studies; L.-K.Z., K.G., J.K.E., and L.L. conducted the in vitro experiments; D.-Y.O. established the healthy control cohort; L.H. performed and interpreted the genetic analyses; S.S., M.P., and A.N.R.W. performed in silico analysis; O.K., R.R.S., and S.S. analyzed the data; O.K. and R.R.S wrote the manuscript; and all authors edited the manuscript.

[1]O.K. and K.G. contributed equally to this manuscript.

Abbreviations used in this article: CI, confidence interval; ICU, intensive care unit; ID, identifier; LBP, LPS binding protein; OR, odds ratio; PDB, Protein Data Bank; Phe, phenylalanine; PLTP, phospholipid transfer protein; SNP, single nucleotide polymorphism.

The online version of this article contains supplemental material.

https://doi.org/10.4049/immunohorizons.2100095

ImmunoHorizons is published by The American Association of Immunologists, Inc.

INTRODUCTION

The LPS binding protein (LBP) is an acute-phase protein primarily secreted from the liver with substantial concentrations also released from pulmonary and gut epithelial cells (1–4). It belongs to a larger family of phospholipid transfer proteins (PLTPs), which transfer lipid derivates and lipopeptides throughout the body influencing lipid homeostasis (5, 6). These functions are associated with common diseases like vascular and heart disease but are also known to be involved in innate immunity (7, 8). It has recently been shown that LBP particularly facilitates the transfer of multimers of LPS to its sensing receptor consisting of CD14, TLR4, and MD2, initiating the inflammatory response (9–11). Furthermore, it plays a role in detoxification of LPS by transferring LPS into lipoproteins (4, 12–15). In addition, LBP is also able to bind lipopeptides originating from both Gram-negative and Gram-positive bacteria and to mediate their proinflammatory effects (16–18). Recently, it has been postulated to be associated with bacterial translocation in the gut, potentially adding function to this molecule by sensing/scavenging bacterial material entering the body through a deranged gut wall (19). Finally, it has been shown that LBP, in a similar manner as other members of the genetically related family of PLTPs, such as cholesterol ester transfer protein and PLTP, can bind and transfer phospholipids. This mechanism most likely is important for LPS transfer from micelles to HDL particles and into membranes but potentially may represent a general lipid transport system (20, 21).

In critically ill patients, LBP levels are markedly increased severalfold (22). LBP effects within the host depend strongly on its concentrations in serum, in which lower concentrations are responsible for effective initiation of LPS sensing. However, high acute-phase concentrations of LBP exert a rather inhibiting effect on the immune response (23–25). Underlying mechanisms of this phenomenon are not yet completely understood but may involve facilitation of LPS internalization brought about by LBP (26).

Hereditary factors have been studied in the context of sepsis, and consequently, a growing number of genetic factors was identified that contribute to risk and the course of severe forms of sepsis (27, 28). Single nucleotide polymorphisms (SNPs) of the innate immune system have been described that influence individual responses to invading pathogens (29).

For the LBP gene on chromosome 20, at least two studies were able to show association of mutations with altered inflammatory responses (30, 31), and haplotype studies were able to associate genetic alteration to outcome (32, 33). In a very recent comprehensive review of this year, it was concluded that genetic variations of LBP alter the risk for inflammatory complications (34). For the purposes of this study, nonsynonymous LBP SNPs were deemed as appropriate candidates to assess structural changes in the molecule in combination with functional and clinical data. Other LBP SNPs identified with regard to infections and sepsis were mostly promotor variants or synonymous SNPs (34). In this study, we compared patients carrying different variants of LBP regarding a coding SNP (rs2232618) at position 436, leading to an amino acid exchange from phenylalanine (Phe) to leucine in the LBP molecule (31, 35, 36). We previously studied a different SNP (rs2232613) leading to a change at amino acid position 333 in a comparable experimental setting with patient data from the same cohort also partly included in this study. These results showed an altered molecular response and an influence on clinical outcome (37). Patients carrying this SNP were excluded from the primary analysis. The SNP further evaluated in this study has been shown by others to be associated with altered sepsis prevalence and mortality in Chinese trauma victims (38, 39).

The SNP was initially thought to cause an exchange from leucine to Phe, but recent sequence analysis revealed that the cystine to thymidine exchange is more frequent in Western European inhabitants. Therefore, the c1341t genotype (nucleotide sequence: TTC leading to Phe) was considered to be the common variant. As a continuation of a previous study, we show in this study how functional properties of the LBP molecule are altered by this SNP (37). We assessed binding of several ligands to the variants of LBP. As molecular patterns originating from bacteria, we used LPS and lipopeptides. Phosphatidylethanolamine was used as a nonbacterial ligand to assess transfer ability to LBP as has been done in previous experiments (21). Furthermore, we used the murine RAW 246.7 cell line and stimulated the cells with the ligands in the presence and absence of serum from patients carrying the rare variant of LBP. We used this as a macrophage model for LPS recognition and measured the in vitro release of a proinflammatory cytokine (TNF). In this way, we were able to simulate the structural and biochemical influence of this SNP on the basis of the recently discovered molecular structure of the whole LBP molecule using different bioinformatic tools (40). We also examined this functionally relevant SNP in a cohort of 363 surgical intensive care unit (ICU) patients from European ancestry and associated it with the susceptibility to postoperative infections and outcome. We hypothesized that the variant of LBP studied in this study would affect its ability to confer its main biological function. We sought to determine whether structural changes in the molecule could explain this behavior. Finally, we tried to determine whether these findings of altered structure and function would influence the clinical course of patients with postoperative infections carrying this SNP.

MATERIALS AND METHODS

Binding assays of LBP-containing sera of distinct genotypes with bacterial and synthetic ligands

For binding assays, either LPS (*Escherichia coli* O111:B4 "smooth" LPS, Sigma-Aldrich, Taufkirchen, Germany), Pam_2Cys [Pam_2 Cys-Ser-$(Lys)_4$ × 3 trifluoroacetic acid, EMC Microcollections, Tübingen, Germany], Pam_3Cys (Pam_2Cys-Ser-Lys_4, EMC Microcollections), or 3-sn-PE (3-sn-phosphatidylethanolamine, Sigma-Aldrich) were placed on an ELISA plate in a concentration of 30

https://doi.org/10.4049/immunohorizons.2100095

μg/ml each in carbonate buffer (pH 8.2). Plates were incubated with sera containing LBP of individuals carrying either the common or the rare genotype in increasing concentrations (0.2, 0.39, 0.78, 1.56, 3.13, 6.25, 12.5, and 25%, respectively). These sera were diluted 1:2 from a maximal concentration of 25%. We used sera from different individuals with a mean LBP concentration of 17 ng/ml for common variant sera and 15.8 ng/ml for sera of heterozygous individuals. Following incubation, the photometric reaction was stopped with 1 M H_2SO_4. OD of the bound ligands was photometrically measured at 450 nm in an ELISA reader (Photometer Spectra Fluor Plus, Tecan, Crailsheim, Germany).

Stimulation of murine macrophage cells

Murine macrophage cells (RAW 264.7, Leibniz-Institut DSMZ, Braunschweig, Germany) were stimulated with 1, 10, and 100 ng/ml of two different LPS types (smooth LPS [*E. coli* 0111:B4] and "rough" LPS [*Salmonella minnesota* Re595, Sigma-Aldrich]) and two different lipopeptides (Pam_2Cys [Pam_2Cys-Ser-$(Lys)_4$ × 3 TFA, EMC Microcollections] and Pam_3Cys [Pam_3Cys-Ser-$(Lys)_4$, EMC Microcollections]) in addition to serum of individuals with different genotypes (concentrations of either 1, 2, and 5%). Concentrations of TNF were determined at 4 h using ELISA (DPC Biermann, Bad Nauheim, Germany). All measurements were performed in duplicate, resulting in four values per experiment.

In silico analysis

The sequence information about human LBP SNP rs2232618 was retrieved from dbSNP (http://www.ncbi.nlm.nih.gov/SNP/). MutPred was used to determine the effect of the amino acid substitutions (41). To investigate the secondary structures of common and rare variants, PSIPRED was used (42). I-Mutant 3.0 (http://gpcr2.biocomp.unibo.it/cgi/predictors/I-Mutant3.0/I-Mutant3.0.cgi) was applied for the determination of free energy change (ΔΔG) and protein stability changes owing to single-site mutations (43). The crystal structure of the LBP protein was obtained from Protein Data Bank (PDB identifier [ID]: 4M4D) (44). This was used as a template for generating the three-dimensional structure of common and rare variant human LBP. The three-dimensional structures were generated and energy minimized with SWISS-MODEL and Swiss-PdbViewer, respectively (45, 46). For the purpose of validating these structures, PROSA, ProQ, and SAVES (https://saves.mbi.ucla.edu/) were used (47, 48). Finally, the modeled structures of human LBP common and rare variant types were visualized with PyMOL. Docking of LPS with variants of human LBP were carried out using PatchDock and Firedock software (49, 50). The software DUET (http://biosig.unimelb.edu.au/duet/) was applied to study the role of mutation on the protein structure, using a combination of support vector machine and machine learning algorithms. The implication of mutation on the domain core stability was predicted using ELASPIC (51). ProFunc was used to figure out the alterations between common and rare variants of the proteins regarding functional clefts and cavities (52). ConSurf estimated the conservation profile of the key residues related to functional regions in the structures (53). The differences in the conserved residues of the major functional clefts were studied. CASTp was employed to examine the prevalence of functional pockets in the modeled structures (54). The solvent-accessible area and changes because of mutations were determined with GETAREA (55).

We also subjected the sequence information from the L variant of LBP SNP rs2232613 described in (37) to MutPred, PSIPRED, and I-Mutant 3.0, respectively, and analyzed the modeled structures of this variant with DUET, ELASPIC, ProFunc, ConSurf, CASTp, and GETAREA.

Genotyping

The frequency of the LBP SNP F436L (rs2232618) was determined by real-time PCR assays with subsequent melting curve analysis using the LightCycler 1.5 (Roche Diagnostics, Mannheim, Germany). Sequenced controls representing different genotypes were included in each reaction. Oligonucleotides used for genotyping were as follows: primers, forward: 5′-TTTGCTTTTCCCAAGCGTT-3′ and reverse: 5′-GAGCCCTGTTTTCCAAGTCC-3′; and probes, sensor: 5′-CTATTACATCCTTAACACCCTCTAC-FL-3′ and anchor: red 5′-640-CCAAGTTCAATGGTAAGAATCACTGTGG-3′. One reaction volume of 20 μl contained 2 μl 10× PCR Buffer, 2 mM $MgCl_2$, 125 μM NTPs, 5 U Taq polymerase, 3 μg BSA, primers at 0.5 μM (LBP forward/reverse), fluorescence probes at 0.2 μM each, and 5–20 ng DNA. On the LightCycler 1.5 platform, PCR parameters were as follows: initial denaturation at 95°C for 4 min, 40 cycles of denaturation (95°C for 1 s), annealing (56°C for 10 s), and extension (72°C for 8 s) with subsequent melting curve analysis: 1 cycle at 95°C for 10 s, 40°C for 30 s, followed by an increase of temperature to 80°C at a slope of 0.1°C/s. All oligonucleotides were manufactured by TIB MOLBIOL (Berlin, Germany). PCR reagents were obtained from Rapidozym (Berlin, Germany).

Patient selection

The local ethics committee of the Charité – Universitätsmedizin Berlin approved this clinical study (AA3/03/45). DNA testing was permitted by a signed broad written consent including DNA testing before surgery. All steps were performed according to the Helsinki declaration. Statistical analysis was carried out after anonymization of the patients' data. Definition of sepsis (systemic inflammatory response syndrome, sepsis, severe sepsis, and septic shock) was based on published criteria (56). We did not reclassify the patients according to new sepsis definitions because recent publications show that matching is not reliable (57, 58).

The patient cohort from this study was previously described (59). Infections were defined as described by the clinical classification for nosocomial infections of the National Institutes of Health (60). A total number of 363 patients fulfilled the inclusion criteria. Severity of disease was assessed by the Simplified Acute Physiology Score on admission (61). Patients were followed up until discharge from the hospital. Patient DNA was extracted

from blood or tissue specimens collected prior to surgery and were examined for the LBP SNPs.

Then, 675 individuals from a group of 692 volunteers (healthy individuals and blood donors) served as controls for frequencies of these SNPs. Characteristics of these individuals were published recently (62). All individuals consented to genetic testing. Blood donors were anonymized, and the healthy individuals gave written informed consent. Either blood or oral swabs were used for DNA extraction using QIAamp DNA Mini Kit (QIAGEN, Hilden, Germany).

Statistical analysis

Contingency tables were statistically tested with the χ^2 test or Fisher exact test where appropriate for differences in frequencies. Odds ratios (OR) were determined using the χ^2 test. Differences in numerical data were compared with unpaired *t* test or Mann–Whitney *U* test. For statistical analysis, the IBM SPSS Statistics 20.0 software package (IBM) and the Prism 8 Software package (GraphPad Software) were used. A two-tailed $p < 0.05$ was considered statistically significant.

RESULTS

Binding of bacterial or synthetic ligands to serum of carriers with the F436L genotype

We hypothesized that the F436L variant of LBP was associated with altered binding of bacterial ligands. To study this, we incubated plates containing different bacterial ligands to the binding of progressively diluted serum of individuals with different genotypes. For all tested ligands, we were able to record reduced binding in carriers of the F436L mutation of LBP as shown in Fig. 1. Very low concentrations showed only little influence that was not statistically significant. When reaching increased concentrations (3.13% up to 25% of serum), carriers of the mutation bound ligands to a lesser degree.

This was detectable for ligands originating from Gram-negative bacteria (LPS 0111:B4) for serum concentrations of 6.25 and 12.5%, in which binding of LPS differed significantly between common and rare variant LBP (6.25: 0.507 versus 0.354, $p = 0.048$ and 12.5: 0.734 versus 0.526, $p = 0.010$) (Fig. 1A). This was as detectable in ligands from Gram-positive bacteria, although to a lesser degree. In this study, binding of the lipopeptide Pam_2Cys was markedly reduced in all experiments (0.78%: 0.169 versus 0.155, $p = 0.026$; 1.56%: 0.231 versus 0.179, $p = 0.002$; 3.125%: 0.248 versus 0.187, $p < 0.001$; 6.25%: 0.254 versus 0.187, $p < 0.001$; 12.5%: 0.250 versus 0.196, $p < 0.001$; and 25%: 0.234 versus 0.194, $p < 0.001$) (Fig. 1B). Similar results were seen in binding of the lipopeptide Pam_3Cys, although only for higher concentrations of serum (6.25%: 0.291 versus 0.226, $p = 0.047$; 12.5%: 0.327 versus 0.245, $p = 0.034$; and 25%: 0.311 versus 0.21, $p = 0.003$). (Fig. 1C). Binding of the artificial ligand 3-*sn*-phosphatidylethalonamine was also markedly reduced in patients carrying the genetic variation (0.78%: 0.175 versus 0.136, $p = 0.004$; 1.56%: 0.274 versus 0.198, $p = 0.006$; 3.125%: 0.361 versus 0.251, $p < 0.001$; 6.25%: 0.378 versus 0.263, $p < 0.001$; 12.5%: 0.426 versus 0.297, $p = 0.002$; and 25%: 0.491 versus 0.354, $p = 0.003$) (Fig. 1D). An additional finding was a saturation effect seen with increasing serum concentrations. This effect was detectable for all ligands, confirming previous observations (12). We saw no influence of the genotype with this regard.

Differences in genotypes affect LPS stimulation of murine macrophage cell lines

After we found an effect on binding of ligands induced by the protein changes brought about by the genetic variations of LBP, we investigated whether this would affect their ability to facilitate the LPS transfer to TLR4 and thus the release of the proinflammatory cytokine TNF. We incubated RAW cells with LPS and other ligands in the absence and presence of sera obtained from individuals differing in their LBP genotype. As expected, we found the LPS-induced release of TNF to depend on the addition of LBP-containing serum. Mean concentrations of TNF induced by the smooth LPS 0111:B4 (containing carbohydrates in addition to the lipid A core) increased markedly stronger as compared with the rough variant of LPS Re595 (see Supplemental Table I). As is shown in Fig. 1E, the addition of LBP-containing serum induced a severalfold stronger release of TNF as compared with LPS 0111:B4 alone. In detail, 100 ng/ml LPS 0111:B4 with 1% serum resulted in a mean ± SEM of 6514 ± 667.0 ng/ml TNF with serum of rare variant LBP compared with 8655 ± 538.6 ng/ml TNF with added common variant serum (*p* value: 0.012; Mann–Whitney *U* test).

In the experiments with lower concentrations of LPS 0111:B4 (1 and 10ng/ml) with 1% serum either from common variant or rare variant, the results in individuals was lower TNF values with a similar trend between the genotypes just failing to reach statistical significance. Mean ± SEM of TNF was 4248 ± 1006 ng/ml for the rare variant and 2327 ± 626.8 ng/ml for common variant serum ($p = 0.16$, unpaired *t* test). Interestingly, adding 2 or 5% serum to the above-mentioned doses resulted in a less pronounced difference (LPS 0111:B4 10 ng/ml + 5% serum, $p = 0.98$; LPS B4 100 ng/ml + 5% serum, $p = 0.61$, unpaired *t* test) (Fig. 1E, Supplemental Table I). Overall, the "response curve" was flatter, with individuals carrying the rare variant.

Adding rough LPS (Re595) to the LBP-containing sera resulted in an overall lower induction of TNF and no statistically significant differences between the genotypes. Other experiments with lipopeptides (Pam_2Cys or Pam_3Cys) and LBP-containing sera with different genotypes showed an increase in TNF concentrations, but there was no statistical difference between the genotype groups (see Supplemental Table I). Of note, the number of repetitions in these experiments was low because of sparse amounts of human sera available for the different genotypes.

Computational analysis of the LBP SNP F436L

We assessed a potential impact of the F436L LBP genotype on protein function on a structural level by computer modeling.

https://doi.org/10.4049/immunohorizons.2100095

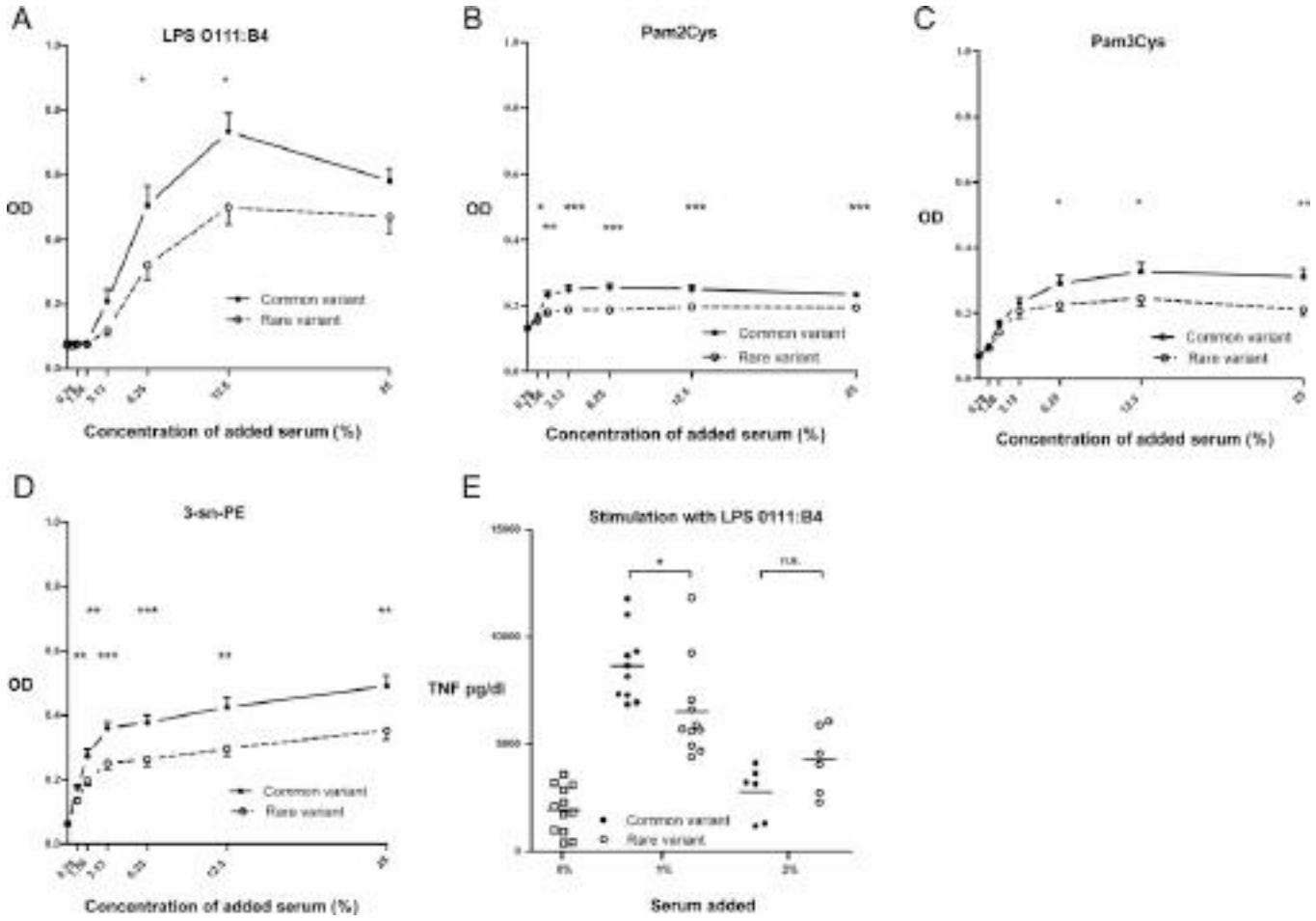

FIGURE 1. (A) Binding of progressively diluted serum of individuals with common and rare LBP variant with the known LBP ligands LPS O111:B4 and (B) Pam_2Cys, (C) Pam_3Cys, and (D) 3-sn-PE.

Binding was assessed by OD. OD values were compared using the Mann–Whitney nonparametric test. All data are expressed as mean ± SEM. Error bars are shown either above or below respective values. *$p < 0.05$, **$p < 0.01$, ***$p < 0.001$ denote statistically significant differences. (**E**) Stimulation of RAW 264.7 cells with 100 ng LPS 0111:B4. Left shows stimulation with no additional LBP. Middle and right show costimulation with LBP-containing serum 1 and 2%, respectively, from carriers with either common or rare variants. *$p < 0.05$. n.s., not statistically significant.

Three-dimensional structural models of the common and rare variant human LBP protein were generated by homology modeling based on the crystal structure of LBP recently published (37, 63). The LBP molecule is boomerang shaped with three functionally distinct parts. The first is the N-terminal part, which is believed to primarily interact with LPS (9). The C-terminal portion is potentially interacting with CD14, and this subsequently leads to TLR4 interaction and thus may initiate signaling. The groove in human LBP is a unique region differing from related proteins such as bactericidal/permeability increasing protein (21). Position 436 is buried and located inside the C-terminal domain of LBP between the A′ loop and the Phe core at the tip of the molecule. In both models, F436/L436 was positioned within an α-helix (helix B) lining the inner surface of the C-terminal phospholipid binding pocket formed by helix A and B and the β2 and β6 sheets (23). Fig. 2A shows the three-dimensional structure of the LBP variant and the location of the F436L exchange in the groove region.

We compared hydrophobicity, surface charge, and the intactness of LBP-specific structural features such as the Phe core and the LPS binding groove formed by the A′ loop (21). The close ups and top view portrayed the nature of the interior surface of common and rare variant protein in Fig. 2B–E.

When analyzing the inner surface of this pocket, we noted that one continuous hydrophobic channel is formed in the common variant model, similar to the murine LBP crystal structure in which both phospholipid acyl chains that were seen in the crystal could be accommodated in the channel (23). In the L436 model, however, the leucine side chain protruded into this channel, thus effectively blocking the channel and reducing the accessible size of the pocket by 50%. This means in the L436 structure, only one acyl chain could be accommodated as

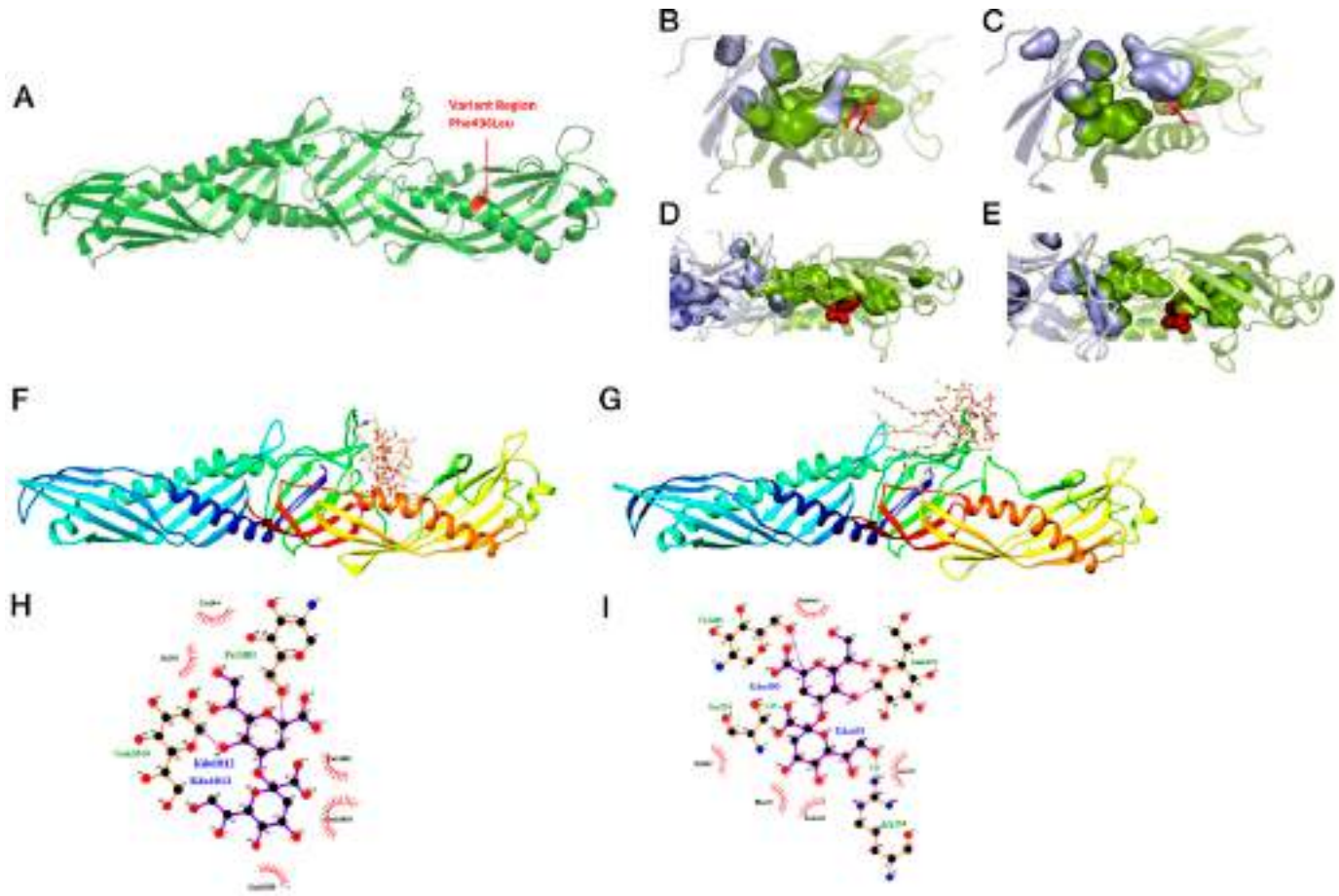

FIGURE 2. Overview of the F436L and the common variant with regard to location, effects on molecular structure, and LPS binding caused by mutational changes in the amino acid chain.

(**A**) Ribbon diagram of the three-dimensional structures of human LBP highlighting the location of the variant region in red. Left, central and right portion of the structures represented N-terminal, central, and C-terminal regions. (**B** and **C**) Close up of the interior surface of the common variant showing either Phe (F436) residue (B) or leucine (L436) residue (C) in red. (**D** and **E**) Top views of the interior surfaces from the common (D) and rare human LBP variant (E) showing conformational differences as a result of the amino acid change. (**F** and **G**) Docking of LPS to the common variant (F) in the groove region shows a marked difference as compared with the rare human LBP (G) variant with LPS. (**H** and **I**) The comparison of ligand plots of the common human LBP variant (H) and the rare variant (I) shows that there are potentially changes in the molecular interaction between the LBP residues and LPS based on our analysis.

evident from superpositions with phospholipid molecules. We also found that the rare variant differed in size of the first major cleft from the common variant (2845.0 versus 2416.08 $Å^3$). These clefts are known to harbor functional residues (64). The highlighted alterations in surface topography may therefore cause changes in molecular function.

Molecular docking simulations show the interaction between human LBP and LPS. Fig. 2 H–I demonstrates the differences in docking residues of human LBP with LPS in both variants in the groove region. In the common variant, Ile251 and Tyr284 were the supporting residues for a potential interaction with LPS. Interestingly, Ser224 and Arg254 residues can interact with LPS in the rare variant in addition to other supporting residues. This difference in docking residues in the common variant and rare variant could cause structural conformational rearrangements influencing molecule function. These results are supported by the observations from MutPred, I-Mutant 3.0, DUET, and ELASPIC, which indicate a loss of stability of the rare variant LBP. This is further supported by solvent accessibility analysis showing a change in polar energy, surface atoms, and buried atoms.

The results are presented in Tables I and II. An additional comparison with the rs2232613 rare variant described in a previous study is presented in Supplemental Table III.

Distribution of genotypes in the study cohorts

To evaluate if the tested genotypes would potentially influence susceptibility to and course of clinical infections, we examined a cohort of patients following surgery. In this cohort, 290 of 363 patients carried the more frequent variant. In 73 patients,

https://doi.org/10.4049/immunohorizons.2100095

TABLE I. Comparison of structural stability between human LBP common and rare variant (F436L) using in silico tools

Analysis with MutPred (Result of nsSNP rs2232618 [F436L])			
nsSNP	Amino acid change	Loss of stability	Loss of helix
rs2232618	F436L	$p = 0.07$	$p = 0.1299$
Analysis of Stability Changes in LBP Variants Using I-Mutant3.0, DUET, and ELASPIC			
Amino acid change	I-Mutant3.0	DUET	ELASPIC domain core
F436L	−1.29 (destabilizing)[a]	−0.151 (destabilizing)[a]	−0.794 (destabilizing)[a]

[a]All values shown as ΔΔG/kcal/mol.

the LBP SNP F436L (rs2232618) was present. Of these, 69 patients were heterozygous and 4 were homozygous carriers of the mutated alleles. We found a similar distribution of frequency in the control group consisting of 675 healthy volunteers: 555 were carriers of the common variant alleles only, 112 were heterozygous, and 8 were homozygous. The resulting allele frequencies were 0.091 and 0.095, respectively, as shown in Table III. The SNP was in complete Hardy–Weinberg equilibrium in both groups (patients: $\chi^2 < 0.002$, $p = 0.96$; control group: $\chi^2 = 0.75$, $p = 0.39$). The distribution of the SNP is in accordance with available data (http://www.ensembl.org/Homo_sapiens/Transcript/Haplotypes?db=core;g=ENSG00000129988;r=20:38346482-38377013;t=ENST00000217407).

Influence of LBP SNP F436L on infection susceptibility and clinical course in ICU patients

Comparison of clinical characteristics between the genotype groups revealed no differences with regard to age, gender distribution, or preexisting conditions. Overall, preadmission disease severity scores (American Society of Anesthesiologists classification and Simplified Acute Physiology Score) were equal, as shown in Supplemental Table II. After performing risk calculation, none of these conditions influenced susceptibility to infections or outcome (data not shown). Of the 363 studied patients, 202 (55.7%) developed infections in the ICU. In terms of sepsis susceptibility, no influence of the studied genotype could be found (common variant: 163/290 [56.2%]; F436L: 39/73 [53.4%]), which was also the case for the type of infection. These results are presented in Table IV. The most frequent infection in three groups was pneumonia followed by abdominal and wound infections. The genotypes had no influence on the prevalence of infections nor on the causing pathogens. The distribution of pathogens was equal in all groups. In ∼10% of the patients, there was more than one pathogen identified, and in a similar number of patients, no pathogen could be retrieved by microbiological examination. Both facts were not different between the groups and did not influence further outcome (data not shown).

As compared with the prevalence of infections, we found an association with severity of infection between the genotype groups. The F436L genotype group showed a lower risk for septic shock (OR 0.34; 95% confidence interval [CI] 0.11–1.02; $p < 0.05$) as compared with the common variant group. Furthermore, patients carrying the F436L allele had a lower mortality associated with overall infectious complications (2.6 versus 10.4%) or septic shock (25.0 versus 39.0%) as compared with common variant patients. The latter fact was not statistically significant (OR 0.23; 95% CI 0.03–1.75; $p = 0.21$ for infectious complications;

TABLE II. Structural comparison of human LBP common and rare variant (F436L) using in-silico tools

Difference in Secondary Structure between LBP Variants		
Feature	CV[a]	RV[a]
Coil	32.01	30.56
Helix	26.40	26.40
Strands	41.58	43.03
Difference in Highly Conserved Residues of Cleft 1 and Cleft 2 between LBP Variants		
Clefts	CV	RV
Cleft 1	287, 289	287, 289, 316, 379, 400
Cleft 2	38, 39, 93, 142, 205, 209, 215, 236, 276, 451	38, 39, 50, 93, 142, 205, 209, 215, 236, 276, 451, 478
Analysis of LBP Variants for Functional Pockets Using CASTp		
No. of pockets	CV	RV
	64	65
Comparison of the Solvent Accessibility Analyzed by GETAREA between LBP Variants		
Feature	CV	RV
Polar energy	8726.01	8781.85
No. of surface atoms	2137	2149
No. of buried atoms	1446	1408

[a]Values as percentage of structural components.
CV, common variant; RV, rare variant.

TABLE III. Distribution of genotypes in the studied cohorts

	Number of Individuals (%)		Allele Frequencies	
	Patients (n = 363)	Controls (n = 675)	Patients	Controls
Common variant F436L	290 (77.3%)	555 (82.2%)		
Heterozygous	69 (18.4%)	112 (16.6%)	0.091	0.095
Homozygous	4 (1.1%)	8 (1.2%)		

The genotyping data reported in this study reveal a similar distribution of alleles as compared with HapMap data and The Innate Immunity Program for Genomic Applications data regarding populations of European ancestry (HapMap: 0.084 and 0.103, The Innate Immunity Program for Genomic Applications: 0.043; p = 0.794, using χ^2 test).

OR 0.47; 95% CI 0.05–4.92; p = 0.64 for septic shock, respectively). We found no difference in the clinical course of homozygous compared with heterozygous patients.

Interestingly, we found that the previously studied P333L SNP showed almost opposite effects in most of the studied aspects (37). With the additional genotyping data for the study cohort, we were able to directly compare both rare variants. We found mortality was significantly higher in the P333L group than in the F436L group (21.2%: 7/33 versus 2.4%: 1/39; p = 0.02 tested with Fisher exact test). However, we noted differences in the rate of preexisting conditions between the genotype groups that did not reach statistical significance, except for diabetes. More details for the comparison of these variants are provided in the supplemental material (Supplemental Table IV). Overall, the genotype groups did not differ with regards to risk factors for worse outcome.

DISCUSSION

This work shows a series of phenotypic effects of a genetic variation in the LBP gene on either functional properties of the molecule as well as clinical effects. We found that ligand binding to LPS was reduced when the serum of carriers of the rare variant was added as compared with serum of individuals carrying the common variant. This might be explained by a physically impaired adherence of these molecules to the ligand binding domain of LBP. To effectively exert its function, LBP must bind to its ligands to induce CD14 and thus TLR binding and consecutively induce intracellular signal transduction (65). The experimental concept employed in this study aimed at simulating macrophage function in the presence of serum proteins that are also part of the ligand transfer like MD-2 or CD14. In our cell stimulation experiments, we found lower cytokine concentrations induced in macrophages by bacterial ligands associated with the rare variant of LBP. This was particularly the case with high concentrations of LPS and the serum of individuals carrying the rare variant. Taken together, it appears that reduced binding of LBP ligands associated with the rare variant leads to lesser pronounced induction of proinflammatory cytokines. In the early response to bacterial infection, the release of high concentrations of proinflammatory cytokines might be associated with a more pronounced inflammatory reaction. Recent sepsis definitions articulate a dysregulated or uncontrolled immune reaction as a major factor for morbidity and mortality in this setting (66). However, the host ability to combat bacteria might also be related to adequate amounts of cytokines released (67).

The function of LBP is not only restricted to the transfer from LPS or other ligands to its innate immune receptors but also has immune inhibiting properties, particularly in higher acute-phase concentrations, by scavenging LPS (23). The observed genetic changes might affect this function of the molecule as well. In our experiments, higher concentrations of LBP did not result in increased binding of the molecule. However, we also could confirm previous findings, which show that high concentrations of serum tend to scavenge LPS, but this effect was reduced in the rare variant (Fig. 1A). This effect was also seen with binding to bacterial lipopeptides, although the effect was less pronounced. Interestingly, binding to a nonbacterial ligand did not show this effect.

TABLE IV. Clinical characteristics of patients with infections (n = 202)

Characteristic	Common Variant Group (n = 163)	Rare Variant Group F436L (n = 39)	p Value
Site of infection (No. [%])			
Pneumonia	67 (41.1)	17 (43.6)	0.86
Peritonitis	29 (17.8)	5 (12.8)	0.63
Abscess	45 (27.6)	12 (30.8)	0.70
Urinary tract infections	4 (2.5)	–	1.00
Other	18 (11.0)	5 (12.8)	0.78
Type of microorganism (No. [%])[a]			
Gram negative	95 (58.3)	24 (61.5)	0.86
Gram positive	61 (37.4)	18 (46.2)	0.36
Fungi	12 (7.4)	2 (5.1)	1.00
Outcome (No. [%])			
Sepsis	122 (74.8)	35 (89.7)	–
Septic Shock	41 (25.2)	4 (10.3)	<0.05
Mortality	17 (10.4)	1 (2.6)	0.21

[a]Numbers not adding up to 100% because of missing data or more than one detected microorganism in a patient. Statistical analysis for contingency tables using χ^2 test except for mortality, where Fisher's exact test was applied.

In an in silico approach, we tried to explain the results through molecular modeling of the rare variant as compared with the common variant. In the F436L variant, the changed amino acid is situated close to the groove of the molecule near the center. This means that in the L436 structure, only one acyl chain could be accommodated, as evident from superpositions with phospholipid molecules. Although this has not been formally proven, from a structural perspective, it appears plausible that the two hydrophobic channels in LBP contribute to LPS or lipopeptide binding. Therefore, the F436L variant might alter the ability to bind these hydrophobic substances. Analysis of MutPred implied change in function of the protein because of destabilization.

Examination of the three-dimensional structures revealed some structural changes because of amino acid change from F436L. This is further supported by the destabilization occurring owing to free energy change based on I-Mutant 3.0, DUET, and ELASPIC analysis. Additionally, docking analysis revealed a shift in the amino acids residues binding to LPS in the rare variant compared with the common variant. Topographical and conformational changes associated with the amino acid change from F436 to L436 is evident from the altered binding of the rare variant to LPS. An increase in size of cleft 1 in the rare variant of LBP demonstrated that it had a higher number of active sites and was more receptive for ligand binding interactions owing to extra structural rearrangements. Finally, functional pockets and the overall number of highly conserved residues from two major functional clefts of the rare variant were higher in number as compared with the common variant. Comparatively higher number of pockets in the rare variant point to the fact that it may be slightly more flexible than the common variant.

From the clinical data of our study, we show a lower risk of septic shock in the presence of the rare LBP variant. It was not associated with sepsis prevalence and susceptibility to infection. Although not statistically significant, we also found an association with reduced mortality. Clinical effects of LBP variants have been observed in previous studies showing an influence on susceptibility to and also severity of infections or other inflammatory diseases (34). As we have shown in a previous study, another functional LBP SNP (P333L and rs2232613) was associated with a more severe course of sepsis (37). By direct comparison of these SNPs in our clinical cohort, we observed a marked difference in the clinical course of infections, suggesting an opposite effect.

In other studies, LBP variants like an LBP haplotype variation were associated with an increased rate of Gram-negative infections in recipients of homolog bone marrow for hematologic malignancies (30). In other patients, LBP haplotype variation was a risk factor for ventilator-associated pneumonia and sepsis in pediatric patients (32, 33). The LBP haplotypes variations did include wildtype and mutated variants. Therefore, no conclusive picture regarding risk alleles could be drawn from these data. Interestingly, the F436L SNP examined in this study was associated with a higher prevalence of sepsis in a cohort of trauma victims of Han Chinese origin with a different demographic composition (38, 39).

In conclusion, this study shows a functional relevant SNP in the LBP gene that is associated with changes in its properties regarding binding capability and function with regard to stimulation of macrophages. In silico analysis revealed molecular alterations that could be associated with these functional changes. We found a favorable outcome following severe infections in patients after surgery. We propose several potential ways of how a loss of function or a gain of function could be explained by this variant and potentially contribute to patient outcome.

There are potential limitations of our study. First, in our experimental approach, we used a xenogenic model, including mouse macrophages and human serum. In our view, this is justified by the fact that human macrophages (i.e., derived from transformed THP-1 cells) are not readily available and might not display full functional capacity. Human serum used in this study, in addition, contains functional molecules that are needed for sufficient signal transduction in contrast to recombinant protein. The retrospective analysis of only two variants of LBP, furthermore, is a limitation of this study. The association found should be studied prospectively in a broader approach, including other nonsynonymous SNPs.

To further delineate functional consequences regarding concentration-dependent effects of this SNP, however, more experiments may be necessary. Elucidating the complex cascade of events leading from recognition of pathogens to systemic inflammation and disease may in the future lead to novel intervention strategies currently needed to improve the outcome of sepsis. Furthermore, a genetic risk stratification may allow for better prevention of clinical complications in patients at risk for infectious diseases.

DISCLOSURES

The authors have no financial conflicts of interest.

ACKNOWLEDGMENTS

We thank Fränzi Creutzburg, Diana Woellner, and Ina Wendler (Institute of Microbiology, Charité, Berlin, Germany) for excellent technical assistance throughout this project. Michael Kabesch (Children's University Hospital Regensburg, Department of Pediatric Pneumology and Allergy, Campus St. Hedwig, Regensburg, Germany) is acknowledged for providing sera containing mutant LBP.

REFERENCES

1. Schumann, R. R., C. J. Kirschning, A. Unbehaun, H. P. Aberle, H. P. Knope, N. Lamping, R. J. Ulevitch, and F. Herrmann. 1996. The lipopolysaccharide-binding protein is a secretory class 1 acute-phase protein whose gene is transcriptionally activated by APRF/STAT/3 and other cytokine-inducible nuclear proteins. *Mol. Cell. Biol.* 16: 3490–3503.

2. Schumann, R. R., S. R. Leong, G. W. Flaggs, P. W. Gray, S. D. Wright, J. C. Mathison, P. S. Tobias, and R. J. Ulevitch. 1990. Structure and function of lipopolysaccharide binding protein. *Science* 249: 1429–1431.
3. Knapp, S., S. Florquin, D. T. Golenbock, and T. van der Poll. 2006. Pulmonary lipopolysaccharide (LPS)-binding protein inhibits the LPS-induced lung inflammation in vivo. *J. Immunol.* 176: 3189–3195.
4. Vreugdenhil, A. C., M. A. Dentener, A. M. Snoek, J. W. Greve, and W. A. Buurman. 1999. Lipopolysaccharide binding protein and serum amyloid A secretion by human intestinal epithelial cells during the acute phase response. *J. Immunol.* 163: 2792–2798.
5. Albers, J. J., S. Vuletic, and M. C. Cheung. 2012. Role of plasma phospholipid transfer protein in lipid and lipoprotein metabolism. *Biochim. Biophys. Acta* 1821: 345–357.
6. Alva, V., and A. N. Lupas. 2016. The TULIP superfamily of eukaryotic lipid-binding proteins as a mediator of lipid sensing and transport. *Biochim. Biophys. Acta* 1861(8, 8 Pt B)913–923.
7. Gautier, T., and L. Lagrost. 2011. Plasma PLTP (phospholipid-transfer protein): an emerging role in 'reverse lipopolysaccharide transport' and innate immunity. *Biochem. Soc. Trans.* 39: 984–988.
8. Levels, J. H., D. Pajkrt, M. Schultz, F. J. Hoek, A. van Tol, J. C. Meijers, and S. J. van Deventer. 2007. Alterations in lipoprotein homeostasis during human experimental endotoxemia and clinical sepsis. *Biochim. Biophys. Acta* 1771: 1429–1438.
9. Ryu, J. K., S. J. Kim, S. H. Rah, J. I. Kang, H. E. Jung, D. Lee, H. K. Lee, J. O. Lee, B. S. Park, T. Y. Yoon, and H. M. Kim. 2017. Reconstruction of LPS Transfer Cascade Reveals Structural Determinants within LBP, CD14, and TLR4-MD2 for Efficient LPS Recognition and Transfer. *Immunity* 46: 38–50.
10. Tobias, P. S., K. Soldau, N. M. Iovine, P. Elsbach, and J. Weiss. 1997. Lipopolysaccharide (LPS)-binding proteins BPI and LBP form different types of complexes with LPS. *J. Biol. Chem.* 272: 18682–18685.
11. Tapping, R. I., and P. S. Tobias. 1997. Cellular binding of soluble CD14 requires lipopolysaccharide (LPS) and LPS-binding protein. *J. Biol. Chem.* 272: 23157–23164.
12. Schumann, R. R. 2011. Old and new findings on lipopolysaccharide-binding protein: a soluble pattern-recognition molecule. *Biochem. Soc. Trans.* 39: 989–993.
13. Wurfel, M. M., S. T. Kunitake, H. Lichenstein, J. P. Kane, and S. D. Wright. 1994. Lipopolysaccharide (LPS)-binding protein is carried on lipoproteins and acts as a cofactor in the neutralization of LPS. *J. Exp. Med.* 180: 1025–1035.
14. Vreugdenhil, A. C., A. M. Snoek, C. van 't Veer, J. W. Greve, and W. A. Buurman. 2001. LPS-binding protein circulates in association with apoB-containing lipoproteins and enhances endotoxin-LDL/VLDL interaction. *J. Clin. Invest.* 107: 225–234.
15. Mueller, M., K. Brandenburg, R. Dedrick, A. B. Schromm, and U. Seydel. 2005. Phospholipids inhibit lipopolysaccharide (LPS)-induced cell activation: a role for LPS-binding protein. *J. Immunol.* 174: 1091–1096.
16. Schröder, N. W., H. Heine, C. Alexander, M. Manukyan, J. Eckert, L. Hamann, U. B. Göbel, and R. R. Schumann. 2004. Lipopolysaccharide binding protein binds to triacylated and diacylated lipopeptides and mediates innate immune responses. *J. Immunol.* 173: 2683–2691.
17. Schröder, N. W., B. Opitz, N. Lamping, K. S. Michelsen, U. Zähringer, U. B. Göbel, and R. R. Schumann. 2000. Involvement of lipopolysaccharide binding protein, CD14, and Toll-like receptors in the initiation of innate immune responses by *Treponema* glycolipids. *J. Immunol.* 165: 2683–2693.
18. Weber, J. R., D. Freyer, C. Alexander, N. W. Schröder, A. Reiss, C. Küster, D. Pfeil, E. I. Tuomanen, and R. R. Schumann. 2003. Recognition of pneumococcal peptidoglycan: an expanded, pivotal role for LPS binding protein. *Immunity* 19: 269–279.
19. Nyström, J., J. Stenkvist, A. Häggblom, O. Weiland, and P. Nowak. 2015. Low levels of microbial translocation marker LBP are associated with sustained viral response after anti-HCV treatment in HIV-1/HCV co-infected patients. *PLoS One* 10: e0118643.
20. Wurfel, M. M., and S. D. Wright. 1997. Lipopolysaccharide-binding protein and soluble CD14 transfer lipopolysaccharide to phospholipid bilayers: preferential interaction with particular classes of lipid. *J. Immunol.* 158: 3925–3934.
21. Yu, B., E. Hailman, and S. D. Wright. 1997. Lipopolysaccharide binding protein and soluble CD14 catalyze exchange of phospholipids. *J. Clin. Invest.* 99: 315–324.
22. Cunningham, S. C., D. L. Malone, G. V. Bochicchio, T. Genuit, K. Keledjian, J. K. Tracy, and L. M. Napolitano. 2006. Serum lipopolysaccharide-binding protein concentrations in trauma victims. *Surg. Infect. (Larchmt.)* 7: 251–261.
23. Zweigner, J., H. J. Gramm, O. C. Singer, K. Wegscheider, and R. R. Schumann. 2001. High concentrations of lipopolysaccharide-binding protein in serum of patients with severe sepsis or septic shock inhibit the lipopolysaccharide response in human monocytes. *Blood* 98: 3800–3808.
24. Lamping, N., R. Dettmer, N. W. J. Schröder, D. Pfeil, W. Hallatschek, R. Burger, and R. R. Schumann. 1998. LPS-binding protein protects mice from septic shock caused by LPS or gram-negative bacteria. *J. Clin. Invest.* 101: 2065–2071.
25. Hamann, L., C. Alexander, C. Stamme, U. Zähringer, and R. R. Schumann. 2005. Acute-phase concentrations of lipopolysaccharide (LPS)-binding protein inhibit innate immune cell activation by different LPS chemotypes via different mechanisms. *Infect. Immun.* 73: 193–200.
26. Kopp, F., S. Kupsch, and A. B. Schromm. 2016. Lipopolysaccharide-binding protein is bound and internalized by host cells and colocalizes with LPS in the cytoplasm: Implications for a role of LBP in intracellular LPS-signaling. *Biochim. Biophys. Acta* 1863: 660–672.
27. Arcaroli, J., M. B. Fessler, and E. Abraham. 2005. Genetic polymorphisms and sepsis. *Shock* 24: 300–312.
28. Nakada, T. A., W. Takahashi, E. Nakada, T. Shimada, J. A. Russell, and K. R. Walley. 2019. Genetic polymorphisms in sepsis and cardiovascular disease: do similar risk genes suggest similar drug targets? *Chest* 155: 1260–1271.
29. Kumpf, O., and R. R. Schumann. 2010. Genetic variation in innate immunity pathways and their potential contribution to the SIRS/CARS debate: evidence from human studies and animal models. *J. Innate Immun.* 2: 381–394.
30. Chien, J. W., M. J. Boeckh, J. A. Hansen, and J. G. Clark. 2008. Lipopolysaccharide binding protein promoter variants influence the risk for Gram-negative bacteremia and mortality after allogeneic hematopoietic cell transplantation. *Blood* 111: 2462–2469.
31. Barber, R. C., and G. E. O'Keefe. 2003. Characterization of a single nucleotide polymorphism in the lipopolysaccharide binding protein and its association with sepsis. *Am. J. Respir. Crit. Care Med.* 167: 1316–1320.
32. Flores, C., L. Pérez-Méndez, N. Maca-Meyer, A. Muriel, E. Espinosa, J. Blanco, R. Sangüesa, M. Muros, J. G. Garcia, and J. Villar; GRECIA and Gen-SEP groups. 2009. A common haplotype of the LBP gene predisposes to severe sepsis. *Crit. Care Med.* 37: 2759–2766.
33. Jabandziev, P., M. Smerek, J. Michalek, M. Fedora, L. Kosinova, J. A. Hubacek, and J. Michalek. 2014. Multiple gene-to-gene interactions in children with sepsis: a combination of five gene variants predicts outcome of life-threatening sepsis. *Crit. Care* 18: R1.
34. Meng, L., Z. Song, A. Liu, U. Dahmen, X. Yang, and H. Fang. 2021. Effects of Lipopolysaccharide-Binding Protein (LBP) Single Nucleotide Polymorphism (SNP) in Infections, Inflammatory Diseases, Metabolic Disorders and Cancers. *Front. Immunol.* 12: 681810.
35. Hubacek, J. A., F. Stüber, D. Fröhlich, M. Book, S. Wetegrove, M. Ritter, G. Rothe, and G. Schmitz. 2001. Gene variants of the bactericidal/permeability increasing protein and lipopolysaccharide

binding protein in sepsis patients: gender-specific genetic predisposition to sepsis. *Crit. Care Med.* 29: 557–561.
36. Korhonen, T., S. Grauling-Halama, N. Halama, S. Silvennoinen-Kassinen, M. Leinonen, and P. Saikku. 2006. Rapid genotyping of lipopolysaccharide-binding protein (LBP) C(1341)-->T (Leu(436)-->Phe) polymorphism by LightCycler real-time PCR. *J. Immunol. Methods* 317: 171–174.
37. Eckert, J. K., Y. J. Kim, J. I. Kim, K. Gürtler, D. Y. Oh, S. Sur, L. Lundvall, L. Hamann, A. van der Ploeg, P. Pickkers, et al. 2013. The crystal structure of lipopolysaccharide binding protein reveals the location of a frequent mutation that impairs innate immunity. *Immunity* 39: 647–660.
38. Zeng, L., W. Gu, A. Q. Zhang, M. Zhang, L. Y. Zhang, D. Y. Du, S. N. Huang, and J. X. Jiang. 2012. A functional variant of lipopolysaccharide binding protein predisposes to sepsis and organ dysfunction in patients with major trauma. *Ann. Surg.* 255: 147–157.
39. Lu, H. X., J. H. Sun, D. L. Wen, J. Du, L. Zeng, A. Q. Zhang, and J. X. Jiang. 2018. LBP rs2232618 polymorphism contributes to risk of sepsis after trauma. *World J. Emerg. Surg.* 13: 52.
40. Niroula, A., and M. Vihinen. 2016. Variation Interpretation Predictors: Principles, Types, Performance, and Choice. *Hum. Mutat.* 37: 579–597.
41. Li, B., V. G. Krishnan, M. E. Mort, F. Xin, K. K. Kamati, D. N. Cooper, S. D. Mooney, and P. Radivojac. 2009. Automated inference of molecular mechanisms of disease from amino acid substitutions. *Bioinformatics* 25: 2744–2750.
42. McGuffin, L. J., K. Bryson, and D. T. Jones. 2000. The PSIPRED protein structure prediction server. *Bioinformatics* 16: 404–405.
43. Bava, K. A., M. M. Gromiha, H. Uedaira, K. Kitajima, and A. Sarai. 2004. ProTherm, version 4.0: thermodynamic database for proteins and mutants. *Nucleic Acids Res.* 32: D120–D121.
44. Berman, H. M., J. Westbrook, Z. Feng, G. Gilliland, T. N. Bhat, H. Weissig, I. N. Shindyalov, and P. E. Bourne. 2000. The Protein Data Bank. *Nucleic Acids Res.* 28: 235–242.
45. Guex, N., M. C. Peitsch, and T. Schwede. 2009. Automated comparative protein structure modeling with SWISS-MODEL and Swiss-PdbViewer: a historical perspective. *Electrophoresis* 30(S1, Suppl 1)S162–S173.
46. Waterhouse, A., M. Bertoni, S. Bienert, G. Studer, G. Tauriello, R. Gumienny, F. T. Heer, T. A. P. de Beer, C. Rempfer, L. Bordoli, et al. 2018. SWISS-MODEL: homology modelling of protein structures and complexes. *Nucleic Acids Res.* 46(W1): W296–W303.
47. Wiederstein, M., and M. J. Sippl. 2007. ProSA-web: interactive web service for the recognition of errors in three-dimensional structures of proteins. *Nucleic Acids Res.* 35: W407–W410.
48. Wallner, B., and A. Elofsson. 2003. Can correct protein models be identified? *Protein Sci.* 12: 1073–1086.
49. Zhang, C., G. Vasmatzis, J. L. Cornette, and C. DeLisi. 1997. Determination of atomic desolvation energies from the structures of crystallized proteins. *J. Mol. Biol.* 267: 707–726.
50. Mashiach, E., D. Schneidman-Duhovny, N. Andrusier, R. Nussinov, and H. J. Wolfson. 2008. FireDock: a web server for fast interaction refinement in molecular docking. *Nucleic Acids Res.* 36: W229–W232.
51. Brender, J. R., and Y. Zhang. 2015. Predicting the Effect of Mutations on Protein-Protein Binding Interactions through Structure-Based Interface Profiles. *PLOS Comput. Biol.* 11: e1004494.
52. Laskowski, R. A., J. D. Watson, and J. M. Thornton. 2003. From protein structure to biochemical function? *J. Struct. Funct. Genomics* 4: 167–177.
53. Ashkenazy, H., E. Erez, E. Martz, T. Pupko, and N. Ben-Tal. 2010. ConSurf 2010: calculating evolutionary conservation in sequence and structure of proteins and nucleic acids. *Nucleic Acids Res.* 38: W529–W533.
54. Liang, J., H. Edelsbrunner, and C. Woodward. 1998. Anatomy of protein pockets and cavities: measurement of binding site geometry and implications for ligand design. *Protein Sci.* 7: 1884–1897.
55. Fraczkiewicz, R., and W. Braun. 1998. Exact and efficient analytical calculation of the accessible surface areas and their gradients for macromolecules. *J. Comput. Chem.* 19: 319–333.
56. Levy, M. M., M. P. Fink, J. C. Marshall, E. Abraham, D. Angus, D. Cook, J. Cohen, S. M. Opal, J. L. Vincent, and G. Ramsay; SCCM/ESICM/ACCP/ATS/SIS. 2003. 2001 SCCM/ESICM/ACCP/ATS/SIS International Sepsis Definitions Conference. *Crit. Care Med.* 31: 1250–1256.
57. Shankar-Hari, M., G. S. Phillips, M. L. Levy, C. W. Seymour, V. X. Liu, C. S. Deutschman, D. C. Angus, G. D. Rubenfeld, and M. Singer; Sepsis Definitions Task Force. 2016. Developing a new definition and assessing new clinical criteria for septic shock: for the third international consensus definitions for sepsis and septic shock (sepsis-3). *JAMA* 315: 775–787.
58. Poutsiaka, D. D., M. C. Porto, W. A. Perry, J. Hudcova, D. J. Tybor, S. Hadley, S. Doron, J. A. Reich, D. R. Snydman, and S. A. Nasraway. 2019. Prospective Observational Study Comparing Sepsis-2 and Sepsis-3 Definitions in Predicting Mortality in Critically Ill Patients. *Open Forum Infect. Dis.* 6: ofz271.
59. Kumpf, O., E. J. Giamarellos-Bourboulis, A. Koch, L. Hamann, M. Mouktaroudi, D. Y. Oh, E. Latz, E. Lorenz, D. A. Schwartz, B. Ferwerda, et al. 2010. Influence of genetic variations in TLR4 and TIRAP/Mal on the course of sepsis and pneumonia and cytokine release: an observational study in three cohorts. *Crit. Care* 14: R103.
60. Garner, J. S., W. R. Jarvis, T. G. Emori, T. C. Horan, and J. M. Hughes. 1996. CDC definitions for nosocomial infections. In *PIC Infection Control and Applied Epidemiology: Principles and Practice.* R. N. Olmsted, ed. Mosby, St. Louis, p. A1–A20.
61. Le Gall, J. R., S. Lemeshow, and F. Saulnier. 1993. A new Simplified Acute Physiology Score (SAPS II) based on a European/North American multicenter study. *JAMA* 270: 2957–2963.
62. Oh, D. Y., S. Taube, O. Hamouda, C. Kücherer, G. Poggensee, H. Jessen, J. K. Eckert, K. Neumann, A. Storek, M. Pouliot, et al. 2008. A functional toll-like receptor 8 variant is associated with HIV disease restriction. *J. Infect. Dis.* 198: 701–709.
63. Kubarenko, A. V., S. Ranjan, E. Colak, J. George, M. Frank, and A. N. Weber. 2010. Comprehensive modeling and functional analysis of Toll-like receptor ligand-recognition domains. *Protein Sci.* 19: 558–569.
64. Laskowski, R. A., N. M. Luscombe, M. B. Swindells, and J. M. Thornton. 1996. Protein clefts in molecular recognition and function. *Protein Sci.* 5: 2438–2452.
65. Weiss, J., and J. Barker. 2018. Diverse pro-inflammatory endotoxin recognition systems of mammalian innate immunity. *F1000 Res.* 7: F1000.
66. Singer, M., C. S. Deutschman, C. W. Seymour, M. Shankar-Hari, D. Annane, M. Bauer, R. Bellomo, G. R. Bernard, J. D. Chiche, C. M. Coopersmith, et al. 2016. The Third International Consensus Definitions for Sepsis and Septic Shock (Sepsis-3). *JAMA* 315: 801–810.
67. Netea, M. G., J. W. van der Meer, M. van Deuren, and B. J. Kullberg. 2003. Proinflammatory cytokines and sepsis syndrome: not enough, or too much of a good thing? *Trends Immunol.* 24: 254–258.

Supplemental material

Table SI: Stimulation of RAW cells with different ligands (LPS 0111:B4, LPS 595, Pam_2Cys and Pam_3Cys) with increasing concentrations of LBP (either common (CV) or rare variant (RV)). All values are concentrations of TNF in pg/dl.

		No serum RV	**No serum CV**		**LBP 2% RV**	**LBP 2% CV**		**LBP 5% RV**	**LBP 5% CV**	
		TNF (pg/dl) mean (+/-SEM)	**TNF (pg/dl) mean (+/-SEM)**	**p-value**	**TNF (pg/dl) mean (+/-SEM)**	**TNF (pg/dl) mean (+/-SEM)**	**p-value**	**TNF (pg/dl) mean (+/-SEM)**	**TNF (pg/dl) mean (+/-SEM)**	**p-value**
Pam_2Cys in ng/ml	0	436.8 (178.3)	557.7 (227.7)	n.s.	735.7 (300.4)	567.8 (231.8)	n.s.	865.3 (353.3)	598.8 (244.5)	n.s.
	1	726.4 (296.6)	626.0 (255.6)	n.s.	1468.8 (599.6)	849.8 (346.9)	n.s.	1496.6 (611.0)	1119.9 (457.2)	n.s.
	10	797.6 (325.6)	686.7 (280.3)	n.s.	1810.1 (739.0)	1433.1 (585.1)	n.s.	2114.9 (863.4)	1470.2 (600.2)	n.s.
	100	761.8 (311.0)	564.8 (230.6)	n.s.	1823.2 (744.3)	1231.7 (502,8)	n.s.	2545.7 (1039.3)	1466.2 (598.6)	n.s.
Pam_3Cys in ng/ml	0	404.1 (165.0)	509.1 (207.8)	n.s.	605.3 (247.1)	536.6 (219.0)	n.s.	564.9 (230.6)	534.8 (218.3)	n.s.
	1	447.4 (182.7)	508.1 (207.4)	n.s.	826.5 (337.4)	632.9 (258.4)	n.s.	1127.3 (460.2)	642.4 (262.2)	n.s.
	10	756.5 (308.8)	552.4 (225.5)	n.s.	1619.2 (661.0)	1345.5 (549.3)	n.s.	2112.6 (862.5)	1811.7 (739.6)	n.s.
	100	1148.2 (468.7)	742.5 (303.1)	n.s.	3984.6 (1626.7)	3636.2 (1484.5)	n.s.	4271.4 (1743.8)	2876.7 (1174.4)	n.s.
LPS 0111:B4 in ng/ml	0	590.3 (241.0)	524.5 (214.1)	n.s.	685.4 (279.8)	496.4 (202.6)	n.s.	663.2 (270.8)	640.6 (261.5)	n.s.
	1	361.3 (147.5)	444.3 (181.4)	n.s.	1340.6 (547.3)	1045.4 (426.8)	n.s.	1156.9 (472.3)	1069.3 (436.5)	n.s.
	10	970.8 (396.3)	854.8 (349.0)	n.s.	2094.0 (854.9)	1950.7 (796.4)	n.s.	2184.8 (891.9)	2139.8 (873.6)	n.s.
	100	2440.8 (996.4)	1463.2 (597.4)	n.s.	4272.0 (1744.0)	2773.2 (1132.1)	n.s.	3783.6 (1544.6)	2738.5 (1118.0)	n.s.
LPS Re595 in ng/ml	0	510.3 (208.3)	509.7 (208.1)	n.s.	696.6 (284.4)	555.4 (226.7)	n.s.	551.8 (225.3)	527.0 (215.2)	n.s.
	1	538.6 (219.9)	489.0 (199.6)	n.s.	656.4 (268.0)	520.5 (212.5)	n.s.	613.3 (250.4)	588.2 (240.1)	n.s.
	10	637.4 (260.2)	516.4 (210.8)	n.s.	1337.3 (545.9)	649.1 (265.0)	n.s.	1229.5 (501.9)	796.7 (325.3)	n.s.
	100	1207.5 (493.0)	692.6 (282.8)	n.s.	3069.0 (1252.9)	2401.3 (980.3)	n.s.	3745.2 (1529.0)	2757.5 (1125.7)	n.s.

Statistical analysis with Mann-Whitney-U test.

Supplemental material

Table SII: Characteristics of 363 patients in the clinical cohort

Clinical cohort (n=363)			
Characteristics information	**Common variant (n=290)**	**Rare variant F436L (n=73)**	**p-Value**
Age (years, mean ± SD))	62.1 ± 12.2	60.1 ± 13.2	0.94
Male/female	182/108	47/26	0.89
[a]ASA Score (mean ± SD)	2.8 ± 0.6	2.8 ± 0.7	0.92
[b]SAPS-II–Score (mean ± SD)	25.1 ± 11.0	24.3 ± 11.2	0.44
Pre-existing condition [No (%)]			
Arterial hypertension	126 (43.4)	24 (32.9)	0.11
Myocardial disease	101 (34.8)	21 (28.8)	0.41
Diabetes	56 (19.3)	9 (12.3)	0.23
Lung pathology	51 (17.6)	13 (17.8)	1.00
Renal pathology	18 (6.2)	5 (6.8)	0.79

[a]ASA = American Society of Anesthesiologists. [b]SAPS = Sequential Acute Physiology Score recorded at admission to the ICU. Statistical analysis for contingency tables using Chi-square test except for mortality where Fisher's exact test was applied

Supplemental material

Table SIII: **In silico-analysis of LBP common variant and rare variants (rs2232618 and rs2232613)**.

Feature	Method	Effect feature	CV	rs2232618	rs2232613	Interpretation
Protein stability	MutPred	Loss of stability	--	P=0.07	P=0.05	- loss of stability of the helix in rs2232618 and in rs2232613.
		Loss of helix	--	P=0.1299	P=0.105	- differences in protein stability and structure in all relevant molecule areas (coil, helix and strand)
	I-Mutant 3.0	free energy	--	-1.29 (destabilizing)*	-0.64 (destabilizing)*	- Free energy levels hint towards destabilization of the mutated molecules (more pronounced in rs2232618)
	DUET	folding and unfolding free energy	--	-0.151 (destabilizing)*	-0.163 (destabilizing)*	
	ELASPIC	Domain core	--	-0.794 (destabilizing)*	0.497*	Conclusion: Overall both rare variants show a decrease in protein stability. Destabilizing effects with ΔΔG values below -0.5/kcal/mol are considered functional when they are located in binding sites.
Protein structure	PSIPRED	Coil	32.01%	30.56%	32.64%	- Sizable increase in volume in Cleft 1 and minor increase in Cleft 2 for the rare variant type rs2232618
		Helix	26.40%	26.40%	26.19%	
		Strands	41.58%	43.03%	41.16%	- The number of functional pockets differed slightly.
	ProFunc	Cleft 1 (conserved residues)	223, 286, 287, 309, 400, 444, 447	223, 286, 287, 289, 309, 400, 444, 447	223, 286, 287, 289, 309, 400, 444, 447	- Analysis of polar energy and surface atoms in this variant and no difference in the number of buried atoms.
		Cleft 2 (conserved residues)	38, 39, 41, 50, 101, 142, 215, 236, 276, 451, 478	38, 39, 41, 50, 101, 142, 215, 236, 276, 451, 478	38, 39, 41, 50, 101, 215, 236, 276, 451, 478	
	CASTp	No. of pockets	64	65	66	- The rs2232618 variant seems more accessible compared to the other variants as shown by larger surface area and stronger polar energy
	GETAREA	Polar energy	8726.01	8781.85	8727.03	
		No. of surface atoms	2137	2149	2138	
		No. of buried atoms	1446	1408	1446	Conclusion: These facts point towards structural conformational differences as a consequence of the LBP gene variations.

*All values shown as (ΔΔG/kcal/mol)

Supplemental material

Table SIV: Characteristics of patients in the complete clinical cohort (n=424) and the subgroup with infections (n=235). Comparison of all tested LBP-variants (common variant, F436L-variant and P333L-variant)

Clinical cohort (n=424)				
Characteristics information	**Common variant (n=290)**	**Rare variant F436L (n=73)**	**Rare variant P333L (n=61)**	**p-Value**
Age (years, mean ± SD))	62.1 ± 12.2	60.1 ± 13.2	63.0 ± 12.0	[c]n. s.
Male/female	182/108	47/26	40 / 21	n. s.
[a]ASA Score (mean ± SD)	2.8 ± 0.6	2.8 ± 0.7	2.8 ± 0.7	n. s.
[b]SAPS-II–Score (mean ± SD)	25.1 ± 11.0	24.3 ± 11.2	25.4 ± 12.6	n. s.
Pre-existing condition [No (%)]				
Arterial hypertension	126 (43.4)	24 (32.9)	32 (52.5)	n. s.
Myocardial disease	101 (34.8)	21 (28.8)	26 (42.6)	n. s.
Diabetes	56 (19.3)	9 (12.3)	19 (31.1)	0.02
Lung pathology	51 (17.6)	13 (17.8)	17 (27.9)	n. s.
Renal pathology	18 (6.2)	5 (6.8)	1 (1.6)	n. s.
Clinical cohort with infections (n=235)				
Site of infection [No (%)]				
Pneumonia	67 (41.1)	17 (43.6)	15 (45.5)	n. s.
Peritonitis	29 (17.8)	5 (12.8)	6 (18.2)	n. s.
Abscess	45 (27.6)	12 (30.8)	9 (27.3)	n. s.
Urinary tract infections	4 (2.5)	--	- -	n. s.
Other	18 (11.0)	5 (12.8)	3 (9.1)	n. s.
[d]Type of microorganism [No (%)]				
Gram negative	95 (58.3)	24 (61.5)	20 (60.1)	n. s.
Gram positive	61 (37.4)	18 (46.2)	10 (30.3)	n. s.
Fungi	12 (7.4)	2 (5.1)	1 (3.0)	n. s.
Length of stay [LOS] / Severity of disease				
LOS ICU (mean ± SD)	19.2 ± 17.1	14.7 ± 8.3	19.7 ± 14.5	n. s.
SAPS-II–Score (mean ± SD)	25.1 ± 11.0	24.3 ± 11.2	25.0 ± 11.2	n. s.
Mortality (n / %)	17 (10.4)	1 (2.6)	7 (21.2)	0.02

[a]ASA = American Society of Anesthesiologists. [b]SAPS = Sequential Acute Physiology Score recorded at admission to the ICU. Statistical analysis for contingency tables using Chi-square test or Fisher's exact test, where appropriate. [c]n. s. = not statistically significant. [d]Numbers not adding up to 100% due to missing data or more than one detected microorganism in a patient. Contingency table analyzed with Chi²-test; mortality analyzed with Fisher's exact test; LOS and SAPS-II-Score analyzed with ANOVA.

Critical Reviews in Microbiology

ISSN: (Print) (Online) Journal homepage: https://www.tandfonline.com/loi/imby20

Mycobacterium abscessus: insights from a bioinformatic perspective

Saubashya Sur, Tanushree Patra, Mistu Karmakar & Anindita Banerjee

To cite this article: Saubashya Sur, Tanushree Patra, Mistu Karmakar & Anindita Banerjee (2022): *Mycobacterium abscessus*: insights from a bioinformatic perspective, Critical Reviews in Microbiology, DOI: 10.1080/1040841X.2022.2082268

To link to this article: https://doi.org/10.1080/1040841X.2022.2082268

Published online: 13 Jun 2022.

CRITICAL REVIEWS IN MICROBIOLOGY
https://doi.org/10.1080/1040841X.2022.2082268

Taylor & Francis
Taylor & Francis Group

REVIEW ARTICLE

Mycobacterium abscessus: insights from a bioinformatic perspective

Saubashya Sur, Tanushree Patra, Mistu Karmakar and Anindita Banerjee

Postgraduate Department of Botany, Ramananda College, Bishnupur, India

ABSTRACT

Mycobacterium abscessus is a nontuberculous mycobacterium, associated with broncho-pulmonary infections in individuals suffering from cystic fibrosis, bronchiectasis, and pulmonary diseases. The risk factors for transmission include biofilms, contaminated water resources, fomites, and infected individuals. *M. abscessus* is extensively resistant to antibiotics. To date, there is no vaccine and combination antibiotic therapy is followed. However, drug toxicities, low cure rates, and high cost of treatment make it imperfect. Over the last 20 years, bioinformatic studies on *M. abscessus* have advanced our understanding of the pathogen. This review integrates knowledge from the analysis of genomes, microbiomes, genomic variations, phylogeny, proteome, transcriptome, secretome, antibiotic resistance, and vaccine design to further our understanding. The utility of genome-based studies in comprehending disease progression, surveillance, tracing transmission routes, and epidemiological outbreaks on a global scale has been highlighted. Furthermore, this review underlined the importance of using computational methodologies for pinpointing factors responsible for pathogen survival and resistance. We reiterate the significance of interdisciplinary research to fight *M. abscessus*. In a nutshell, the outcome of computational studies can go a long way in creating novel therapeutic avenues to control *M. abscessus* mediated pulmonary infections.

GRAPHICAL ABSTRACT

ARTICLE HISTORY
Received 8 March 2022
Revised 16 May 2022
Accepted 20 May 2022
Published online 11 June 2022

KEYWORDS
Mycobacterium abscessus; pulmonary infections; nontuberculous mycobacteria (NTM); infectious diseases; bioinformatics

Introduction

Mycobacteria are a diverse group of bacteria characterised by their varying ability to cause diseases. Mycobacteria are categorised into nontuberculous mycobacteria (NTM) and tuberculosis-causing mycobacteria (Johansen et al. 2020). NTM is ubiquitous, heterogeneous (Locatelli et al. 2020), and responsible for pulmonary infections, disseminated infections, cervical lymphadenitis, and infections in the bones and soft tissues (Baldwin et al. 2019). NTM infections are increasing worldwide and have surpassed the incidence of tuberculosis in many countries (Adjemian et al. 2012; Ryan and Byrd 2018; Baldwin et al. 2019). Age, bronchiectasis, exposure to aerosols, indiscriminate use of antibiotics and immunosuppressants, use of showers, and human-pathogen interaction, coupled with improved diagnostic capabilities are the reasons for an increased incidence of NTM induced diseases (Collins 1989; Feazel et al. 2009; Bryant et al. 2016; Johansen et al. 2020; Yoon et al. 2020). The cost of treating NTM is high.

CONTACT Saubashya Sur saubashya@gmail.com Postgraduate Department of Botany, Life Sciences Block, Ramananda College, Bishnupur-722122, India

Prolonged treatment, extensive antibiotic resistance, relapse of infection, and lack of suitable vaccines has become a matter of concern (Baldwin et al. 2019).

First isolated in 1953 (Moore and Frerichs 1953), *Mycobacterium abscessus* is a rapidly growing NTM species having worldwide distribution (Tortoli et al. 2017). It is an emerging pathogen that is present in contaminated soil and potable water (Thomson et al. 2013; Lee et al. 2015; Kimble 2021). *M. abscessus* is heterogeneous and incorporates three subspecies viz., *M. abscessus* subsp. *abscessus*, *M. abscessus* subsp. *massiliense*, and *M. abscessus* subsp. *bolletii* (Mougari et al. 2014). *M. abscessus* is one of the major respiratory infections causing mycobacteria (Mougari et al. 2014). It causes respiratory infections in immunocompromised individuals and patients with cystic fibrosis, bronchiectasis, and other pulmonary diseases (Hull and Thomson 1998; Howard et al. 2006; Mougari et al. 2014). The decline in lung function owing to *M. abscessus* infection has resulted in increased mortality (Qvist et al. 2016). Moreover, there is evidence of *M. abscessus* mediated nosocomial infection as a result of lung transplantation, tattooing, and surgical tourism (Sanguinetti et al. 2001; Nessar et al. 2012; Maurer et al. 2014; Chouhan et al. 2019).

The presence of an intact ESX-4 system is essential for *M. abscessus* virulence (Newton-Foot et al. 2016; Roy et al. 2020). It catalyses the breakdown of phagosomes and facilitates bacterial cytosolic escape (Bunduc et al. 2020). Phenotypic heterogeneity allows *M. abscessus* to transit between smooth (own glycopeptidolipid) and rough (lacking glycopeptidolipid) colonies (Howard et al. 2006; Catherinot et al. 2009). The latter is responsible for the severity and persistence of infection (Johansen et al. 2020). *M. abscessus* is notorious for its extensive resistance to several antibiotics and disinfectants (Lee et al. 2015; Novosad et al. 2016). This has been attributed to the presence of mycobacterial cell envelope, production of antibiotic degrading enzymes, resistance to macrolides, the existence of active efflux pumps, expression of *whiB* gene family, gene polymorphisms, mutations in *rrs* and *rrl* genes, etc. (Nessar et al. 2012; Johansen et al. 2020). Despite the use of combination antibiotic therapy, lengthy regimens, multiple side effects, and variable drug susceptibility of the subspecies became limiting factors (Koh et al. 2011; Novosad et al. 2016; Johansen et al. 2020).

Publication of the human genome in 2000, led to a proliferation of genome sequencing projects spanning living kingdoms. The outcome was a deluge of information from the perspective of genome, proteome, transcriptome, epigenome, metabolome, resistome, structure, etc. (Sur et al. 2010). It revolutionised the science of bioinformatics. This was complemented by advances in computational facilities, the development of new algorithms, databases, and high throughput technologies (Sur and Pal 2021). Furthermore, research utilising various bioinformatics techniques enriched our understanding of an organism or a biological system holistically. This included *M. abscessus* as well. This review focuses on the outcome and significance of *M. abscessus* research from a bioinformatic perspective. We showcase the implication of such research in understanding the nature and dynamics of this pathogen. Additionally, we also highlight the significance of computational studies in formulating strategies to combat *M. abscessus* infection. Taking these into consideration, we searched PubMed/Google Scholar to collect suitable articles until November 2021.

Understanding genome architecture, regulatory networks, transmission and pathogen adaptation from whole-genome, genomics, and comparative genomics research

Preliminary sequence-based studies concerning *M. abscessus* centred around 16S rRNA, 23S rRNA, *rpoB,* and housekeeping genes (Bastian et al. 2011; Macheras et al. 2011). The whole-genome sequence of *M. abscessus* was first published in 2009. It illustrated the genetic basis of pathogenicity and housed numerous virulence genes of non-mycobacterial origin (Ripoll et al. 2009). This was followed by whole-genome sequences of numerous other strains (Chan et al. 2012; Choi et al. 2012; Choo, Wong, Yusoff et al. 2012; Ngeow et al. 2012; Choo, Wong, Leong et al. 2012; Caverly et al. 2016; Yee et al. 2017; Yoshida et al. 2018; Machado et al. 2021). They were sequenced using Roche 454, Illumina, and PacBio technologies. *M. abscessus* strain M94 possessed a distinctive cluster of tRNA's linked to pathogenicity (Choo, Wong, Leong et al. 2012). Genome sequence analysis of *M. abscessus* strain M139 revealed a conflicting taxonomic position, owing to its resemblance with both *M. abscessus* subsp. *abscessus* and *M. abscessus* subsp. *massiliense* (Ngeow et al. 2012). Besides, the whole genome sequence of clinical isolates of *M. abscessus* from cystic fibrosis patients in different continents threw light on genome plasticity, transmission, adaptation patterns, drug susceptibility, and antibiotic resistance (Choo et al. 2014; Davidson et al. 2014; Harris et al. 2015; Everall et al. 2017; Lipworth et al. 2019). Recent times, witnessed genome sequencing and characterisation of the prophage and mycobacteriophage of *M. abscessus* (Amarh et al. 2021; Kimble 2021). These studies exemplified the relation of polymorphic toxin-linked type VII secretion systems with antibiotic resistance.

Ever-increasing whole-genome sequences of various mycobacteria catalysed the growth of new databases and computational resources. The challenges posed by large-scale genome-wide studies, comparative genomics, etc. demanded resources with higher resolution and sensitivity (Cheung et al. 2011). MabsBase supported accessibility, annotation, and computational studies of *M. abscessus* strains (Heydari et al. 2013). Likewise, MycoCAP was optimised for comparative genomic analysis of various mycobacteria including *M. abscessus* (Choo et al. 2015). It facilitated an understanding of the pathobiology and evolution of these bacteria. While MabsBase and MycoCAP focussed on genomic characteristics, Mabellini provided a platform for realising the structural proteome of *M. abscessus* (Skwark et al. 2019). Furthermore, antimicrobial targets can also be designed. Accurate identification of subspecies from the whole genome sequences of *M. abscessus* complex clinical isolates was facilitated by user-friendly software (Lin et al. 2020). This held promise for discriminate therapies. BacWGSTdb 2.0 was developed as a fast, one-stop repository for analysing whole-genome sequences of nine clinically important bacteria (Feng et al. 2021). It housed information on 1611 *M. abscessus* isolates for the benefit of clinicians and epidemiologists.

The accessibility of sequence data and appropriate tools paved the way for genomic and comparative studies. Genomic analyses of *M. abscessus* ATCC 19977 recognised β prism II lectins, MVL lectins, and heparin-binding haemagglutinin associated with host-pathogen interactions (Abhinav et al. 2013). Sequence analysis of *M. abscessus* ATCC 19977 revealed the occurrence of a DNA degradation (Dnd) phenotype within the genomic island (Howard et al. 2013). Exploration of genome sequences within the *M. abscessus* group (Macheras et al. 2011; Sekizuka et al. 2014) revealed that *M. massiliense* possessed a genomic island MmGI-1 associated with lipid metabolism. This aided the bacterium to survive in a lipid-rich ecological niche (Sekizuka et al. 2014). The difference in virulence patterns amongst *M. abscessus*, *M. bolletii*, and *M. massiliense* was delineated by comparative genomics. This is significant in the context of designing specific drug targets (Sassi and Drancourt 2014).

A survey of the whole genomes of *M. abscessus* clinical isolates reported the incidence of innumerable strain-specific accessory genes. It warranted increased surveillance since the outcome indicated a fast-evolving open pangenome (Choo et al. 2014). Pangenome analysis of various mycobacteria including *M. abscessus* pointed out the role of ESX-encoding plasmids in enabling the diversification of type VII secretion systems (Dumas et al. 2016). This diversification catalysed bacterial survival within the host and pathogenicity. Other observations supported this fact (Laencina et al. 2018). Further pangenome analysis of *M. abscessus* and twenty-seven other mycobacterial species demonstrated 811 *M. abscessus* specific genes linked to quorum sensing. A high number of quorum sensing genes correlated with adaptation and overwintering hostile conditions (Wee et al. 2017).

Bioinformatic studies of mycobacterial genomes underlined the role of tRNA array units, virulence factors and gene regulatory networks in inferring organism biology. *M. abscessus* complex showed myriad tRNA array units located within the genomes, bacteriophages, and plasmids. The incidence of tRNA arrays in the bacteriophages and plasmids was attributed to horizontal gene transfer (Morgado and Vicente 2018). Genome analysis of the *Mycobacterium chelonae-abscessus* complex (Simmon et al. 2011; Behra et al. 2019) disclosed that the virulence factor phospholipase C (plcC) housed by *M. abscessus,* was shared with *Mycobacterium salmoniphilum*-like strains (Behra et al. 2019). Computational modelling recognised conservation of transcriptional control in *M. tuberculosis* and *M. abscessus,* as well as 54 regulator-target pairs, over 5 transcription factors in the latter (Staunton et al. 2019).

Whole-genome sequence analysis of the clinical isolates of *M. abscessus* complex from Ireland revealed the dominance of two different strains of *M. abscessus* subsp. *abscessus*. On top of that, *M. abscessus* complex (Lee et al. 2015; Tan et al. 2017) isolates from non-cystic fibrosis patients were more diverse than the cystic fibrosis counterpart (Redondo et al. 2020). Despite the lack of patient-to-patient transmission, monitoring infections and spotting transmission routes were recommended, owing to the elevated incidence of cystic fibrosis in Ireland. Genomic analysis and comparative studies of *M. abscessus* subsp. *massiliense,* from sporadic, non-cystic fibrosis, cystic fibrosis, and outbreak clone 1 isolates out of the USA unfolded some interesting facts. Examination of the pangenome and core genome analyses divulged similarities between sporadic and outbreak isolates, concerning single nucleotide polymorphism numbers. However, the absence of acquired antimicrobial resistance mutations in the sporadic isolates signalled cross-transmission (Bryant et al. 2016; Davidson et al. 2021). One population genomics study explored 588 *M. abscessus* isolate genomes from cystic fibrosis care facilities across the USA and compared them with genomes from earlier studies. It divulged the prevalence of dominant clones that in all likelihood could spread in the environment (Davidson et al. 2021a). Besides, these sorts of analyses warranted

the integration of epidemiological, genomic, and evidence-based studies to understand transmission.

Of late several *in silico* techniques have been applied for distinguishing *M. abscessus* subspecies and other NTMs. Subspecies-Specific Sequence Detection (SSSD) methodology differentiated *M. abscessus* subspecies, from 1505 genome sequences of the *M. abscessus* complex with high precision (Minias et al. 2020). Machine learning and comparative genomics methodologies recognised marker genes and SNPs for distinguishing *M. abscessus* and other NTMs (Jia et al. 2021). A whole-genome sequence analysis method successfully identified *M. abscessus* and NTMs from a mixed infection. Amongst PubMLST, MetaPhlAn3, Kraken2, and Mykrobe-Predictor tools, Kraken2 demonstrated absolute sensitivity and specificity in detecting and identifying mixed NTM species (Khieu et al. 2021). Moreover, accurate detection of the relative abundance of individual NTM species from a mixture signified its potency and relevance.

Microbiome and methylome profiling of *M. abscessus* mediated diseases

Microbiome refers to the entire genetic material of all microorganisms present in a habitat (Richardson et al. 2019). Microbiome analysis facilitates understanding of the intracellular mechanisms and interactions of the microorganisms with their host (Marchesi and Ravel 2015; Francoise and Héry-Arnaud 2020). The fast-developing technique of microbiome sequencing is relevant for recognising the microbiome's role in disease progression.

A distinct relationship between the lower airway microbiota and NTM disease has been recognised. The contribution of NTM bacteria including *M. abscessus,* in disease progression, underlined the need for comprehending therapeutic implications (Sulaiman et al. 2018). The challenges posed by *M. abscessus* along with other pathogens in the cystic fibrosis microbiome have consequences on diagnosis and therapy (Mahenthiralingam 2014; Surette 2014). That *M. abscessus* was more susceptible to antibiotics compared to *Pseudomonas aeruginosa*, demanded effective monitoring of the lung microbiome in cystic fibrosis patients (Vandeplassche et al. 2019).

The sputum microbiome demonstrated the influence of *M. abscessus* complex infection on cystic fibrosis patients. The patients had a significantly different microbiome community compared to the control set (Bharadwaj 2021). Nevertheless, antibacterial treatments brought about a change in the microbiome community. Therefore, it is evident that surveillance of the lung and sputum microbiome of *M. abscessus* infected patients, during infection, therapy (with antibiotics, probiotics, etc.) and recovery may assist in clinical management (Thornton et al. 2021).

The limitations imposed by traditional molecular methods in understanding bacterial pathogenicity can be overcome by ascertaining methylome profiles from genomes. This holds importance owing to its modification in response to stress (Chhotaray et al. 2020). Genome-wide methylome profiling of smooth and rough *M. abscessus* clinical isolates illustrated significant differences. The differences shaped by mutations in the genes associated with antibiotics and stress tolerance influenced pathogenicity and resistance (Chhotaray et al. 2020). DNA methylation profiling also facilitated the recognition of biomarkers in patients with lung diseases (Oh et al. 2021).

Genetic and genomic variation studies highlighted the role of mutations and *M. abscessus* subspecies in disease outbreaks

Technological advances in high-throughput sequencing over the last two decades resulted in the generation of a substantial amount of functionally relevant genetic variation data (Wang et al. 2010). This incorporated information from pulmonary diseases including those caused *by M. abscessus,* critical for understanding disease pathophysiology and designing strategies (Yarden et al. 2005; Knowles and Drumm 2012, Howard et al. 2013, Shmarina et al. 2013). Preliminary researchers studied *rpoB*, *hsp65*, *secA,* etc. utilising multi-locus sequence typing to ascertain the role of subspecies in disease outbreaks (Davidson 2018). Using R studio, a novel workflow for multilocus sequence typing was developed with 104 whole genomes from the *M. abscessus* complex and 14 loci. It identified 62 distinct sequence types and underlined the impact of a few discriminatory genes and antibiotic resistance genes in diversifying *M. abscessus* subspecies (Wuzinski and Sharma 2018).

A Malaysian survey of tandem repeat polymorphisms data from 38 clinical isolates of *M. abscessus* underscored its significance in interpreting epidemiology, strain differentiation, and subspecies identification (Wong et al. 2012). Analysis of clinical isolates from the outbreaks of *M. abscessus* in different parts of the world underlined the role of dominant antibiotic-resistant clones. While *M. abscessus* subsp. *bolletii* BRA100 clone was responsible for the outbreak in southern Brazil, dominant clones of *M. abscessus* subsp. *massiliense* and *M. abscessus* subsp. *abscessus* caused respiratory infections in cystic fibrosis patients in other countries (Nunes et al. 2014; Bryant et al. 2016; Davidson 2018). SNP analysis revealed similarity among these dominant clone

isolates in the core genome, and genomic variations in the accessory genome (Davidson 2018). Whole-genome sequencing of *M. abscessus* clinical isolates from a hospital setting in Australia identified a related cluster varying only by few a SNPs. The study divulged cross-transmission among cystic fibrosis patients (Yan et al. 2020). A different pattern was noticed in cystic fibrosis isolates from Germany. Genome sequencing, phylogenetic and variant analysis revealed a new adaptation strategy for *M. abscessus* within the lungs (Lewin et al. 2021). The pathogen accumulated an assortment of variants in the population, that housed numerous virulent and antibiotic-resistant genes containing non-synonymous variations. Consequently, there appears to be a strategic shift from employing a handful of dominant clones to harbouring numerous genetic variants at a time to sustain chronic lung infection. These genetic and genomic variation analyses may be beneficial for large-scale population genomics studies. This holds especially in the context of understanding clinically relevant mutations that facilitate pathogen survival and transmission.

Phylogenetic research reveals a multitude of factors shaping the evolution of *M. abscessus*

Evolution in microorganisms is crafted by the events of mutations, genomic rearrangements, and horizontal gene transfer mechanisms (Juhas et al. 2009). These events are responsible for the adaptation of the microorganism to environmental conditions and diversification. The pulmonary pathogen *M. abscessus* (Howard et al. 2006) is important from the evolutionary perspective, owing to its adaptability within the host and causing diseases.

Over the years microbiologists were perplexed by the taxonomic position of the *M. abscessus* subspecies. Some researchers divided *M. abscessus* into three subspecies viz. *M. abscessus* sensu stricto, *M. massiliense,* and *M. bolletii* based on single-gene sequencing (Adékambi et al. 2006). Multilocus sequencing and phylogenetic analysis of *hsp65*, *rpoB*, and *secA* sequences of the clinical isolates and type strains of *M. abscessus* and closely related species, clearly differentiated *M. abscessus* from *M. massiliense*, and *M. bolletii* (Zelazny et al. 2009). However, others emended them into *M. abscessus* subspecies *abscessus* and *M. abscessus* subspecies *bolletii* (Leao et al. 2011). Phylogenetic and phylogenomic analysis of *rpoB, hsp65, sodA, recA, secA, erm*41,16S-23S internal transcribed spacer (ITS) genes and 12 *M. abscessus* whole genomes, efficiently classified its subspecies (Tan et al. 2013). It emphasised the importance of using minimal gene marker sets for classifying *M. abscessus*. Computational pairwise comparison of 43 *M. abscessus* strains and 3 genomes, divided *M. abscessus* into *M. abscessus* subsp. *abscessus*, *M. abscessus* subsp. *massiliense* and *M. abscessus* subsp. *bolletii* (Tortoli et al. 2016). Phylogenomic network analysis and examination of thymidylate kinase protein and 30S ribosomal protein S3 supported the splitting of *M. abscessus* into three subspecies (Tan et al. 2015). Additionally, it provided evidence that *M. massiliense* is different from *M. bolletii* in the context of antibiotic susceptibility. This was reinforced by another phenotypic and phylogenomic analysis, proposing the distinction of *M. massiliense* and *M. bolletii* within the *M. abscessus* complex (Adekambi et al. 2017). Microevolution of subspecies within the *M. abscessus* complex was accomplished by the influence of homologous recombination and positive selection of isochorismate, beta-lactamase-like protein, deoxyribonuclease tatD, thymidylate kinase Tmk, 30S ribosomal protein S3, and some hypothetical proteins (Tan et al. 2017). A phylogenomic survey emended the name *Mycobacterium abscessus* to *Mycobacteroides abscessus* and its subspecies. This was due to the occurrence of 27 unique molecular marker proteins distinct from other members of Mycobacteriaceae (Gupta et al. 2018). A computational study precisely classified *M. abscessus* subspecies using the housekeeping gene *gnd* (Ng and Ngeow 2020). Recently, the name *Mycobacterium abscessus* was reapplied on the basis of genomic and computational analyses (Meehan et al. 2021).

An integrative phylogenomic analysis of the epidemic isolates of *M. abscessus* from Brazil with related outbreak isolates from the UK, USA, Malaysia, and France underscored the obligation to study epidemiological outbreaks across continents (Davidson et al. 2013). The Brazilian outbreak strains belonging to a monophyletic clade had many deletions and differences in their gene content. Moreover, they were similar to the UK outbreak strains compared to that from the USA, Malaysia, and France. This portrayed that the Brazilian and UK outbreak isolates were a clone devoid of genetic variation and circulating over wide geographic regions (Davidson et al. 2013). Again, variation with outbreak strains from USA, Malaysia, and France indicated independent localised evolution. Further phylogenetic investigation of the Brazilian outbreak divulged convergent evolution in the isolates. It affirmed that this nosocomial outbreak was caused by *M. abscessus* subsp. *massiliense* lineage (Everall 2019). Similar phylogenetic characterisation of the *M. abscessus* subsp. *massiliense* strains from an outbreak in USA, and comparison with UK outbreak strains indicated relatedness (Tettelin et al. 2014). The researchers employed MEGA,

Mugsy, Phylomark, and GATK software to infer the relatedness, and stressed using whole-genome sequence data for understanding transmission routes.

Bacteriophage insertions are one of the factors responsible for variations amongst *M. abscessus* strains (Davidson et al. 2013; Sassi and Drancourt 2014). Exploration of 48 *M. abscessus* genomes suggested that numerous mycobacteriophages co-evolving with the mycobacterium were accountable for heterogeneity resulting from gene loss, gain, and exchanges (Sassi and Drancourt 2014).

PE/PPE proteins from *M. abscessus* ATCC 19977, other mycobacterial species, and non-mycobacteria were investigated using various phylogenetic software, to recognise their origin and evolution (Bavishi et al. 2014). It divulged an accommodation of a wide variety of these fast-evolving proteins in pathogenic mycobacteria.

Mosaicism in *M. abscessus* genomes obtained from cystic fibrosis patients has been attributed to pRAW-like genetic elements (Sapriel et al. 2016). These extrachromosomal elements influenced evolution through genome re-modelling and shaped pathogenicity. Lateral transfer of a *rpoB* gene from *M. abscessus* to *M. massiliense* bolstered the view that these events contributed to diversity among *M. abscessus* strains (Kim et al. 2017). Whole-genome phylogenetic analysis revealed that *M. abscessus* belonged to the ancestral group of rapidly growing mycobacteria. It possessed distant homologs of genes belonging to the mammalian cell entry operon and had numerous genes linked to amino acid transport and transcription (Bachmann et al. 2020). These had a role in metabolism and adaptation to pathogenic lifestyles. A recent study showed the stepwise evolution of *M. abscessus* pathogenicity. Certain epigenetic modifiers resulted in the saltational increase of pathogenicity in some clones (Bryant et al. 2021). This has been ascribed to horizontal gene transfer events. Also, allopatric parallel evolution possibly resulted in an escalation of virulence as a consequence of mutations in chronic patients. The outcome underlined testing several colonies from various samples to understand antibiotic resistance and launch measures to prevent human to human transmission.

Phylogenetic studies based on whole-genome sequencing and single-nucleotide polymorphism analysis, in a German patient cohort, identified macrolide resistance and aminoglycoside susceptibility (Wetzstein et al. 2020). *erm* (41) methyltransferases were responsible for macrolide resistance in *M. abscessus* subsp. *abscessus* and *M. abscessus* subsp. *bolletii*. Phylogenomic analysis of *M. abscessus* genomes from cystic fibrosis and non-cystic fibrosis patients, also recognised a clade possessing *erm* (41) T28C mutation that was responsible for macrolide susceptibility (Bronson et al. 2021). These studies offer a new direction in designing therapeutics.

Computational proteomics research on *M. abscessus*

An assortment of protein contents within a cell at a particular time and environmental condition is the proteome. Whole proteome profiling, liquid chromatography, mass spectrometry (LC-MS), MALDI-TOF MS-based experiments, and spatial proteomics (Zhao et al. 2016; Nicholson et al. 2021) have catalysed proteomics research. It resulted in the generation of abundant, reliable, quantitative, and target enriched data, that can be investigated by robust computational techniques (Nicholson et al. 2021). That related mycobacterial species tend to show variable phenotypes linked to virulence, bolstered proteomics research in mycobacteria (Bajaj et al. 2020).

Examination of the predicted proteomes from mycobacterial strains including *M. abscessus* ATCC 19977 using BLAST matrix, demonstrated that the latter shared a few genes with other slow-growing mycobacteria (Zakham et al. 2012). Proteome analysis using MALDI-TOF MS successfully identified different subspecies of *M. abscessus*. The outcome accelerated the diagnosis and treatment of *M. abscessus* subspecies mediated diseases (Luo et al. 2016). It highlighted having appropriate antibiotic therapies in place since subspecies of *M. abscessus* are notorious for showing variation in antibiotic susceptibility (Luo et al. 2016). Integration of proteomic and genomic data offered a better resolution in demonstrating drug resistance in *M. abscessus* UC22. It had 30 variant peptides associated with 16 single-nucleotide variations linked to drug resistance (Advani et al. 2019).

In addition to the identification of different subspecies and illustrating drug resistance, computational proteomics research provided insights into the identification of immunogenic proteins, adaptation to antibiotic stress, and survival within the host. One study recognised 12 immunogenic species-specific proteins, from the *M. abscessus* complex suitable for T-cell and B-cell epitope prediction. They hold promise for future diagnostic immunoassays in combating *M. abscessus* complex diseases (Steindor et al. 2019). Tandem mass tag spectrometry data from *M. abscessus* subsp. *abscessus,* showcased its adjustment to outsmart environmental and antibiotic stress. *M. abscessus* subsp. *abscessus* synthesised enzymes, that enabled it to alter the cell surface and bring about

changes in the metabolites. It underscored the survival strategies to overcome low nutrient conditions and neutralise the impact of amikacin and linezolid (Rojony et al. 2020). Investigation of multi-omics and proteomics datasets from *M. abscessus* illustrated the role of non-coding RNAs, internal transcription sites, and novel open reading frames in pathogenicity and adjustment within the host (Nicholson et al. 2021). Despite being constrained by limited works, proteomics research on *M. abscessus* is significant in shedding new light on pathogen physiology, resistance patterns, and virulence.

In silico secretome characterisation

The secretome comprises the complete set of secreted proteins. It involves different types of molecules (Ranganathan and Garg 2009). The secretome is associated with cell adhesion, migration, cell-to-cell communication, signal transduction, etc. (Bonin-Debs et al. 2004). Exploration of the secretomes from pathogenic bacteria opened up opportunities to develop new vaccine candidates and diagnostic markers. Over the years computational approaches have become popular to profile the secretome of various pathogens (Ranganathan et al. 2009; Ranganathan and Garg 2009; Robinson et al. 2009).

A combinatorial approach using 2-D gel electrophoresis, MALDI-TOF, and bioinformatics tools identified species-specific 32 major secreted proteins from *M. abscessus* ATCC23006 (Yadav and Gupta 2012). The majority of them were linked to cellular functions and virulence. Moreover, the secretome of *M. abscessus* ATCC23006 revealed a substantial difference with *Mycobacterium chelonae* ATCC35752. These bacteria are closely related, yet variation in their secretome stressed the need for developing novel diagnostic tools based on contrasting secreted proteins. Extensive computational analyses of clinical isolates revealed 85% secretome similarity within *M. abscessus* subspecies (Cornejo-Grandos et al. 2021). Larger secretome and antigenic densities in clinical isolates from rough colonies compared to smooth colonies signified the former's role in pathogenicity. Additionally, the incidence of a plethora of excreted/secreted (ES) proteins and proteins associated with quorum sensing portrayed their implication on virulence (Cornejo-Granados et al. 2021). Analysing the secretome of *M. abscessus* using computational techniques holds promise in the context of developing novel drugs and vaccines. However, an insufficient number of studies coupled with the lack of experimental validation are some of the limitations.

New insights into infection, adaptability, and drug responses from transcriptomic research on *M. abscessus*

Transcriptomic analysis using microarray and RNA-seq datasets from pathogenic bacteria has the potential to unravel significant insights into the lifestyle patterns, host responses, antibiotic resistance patterns, etc. One of the pioneering studies on the whole transcriptome of THP1- derived macrophages using RNA-seq data, revealed a substantial correlation between the smooth and rough morphotypes of *M. abscessus* during early infection (Aulicino et al. 2015). However, later stages of infection revealed some degree of the strain-specific differential immune response. That, strains belonging to the *M. abscessus* complex are phenotypically diverse and were also identified using phenotype microarray technology (Ameen 2018). Analysis of RNA-seq data from human THP1 exposed to *M. abscessus* and other pathogens indicated a more pronounced response to *M. abscessus* (Thuer and Gabaldón 2017).

The adaptive capability of *M. abscessus* under stress conditions was shown by transcriptomic studies. The amalgamation of dRNA-seq, RNA-seq, and ribosome profiling technologies for characterising *M. abscessus,* underlined its effective capability to adapt itself within the cystic fibrosis lung (Miranda-CasoLuengo et al. 2016). Therefore, *M. abscessus* employed certain metabolic strategies, that enabled it to overcome nutrient-deficient conditions within the human macrophages and persist longer in the cystic fibrosis lung. These strategies were quite common amongst other cystic fibrosis pathogens. Examination of the transcriptomic profiles of *M. abscessus* in amoeba and murine macrophages demonstrated that some amoeba proteins allowed *M. abscessus* to overcome environmental stress and catalyse its defense mechanism (Dubois et al. 2019). This adaptation of *M. abscessus* to intracellular lifestyle was an outcome of its shift to fatty acid metabolism from carbohydrate metabolism.

Transcriptomic analysis of the *M. abscessus* infected respiratory epithelia using DESeq2 package, ToppGene Suite, and Ingenuity pathway analysis software specified that ciliary genes were downregulated whereas inflammatory genes like IL-32, and those linked to cholesterol biosynthesis and cytokines were upregulated (Matsuyama et al. 2018). This provided a solid understanding of numerous pathways that may be suitable targets for drug development. RNA-seq analyses have also been successful in underscoring drug-specific responses and tolerance to clofazimine and tigecycline by *M. abscessus* (Schildkraut et al. 2021). Thus, it is evident from transcriptomic studies that understanding

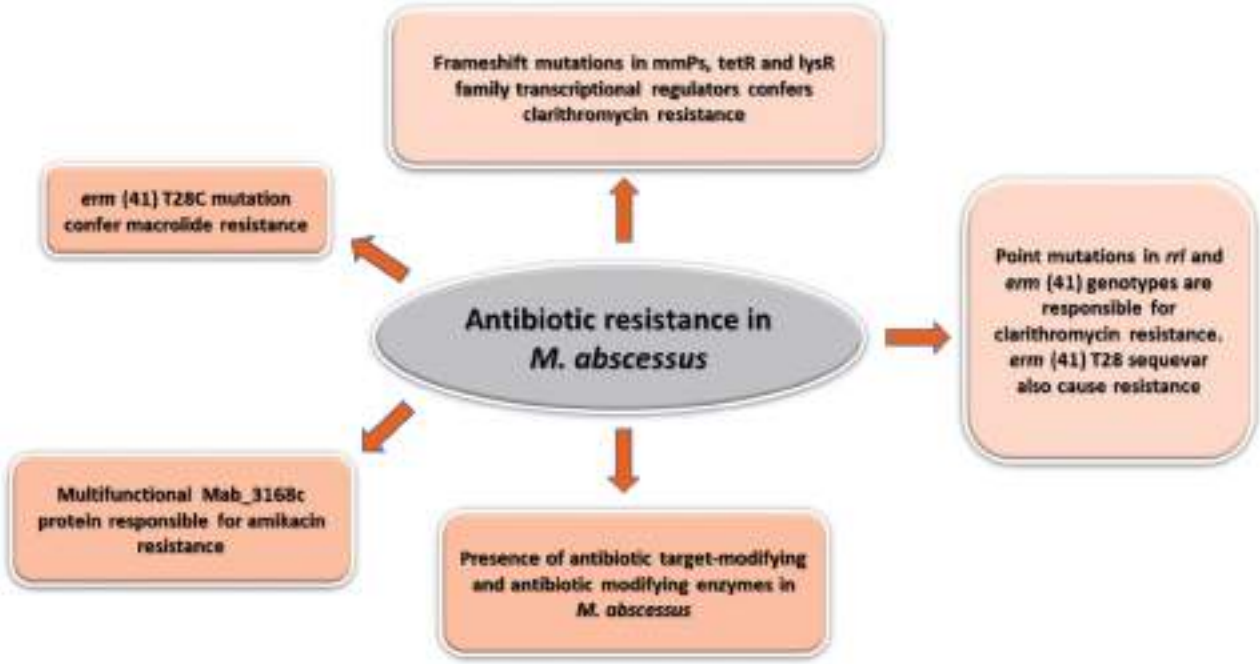

Figure 1. Illustration of the major factors responsible for resistance to different antibiotics by *M. abscessus* (Wallace et al. 1996; Bastian et al. 2011; Tsai et al. 2013; Li et al. 2017; Luthra et al. 2018; Li et al. 2020; Bronson et al. 2021).

gene expression patterns of *M. abscessus* is crucial for developing therapeutic strategies.

In silico studies on antibiotic resistance in *M. abscessus* provide knowledgebase to catalyse new treatment strategies

M. abscessus is notoriously resistant to clinically available antibiotics (Novosad et al. 2016; Joob and Wiwanitkit 2019). Intrinsic resistance to ethambutol, fluoroquinolones, rifampicin, thiacetazone analogs, clofazimine, and bedaquiline is caused by low cell wall permeability, expression of antibiotic modifying enzymes, and induction of drug efflux pumps (Luthra et al. 2018; Johansen et al. 2020). Acquired macrolide resistance to aminoglycosides, kanamycin, and amikacin occurs by a mutation in the genes encoding targets owing to prolonged treatment (Nessar et al. 2012, Luthra et al. 2018). Antibiotic resistance caused progressive lung damage, reduced functionality, and mortality in patients with cystic fibrosis (Le Moigne et al. 2016; de Carvalho et al. 2021). The availability of the genomic data of *M. abscessus* opened up opportunities to understand antibiotic resistance using computational approaches.

Sequence analysis of *rrl* (23S rRNA gene), revealed point mutations accountable for clarithromycin resistance (Figure 1) in 36 out of 51 cystic fibrosis patients (Wallace et al. 1996; Bastian et al. 2011). A bioinformatic study supported by experimental evidence showcased the role of multi-functional Mab_3168c protein behind amikacin resistance (Figure 1) in *M. abscessus* cells (Tsai et al. 2013). Investigation of the *M. abscessus* clinical isolates from China using whole-genome sequencing, SNP and BLAST analysis predicted the role of *rrl* and *erm* (41) genotypes (Figure 1) in clarithromycin resistance (Li et al. 2017). Around, 41.7% of these isolates housed the *erm* (41) T28 sequevar associated with resistance. The significance of *erm* (41) T28C mutation in *M. abscessus* has been substantiated by another study in the context of macrolide resistance (Figure 1, Bronson et al. 2021). The emergence and reversion of *erm* (41) T28C mutation were catalysed by selective pressure. This had a bearing on the patterns of macrolide resistance. An in-depth statistical exploration of *M. abscessus* complex isolates from Florida showed 100%, 98.4%, 93.4%, and 87.7% resistance to trimethoprim/sulfamethoxazole, ciprofloxacin, moxifloxacin, and doxycycline (Sfeir et al. 2018).

Genetic toolkit analysis successfully identified seven enzymes, that altered antibiotic targets together with the antibiotics (Figure 1) and formed a complicated resistome of *M. abscessus* (Luthra et al. 2018). These enzymes offered a safeguard against antibiotics targeting cell wall synthesis, RNA synthesis, and protein synthesis.

Genomic DNA analysis of *M. abscessus* complex isolates from China, and sequence comparisons using BLAST highlighted variation in antimicrobial resistance amongst them (Guo et al. 2020). Clarithromycin

resistance was higher in *M. abscessus* isolates (74.3%) compared to *M. bolletii* (68.4%). Furthermore, imipenem and ceftazidime seemed to work in a unison against the isolates. Bioinformatic studies of whole-genome sequences from Chinese *M. abscessus* isolates resistant to clarithromycin, spotted genes encoding resistance factors (Li et al. 2020). Frameshift mutations in *mmpS,* tetR, and lysR family transcriptional regulators were accountable for the resistance (Figure 1).

Transposon-sequencing showed promise in pinpointing essential genes in *M. abscessus* and drive the development of bactericidal drugs against the pathogen. PBP-lipo was recognised as one such gene having the ability to sensitise *M. abscessus* to ampicillin, amoxicillin, and other antibiotics (Akusobi et al. 2021). Saturated transposon mutagenesis and deep sequencing of *M. abscessus* identified essential genes, tRNAs, and short open reading frames associated with pathogenesis and antibiotic resistance (Rifat et al. 2021).

In addition to these, many other genes and their polymorphisms have been reported to show innate and adaptive drug resistance (Johansen et al. 2020). Computational studies on these could enhance our understanding by providing novel insights. Moreover, improved computational tools coupled with the analysis of antibiotic resistance datasets from different parts of the world could be fruitful. The knowledge from such studies may assist clinicians and drug manufacturers in controlling the pathogen.

Computational prediction of drug targets and multi-epitope vaccine candidates

M. abscessus infections are chronic and hard to control with existing chemotherapeutic agents (Nash et al. 2009). This demanded research on novel therapeutic strategies and vaccines. Sequence analysis and structural studies hold potential in drug discovery against *M. abscessus*. Comparative homology modelling can determine high-quality structures that may assist in screening and ligand design (Waman et al. 2019). While, metabolic reconstructions are suitable for understanding pathogenesis, systematic mutagenesis analysis with SDM and mCSM software might rapidly assess mutations causing drug resistance (Waman et al. 2019). A combination of *in vitro* and *in silico* methods can usher new possibilities (Omeershffudin and Kumar 2019).

A hierarchical *in silico* analysis identified 40 target candidates associated with manifold metabolic activities, crucial for pathogen survival (Shanmugham and Pan 2013). Further characterisation of these targets based on subcellular localisation, interactions, functionality, and druggability, divulged appropriateness against *M. abscessus* infections (Shanmugham and Pan 2013). Computerised drug screening, data analysis and phenotype characterisation identified niclosamide (Berube et al. 2018) and 11 compounds targeting *M. abscessus* (Richter et al. 2018). *In silico* and *in vitro* investigation of tetrahydropyridine compounds demonstrated their role in inhibiting the efflux mechanism of *M. abscessus* subsp. *abscessus* (Ramis et al. 2019). Molecular modelling and molecular docking analysis of MmpL5 and Tap efflux transporters with different ligands were carried out. NUNM01 was identified as the most suitable adjuvant candidate against *M. abscessus* (Ramis et al. 2019).

In vitro and mass spectrometric data analysis using bioinformatic tools, found TLR2eF (TLR2 enriched fraction) housing numerous lipoproteins and proteins. These TLR2eF compounds had the potential to prevent *M. abscessus* infections as vaccine and diagnostic molecules (Le Moigne et al. 2020). Comparative genomics studies of NTMs including *M. abscessus* identified 15 druggable proteins to be broad-spectrum vaccine and drug targets (Swain et al. 2021). It consisted of pathogen-specific essential proteins, that functioned as carriers, transcriptional regulators, enzymes, and ribosomal binding proteins (Swain et al. 2021).

Reverse genetics is a powerful and advantageous strategy for designing vaccines (Nogales and Martínez-Sobrido 2017). One such study recognised the significance of MgtC, as a probable vaccine candidate for protecting cystic fibrosis patients from *M. abscessus* (Le Moigne et al. 2016). A pangenome based reverse-vaccinology approach (Figure 2) using bioinformatic tools, determined multi-epitope vaccine candidates against *M. abscessus* (Dar et al. 2021). Antigenic target detection and physiochemical characterisation of the core genome proteins culminated in the recognition of 4 antigenic proteins. CD8 and CD4 T-cell interacting epitopes were predicted from these antigenic proteins and a multi-epitope vaccine candidate was designed. It was non-allergenic, antigenic, and immunogenic (Dar et al. 2021). Interestingly, the T-cell epitopes displayed substantial population coverage. Construction of the structural model followed by conformation B-cell mapping identified B-cell epitopes. The outcome of *in silico* cloning and immune stimulation was encouraging (Dar et al. 2021). Additionally, molecular docking studies highlighted strong interaction between the multi-epitope vaccine and Toll-like receptor 2. Binding affinity studies and molecular dynamics simulation further substantiated the findings. Despite the robustness of this

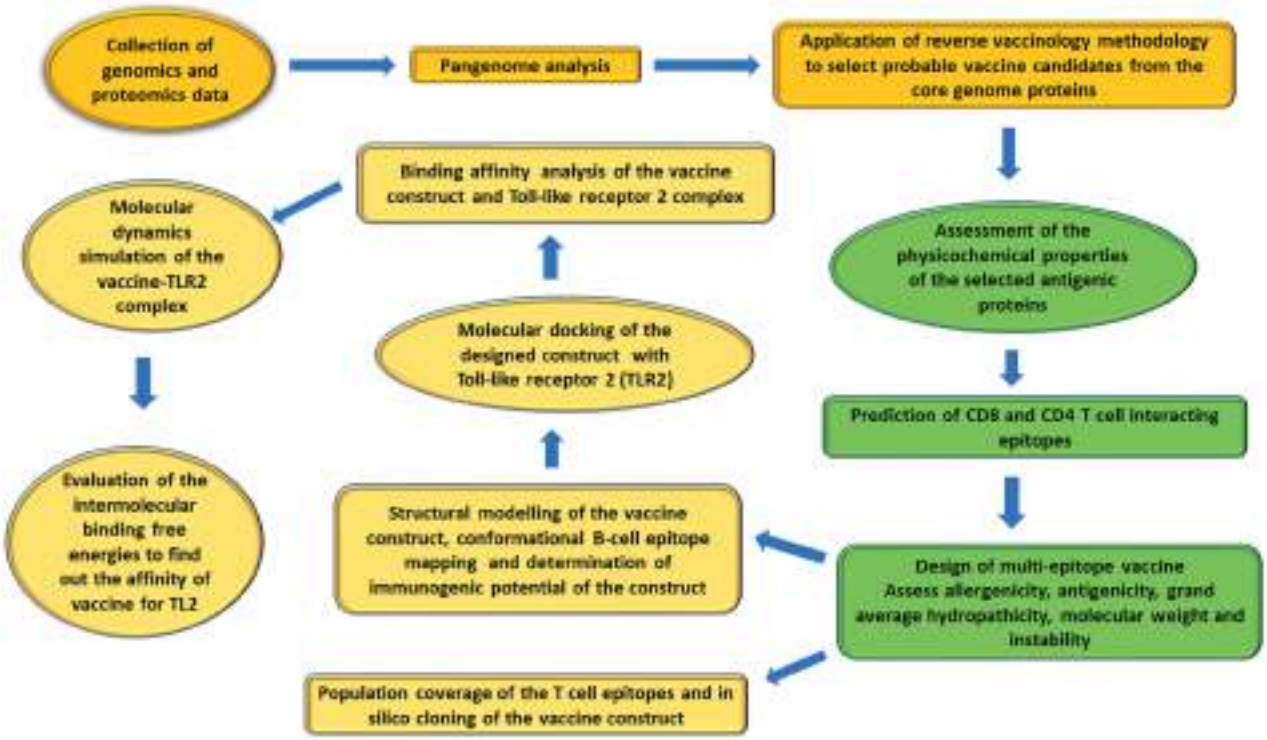

Figure 2. Demonstration of the pangenome-based reverse-vaccinology approach for designing multi-epitope vaccine candidates (Dar et al. 2021).

approach, the outcome of this work is yet to be validated by experimental studies.

Overall, knowledge from these *in silico* studies on bactericidal compounds and vaccines can go a long way in assisting experimental analysis by saving time and expenses.

Conclusions

The burden of pulmonary diseases caused by *M. abscessus* is increasing globally. Undeniably, the biggest challenge posed by this pathogen lies with the effective diagnosis and development of appropriate drugs. Since 2009, genomes of numerous *M. abscessus* strains have been sequenced. These high-quality sequence data provided a basis for numerous computational studies, leading to a wealth of information. Despite concerns over the lack of functional data, knowledge from myriad *in silico* analyses furnished valuable insights into the nature of *M. abscessus* and its diseases.

Whole-genome analysis and comparative genomics provided information about virulence patterns and stressed the need for surveillance of clinical isolates on a global scale. Moreover, it demonstrated the role of advanced methodologies in detecting transmission routes, virulence proteins (especially the ES proteins), resistance patterns, subspecies identification, and pinpointing *M. abscessus* from mixed infections. Knowledge from genome studies may favour ease of diagnosis and treatment. Microbiome and methylome analyses highlighted therapeutic implications and improvements associated with drug therapies. While genetic variation studies illustrated the role of subspecies and dominant clones in disease outbreaks and cross-transmission, phylogenetic analysis showcased factors shaping the evolution of *M. abscessus*. Investigation of the proteome, secretome and transcriptome enhanced our understanding of the pathogen physiology, and the influence of metabolites on virulence, adaptability, and gene expression patterns. These findings are likely to catalyse the development of novel drugs and vaccines. Likewise, precise identification of the factors conferring antibiotic resistance in *M. abscessus* through computational techniques may facilitate advancements in therapeutic strategies. Efforts should also be in place to integrate computational and experimental studies of plant-based compounds, that may act as inhibitors of the pathogen.

Hence, it is evident that in addition to clinical, microbiological, and molecular techniques, computational studies are necessary to advance our understanding of *M. abscessus*. Pharmaceutical and biomedical industries should collaborate with researchers and clinicians, to reduce vulnerability to cystic fibrosis and bronchiectasis that allow *M. abscessus* to become a chronic infection. Although a lot needs to be done, future computational

studies should be aimed at technological innovations for large-scale analysis of different types of data. Technological know-how should be shared amongst developed and emerging economies. In essence, this review underscores the significance of utilising the outcome of various computational studies, for a better understanding of the pathogen and for developing novel therapies.

Acknowledgments

The authors thank Ramananda College for providing infrastructure to carry out the work.

Author contributions

SS conceived the idea and supervised the study. TP performed the literature review. SS wrote the manuscript with support from TP. MK and AB assisted with the figures and manuscript editing. All authors have read and approved the submitted version of the manuscript.

Disclosure statement

The authors report no potential conflict of interest(s).

Funding

The authors reported there is no funding associated with the work featured in this article.

ORCID

Saubashya Sur http://orcid.org/0000-0001-7002-628X
Tanushree Patra http://orcid.org/0000-0001-7573-201X
Mistu Karmakar http://orcid.org/0000-0001-6653-8282
Anindita Banerjee http://orcid.org/0000-0002-1016-2295

References

Abhinav KV, Sharma A, Vijayan M. 2013. Identification of mycobacterial lectins from genomic data. Proteins. 81(4): 644–657.

Adékambi T, Berger P, Raoult D, Drancourt M. 2006. rpoB gene sequence-based characterization of emerging nontuberculous mycobacteria with descriptions of *Mycobacterium bolletii* sp. nov., *Mycobacterium phocaicum* sp. nov. and *Mycobacterium aubagnense* sp. nov. Int J Syst Evol Microbiol. 56:133–143.

Adekambi T, Sassi M, van Ingen J, Drancourt M. 2017. Reinstating *Mycobacterium massiliense* and *Mycobacterium bolletii* as species of the *Mycobacterium abscessus* complex. Int J Syst Evol Microbiol. 67(8):2726–2730.

Adjemian J, Olivier KN, Seitz AE, Holland SM, Prevots DR. 2012. Prevalence of nontuberculous mycobacterial lung disease in U.S. medicare beneficiaries. Am J Respir Crit Care Med. 185(8):881–886.

Advani J, Verma R, Chatterjee O, Devasahayam Arokia Balaya R, Najar MA, Ravishankara N, Suresh S, Pachori PK, Gupta UD, Pinto SM, et al. 2019. Rise of clinical microbial proteogenomics: a multiomics approach to nontuberculous *Mycobacterium*-the case of *Mycobacterium abscessus* UC22. OMICS. 23(1):1–16.

Akusobi C, Benghomari BS, Wolf ID, Singhvi S, Zhao J, loerger TJ, Rubin EJ. 2021. High-density transposon mutagenesis in *Mycobacterium abscessus* identifies an essential penicillin-binding lipo-protein (PBP-lipo) involved in septal peptidoglycan synthesis and antibiotic sensitivity. bioRxiv. doi:10.1101/2021.07.01.450732.

Amarh ED, Dedrick RM, Garlena RA, Russell DA, Jacobs-Sera D, Hatfull GF. 2021. Genome sequence of *Mycobacterium abscessus* phage phiT46-1. Microbiol Resour Announc. 10: e01421-20.

Ameen SMM, University of Sulaimani 2018. High throughput phenotypic microarray profiling of *Mycobacterium abscessus*. JZS-A. 20(2):9–20.

Aulicino A, Dinan AM, Miranda-CasoLuengo AA, Browne JA, Rue-Albrecht K, MacHugh DE, Loftus BJ. 2015. High-throughput transcriptomics reveals common and strain-specific responses of human macrophages to infection with *Mycobacterium abscessus* smooth and rough variants. BMC Genom. 16:1046.

Bachmann NL, Salamzade R, Manson AL, Whittington R, Sintchenko V, Earl AM, Marais BJ. 2020. Key transitions in the evolution of rapid and slow growing mycobacteria identified by comparative genomics. Front Microbiol. 10: 3019.

Bajaj A, Saraswat S, Freeke J, Barker A. 2020. Method of extraction and proteome profiling of mycobacteria using liquid chromatography-high resolution mass spectrometry. SN Appl Sci. 2(11):1863.

Baldwin SL, Larsen SE, Ordway D, Cassell G, Coler RN. 2019. The complexities and challenges of preventing and treating nontuberculous mycobacterial diseases. PLoS Negl Trop Dis. 13(2):e0007083.

Bastian S, Veziris N, Roux A-L, Brossier F, Gaillard J-L, Jarlier V, Cambau E. 2011. Assessment of clarithromycin susceptibility in strains belonging to the *Mycobacterium abscessus* group by erm(41) and rrl sequencing. Antimicrob Agents Chemother. 55(2):775–781.

Bavishi A, Lin L, Choudhary M, Primm TP. 2014. Evolution of PE35 and PPE68 gene families in *Mycobacterium*: roles of horizontal gene transfer and evolutionary constraints. JTR. 02(04):181–198.

Behra PRK, Das S, Pettersson BMF, Shirreff L, DuCote T, Jacobsson KG, Ennis DG, Kirsebom LA. 2019. Extended insight into the *Mycobacterium chelonae-abscessus* complex through whole genome sequencing of *Mycobacterium salmoniphilum* outbreak and *Mycobacterium salmoniphilum*-like strains. Sci Rep. 9(1): 4603.

Berube BJ, Castro L, Russell D, Ovechkina Y, Parish T. 2018. Novel screen to assess bactericidal activity of compounds against non-replicating *Mycobacterium abscessus*. Front Microbiol. 9:2417.

Bharadwaj L. 2021. The Cystic Fibrosis Microbiome and its Association with Incident Infections with *Mycobacteroides (Mycobacterium) abscessus* [Unpublished master's thesis]. Calgary (AB): University of Calgary.

Bonin-Debs AL, Boche I, Gille H, Brinkmann U. 2004. Development of secreted proteins as biotherapeutic agents. Expert Opin Biol Ther. 4(4):551–558.

Bronson RA, Gupta C, Manson AL, Nguyen JA, Bahadirli-Talbott A, Parrish NM, Earl AM, Cohen KA. 2021. Global phylogenomic analyses of *Mycobacterium abscessus* provide context for non cystic fibrosis infections and the evolution of antibiotic resistance . Nat Commun. 12(1):5145.

Bryant JM, Brown KP, Burbaud S, Everall I, Belardinelli JM, Rodriguez-Rincon D, Grogono DM, Peterson CM, Verma D, Evans IE, et al. 2021. Stepwise pathogenic evolution of *Mycobacterium abscessus*. Science. 372(6541):eabb8699.

Bryant JM, Grogono DM, Rodriguez-Rincon D, Everall I, Brown Kar P, Moreno P, Verma D, Hill E, Drijkoningen J, Gilligan P, et al. 2016. Emergence and spread of a human-transmissible multidrug-resistant nontuberculous mycobacterium. Science. 354(6313):751–757.

Bunduc CM, Bitter W, Houben ENG. 2020. Structure and function of the mycobacterial Type VII secretion systems. Annu Rev Microbiol. 74:315–335.

Catherinot E, Roux A-L, Macheras E, Hubert D, Matmar M, Dannhoffer L, Chinet T, Morand P, Poyart C, Heym B, et al. 2009. Acute respiratory failure involving an R Variant of *Mycobacterium abscessus*. J Clin Microbiol. 47(1):271–274.

Caverly LJ, Spilker T, LiPuma JJ. 2016. Complete genome sequence of *Mycobacterium abscessus* subsp. *bolletii*. Genome Announc. 4(3):e00543–16.

Chan J, Halachev M, Yates E, Smith G, Pallen M. 2012. Whole-genome sequence of the emerging pathogen *Mycobacterium abscessus* strain 47J26. J Bacteriol. 194(2): 549.

Cheung MS, Down TA, Latorre I, Ahringer J. 2011. Systematic bias in high-throughput sequencing data and its correction by BEADS. Nucleic Acids Res. 39(15):e103.

Chhotaray C, Wang S, Tan Y, Ali A, Shehroz M, Fang C, Liu Y, Lu Z, Cai X, Hameed HMA, et al. 2020. Comparative analysis of whole-genome and methylome profiles of a smooth and a rough *Mycobacterium abscessus* clinical strain. G3 (Bethesda). 10(1):13–22.

Choi GE, Cho YJ, Koh WJ, Chun J, Cho SN, Shin SJ. 2012. Draft genome sequence of *Mycobacterium abscessus* subsp. *bolletii* BD(T). J Bacteriol. 194(10):2756–2757.

Choo SW, Ang MY, Dutta A, Tan SY, Siow CC, Heydari H, Mutha NVR, Wee WY, Wong GJ.,. 2015. MycoCAP - *Mycobacterium* comparative analysis platform. Sci Rep. 5: 18227.

Choo SW, Wee WY, Ngeow YF, Mitchell W, Tan JL, Wong GJ, Zhao Y, Xiao J, 2014. Genomic reconnaissance of clinical isolates of emerging human pathogen *Mycobacterium abscessus* reveals high evolutionary potential. Sci Rep. 4: 4061.

Choo SW, Wong YL, Leong ML, Heydari H, Ong CS, Ng KP, Ngeow YF. 2012. Analysis of the genome of *Mycobacterium abscessus* strain M94 reveals an uncommon cluster of tRNAs. J Bacteriol. 194(20):5724.

Choo SW, Wong YL, Yusoff AM, Leong ML, Wong GJ, Ong CS, Ng KP, Ngeow YF. 2012. Genome sequence of the *Mycobacterium abscessus* strain M93. J Bacteriol. 194(12): 3278.

Chouhan D, Barani Devi T, Chattopadhyay S, Dharmaseelan S, Nair GB, Devadas K, Radhakrishna Pillai M. 2019. *Mycobacterium abscessus* infection in the stomach of patients with various gastric symptoms. PLoS Negl Trop Dis. 13(11):e0007799.

Collins FM. 1989. Mycobacterial disease, immunosuppression, and acquired immunodeficiency syndrome. Clin Microbiol Rev. 2(4):360–377.

Cornejo-Granados F, Kohl TA, Sotomayor FV, Andres S, Hernandez-Pando R, Hurtado-Ramirez JM, et al. 2021. Secretome characterization of clinical isolates from the *Mycobacterium abscessus* complex provides insight into antigenic differences. BMC Genom. 22:385.

Dar HA, Ismail S, Waheed Y, Ahmad S, Jamil Z, Aziz H, Hetta HF, Muhammad K. 2021. Designing a multi-epitope vaccine against *Mycobacteroides abscessus* by pangenome-reverse vaccinology. Sci Rep. 11(1):11197.

Davidson RM, Benoit JB, Kammlade SM, Hasan NA, Epperson LE, Smith T, Vasireddy S, et al. 2021. Genomic characterization of sporadic isolates of the dominant clone of *Mycobacterium abscessus* subspecies *massiliense*. Sci Rep. 11:5336.

Davidson RM, Hasan NA, de Moura VC, Duarte RS, Jackson M, Strong M. 2013. Phylogenomics of Brazilian epidemic isolates of *Mycobacterium abscessus* subsp. *bolletii* reveals relationships of global outbreak strains. Infect Genet Evol. 20:292–297.

Davidson RM, Hasan NA, Epperson LE, Benoit JB, Kammlade SM, Levin AR, Calado de Moura V, Hunkins J, Weakly N, Beagle S, et al. 2021a. Population genomics of *Mycobacterium abscessus* from U.S. cystic fibrosis care centers. Ann Am Thorac Soc. 18(12):1960–1969.

Davidson RM, Hasan NA, Reynolds PR, Totten S, Garcia B, Levin A, Ramamoorthy P, Heifets L, Daley CL, Strong M, et al. 2014. Genome sequencing of *Mycobacterium abscessus* isolates from patients in the United States and comparisons to globally diverse clinical strains. J Clin Microbiol. 52(10):3573–3582.

Davidson RM. 2018. A closer look at the genomic variation of geographically diverse *Mycobacterium abscessus* clones that cause human infection and disease. Front Microbiol. 9:2988.

de Carvalho N, Leao S, Bombarda S, Arbeit RD, Chimara E. 2021. Evaluation of the MGIT 960/EpiCenter TB eXiST system for drug susceptibility testing for *Mycobacterium abscessus* complex. Research Square. doi:10.21203/rs.3.rs-62195/v2

Dubois V, Pawlik A, Bories A, Le Moigne V, Sismeiro O, Legendre R, Varet H, Rodríguez-Ordóñez MDP, Gaillard J-L, Coppée J-Y, et al. 2019. *Mycobacterium abscessus virulence traits unraveled by transcriptomic profiling in amoeba and macrophages*. PLoS Pathog. 15(11):e1008069.

Dumas E, Christina Boritsch E, Vandenbogaert M, Rodríguez de la Vega RC, Thiberge J-M, Caro V, Gaillard J-L, Heym B, Girard-Misguich F, Brosch R, et al. 2016. Mycobacterial pan-genome analysis suggests important role of plasmids in the radiation of Type VII secretion systems. Genome Biol Evol. 8(2):387–402.

Everall I, Nogueira CL, Bryant JM, Sánchez-Busó L, Chimara E, Duarte RdS, Ramos JP, Lima KVB, Lopes Mar L, Palaci M, et al. 2017. Genomic epidemiology of a national outbreak of post-surgical *Mycobacterium abscessus* wound infections in Brazil. Microb Genom. 3(5):e000111.

Everall I. 2019. Evolutionary Genomics of Cystic Fibrosis and Nosocomial Pathogens of the *Mycobacterium abscessus*

species complex. [Doctoral thesis]. University of Cambridge. Cambridge. https://doi.org/10.17863/CAM.37771

Feazel LM, Baumgartner LK, Peterson KL, Frank DN, Harris JK, Pace NR. 2009. Opportunistic pathogens enriched in showerhead biofilms. Proc Natl Acad Sci U S A. 106(38): 16393–16399.

Feng Y, Zou S, Chen H, Yu Y, Ruan Z. 2021. BacWGSTdb 2.0: a one-stop repository for bacterial whole-genome sequence typing and source tracking. Nucleic Acids Res. 49(D1):D644–D650.

Francoise A, Héry-Arnaud G. 2020. The microbiome in cystic fibrosis pulmonary disease. Genes. 11(5):536.

Guo Y, Cao X, Yu J, Zhan Q, Yang J, Wu X, Wan B, Liu Y, Yu F.,. 2020. Antimicrobial susceptibility of *Mycobacterium abscessus* complex clinical isolates from a Chinese tertiary hospital. IDR. 13:2001–2010.

Gupta RS, Lo B, Son J. 2018. Phylogenomics and comparative genomic studies robustly support division of the genus *Mycobacterium* into an emended genus *Mycobacterium* and four novel genera. Front Microbiol. 9:67.

Harris KA, Underwood A, Kenna DT, Brooks A, Kavaliunaite E, Kapatai G, Tewolde R, et al. 2015. Whole-genome sequencing and epidemiological analysis do not provide evidence for cross-transmission of *Mycobacterium abscessus* in a cohort of pediatric cystic fibrosis patients. Clin Infect Dis. 60:1007–1016.

Heydari H, Wee WY, Lokanathan N, Hari R, Mohamed Yusoff A, Beh CY, Yazdi AH, Wong GJ, Ngeow YF, Choo SW, et al. 2013. MabsBase: A *Mycobacterium abscessus* genome and annotation database. PLoS One. 8(4):e62443.

Howard ST, Newman KL, McNulty S, Brown-Elliott BA, Vasireddy R, Bridge L, Wallace RJ. 2013. Insertion site and distribution of a genomic island conferring DNA phosphorothioation in the *Mycobacterium abscessus* complex. Microbiology. 159(Pt 11):2323–2332.

Howard ST, Rhoades E, Recht J, Pang X, Alsup A, Kolter R, Lyons CR, Byrd TF. 2006. Spontaneous reversion of *Mycobacterium abscessus* from a smooth to a rough morphotype is associated with reduced expression of glycopeptidolipid and reacquisition of an invasive phenotype. Microbiology. 152(Pt 6):1581–1590.

Howard ST. 2013. Recent progress towards understanding genetic variation in the *Mycobacterium abscessus* complex. Tuberculosis. 93:S15–S20.

Hull J, Thomson AH. 1998. Contribution of genetic factors other than CFTR to disease severity in cystic fibrosis. Thorax. 53(12):1018–1021.

Jia X, Yang L, Li C, Xu Y, Yang Q, Chen F. 2021. Combining comparative genomic analysis with machine learning reveals some promising diagnostic markers to identify five common pathogenic non-tuberculous mycobacteria. Microb Biotechnol. 14(4):1539–1549.

Johansen MD, Herrmann JL, Kremer L. 2020. Non-tuberculous mycobacteria and the rise of Mycobacterium abscessus. Nat Rev Microbiol. 18(7):392–407.

Joob B, Wiwanitkit V. 2019. Drug resistance pattern of *Mycobacterium abscessus*: change of pattern in 20-year period after the first report of human pulmonary infection in Thailand. Biomed Biotechnol Res J. 3(2):92–94.

Juhas M, van der Meer JR, Gaillard M, Harding RM, Hood DW, Crook DW. 2009. Genomic islands: tools of bacterial horizontal gene transfer and evolution. FEMS Microbiol Rev. 33(2):376–393.

Khieu V, Ananta P, Kaewprasert O, Laohaviroj M, Namwat W, Faksri K. 2021. Whole-genome sequencing analysis to identify infection with multiple species of nontuberculous mycobacteria. Pathogens. 10(7):879.

Kim BJ, Kim GN, Kim BR, Shim TS, Kook YH, Kim BJ. 2017. Phylogenetic analysis of *Mycobacterium massiliense* strains having recombinant rpoB gene laterally transferred from *Mycobacterium abscessus*. PLoS One. 12(6):e0179237.

Kimble M. 2021. Characterizing Mab Cluster R Prophage of Pathogen *Mycobacterium abscessus* (Mab). Honors College. https://digitalcommons.library.umaine.edu/honors/669

Knowles MR, Drumm M. 2012. The influence of genetics on cystic fibrosis phenotypes. Cold Spring Harb Perspect Med. 2(12):a009548.

Koh W-J, Jeon K, Lee NY, Kim B-J, Kook Y-H, Lee S-H, Park YK, Kim CK, Shin SJ, Huitt GA, et al. 2011. Clinical significance of differentiation of *Mycobacterium massiliense* from *Mycobacterium abscessus*. Am J Respir Crit Care Med. 183(3):405–410.

Laencina L, Dubois V, Le Moigne V, Viljoen A, Majlessi L, Pritchard J, Bernut A, Piel L, Roux A-L, Gaillard J-L, et al. 2018. Identification of genes required for *Mycobacterium abscessus* growth in vivo with a prominent role of the ESX-4 locus. Proc Natl Acad Sci U S A. 115(5):E1002–E1011.

Le Moigne V, Belon C, Goulard C, Accard G, Bernut A, Pitard B, Gaillard J-L, Kremer L, Herrmann J-L, Blanc-Potard A-B, et al. 2016. MgtC as a host-induced factor and vaccine candidate against *Mycobacterium abscessus* infection. Infect Immun. 84(10):2895–2903.

Le Moigne V, Gaillard JL, Herrmann JL. 2016. Vaccine strategies against bacterial pathogens in cystic fibrosis patients. Med Mal Infect. 46(1):4–9.

Le Moigne V, Roux A-L, Jobart-Malfait A, Blanc L, Chaoui K, Burlet-Schiltz O, Gaillard J-L, Canaan S, Nigou J, Herrmann J-L, et al. 2020. A TLR2-activating fraction from *Mycobacterium abscessus* rough variant demonstrates vaccine and diagnostic potential. Front Cell Infect Microbiol. 10:432.

Leao SC, Tortoli E, Euzeby JP, Garcia MJ. 2011. Proposal that *Mycobacterium massiliense* and *Mycobacterium bolletii* be united and reclassified as *Mycobacterium abscessus* subsp. *bolletii* comb. nov., designation of *Mycobacterium abscessus* subsp. *abscessus* subsp. nov. and emended description of *Mycobacterium abscessus*. Int J Syst Evol Microbiol. 61(Pt 9):2311–2313.

Lee MR, Sheng WH, Hung CC, Yu CJ, Lee LN, Hsueh PR. 2015. *Mycobacterium abscessus* complex infections in humans. Emerg Infect Dis. 21(9):1638–1646.

Lewin A, Kamal E, Semmler T, Winter K, Kaiser S, Schäfer H, Mao L, Eschenhagen P, Grehn C, Bender J, et al. 2021. Genetic diversification of persistent *Mycobacterium abscessus* within cystic fibrosis patients. Virulence. 12(1): 2415–2429.

Li B, Guo Q, Mao Y, Zou Y, Zhang Y, Zhang Z, Chu H. 2020. Genetic evolution of *Mycobacterium abscessus* conferring clarithromycin resistance during long-term antibiotic therapy. Can Respir J. 2020:7623828.

Li B, Yang S, Chu H, Zhang Z, Liu W, Luo L, Ma W, Xu X, 2017. Relationship between antibiotic susceptibility and

genotype in *Mycobacterium abscessus* clinical isolates. Front Microbiol. 8:1739.
Lin D, Sun R, Tan Y, Wang J, Chen X. 2020. Improved subspecies identification in clinical *Mycobacterium abscessus* complex isolates using whole genome sequence. bioRxiv. doi: 10.1101/2020.01.02.893412.
Lipworth S, Hough N, Leach L, Morgan M, Jeffery K, Andersson M, Robinson E, et al. 2019. Whole-genome sequencing for predicting clarithromycin resistance in *Mycobacterium abscessus*. Antimicrob. Agents Chemother. 63:e01204-18.
Locatelli ME, Tosto S, D'Agata V, Bonaventura P, Grasso RS, Marino A, et al. 2020. Disseminated disease by *Mycobacterium abscessus* and *Mycobacterium celatum* in an immunocompromised host. Am. J. Case Rep. 21:e921517-1–e921517-5.
Luo L, Liu W, Li B, Li M, Huang D, Jing L, Chen H, Yang J, Yue J, Wang F, et al. 2016. Evaluation of matrix-assisted laser desorption ionization-time of flight mass spectrometry for identification of *Mycobacterium abscessus* subspecies according to whole-genome sequencing. J Clin Microbiol. 54(12):2982–2989.
Luthra S, Rominski A, Sander P. 2018. The role of antibiotic-target-modifying and antibiotic-modifying enzymes in *Mycobacterium abscessus* drug resistance. Front Microbiol. 9:2179.
Machado E, Oliveira FC, Silva Duarte R, Carvalho AC, Cândido PHC, Conceição EC, Gomes L, et al. 2021. Whole-genome sequences of *Mycobacterium abscessus* subsp. Massiliense Isolates from Brazil. Microbiol Resour Announc. 10: e00361–21.
Macheras E, Roux A-L, Bastian S, Leão SC, Palaci M, Sivadon-Tardy V, Gutierrez C, Richter E, Rüsch-Gerdes S, Pfyffer G, et al. 2011. Multilocus sequence analysis and rpoB sequencing of *Mycobacterium abscessus* (sensu lato) strains. J Clin Microbiol. 49(2):491–499.
Mahenthiralingam E. 2014. Emerging cystic fibrosis pathogens and the microbiome. Paediatr Respir Rev. 15:13–15.
Marchesi JR, Ravel J. 2015. The vocabulary of microbiome research: a proposal. Microbiome. 3:31.
Matsuyama M, Martins AJ, Shallom S, Kamenyeva O, Kashyap A, Sampaio EP, Kabat J, Olivier KN, Zelazny AM, Tsang JS, et al. 2018. Transcriptional response of respiratory epithelium to nontuberculous mycobacteria. Am J Respir Cell Mol Biol. 58(2):241–252.
Maurer FP, Castelberg C, von Braun A, Wolfensberger A, Bloemberg GV, Böttger EC, Somoskovi A. 2014. Postsurgical wound infections due to rapidly growing mycobacteria in Swiss medical tourists following cosmetic surgery in Latin America between 2012 and 2014. Euro Surveill. 19:20905.
Meehan CJ, Barco RA, Loh YE, Cogneau S, Rigouts L. 2021. Reconstituting the genus *Mycobacterium*. Int J Syst Evol Microbiol. 71:004922.
Minias A, Żukowska L, Lach J, Jagielski T, Strapagiel D, Kim S-Y, Koh W-J, Adam H, Bittner R, Truden S, et al. 2020. Subspecies-specific sequence detection for differentiation of *Mycobacterium abscessus* complex. Sci Rep. 10(1):16415.
Miranda-CasoLuengo AA, Staunton PM, Dinan AM, Lohan AJ, Loftus BJ. 2016. Functional characterization of the *Mycobacterium abscessus* genome coupled with condition-specific transcriptomics reveals conserved molecular strategies for host adaptation and persistence. BMC Genom. 17:553.
Moore M, Frerichs JB. 1953. An unusual acid-fast infection of the knee with subcutaneous, abscess-like lesions of the gluteal region; report of a case with a study of the organism, *Mycobacterium abscessus*, n. sp. J Invest Dermatol. 20(2):133–169.
Morgado SM, Vicente ACP. 2018. Beyond the limits: tRNA array units in *Mycobacterium* genomes. Front Microbiol. 9: 1042.
Mougari F, Raskine L, Ferroni A, Marcon E, Sermet-Gaudelus I, Veziris N, Heym B, Gaillard J-L, Nassif X, Cambau E, et al. 2014. Clonal relationship and differentiation among *Mycobacterium abscessus* isolates as determined using the semiautomated repetitive extragenic palindromic sequence PCR-Based diversiLab system. J Clin Microbiol. 52(6):1969–1977.
Nash KA, Brown-Elliott BA, Wallace RJ. Jr. 2009. A novel gene, *erm* (41), confers inducible macrolide resistance to clinical isolates of *Mycobacterium abscessus* but is absent from *Mycobacterium chelonae*. Antimicrob Agents Chemother. 53(4):1367–1376.
Nessar R, Cambau E, Reyrat JM, Murray A, Gicquel B. 2012. *Mycobacterium abscessus*: a new antibiotic nightmare. J Antimicrob Chemother. 67(4):810–818.
Newton-Foot M, Warren RM, Sampson SL, van Helden PD, van Pittius NCG. 2016. The plasmid-mediated evolution of the mycobacterial ESX (Type VII) secretion systems. BMC Evol Biol. 16:62.
Ng HF, Ngeow YF. 2020. A single-gene approach for the subspecies classification of *Mycobacteroides abscessus*. Pathog Dis. 78:ftaa055.
Ngeow YF, Wee WY, Wong YL, Tan JL, Ongi CS, Ng KP, Choo SW. 2012. Genomic analysis of *Mycobacterium abscessus* strain M139, which has an ambiguous subspecies taxonomic position. J Bacteriol. 194(21):6002–6003.
Nicholson KR, Mousseau CB, Champion MM, Champion PA. 2021. The genetic proteome: Using genetics to inform the proteome of mycobacterial pathogens. PLoS Pathog. 17(1): e1009124.
Nogales A, Martínez-Sobrido L. 2017. Reverse genetics approaches for the development of influenza vaccines. IJMS. 18(1):20.
Novosad SA, Beekmann SE, Polgreen PM, Mackey K, Winthrop KL, *M. abscessus* Study Team 2016. Treatment of *Mycobacterium abscessus* Infection. Emerg Infect Dis. 22(3): 511–514.
Nunes LdS, Baethgen LF, Ribeiro MO, Cardoso CM, de Paris Fnd, De David SMM, da Silva MG, Duarte RS, Barth AL. 2014. Outbreaks due to *Mycobacterium abscessus* subsp. *bolletii* in southern Brazil: persistence of a single clone from 2007 to 2011. J Med Microbiol. 63(Pt 10):1288–1293.
Oh JY, Ko YK, Gim JA. 2021. DNA methylation profiling for the diagnosis and prognosis of patients with nontuberculous *Mycobacterium* lung disease. CIMB. 43(2):501–512.
Omeershffudin UNM, Kumar S. 2019. In silico approach for mining of potential drug targets from hypothetical proteins of bacterial proteome. IJMBOA. 4(4):145–152.
Qvist T, Taylor-Robinson D, Waldmann E, Olesen HV, Hansen Cst R, Mathiesen IH, Høiby N, Katzenstein TL, Smyth RL, Diggle PJ, et al. 2016. Comparing the harmful effects of nontuberculous mycobacteria and gram negative bacteria

on lung function in patients with cystic fibrosis. J Cyst Fibros. 15(3):380–385.

Ramis IB, Vianna JS, Silva Junior L, von Groll A, Ramos DF, Lobo MM, Zanatta N, Viveiros M, Silva PEAd.,. 2019. *In silico* and *in vitro* evaluation of tetrahydropyridine compounds as efflux inhibitors in *Mycobacterium abscessus*. Tuberculosis. 118:101853.

Ranganathan S, Garg G. 2009. Secretome: clues into pathogen infection and clinical applications. Genome Med. 1(11):113.

Ranganathan S, Menon R, Gasser RB. 2009. Advanced *in silico* analysis of expressed sequence tag (EST) data for parasitic nematodes of major socio-economic importance-fundamental insights toward biotechnological outcomes. Biotechnol Adv. 27(4):439–448.

Redondo N, Mok S, Montgomery L, Flanagan PR, McNamara E, Smyth EG, O'Sullivan N, et al. 2020. Genomic analysis of *Mycobacterium abscessus* complex isolates collected in Ireland between 2006 and 2017. J Clin Microbiol. 58: e00295-20.

Richardson H, Dicker AJ, Barclay H, Chalmers JD. 2019. The microbiome in bronchiectasis. Eur Respir Rev. 28(153): 190048.

Richter A, Strauch A, Chao J, Ko M, Av-Gay Y. 2018. Screening of preselected libraries targeting *Mycobacterium abscessus* for drug discovery. Antimicrob Agents Chemother. 62:e00828-18.

Rifat D, Chen L, Kreiswirth BN, Nuermberger EL. 2021. Genome-wide essentiality analysis of *Mycobacterium abscessus* by saturated transposon mutagenesis and deep sequencing. mbio. 12:e01049–21.

Ripoll F, Pasek S, Schenowitz C, Dossat C, Barbe V, Rottman M, Macheras E, Heym B, Herrmann J-L, Daffé M, et al. 2009. Non mycobacterial virulence genes in the genome of the emerging pathogen *Mycobacterium abscessus*. PLoS One. 4(6):e5660.

Robinson MW, Menon R, Donnelly SM, Dalton JP, Ranganathan S. 2009. An integrated transcriptomics and proteomics analysis of the secretome of the helminth pathogen *Fasciola hepatica*: proteins associated with invasion and infection of the mammalian host. Mol Cell Proteomics. 8(8):1891–1907.

Rojony R, Danelishvili L, Campeau A, Wozniak JM, Gonzalez DJ, Bermudez LE. 2020. Exposure of *Mycobacterium abscessus* to environmental stress and clinically used antibiotics reveals common proteome response among pathogenic mycobacteria. Microorganisms. 8(5):698.

Roy S, Ghatak D, Das P, Bose Dasgupta S. 2020. ESX secretion system: the gatekeepers of mycobacterial survivability and pathogenesis. Eur J Microbiol Immunol. 10(4):202–209.

Ryan K, Byrd TF. 2018. *Mycobacterium abscessus*: shapeshifter of the mycobacterial world. Front Microbiol. 9:2642.

Sanguinetti M, Ardito F, Fiscarelli E, La Sorda M, D'Argenio P, Ricciotti G, Fadda G. 2001. Fatal pulmonary infection due to multidrug-resistant *Mycobacterium abscessus* in a patient with cystic fibrosis. J Clin Microbiol. 39(2):816–819.

Sapriel G, Konjek J, Orgeur M, Bouri L, Frézal L, Roux AL, Dumas E. 2016. Genome-wide mosaicism within *Mycobacterium abscessus*: evolutionary and epidemiological implications. BMC Genom. 17:118.

Sassi M, Drancourt M. 2014. Genome analysis reveals three genomospecies in *Mycobacterium abscessus*. BMC Genomics. 15:359.

Sassi M, Gouret P, Chabrol O, Pontarotti P, Drancourt M. 2014. Mycobacteriophage-drived diversification of *Mycobacterium abscessus*. Biol Direct. 9:19.

Schildkraut JA, Coolen JPM, Burbaud S, Sangen JJN, Kwint MP, Floto RA, op den Camp HJM. 2021. RNA-sequencing elucidates drug-specific mechanisms of antibiotic tolerance and resistance in *M. abscessus*. Antimicrob. Agents Chemother. 66(1):e0150921.

Sekizuka T, Kai M, Nakanaga K, Nakata N, Kazumi Y, Maeda S, Makino M, Hoshino Y, Kuroda M. 2014. Complete genome sequence and comparative genomic analysis of *Mycobacterium massiliense* JCM 15300 in the *Mycobacterium abscessus* group reveal a conserved genomic island MmGI-1 related to putative lipid metabolism. PLoS One. 9(12):e114848.

Sfeir M, Walsh M, Rosa R, Aragon L, Liu SY, Cleary T, Worley M, et al. 2018. *Mycobacterium abscessus* complex infections: a retrospective cohort study. Open Forum Infect. Dis. 5:ofy022.

Shanmugham B, Pan A. 2013. Identification and characterization of potential therapeutic candidates in emerging human pathogen *Mycobacterium abscessus*: a novel hierarchical in silico approach. PLoS One. 8(3):e59126.

Shmarina G, Pukhalsky A, Petrova N, Zakharova E, Avakian L, Kapranov N, Alioshkin V. 2013. TNF gene polymorphisms in cystic fibrosis patients: contribution to the disease progression. J Transl Med. 11:19.

Simmon KE, Brown-Elliott BA, Ridge PG, Durtschi JD, Mann LB, Slechta ES, Steigerwalt AG, Moser BD, Whitney AM, Brown JM, et al. 2011. *Mycobacterium chelonae-abscessus* complex associated with sinopulmonary disease, Northeastern USA. Emerg Infect Dis. 17(9):1692–1700.

Skwark MJ, Torres PHM, Copoiu L, Bannerman B, Floto RA, Blundell TL. 2019. Mabellini: a genome-wide database for understanding the structural proteome and evaluating prospective antimicrobial targets of the emerging pathogen *Mycobacterium abscessus*. Database. 2019:baz113.

Staunton PM, Miranda-CasoLuengo AA, Loftus BJ, Gormley IC. 2019. BINDER: computationally inferring a gene regulatory network for *Mycobacterium abscessus*. BMC Bioinform. 20:466.

Steindor M, Nkwouano V, Stefanski A, Stuehler K, Ioerger TR, Bogumil D, Jacobsen M, Mackenzie CR, Kalscheuer R. 2019. A proteomics approach for the identification of species-specific immunogenic proteins in the *Mycobacterium abscessus* complex. Microbes Infect. 21(3-4):154–162.

Sulaiman I, Wu BG, Li Y, Scott AS, Malecha P, Scaglione B, Wang J, Basavaraj A, Chung S, Bantis K, et al. 2018. Evaluation of the airway microbiome in nontuberculous mycobacteria disease. Eur Respir J. 52(4):1800810.

Sur S, Bothra AK, Sen A. 2010. Symbiotic nitrogen fixation-a bioinformatics perspective. Biotechnology. 9(3):257–273.

Sur S, Pal B. 2021. Comprehensive review of *Mycobacterium ulcerans* and Buruli ulcer from a bioinformatics perspective – what have we learnt? Acta Biol Szeged. 65:233–245.

Surette MG. 2014. The cystic fibrosis lung microbiome. Annals ATS. 11(Suppl 1):S61–S655.

Swain A, Gnanasekar P, Prava J, Rajeev AC, Kesarwani P, Lahiri C, Pan A. 2021. A comparative genomics approach

for shortlisting broad-spectrum drug targets in nontuberculous mycobacteria. Microb Drug Resist. 27(2):212–226.
Tan JL, Khang TF, Ngeow YF, Choo SW. 2013. A phylogenomic approach to bacterial subspecies classification: proof of concept in *Mycobacterium abscessus*. BMC Genom. 14:879.
Tan JL, Ng KP, Ong CS, Ngeow YF. 2017. Genomic comparisons reveal microevolutionary differences in *Mycobacterium abscessus* subspecies. Front Microbiol. 8: 2042.
Tan JL, Ngeow YF, Choo SW. 2015. Support from phylogenomic networks and subspecies signatures for separation of *Mycobacterium massiliense* from *Mycobacterium bolletii*. J Clin Microbiol. 53(9):3042–3046.
Tettelin H, Davidson RM, Agrawal S, Aitken ML, Shallom S, Hasan NA, Strong M, de Moura VCN, De Groote MA, Duarte RS, et al. 2014. High-level relatedness among *Mycobacterium abscessus* subsp. *massiliense* strains from widely separated outbreaks. Emerg Infect Dis. 20(3): 364–371.
Thomson R, Tolson C, Carter R, Coulter C, Huygens F, Hargreaves M. 2013. Isolation of nontuberculous mycobacteria (NTM) from household water and shower aerosols in patients with pulmonary disease caused by NTM. J Clin Microbiol. 51(9):3006–3011.
Thornton CS, Mellett M, Jarand J, Barss L, Field SK, Fisher DA. 2021. The respiratory microbiome and nontuberculous mycobacteria: an emerging concern in human health. Eur Respir Rev. 30(160):200299.
Thuer E, Gabaldón T. 2017. Comparative transcriptomics of THP-1 monocytes in response to different pathogens. bioRxiv. DOI https://doi.org/10.1101/155853.
Tortoli E, Kohl TA, Brown-Elliott BA, Trovato A, Leão SC, Garcia MJ, Vasireddy S, Turenne CY, Griffith DE, Philley JV, et al. 2016. Emended description of *Mycobacterium abscessus*, *Mycobacterium abscessus* subsp. *abscessus* and *Mycobacterium abscessus* subsp. *bolletii* and designation of *Mycobacterium abscessus* subsp. *massiliense* comb. nov. Int J Syst Evol Microbiol. 66(11):4471–4479.
Tortoli E, Kohl TA, Trovato A, Baldan R, Campana S, Cariani Lis, Colombo C, Costa D, Cristadoro S, Di Serio MC, et al. 2017. *Mycobacterium abscessus* in patients with cystic fibrosis: low impact of inter-human transmission in Italy. Eur Respir J. 50(1):1602525.
Tsai SH, Shen GH, Lin CH, Liau JR, Lai HC, Hu ST. 2013. *Mab_3168c*, a putative acetyltransferase, enhances adherence, intracellular survival and antimicrobial resistance of *Mycobacterium abscessus*. PLoS One. 8(6):e67563.
Vandeplassche E, Tavernier S, Coenye T, Crabbé A. 2019. Influence of the lung microbiome on antibiotic susceptibility of cystic fibrosis pathogens. Eur Respir Rev. 28(152): 190041.
Wallace RJ, Jr, Meier A, Brown BA, Zhang Y, Sander P, Onyi GO, Böttger EC. 1996. Genetic basis for clarithromycin resistance among isolates of *Mycobacterium chelonae* and *Mycobacterium abscessus*. Antimicrob Agents Chemother. 40(7):1676–1681.
Waman VP, Vedithi SC, Thomas SE, Bannerman BP, Munir A, Skwark MJ, Malhotra S, Blundell TL. 2019. Mycobacterial genomics and structural bioinformatics: opportunities and challenges in drug discovery. Emerg Microbes Infect. 8(1): 109–118.
Wang K, Li M, Hakonarson H. 2010. ANNOVAR: functional annotation of genetic variants from high-throughput sequencing data. Nucleic Acids Res. 38(16):e164.
Wee WY, Dutta A, Choo SW. 2017. Comparative genome analyses of mycobacteria give better insights into their evolution. PLoS One. 12(3):e0172831.
Wetzstein N, Kohl TA, Schultze TG, Andres S, Bellinghausen C, Hügel C, Kempf VAJ, et al. 2020. Antimicrobial susceptibility and phylogenetic relations in a German cohort infected with *Mycobacterium abscessus*. J. Clin. Microbiol. 58:e01813-20.
Wong YL, Ong CS, Ngeow YF. 2012. Molecular typing of *Mycobacterium abscessus* based on tandem-repeat polymorphism. J Clin Microbiol. 50(9):3084–3088.
Wuzinski M, Sharma MK. 2018. Developing a genotyping scheme for *Mycobacterium abscessus* complex using whole genome sequencing data. PMUSER. 4:37–45.
Yadav JS, Gupta M. 2012. Secretome differences between the taxonomically related but clinically differing mycobacterial species *Mycobacterium abscessus* and *M. chelonae*. J. Integr. Omics. 2:64–79.
Yan J, Kevat A, Martinez E, Teese N, Johnson K, Ranganathan S, Harrison J, Massie J, Daley A. 2020. Investigating transmission of *Mycobacterium abscessus* amongst children in an Australian cystic fibrosis centre. J. Cyst Fibros. 19(2): 219–224.
Yarden J, Radojkovic D, De Boeck K, Macek M, Zemkova D, Vavrova V, Vlietinck R, Cassiman J-J, Cuppens H. 2005. Association of tumour necrosis factor alpha variants with the CF pulmonary phenotype. Thorax. 60(4):320–325.
Yee M, Klinzing D, Wei J-R, Gengenbacher M, Rubin EJ, Dick T. 2017. Draft genome sequence of *Mycobacterium abscessus* Bamboo. Genome Announc. 5(20):e00388–17.
Yoon JK, Kim TS, Kim JI, Yim JJ. 2020. Whole genome sequencing of nontuberculous *Mycobacterium* (NTM) isolates from sputum specimens of co-habiting patients with NTM pulmonary disease and NTM isolates from their environment. BMC Genom. 21:322.
Yoshida M, Fukano H, Miyamoto Y, Shibayama K, Suzuki M, Hoshino Y. 2018. Complete genome sequence of a type strain of *Mycobacterium abscessus* subsp. *bolletii*, a member of the *Mycobacterium abscessus* complex. Genome Announc. 6(5):e01530-17.
Zakham F, Aouane O, Ussery D, Benjouad A, Ennaji MM. 2012. Computational genomics-proteomics and phylogeny analysis of twenty one mycobacterial genomes (Tuberculosis & non Tuberculosis strains) . Microb Inform Exp. 2(1):7.
Zelazny AM, Root JM, Shea YR, Colombo RE, Shamputa IC, Stock F, Conlan S, McNulty S, Brown-Elliott BA, Wallace RJ, et al. 2009. Cohort study of molecular identification and typing of *Mycobacterium abscessus*, *Mycobacterium massiliense*, and *Mycobacterium bolletii*. J Clin Microbiol. 47(7): 1985–1995.
Zhao L, Chen Y, Bajaj AO, Eblimit A, Xu M, Soens ZT, Wang F, Ge Z, Jung SY, He F, et al. 2016. Integrative subcellular proteomic analysis allows accurate prediction of human disease-causing genes. Genome Res. 26(5):660–669.

Prof. Rajesh Kumar Guin
&
Dr. Asish Mandal

Traditional fishing gears of Bankura District, WB, India: Some uniqueness in fish catching

Article *in* Notulae Scientia Biologicae · February 2022

DOI: 10.15835/nsb14111132

9 authors, including:

Arindam Ganguly
Bankura Sammilani College
11 PUBLICATIONS **14** CITATIONS
SEE PROFILE

Ujjal Konar
Sikkim University
5 PUBLICATIONS **3** CITATIONS
SEE PROFILE

Animesh Kundu
Sikkim University
3 PUBLICATIONS **2** CITATIONS
SEE PROFILE

Sandeep Chatterjee
Raiganj University
3 PUBLICATIONS **2** CITATIONS
SEE PROFILE

Ganguly A *et al.* (2022)
Notulae Scientia Biologicae
Volume 14, Issue 1, Article number 11132
DOI:10.15835/nsb14111132
Research Article

Traditional fishing gears of Bankura District, WB, India: Some uniqueness in fish catching

Arindam GANGULY[1], Ujjal KONAR[1], Animesh KUNDU[1], Sandeep CHATTERJEE[1], Sristishil NANDI[1], Rajesh K. GUIN[2], Madhuchhanda DUARI[3], Asish MANDAL[4], Pradeep K. DAS MOHAPATRA[5]*

[1]*Bankura Sammilani College, Department of Microbiology, Bankura, West Bengal, India; arindam_ganguly@yahoo.com; konaru24@gmail.com; animesh2kundu@gmail.com; sandeepcmicrobio@gmail.com; nandisristishil44@gmail.com*
[2]*Ramananda College, Department of Geography, Bishnupur, Bankura, W.B., India; rajeshguin23@gmail.com*
[3]*Belda College, Department of Zoology, Belda, Paschim Midnapore, West Bengal, India; madhuchhandaduari@beldacollege.ac.in*
[4]*Ramananda College, P.G. Department of Botany, Bishnupur, Bankura-722122, W.B., India; mandalasish71@gmail.com*
[5]*Raiganj University, Department of Microbiology, Raiganj, Uttar Dinajpur, West Bengal, India; pkdmvu@gmail.com (*corresponding author)*

Abstract

The present study was undertaken to furnish the detailed features of the fish trapping devices and methods employed by the fish-farmers of Bankura district, West Bengal, India. It also determines small indigenous freshwater fish diversity. The study was carried out in randomly selected water bodies, ponds, rivers, streams; along with fisherfolk dominated thorps covering twenty-two community development blocks of Bankura district. The study revealed that the fishers of this area are accustomed to old and traditional fishing techniques. They also apply indigenous knowledge to develop some unique fish catching techniques like Gābāna, bamboo piece immersion and bowl trap. However, destructive fishing technique applying harmful chemicals had also been noticed in certain regions. A total of twenty-two traditional fishing gears have been recorded from the study area of which 7 gears were traps, 5 encircling gears, 2 entangling gears, 3 hooks and line, 4 scooping gears and 1 impaling gear. The study has revealed three unique indigenous fishing techniques of fish-farmers. A total of 34 small indigenous freshwater fish species (Least Concern, 29; Near Threatened, 3; Vulnerable, 1; Endangered, 1) were also identified. This study suggests that fishers of the study area still depend on traditional fishing gears and techniques to earn their livelihood.

Keywords: destructive fishing; fisherfolk community; fishing gears; small indigenous fish; traditional fishing techniques

Introduction

Bankura district occupies a transitional zone in India, between the western corrugated plateau of Chota-Nagpur and eastern low-lying alluvial plains. The area is surrounded with red ferruginous laterite soil, jagged terrain land and intermittent dense forest. Bankura district belongs to the tropical dry sub-humid climatic zone. The land receives an annual rainfall of about 1400 mm and almost 80% of the net annual rainfall occurs during

Received: 04 Dec 2021. Received in revised form: 28 Jan 2022. Accepted: 02 Feb 2022. Published online: 10 Feb 2022.
From Volume 13, Issue 1, 2021, Notulae Scientia Biologicae journal uses article numbers in place of the traditional method of continuous pagination through the volume. The journal will continue to appear quarterly, as before, with four annual numbers.

the monsoon season. The area is traversed by Damodar, Dwarakeswar, Gandheswari, Kangsabati, Shilabati and Sali riverine network along with numerous ponds and reservoirs which have made this drought-trodden district as the highest producer of inland freshwater resources (52,341 ha) within the state. 100 species of fish were documented from Bankura district by Roy *et al.* (2013). A good variety (92 species) of fishes in Bankura district was reported by Ganguly *et al.* (2018a).

Small indigenous fishes (maximum length in mature stage: 25-30 cm) are major contributor of nutritional security to the rural people. Nowadays, indigenous fishes are declining alarmingly due to siltation of natural breeding grounds, massive electro-fishing, indiscriminate use of small meshed net and insecticides in water-bodies; that also gives an adverse impact on aquatic ecosystem and food security (Ganguly *et al.*, 2018b; Ganguly *et al.*, 2019). Simultaneously, a large part of fishers is being forced to take tough stance for alternative source of income. Therefore, it becomes necessary to adopt a sound approach for sustainable development of the community.

Indigenous fishing techniques are eco-friendly and cost effective. There are various types and methodologies of the traditional fishing gears. Each gear possesses a unique pattern of operation and is highly variable according to the fabrication material, area and depth of water-bodies as well as season of operation.

A lot of study has been conducted on significant advancement of fishing gears and techniques throughout the India. Manna *et al.* (2011) reported 10 fishing gears from river Krishna. Use of 36 types of fishing gears in Nalbari District of Assam was revealed by Chakravartty and Sharma (2013). Baruah *et al.* (2013) identified 28 different types of fish traps from Brahmaputra valley of Assam. A comprehensive study was conducted by Chourey *et al.* (2014) to record the traditional fishing instruments used in Bhopal district. Operations of 7 traditional gears in Ukari reservoir of Gujrat was stated by Bhakta *et al.* (2016). Study conducted by Rao *et al.* (2016) in Lake Kolleru of Andhra Pradesh documented ten varieties of gear commonly used implements in fish capture. Islam and Hussain (2018) have made an extensive study to evaluate the presence of 43 types of fishing gears in Kumari beel of Goalpara district, Assam. Syed *et al.* (2020) elaborately describes the design and technical characteristics of fishing craft and gear, operated in Wular Lake, Kashmir. Jabeen and Soren (2021) reported one type of fishing craft and nine different types of gears operated by fishermen in the Manas river in Assam. Petetta *et al.* (2021) evaluated the application of pots as an alternative and sustainable fishing gears in the Mediterranean Sea.

However, a very little approach has been made to explore the traditional fishing methodologies of West Bengal. Das and Barat (2014) reported the existence of 22 types of traditional fishing gears in Cooch Behar. Samajdar and Saikia (2014) documented 23 types of indigenous fishing gears in Birbhum district. Twelve different types of fishing gears were obtained by Sandhya *et al.* (2019) from the floodplain wetlands of lower Gangetic plains of West Bengal. Uses of five different kinds of crafts and twelve different kinds of gear in Sundarban region were recorded by Madhu *et al.* (2021). No such attempt has been taken to document the detail features of fishing practice and gears operated by the fish-farmers of Bankura district. Dutta and Mondal (2016) have observed 15 types of fishing gears in Rajagram village of the district. Therefore, the present study is the first kind of effort for documentation of fishing patterns of the entire Bankura district making a multi-faceted impact across a range of fields from their health and food security to cultural and socio-economic improvement.

Materials and Methods

Description of the study site

Bankura district (Figure 1) covers a vast area of about 6,882 km^2, lies between 22°38′ to 23°38′ N latitude and 86°36′ to 87°46′ E longitude. A simple random survey was conducted for acquisition of data from the local fish markets and waterbodies covering twenty-two blocks of Bankura district during the period of June, 2018 to May, 2019.

Geo-spatial representation

The GPS navigation device (eTrex Vista Hcx; Garmin® International, Inc., USA) was used to obtain specific location status. For the mapping, a satellite image was extracted from Goggle earth which was Landsat 8 imagery with 30-meter resolution. The image was then projected on UTM projection with the help of ArcGIS software and for more accuracy in the coordinate system, it was Geo-referenced.

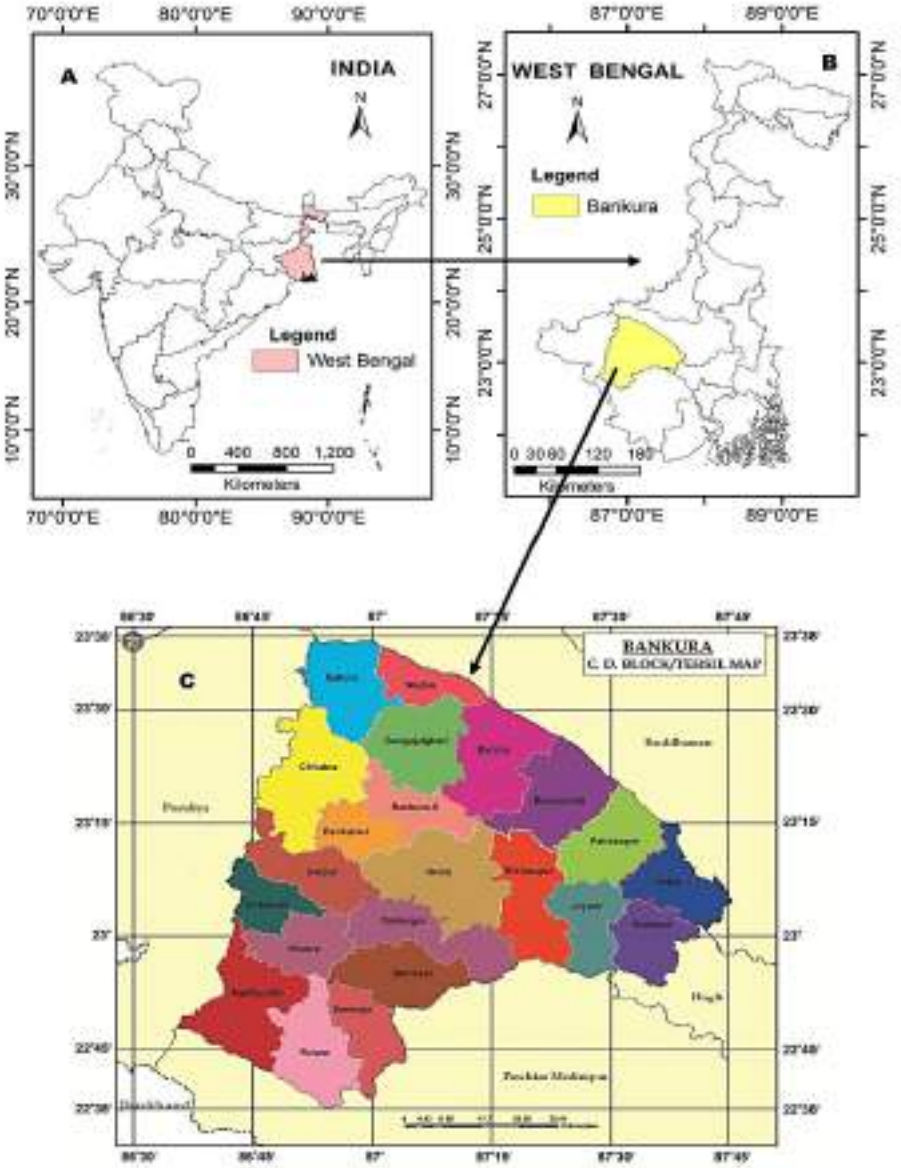

Figure 1. Geographical location of the study area: (A) Map of India; (B) Map of West Bengal; (C) Map showing the study area (Bankura district with twenty-two blocks)

Field survey

The study was conducted by the Participatory Rural Appraisal (PRA) method. At first, 4-5 fish-farmers dominated thorps were randomly chosen from each of twenty-two block and a standard questionnaire has been made to collect the relevant data regarding the fishing gears. Special emphases were conferred on fabrication material, dimension, mesh size, price, season, mode of operation etc.

The primary data was retrieved from the fish farmers, traders and store-houses of each sorted thorp through interactive approach. The semi-structured interviews and group discussions were then conducted with about the 5-10 fishermen of each sorted thorp. Instinctive knowledge and sagacity of fishermen assisted in collecting the required information about traditional fishing gears. Interaction with fishing gear makers and fishing gear retailers also helped to rectify and enrich the recorded data. The mode of operation of the fishing gears was precisely observed and recorded from the onsite during fishing. Appropriate length, height, breadth, mesh size of the fishing gear was measured critically using measuring equipment. The mesh size was calculated by measuring the distance between the centers of two opposite knots in the same mesh when fully extended in N-direction (Petetta *et al.*, 2021). A Measuring tape has been used and cross-checked with vernier caliper to measure the mesh size of fishing gears.

Fishing techniques and uses of traditional fishing gear were documented through photography using a camera (Nikon d5300). Finally, all the obtained data was cross-checked through group discussion with professional fisherman and Govt. Agencies. Microsoft office excel, 2016 software has been used to statistically analyze the recorded data

Sample collection

The conventional fishing gears were also used to collect fish specimen with the help of fish farmers from the study area. The samples were precisely collected and preserved (4-6% formalin) for further identification (Roy *et al.*, 2013). The identification of those samples was performed according to Talwar and Jhingran (1991). The International Union for Conservation of Nature (IUCN, 2021) red list of threatened species was used to evaluate the present conservation status of the obtained species.

Results

Survey result indicated that the fishers of Bankura district mostly handled old fashioned, traditional fishing gears (Figure 3-5). A total of 22 types of traditional fishing gears and 3 types of fishing pots have been observed during the survey. These gears were further subdivided into six categories as per their mode of operation viz. trap, encircling gear, entangling gear, scooping gear, hook and line fishing and impaling gear (Figure 2). Fishing gears along with their detailed features are summarized in Table 1.

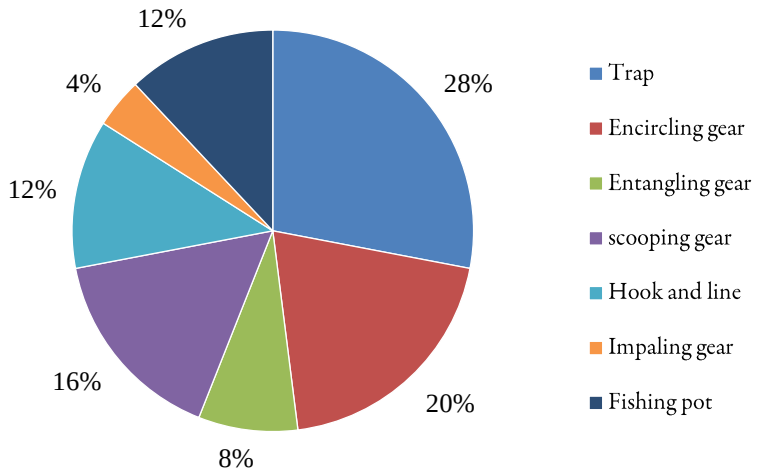

Figure 2. Distribution of various traditional fishing gears in Bankura district

Table 1. Types of fishing gears used by fish-farmers of Bankura district, West Bengal, India

Sl. No	Fishing gears	Local name	Types of gear	Ingredient	Dimension	Mesh size (mm)	Price (INR)	Season	No. of fisherman required	Targeted species	Freq of use
1	Box trap	Ghuṇi	Trap	Bamboo	30-110 cm length and breadth 10-18 cm and height 20-35cm	—	50-380	Monsoon and post-monsoon	1	*Trichogaster chuna, Esomus danricus, Puntius ticto, Parluciosoma daniconius, Salmostoma bacaila, prawn*	Frequent
2	Box trap	Raba Ghuni	Trap	Bamboo	60-90 cm length and breadth 10-18 cm and height 20-35cm	—	120-200	Monsoon and post monsoon	1	*Trichogaster chuna, Esomus danricus, Puntius ticto, Parluciosoma daniconius*	Moderate
3	Barricade tap	Siÿāṛā	Trap	Bamboo	50-90 cm length with 30-60 cm height	—	35-40	Monsoon	1-2	All type of fishes	Frequent
4	Tubular trap	Ghugī	Trap	Bamboo	80-100 cm length and top opening radius 5-7 cm	—	50-80	Monsoon	1	*Esomus danricus, Amblypharyngodon mola, Puntius ticto, Anabas testudineus, Channa punctata*	Frequent
5	Cover pot	Palu'i	Trap	Bamboo	Height 35-45 cm and top opening radius of 5 cm with bottom radius of 25-30 cm	—	160-250	Winter and summer season	1	*Mastacembelus armatus, Channa punctata, Heteropneustes fossilis, Wallago attu*	Frequent
6	Fyke net	Chāka ni jāla	Trap	GI rod and net	110-130 cm length with opening radius of 15-20 cm	4	180-200	Monsoon	1	*Anabas testudineus, Mastacembelus pancalus, Esomus danricus, Puntius ticto*	Moderate
7	Cone shaped trap net	Ghugī jāla	Trap	Net	4-5 m length and bottom radius 1.5-2 m	10-15	250-400	Monsoon	1-2	*Catla catla, Cirrhinus mrigala, Ctenopharyngodon idella, Hypophthalmichthys molitrix*	Rare
8	Drag net	Maśāri jāla	Encircling gear	Net	30-50 m length and 3-4 m breadth	2-3	300-450/ kg	Whole year	4-6	All type of fishes	Frequent
9	Drag net	Ṭānā jāla	Encircling gear	Net	40-80 m length and 3-4 m breadth	40-60	200-300/ kg	Whole year	8-16	*Channa striata, Chitala chitala, Labeo calbasu, Catla catla*	Frequent
10	Drag net	Caṭa jāla	Encircling gear	Jute fibre	6-7 m length and 3-4 m breadth	10	1500	Whole year	6-8	*Labeo calbasu, Hypophthalmichthys molitrix, Aristichthys nobilis, Catla catla, Cirrhinus mrigala*	Rare
11	Small Danish seine	Ghāṭa jāla	Encircling gear	Net	0.5 -1 m length and middle breadth 0.6 m	3-10	150-300	Whole year	1-2	*Clarias gariepinus, Channa gachua, Channa punctata*	Moderate
12	Cast net	Khiÿā jāla	Encircling gear	Net	2-4 m length and bottom radius 1-2m	5-10	650-1200	Whole year	1	*Cirrhinus mrigala, Catla catla, Aristichthys nobilis*	Frequent
13	Gill net	Phām* di jāla	Entangling gear	Net	20-30 m length and 3-4 m breadth	50-80	1000-1500	Whole year	2-4	*Ctenopharyngodon idella, Cyprinus carpio, Labeo rohita, Heteropneustes fossilis, Wallago attu, Clarias gariepinus*	Moderate
14	Small meshed gill net	Kārēṇṭa jāla	Entangling gear	Net	6-8 m length and 1-2 m breadth	20-35	30-60	Whole year	2-3	*Labeo bata, Anabas testudineus, Puntius ticto*	Frequent
15	Push net	Ṭhelā jāla	Scooping gear	Bamboo and net	Triangular with each side length of 90-120 cm	5-7	100-120	Whole year	1	*Aspidoparia jaya, Chanda nama, prawn, snails*	Rare
16	Small scoop net	Ghuṇa jāla	Scooping gear	Bamboo and net	Open radius 20-25 cm	3-4	30-45	Monsoon, post monsoon	1	*Puntius ticto, Amblypharyngodon mola, Danio rerio,* prawn	Frequent
17	Big scoop net	Ghuni jāla	Scooping gear	Bamboo and net	Open radius40-60 cm	3-7	120-150	Whole year	1	*Trichogaster sp., Esomus danricus, Puntius sp.,* prawn	Frequent
18	Circular scoop net	Hāta jāla	Scooping gear	Bamboo and net	Circular net of 15 cm radius and bamboo rod of 2-3 ft long	10-15	35-40	Whole year	1	*Clarias gariepinus, Clarias batrachus, Heteropneustes fossilis*	Moderate
19	Hook and line	Hāta chipa	Hook and line	Bamboo, line and barshi	5-6 ft length	—	20-80	Whole year	1	*Anabas testudineus, Trichogaster fasciata, Puntius ticto, Oreochromis mossambicus*	Frequent
20	Hook and line	Hu'ila chipa	Hook and line	Bamboo, line, wheel and barshi	7-7.5 ft length	—	150	Whole year	1	Indian Major Carp, *Notopterus notopterus, Oreochromis niloticus, Colossoma macropomum*	Moderate
21	Hook and line	Jhima chipa	Hook and line	Glassfiber stick, line and barshi	3 ft length	—	200-1000	Whole year	1	*Labeo rohita, Labeo calbasu, Heteropneustes fossilis, Clarias gariepinus*	Rare
22	Piercing gear	Kēcā	Impaling gear	Bamboo and iron hook	Iron hook is of 30-40 cm long and bamboo piece length is 90-135 cm	—	70-80	Whole year	1	*Ctenopharyngodon idella, Cyprinus carpio, Hypophthalmichthys molitrix, Aristichthys nobilis*	Rare
23	Bamboo basket	Khalui	Fishing pot	Bamboo	15-25 cm height with opening radius of 5-7 cm	—	60-200	Whole year	1	___	Moderate
24	Bamboo basket	Jhuṛi	Fishing pot	Bamboo	25-30 cm height with opening radius of 15-20 cm	—	100-150	Whole year	1	___	Frequent
25	Pipkin	Hāmṛi	Fishing pot	Aluminium	40-60 cm height with opening radius of 20-30 cm	—	1000-1200	Whole year	1	___	Frequent

* June – August = Monsoon; September – November = Post monsoon; December – February = winter; March – May = summer. INR = Indian Rupee

Fishing gears

Trap

Ghuṇi

It is a rectangular-shaped cage trap made up of finely sliced thin bamboo sticks. Sticks are encased with nylon string in a regular gap of 2-3 mm. On the front side, it has 2-4 longitudinal, rectangular notches, and each notch has a vertical opening that directed the fishes to get into the trap. Trapped fishes are collected through the hole situated at any one corner of the upper portion. The length of Ghuṇi differs significantly (30-110 cm) as per the site of operation while the height and breadth are almost identical for all types (height 20-35 cm and breadth 10-18 cm). It is mostly used in monsoon and post-monsoon season when adequate water passes through the canal, stream, and gutter. It is submerged along a blockade made up of mud in shallow and slowly flowing water-bodies (Figure 3A). The front side of Ghuṇi always placed in the opposite direction of water. Ghuṇi is kept overnight in the bushy area and taken out on next morning to collect the entrapped fishes. Mainly prawn and small fishes (*Trichogaster chuna, Esomus danricus, Puntius ticto, Parluciosoma daniconius, Salmostoma bacaila* etc.) are entrapped in Ghuṇi.

Rābā ghuṇi

Rābā ghuṇi on the contrary of Ghuṇi does not possess any vertical notches though they are functionally equivalent. It consists of 3-4 circular openings of a radius of 2 cm, circumambient by thin bamboo sticks that narrows and loosely interspersed inward (Figure 3B).

Siẏāṛā

It is a traditional fishing gear made up of chopped bamboo or thin bamboo sticks or cane. Sticks are designed vertically at a regular gap and fastened with plastic or nylon rope. Siẏāṛā is often fabricated and handled by tribes, and they structured this as per their necessity. Therefore, its length and height vary greatly (50-140 cm in length and 30-120 cm in height). It is used for versatile purposes. Fishes that migrate opposite the current of water are interrupted by Siẏāṛā. Small Siẏāṛā (Figure 3C) is placed in the narrow canal, streams, and drenched paddy fields whereas Big Siẏāṛā (Figure 3D) is used as a barricade in steeped ponds and beels to prevent the fish migration. Small Siẏāṛā is frequently used along with Ghugī to catch fishes, and this entire set up is locally recognised as Āṛāḍāṅā.

Ghugī

It is a funnel-shaped trap made up of finely sliced, flat bamboo sticks (Figure 3E). The proximal opening is circular (5-7 cm in radius) and the body is (80-100 cm in length) gradually narrows towards the tail. The body is made up of flat interweaved bamboo sticks and the tail portion is tied up with small bamboo or wood piece that provides support to the structure. It is usually kept beside the Siẏāṛā in canal, ponds, and paddy fields by making an oozy slope. Fishes (e.g. *Esomus danricus, Amblypharyngodon mola, Puntius ticto, Anabas testudineus, Channa punctata*) that can migrate opposite the water current are interrupted by Siẏāṛā and trapped into the Ghugī.

Palu'i

It is a half oval shaped trap, operated by single person. It is made up of nearly 160-180 finely chopped bamboo sticks which are tied together by 4-5 set of nylon rope at an interval of 10-12 cm. It has two circular openings: a narrow anterior opening (5 cm radius) and a wide distal opening (25-30 cm radius). Height of the trap is about 35-45 cm. A bamboo made ring of apt diameter is inserted inside the trap to provide the support and circular shape (Figure 3F). It is mostly used in dry season to catch medium size fishes (*Mastacembelus armatus, Channa punctata, Heteropneustes fossilis, Wallago attu* etc.) that survive in stagnant muddy water. The distal end of the trap is pushed into mud then the entrapped fishes are collected by hand through the anterior opening.

Chākani jāla

It is a funnel-shaped trap made up of two circular rings of galvanized iron (GI) rod and nylon net. The first ring that act as an opening are connected through net with the second ring at a distance of 30 cm in the form of a hollow tube (Figure 3G). After the second ring, the net gradually narrows like a funnel to capture fishes. Both rings have a radius of 15-20 cm. It is mainly installed in steeped paddy fields in monsoon to catch indigenous fishes (e.g., *Anabas testudineus, Mastacembelus pancalus, Esomus danricus, Puntius ticto).*

Ghugī jāla

It is a funnel-shaped net (Figure 3H) made up of nylon strings. Its circular anterior opening placed in the direction of water in canal and streams. Mesh size of the net is about 10-15 mm. The device is mainly used to catch large fishes like *Catla catla, Cirrhinus mrigala, Ctenopharyngodon idella, Hypophthalmichthys molitrix.* It also plays the role of a barrier alongside the ponds to prevent migration of fishes.

Encircling gear

Maśāri jāla

It is the most densely meshed fishing gear made up of nylon strings. Mesh size of Maśāri jāla is about 2-3 mm. It is effectively operated in ponds as a drag net (Figure 3I) to catch a wide variety of fishes; can be installed as a barrier to restrict horizontal migration of fishes or can be used to set up a four-sided cell (Figure 3J) inside water-bodies to cultivate fish-seed and spawn.

Ṭānā jāla

This large and heavy fishing gear (Figure 4A) requires considerable human resources to operate. Its length, breadth and mesh size alter mainly according to the area of operation. Net is dragged by men or using craft either from both sides or from a side and meet at a point to collect the trapped fishes. It is used throughout the year to catch large fishes (*Channa striata, Chitala chitala, Labeo calbasu, Catla catla*) from the dam and large water-bodies.

Caṭa jāla

Caṭa jāla is made up of very finely meshed jute fibre (Figure 4B). It has a life span of about 6-8 months. Its length and breadth vary between 6-7 m and 3-4 m respectively. The mesh size is about 10 mm. Ten-twelve Caṭa jāla are fastened and operated as a Ṭānā jāla in ponds and beels. Major carps like *Labeo calbasu, Hypophthalmichthys molitrix, Aristichthys nobilis, Catla catla, Cirrhinus mrigala* are caught through this gear.

Ghāṭa jāla

It is a triangular net bag with a cork-line and a lead-line that gradually narrows towards the edges to form two wings (Figure 4C). A 2-3 m long bamboo piece is tied with each of two wings to handle it. The length of the net is about 0.5-1 m, and mesh size ranges from 3-10 cm. Bottom-dwelling fishes like *Clarias gariepinus, Channa gachua, Channa punctata* are mainly targeted through this gear.

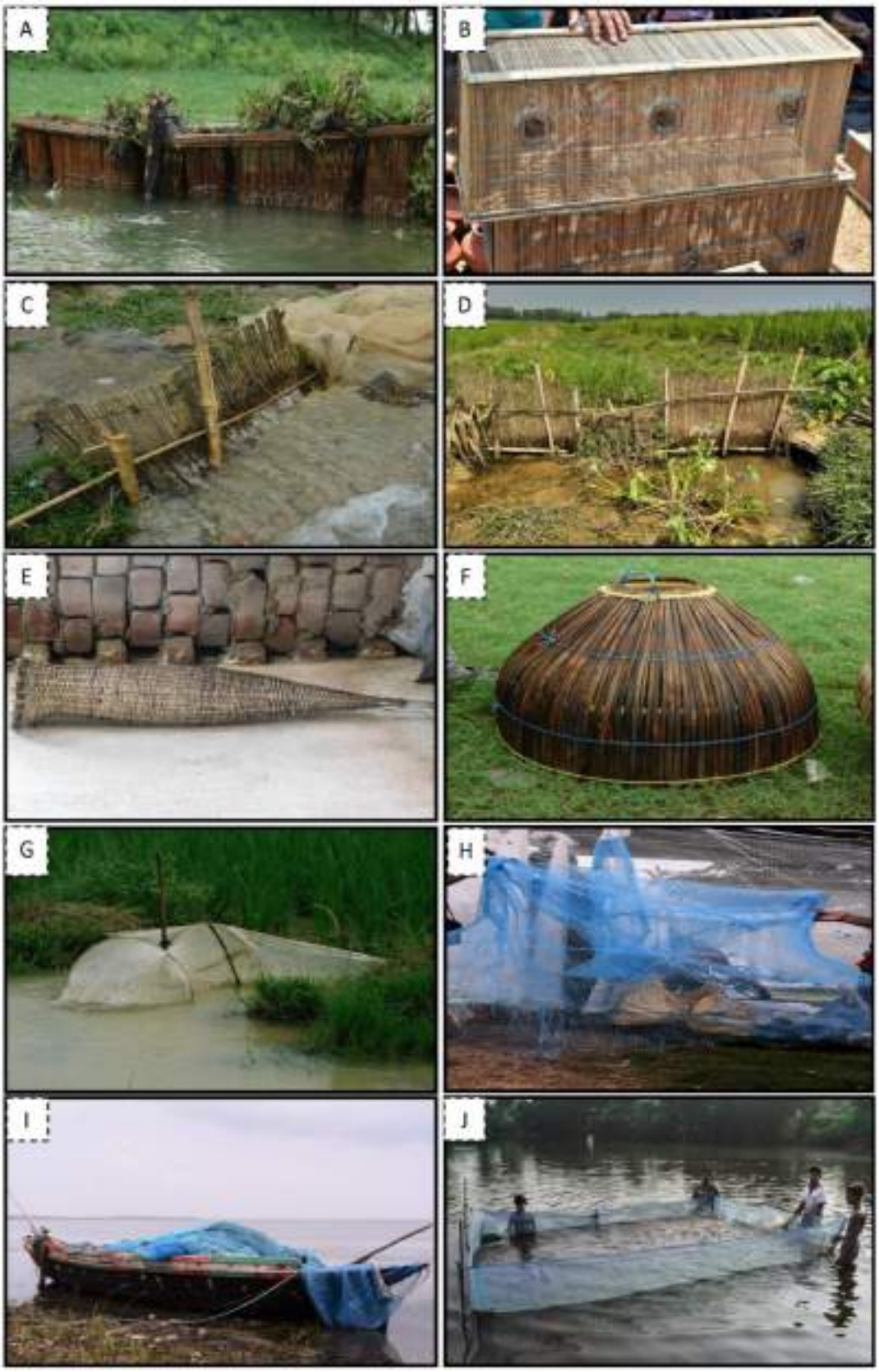

Figure 3. Traditional fishing gears: (A) Ghuṇi; (B) Raba ghuni; (C) Small Siÿāṛā; (D) Big Siÿāṛā; (E) Ghugī; (F) PaluꞋI; (G) Chākani jāla; (H) Ghugī jāla; (I) Maśāri jāla; (J) Maśāri jāla

Khiẏā jāla

It is the most frequently used fishing gear, being operated single-handedly in weed-free water throughout the year. It is also locally known as Māthā ghurānī jāla. This cone-shaped circular net (Figure 4D) is made up of nylon and cotton fibre. A strong rope of 4-5 m remains fastened to the apex of the net, and numerous tubular iron or lead sinkers are fixed with the bottom margin of the net to sink the net during operation. Mesh size of the net varies from 10-20 mm as per targeted fishes. Fishermen throw it over the water surface either from the boat or shoreline or banks of the water-bodies. As the net sinks into the water, fishes are trapped and then the net is lifted with the help of the strong rope. Mainly medium size fishes (e.g., *Cirrhinus mrigala, Catla catla, Aristichthys nobilis*) are targeted by this gear.

Entangling gear

Phāmďi jāla

It is an entangling fishing gear operated in both flowing and stagnant water. It is fabricated with nylon monofilament (Figure 4E). Thermocol and plastic bottles are tied with the upper margin of the net to float whereas cylindrical iron or lead masses are fastened at the bottom edge of the net to immerse it in water during the operation. Its length and breadth vary according to the area and depth of the waterbodies. Fishermen set the net horizontally in the river, dam or large ponds for overnight and picked up early morning to collect the entangled fishes. Mesh size of the net ranges between 50-80 mm. Therefore, it is most commonly used to catch medium and large size fishes (*Ctenopharyngodon idella, Cyprinus carpio, Labeo rohita, Heteropneustes fossilis, Wallago attu, Clarias gariepinus*).

Kārēnṭa jāla

It is a shorter variant of Phāmďi jāla. It is also fabricated with nylon monofilament. Its length and breadth vary from 6-8 m and 1-2 m respectively. Mesh size ranges between 20-35 mm. It is largely operated in small beels, streams, and canals to entangle small fishes like *Mystus tengra, Labeo bata, Anabas testudineus, and Puntius ticto.*

Scooping gear

Ṭhēlā jāla

It is made up of 3 bamboo pieces (3-4 ft length) and a net of mesh size of 5-7 mm. Bamboo pieces are tied together to make a triangular frame and the net is then fitted with it (Figure 4F). Fishermen operate it by pushing under bushes of lentic and lotic water bodies and then lifted up from the water to collect the fishes. It is mainly used to catch the snails, prawns and small fishes like *Aspidoparia jaya, Chanda nama.*

Ghuṇa jāla

It is the most widely operated fishing gear of the study area. It is made up of bamboo and net. A flatly sliced bamboo stick is bent to make a circular ring (radius: 20-25 cm) connected with a conical net (Figure 4G). Peoples use it to catch small indigenous fishes (*Puntius ticto, Amblypharyngodon mola, Danio rerio* etc.) in shallow waterbodies.

Ghuṇi jāla

Ghuṇi jāla is made up of circularly bent bamboo ring and conical net. Generally, the frame consists of circular bamboo ring fitted with four bamboo poles (2-3 ft in length) which are tied together at the top to form a cone (Figure 4H). Prawn, snails and small fishes (e.g. *Trichogaster sp., Esomus danricus, Puntius sp.*) are caught through this gear.

Hāta jāla

It is a circular pocket like net of mesh size 10-15 mm, attached to a 2-3 ft long bamboo rod (Figure 4I). It is mainly used to catch slow-moving air-breathing fishes (*Clarias gariepinus, Clarias batrachus, Heteropneustes fossilis*) and crabs at night.

Figure 4. Traditional fishing gears: (A) Ṭānā jāla; (B) Caṭa jāla; (C) Ghāṭa jāla; (D) Khiẏā jāla; (E) Phāmẚdi jāla; (F) Ṭhēlā jāla; (G) Ghuṇa jāla; (H) Ghuni jāla; (I) Hāta jāla; (J) Hāta chipa

Hook and line

Hāta chipa

It is made up of a bamboo stick and a cotton twine (Figure 4J). Cotton twine is tied with the narrow tip of the stick while the other end of the twine is embedded with one or more barbed hook. A thin plate of lead is used as weight and a float is being attached to the twine at a distance of 1.5-2 ft from the hook. Hooks are baited with wheat flour, earthworm, grasshopper, etc. and sinks into the water. As the fishes swallow the bait, the hook stuck in the fish body, and the fisherman lifts the chip with a jerk to collect the fishes. Small fishes like *Anabas testudineus, Trichogaster fasciata, Puntius ticto, Oreochromis mossambicus* are caught using hooks of different sizes.

Hu'ila chipa

It is also made up of bamboo stick and nylon string. A wheel is fixed with the stick near the thick end, in which the string remains folded (Figure 5A). Another end of the string is tied with 2-4 barbed hooks. The hooks with bait (Figure 5C) are thrown into the water far away from the shore. As the fish swallows the bait and get pierced, nylon string is roll up by wheel to collect the tangled fishes. It is used to catch medium size fishes (*Notopterus notopterus, Oreochromis niloticus, Colossoma macropomum* etc.)

Jhima chipa

Jhima chipa, although they resemble hook and line fishing gears like Hāta chipa and Hu'ila chipa, handled in a different fashion. The fishing rod is composed of glass-fibre or graphite (Figure 5B) and is about 3 ft of length. A long nylon string, tied up with 2-4 hooks, is fixed to the rod by the fishing reel. The fishing reel is used in winding and stowing away the line. This gear is usually operated by the professional fishermen to catch large fishes like *Labeo rohita, Labeo calbasu, Heteropneustes fossilis, and Clarias gariepinus* in the river, dam and large ponds.

Impaling gear

Kēcā

It is an impaling gear[4] mainly used by young tribal people. It has a bamboo stick as a handle and 6-10 iron rods. These rods (20-25 cm in length) are remained firmly attached at one end of the bamboo piece (Figure 5D). The piercing nozzle of these rods consists of a barb at the tip that stuck in the fish body. The fisherman stands still in the shallow water, waits and then pierces the running fish with the sharp end. It is used to catch large fishes (e.g. *Ctenopharyngodon idella, Cyprinus carpio, Hypophthalmichthys molitrix, Aristichthys nobilis*) throughout the year.

Fishing pots

Khalu'i

It is a fishing pot made up of split interweaved bamboo. It has an opening of 5-7 cm radius covered by a net (Figure 5E). It is used along Khiẏā jāla to keep trapped fishes.

Jhuṛi

It is a semi-circular (Figure 5F) fishing pot used to keep caught fishes. It is also made up of split bamboo.

Figure 5. Traditional fishing gears: (A) Hu'ila chipa; (B) Jhima chipa; (C) Bait; (D) Kēcā; (E) Khalu'i; (F) Jhuṛi; (G) Hāmǐṛi; (H) Bamboo piece immersion; (I) Bowl trap; (J) Bamboo slicing

Hāmǐṛi

This fishing pot is made up of Aluminium (Figure 5G). It is used to keep large quantities of fishes. It is frequently used along Ṭānā jāla and Maśāri jāla. It is easy to handle due to its light weight.

Indigenous fishing methods

Gābāna (Group hand picking)

It is a traditional fishing method, mainly practiced by tribal women and children in pre-monsoon in decreased water level. They caught fishes skillfully with their hands from muddy water or mire, without utilizing any fishing gear. *Mastacembelus pancalus, Xenentodon cancila, Channa punctata, Channa sp.* are usually harvested by this method.

Bamboo piece immersion

It is a kind of indigenous fishing method. In this technique, one side-open hollow bamboo stalks are immersed in weed beset solitary water. After few days, bamboo stalks are taken out from the water by blocking the open end with palm (Figure 5H) and the fishes that have entered stalk are collected. Small indigenous fishes (e.g. *Channa punctata, Channa sp., Anabas testudineus*) are generally caught by this technique.

Bowl trap

It is also an indigenous fishing method, practiced largely by farmers in rivers, streams, and other flowing water. At first, the open portion of the bowl is covered with white cloth and a small aperture is being made at the middle of the cloth (Figure 5I). The wheat flour is used as bait in the bowl to attract fishes. The bowl is then placed at the bottom of the water surface. Small fishes like *Parluciosoma daniconius, Amblypharyngodon mola, Aspidoparia jaya* enters into the bowl and trapped. After few hours, bowl is taken out from the water, and trapped fishes are collected.

Destructive fishing

Apart from the traditional and indigenous fishing methods, some instances of destructive fishing were also observed in Bishnupur, Panchmura, Ramsagar and Indpur blocks. Some fishermen use toxic chemicals (e.g. pesticides, insecticides) that alarmingly decrease the dissolved oxygen content of the waterbody (Table 2). As a result, aquatic animals were compelled to come on the upper surface region of the water and get trapped. Thus, the entire aquatic system is getting endangered due to predation of both targeted and non-targeted species. However, electro-fishing was not observed in the study area.

Table 2. Chemicals used for fishing in study area

Serial No.	Name	Type	Cost (INR)	Effect
1	Mahua oil cake	Derivative from the plant *Bassia latifolia*	22/kg	It shrinks the erythrocytes and conduce haemolysis of cells of fishes (Homechaudhuri *et al.*, 1986).
2	*Fenpropathrin* (Meothrin)	Pyrethroid insecticide	630/500 ml	Meothrin is responsible for fish convulsions cough, ataxia, intermittent paralysis and annihilate (Bingsheng *et al.*, 1994). It also reduces the tissue energy level by decreasing glycogen level in liver, muscle and gonads (Chaudhari and Yadav 2013).
3	Sulfoxaflor	Systemic insecticide	780/150 ml	It poses no significant risk to fishes.
4	Cypermethrin	Synthetic pyrethroid insecticide	250/kg	It adversely affects their behavioural patterns, shifting aerobic pathway of fish respiration towards anaerobic pathway and also inhibiting energy production by suppressing ATP synthesis (Tiwari *et al.*, 2012).

INR= Indian Rupee

Small indigenous fish diversity

A total number of 33 small indigenous freshwater fish species were identified during the study period (Table 3). The study area contained 5 globally endemic small indigenous freshwater fish species *(Near Threatened= 3; Vulnerable= 1; Endangered= 1).* The entire northern and southern part of Bankura district is significantly rich in the context of species availability. Saltora, Mejhia and Barjora block located on Damodar basin; Sarenga and Raipur of Kangsabati basin and seven bundhs besiege Bishnupur are major habitats of small indigenous fishes. Maximum amount of fishes were found during the monsoon (June-August) and post monsoon season (September-November) while the less amount were observed during the winter season (December-February).

Table 3. Small indigenous fishes of Bankura district

Sl. No.	Scientific name	Local name	IUCN status
1	*Esomus danricus* (Hamilton, 1822)	Dārkē	LC
2	*Glossogobius giuris* (Hamilton, 1822)	Bhalkōrā/Bēlē	LC
3	*Puntius sophore* (Hamilton, 1822)	Puṁṭi	LC
4	*Puntius ticto* (Hamilton, 1822)	Ciṯpuṁṭi	LC
5	*Amblypharyngodon mola* (Hamilton, 1822)	Mauralā	LC
6	*Parluciosoma daniconius* (Hamilton, 1822)	Dārkē	LC
7	*Aplocheilus panchax* (Hamilton, 1822)	Tēcōkhā	LC
8	*Aspidoparia morar* (Hamilton, 1822)	Ciṛā	LC
9	*Aspidoparia jaya* (Hamilton, 1822)	Chuẏā	LC
10	*Crossocheilus latius* (Hamilton, 1822)	Simsuṁṭi	LC
11	*Salmostoma bacaila* (Hamilton, 1822)	Chuẏā	LC
12	*Securicula gora* (Hamilton, 1822)	Ghōṛācēlā	LC
13	*Glyptothorax dorsalis* (Vinciguerra, 1890)	Tēlsuṁṭi	LC
14	*Anabas testudineus* (Bloch, 1792)	Dēśīkō'i	LC
15	*Gudusia chapra* (Hamilton, 1822)	Khaẏarā	LC
16	*Channa orientalis*(Bloch & Schneider, 1801)	Cyāṁ	VU
17	*Channa stewartii* (Playfair, 1867)	Tēlcyāṁ	LC
18	*Channa punctata* (Bloch, 1793)	Lyāṭā	LC
19	*Parambassis lala* (Hamilton, 1822)	Lāl Cāṁdakōṁṛā	NT
20	*Eutropiichthys vacha* (Hamilton, 1822)	Bāchā	LC
21	*Heteropneustes fossilis* (Bloch, 1794)	Śiṅgī	LC
22	*Ompok pabda* (Hamilton, 1822)	Pābdā	NT
23	*Clarias magur* (Hamilton, 1822)	Dēśī Māgur	EN
24	*Mystus tengara* (Hamilton, 1822)	Tyānrā	LC
25	*Chanda nama* (Hamilton, 1822)	Cāṁdakōṁṛā	LC
26	*Trichogaster chuna*(Hamilton, 1822)	Cūnā	LC
27	*Trichogaster lalius* (Hamilton, 1822)	Khōlsē	LC
28	*Trichogaster fasciata* (Bloch and Schneider, 1801)	Khōlsē	LC
29	*Ailia coila* (Hamilton, 1822)	Bāṁśapātā	NT
30	*Oreochromis niloticus* (Linnaeus, 1758)	Nilaṇṭikā	LC
31	*Mugil cephalus* (Hamilton, 1822)	Pārśē	LC
32	*Lepidocephalus guntea* (Hamilton, 1822)	Guṭē	LC
33	*Xenentodon cancila* (Hamilton, 1822)	Gāntāṛā	LC

LC= Least Concern; NT= Near Threatened; VU= Vulnerable; EN=Endangered

Discussion

A wide variety of traditional fishing gears and techniques with different mode of operation were practiced by fish farmers of Bankura district. A total of twenty-two traditional fishing gears *(bamboo=5; bamboo and net= 4; bamboo-line and hook= 3; bamboo and metal hook=1; GI rod and net=1; jute fibre=1; net=7)* have been recorded from the study area. Use of bamboo made fishing traps were pre-eminently observed specially during monsoon and post-monsoon seasons. However, operation of fishing gears with nylon net was prevalent throughout the year. Ṭānā jāla, Maśāri jāla and Khiẏā jāla were common in appearance whereas Caṭa jāla, Jhima chipa, Kēcā were rarely been observed. Khiẏā jāla was reported from a vast region of all-over India in different local names (Samajdar and Saikia, 2014; Syed *et al.*, 2020; Bhat *et al.*, 2021; Madhu *et al.*, 2021). Frequent use of bamboo made traps like Ghuṇi, Palu'i were also noticed in several areas of Assam and West Bengal (Das and Barat, 2014; Islam and Hussain, 2018; Sandhya *et al.*, 2019; Madhu *et al.*, 2021). Appalling increase in the use of gill net was observed from the study area. It was noticed to kill a wide spectrum of non-fish species like snake, frog, migrating birds. Similar kind of results was reported by Shaji and Laladhas (2013). Present study reveals the use of jute fibre fabricated Caṭajāla in the study area. Jute fibre is bio-degradable; hence, it is most environmentally acceptable and should be operated as an alternative of nylon strings made net.

Traps are made up of bamboo stick which is inexpensive and easily available in the study area. Hence it is primarily adopted by the fisherfolk communities for catching small indigenous fishes from stagnant muddy water, steeped paddy fields, shallow and slowly flowing water-bodies. But, most of the encircling gears are large and heavy fishing gear. These are widely used for catching relatively big fishes in high amount from large water-bodies like dams, ponds and beels. Existence of three indigenous fishing techniques (Gābāna, bamboo piece immersion, bowl trap) was revealed through the study. These indigenous techniques were usually practiced by young tribal people to catch fishes to fulfill their nutritional and economic scarcity. These techniques were highly dependent on fisher's skill. The Bamboo piece immersion method of fishing was also reported by Das and Barat (2014).

Traps were predominantly been structured by local workers. Bamboo strips play a principal role as a raw material of most of the traditional fishing gears. Before slicing (Figure 5J) the bamboo as per the required length and breadth, it was immersed in water for a fortnight and sundried for ensuring resistance to the insects. A large volume of fishing net (except Maśāri jāla) was previously knitted by local people, but nowadays in the era of modernization, handmade nets are downshifted by machine-made nets due to considerable low price (e.g., cost of a hand-knitted Khiẏā jāla is around 2000-2500 INR, while the cost of machine-made net of the same dimension is only 650-1200 INR). Therefore, it adversely affected the gear makers as it was the source of their daily wages. Traditional fish trapping methods supply reliable income (approximately 3000-7000/month) for impecunious communities who reside in the rural area of the district. Some of them also perform various subsidiary activities (e.g., waged labour in agriculture, construction) besides fishing to strengthen their economy. Thus, it plays an emergent role in the improvement of socio-economic life as well as provides nutritional security to thousands of people.

From the study, it was observed that the Bankura district is very rich in the context of fish species availability. The diversity study indicated presence of several near threatened, vulnerable and endangered species in rural waterbodies. *Parambassis lala, Ompok pabda* and *Ailia coila* were identified under the near threatened category. *Channa orientalis* and *Clarias magur* represented vulnerable and endangered fish species respectively. However, they are never been the target prey of fishing due to their endangered nature and being caught accidentally. Gilman *et al.* (2022) proposed a decision tool for integrated fisheries bycatch management that may provide precautionary protection for the most vulnerable aquatic populations.

A large proportion of rural peoples of Bankura district are involved in fish catching with the help of various traditional fishing gears. Those obtained fishes play an important role by providing nutritional security to rural people who can't afford to purchase major carps and other costly fishes. It also noticed that a large

amount of SIIFs is generally been caught and sold by women and thus contribute to livelihood of rural sector. Study conducted by Ganguly *et al.* (2018a) depicted similar findings.

However, siltation of natural water resources, urbanization, unprecedented uses of fine mesh-sized nets (<10 mm) and other illegal procedures were also noticed which possess a threat to the fish community. Indiscriminate uses of insecticides may have wide impact on freshwater flora and fauna diversity as it roundly destroys the natural ecosystem of those water-bodies. Simultaneously, water quality that is the life-line of the entire ecosystem was also been affected. These factors lead to alarmingly decreases in the availability of fish species that also adversely affected the socio-economic status of rural people.

Conclusions

A perspective of fishing techniques and gears used by the fish-farmers along with the fish species availability of Bankura district has been illustrated in the study. It is very evident that the fishers of the study area still depend on traditional fishing gears and techniques to earn their livelihood. A major portion of rural-backward people rely upon traditional fishing for nutritional security. However, most of the fishermen of the study area are basically thriving under poverty. Hence, a transition from the operation of traditional gears to illegal fishing was observed in some cases. Therefore, planned and attractive incentives, proper education and health benefits are needed to ensure the economic prosperity of the rural farmers. The Government and other stakeholders must encourage such indigenous, eco-friendly, cost-effective approaches for the conservation of bioresources. The globally endemic fish species must be exclusively cultivated in their natural habitats to restore fish diversity. Simultaneously, strong legal action must be enacted to restrict the malpractices of destructive fishing. A concerted effort has to be confronted for the sustainable development of the fisherfolk community.

Authors' Contributions

Conceptualization – Dr. Arindam Ganguly, Dr. Pradeep Kumar Das Mohapatra; Investigation – Ujjal Konar, Animesh Kundu, Sandeep Chatterjee, Sristishil Nandi; Methodology – Dr. Arindam Ganguly, Dr. Pradeep Kumar Das Mohapatra; Resources – Madhuchhanda Duari, Rajesh K. Guin; Supervision – Dr. Pradeep Kumar Das Mohapatra; Validation - Dr. Pradeep Kumar Das Mohapatra; Writing (original draft) – Dr. Arindam Ganguly, Ujjal Konar; Writing (review & editing) – Dr. Asish Mandal, Dr. Pradeep Kumar Das Mohapatra

All authors read and approved the final manuscript.

Ethical approval (for researches involving animals or humans)

Not applicable.

Acknowledgements

This research received no specific grant from any funding agency in the public, commercial, or not-for-profit sectors.

Conflict of Interests

The authors declare that there are no conflicts of interest related to this article.

References

Baruah D, Dutta A, Pravin P (2013). Traditional fish trapping devices and methods in the Brahmaputra valley of Assam. Indian Journal of Traditional Knowledge 12(1):123-129.*http://nopr.niscair.res.in/handle/123456789/15344*

Bhakta D, Manna RK, Meetei WA, Solanki JK, Sah RK (2016). Traditional fishing crafts and gears of Ukai reservoir, Gujarat, India. International Journal of Fisheries and Aquatic Studies 4(4):142-145.

Bingsheng Z, Youngyuan Z, Ying X (1994). Toxic effects of Meothrin on the gill ultrastructure in grass carp, *Ctenopharyngodo nidellus*. Journal of Environmental Sciences 6(1):52-61.

Chakravartty P, Sharma S (2013). Different types of fishing gears used by the fishermen in Nalbari district of Assam. International Journal of Social Science & Interdisciplinary Research 2(3):177-191.

Chaudhari PK, Yadav BS (2013). Effect of Meothrin on tissue glycogen content in the fresh water fish *Nemacheilus botia*. Journal of Harmonized Research in Applied Science 1(3):125-127.

Chourey P, Meena D, Varma A, Saxena G (2014). Study on fishing craft and gears of Bhopal District, Madhya Pradesh, India. International Journal of Theoretical & Applied Sciences 6(2):65-67.

Das RK, Barat S (2014). Fishing gears operated in lentic and lotic water bodies of Cooch Behar district, West Bengal, India. Indian Journal of Traditional Knowledge 13(3):619-625.

Dutta TK, Mondal RP (2016). Traditional fishing gears used by the fishermen of Rajagram village, Bankura, West Bengal, India. A diamond collection of research articles. Prantar Publication, pp 47-59.

Ganguly A, Banerjee A, Mandal A, Das Mohapatra PK (2018b). Probiotic-based cultivation of *Clarias batrachus*: importance and future perspective. Acta Biologica Szegediensis 62(2):158-168. *https://doi.org/10.14232/abs.2018.2.158-168*

Ganguly A, Banerjee A, Mandal A, Dutta TK., Das Mohapatra PK (2018a). Study of indigenous freshwater fish diversity of Bankura (West Bengal), India with special reference to *Clarias batrachus*. Journal of Applied and Natural Science 10(4):1162 -1172. *https://doi.org/10.31018/jans.v10i4.1892*

Ganguly A, Banerjee A, Mandal A, Khan MA, Das Mohapatra PK (2019). Isolation and characterization of bacteria from the intestine of *Clarias batrachus* for probiotic organism. Proceedings of the Zoological Society 72:411-419. *https://doi.org/10.1007/s12595-018-0283-x*

Gilman E, Hall M, Booth H, Gupta T, Chaloupka M, Fennell H, Kaiser MJ, Karnad D, Gulland EJM (2022). A decision support tool for integrated fisheries bycatch management. Reviews in Fish Biology and Fisheries. *https://doi.org/10.1007/s11160-021-09693-5*

Homechaudhuri S, Pandit T, Poddar S, Banerjee S (1986). Effect of Mahua oil cake on the blood cells and blood values of an air-breathing catfish, *Heteropneustes fossilis* and a carp, *Cyprinus carpio*. Indian Academy of Sciences 95(5):617-622. *https://doi.org/10.1007/BF03179426*

Islam M, Hussain M (2018). Different types of fishing gears used by the fishermen in "Kumri Beel" of Goalpara district, Assam. International Journal of Fisheries and Aquatic Studies 6(1):128-133.

IUCN (2021). Red List of Threatened Species. Retrieved 2021 August from: *http://www.iucnredlist.org*

Jabeen F, Soren AD (2021). Fishing crafts and gears of the River Manas in Assam, India. AkiNik Publications, India, pp 172-184. *https://doi.org/10.22271/ed.book.1361*

Madhu NR, Sarkar B, Acharya CK (2021). Traditional fishing methods used by the fishermen in the Sundarban region, West Bengal. VEETHIKA-An International Interdisciplinary Research Journal 7(3). *https://doi.org/10.48001/veethika.2021.07.03.0010.48001*

Manna RK, Das AK, Rao DSK, Karthikeyan M, Singh DN (2011). Fishing crafts and gear in river Krishna. Indian Journal of Traditional Knowledge 10(3):491-497. *http://nopr.niscair.res.in/handle/123456789/12026*

Petetta A, Virgili M, Guicciardi S, Lucchetti A (2021). Pots as alternative and sustainable fishing gears in the Mediterranean Sea: an overview. Reviews in Fish Biology and Fisheries 31:773-795 *https://doi.org/10.1007/s11160-021-09676-6*

Rao CS, Rao K, Simhachalam G, Raju C (2016). Fishing methods, use of indigenous knowledge and traditional practices in fisheries management of Lake Kolleru. Journal of Entomology and Zoology Studies 4:37-44.

Roy C, Vass KK, Patra BC, Sanyal AK (2013). Fish diversity in two south-western district of West Bengal - Bankura and Purulia. Records of the Zoological Survey of India 113(4):167-179.

Samajdar I, Saikia SK (2014). Traditional fishing gears of Birbhum district, West Bengal, India. Indian Journal of Traditional Knowledge13(1):187-194.

Sandhya KM, Roy A, Hassan MA, Kumari S, Mishal P, Lianthuamluaia VK, ... Naskar B (2019). Traditional Fishing Gears, Fish Catch and Species Composition of Selected Floodplain Wetlands of Lower Gangetic Plains, West Bengal, India. Fish Technology 56(2):101-109.

Shaji CP, Laladhas KP (2013). Monsoon flood plain fishery and traditional fishing methods in Thrissur district, Kerala. Indian Journal of Traditional Knowledge 12(1):102-108.

Syed N, Mohite A, Sadawarte R, Desai A, Shah TH (2020). Design aspects of fishing crafts and gears of Wular lake of Kashmir, India. Journal of Experimental Zoology India 23(1):861-867.

Talwar PK, Jhingran AG (1991). Inland fishes of India and adjacent countries. Volume-1. Oxford and IBH Publishing Co. Pvt. Ltd., New Delhi, India, pp 541.

Tiwari S, Tiwari R, Singh A (2012). Impact of Cypermethrin on fingerlings of common edible carp (*Labeo rohita*). The Scientific World Journal. *https://doi.org/10.1100/2012/291395*

DR. Asish Mandal

Article PDF Available

Diversity and distribution of wild mushrooms in different forest areas of Bankura district, WB, India

May 2022 · Acta Biologica Szegediensis 65(2):185-198
DOI:10.14232/abs.2021.65.185-198

Authors:

Arindam Ganguly, Susmita Nad, Krishanu Singha, Rituparna Pathak, Palash Hazra, Pritha Singha, Priti Dhua, Pradeep Das Mohapatra, Asish Mandal

Hide

Abstract and Figures

Mushrooms are macroscopic fruit bodies of fungi; one of the most diverse groups of living organisms distributed all over the world. In recent past, they have gained significant scientific attention for their profound nutraceutical potentiality. The objective of the present study was to explore the diversity and ecological distribution of mushrooms in different forest areas of Bankura district. The study area includes intermittent dense forest and flood plains from middle-east to eastern part of Bankura district. However, this area received very little attention from a conservation perspective, and there is no such documentation on mushrooms of this area. The survey was conducted from August 2019 to October 2020 including vivid field surveys in the forest depots. The study has revealed a total of 53 identified mushroom species belonging to 40 genera and 30 families. The study has also identified 25 edible, 18 inedible and 15 medicinally potential mushrooms. The genus Russula and the family Russulaceae dominates the myco-population. The finding shows that this region is rich in macrofungal diversity complicatedly linked to the functioning of the local ecosystem. The present study opens new possibilities regarding the exploration and utilization of wild mushrooms in India.

Study location and map of… | Distribution of mushrooms… | Distribution of mushrooms… | Distribution of mushrooms…

Volume 65(2):185-198, 2021
Acta Biologica Szegediensis
http://abs.bibl.u-szeged.hu/index.php/abs
DOI:10.14232/abs.2021.2.185-198

cta
iologica
zegediensis

ARTICLE

Diversity and distribution of wild mushrooms in different forest areas of Bankura district, WB, India

Arindam Ganguly[1], Susmita Nad[1], Krishanu Singha[2], Rituparna Pathak[1], Palash Hazra[1], Pritha Singha[1], Priti Dhua[1], Pradeep Kumar Das Mohapatra[3], Asish Mandal[4]*

[1]Department of Microbiology, Bankura Sammilani College, Bankura-722102, West Bengal, India
[2]Department of Microbiology, Vidyasagar University, Midnapore-721102, W. B., India
[3]Department of Microbiology, Raiganj University, Raiganj-733134, Uttar Dinajpur, W. B., India
[4]P. G. Department of Botany, Ramananda College, Bishnupur, Bankura-722122, W. B., India

ABSTRACT Mushrooms are macroscopic fruit bodies of fungi; one of the most diverse groups of living organisms distributed all over the world. In recent past, they have gained significant scientific attention for their profound nutraceutical potentiality. The objective of the present study was to explore the diversity and ecological distribution of mushrooms in different forest areas of Bankura district. The study area includes intermittent dense forest and flood plains from middle-east to eastern part of Bankura district. However, this area received very little attention from a conservation perspective, and there is no such documentation on mushrooms of this area. The survey was conducted from August 2019 to October 2020 including vivid field surveys in the forest depots. The study has revealed a total of 53 identified mushroom species belonging to 40 genera and 30 families. The study has also identified 25 edible, 18 inedible and 15 medicinally potential mushrooms. The genus *Russula* and the family *Russulaceae* dominates the myco-population. The finding shows that this region is rich in macrofungal diversity complicatedly linked to the functioning of the local ecosystem. The present study opens new possibilities regarding the exploration and utilization of wild mushrooms in India.
Acta Biol Szeged 65(2):185-198 (2021)

KEY WORDS
bioactive compound
mushroom diversity
nutritional value
therapeutic potentiality

ARTICLE INFORMATION
Submitted
20 August 2021
Accepted
28 December 2021
***Corresponding author**
E-mail: mandalasish71@gmail.com

Introduction

Fungi are one of the most diverse groups of organisms on earth. They are eukaryotic heterotrophs that obtain their energy by absorption of nutrients. The large visible fructification of the underground mycelia of macro-fungi is known as 'Mushrooms'. They mainly belong to the phylum Basidiomycota and Ascomycota with observable spore bearing structure. Mushrooms are abundant in nature and they are the first known fungi. Wild edible mushrooms have been collected and consumed by people from the very early stage of civilization, even when people didn't know about its nutritive value.

Macrofungi varies widely in their habitats. The species diversity of mushrooms is directly related to the habitat. They are found on soil (terrestrial), dead leaves (folicolous), wood (lignicolous) or dung and decomposing organic materials (coprophilous). Macrofungi, based on their nutrition, can be categorized into three groups: saprophytes, parasites, and symbiotic (Kinge et al. 2017). Mushrooms predominantly grow during rainy season in forests and can be epigeous or hypogeous. They vary mostly in shape, size and colour. Some of them are edible whereas some are proven to be poisonous. The various environmental factors that affect the growth of mushrooms are temperature, humidity, light and the substrate over which they grow. All the species of mushrooms shows remarkable diversity in their morphological characteristics.

Mushrooms contain high amounts of nutritious compounds including vitamins, proteins, minerals, fiber and trace elements. Edible mushrooms have been considered to be an ideal food for obese persons due to high fibre, low fat and low starch content. They are considered as "poor man's protein" because of their high nutrient content (Singha et al. 2017b). Chang and Buswell (1996) coined the term 'mushroom nutraceuticals' to describe those compounds that have considerable potentiality as dietary supplements, used for the enhancement of health and prevention of various human diseases.

Mushrooms are seasonal fungi, which earn additional ecological significance. They appear in between reaching a highest point of development with the diverse niches in the forest ecosystem. Their habitat and climate are the

Figure 1. Study location and map of Bankura forest areas.

major factors that indicate their biodiversity. Fungi also play an important role as decomposers. They breakdown plant components like lignin and cellulose and thus are particularly important in woody-ecosystems. They also degrade surface waste and release nitrogen back into the soil in the form of ammonium nitrate, an important nutrient that plants need for their survival. Mushrooms are also known to produce several bioactive compounds that have therapeutic uses. However, they protect themselves from deleterious effect of plant phenolic tannins by producing a hydrolytic enzyme, called tannase that form gallic acid and glucose (Das Mohapatra et al. 2020). It is often been noticed that local people who consume the mushroom *Astraeus hygrometricus* (*Kurkure chhatu*) on regular basis enjoy several health benefits (Dutta and Acharya 2014). This mushroom possesses antitumor, anti-Leishmanial, anti-Candidal, antioxidant and immune-modulatory activity (Biswas et al. 2017).

Macrofungal diversity is an integral component of the global diversity. Diverse abundance of macrofungal species is a helpful indicators to interpret the current status of the ecosystem. Most healthy forest ecosystem contains at least 45% mycorrhizal fungi (Arnolds 1988). Native people living in nearby forest areas relate to the wild mushrooms in respect to their socio-economic lifestyles by means of both food ingredients as well as small business elements. Chang and Miles (2004) reported that out of 14000 known mushroom species, there were nearby 7000 well-studied species that possesses varying degree of edibility. Among them, only 200 species were experimentally cultured; 100 were economically cultivated, 60 were commercially cultivated and about 10 species have gained industrial importance.

The total recorded mushrooms in India are approximately 850 species (Deshmukh 2004). The collection and scientific study of mushrooms in India has started during 19th century (Kaul et al. 2002). Butler and Bisby (1931) published the first list on Indian fungi which was further revised by Vasudeva (1960). Purkayastha and Chandra (1985) published the first comprehensive account of Indian edible mushrooms and their cultivation technology.

India has an ancient history of using mushrooms as food, medicine, minerals and drugs. It has become a centre of herbal therapy (Nad et al. 2021). However, such kind

of studies is very rare in West Bengal. Dutta and Acharya (2014) obtained 31 edible and 3 medicinally important macrofungi that were used by local and indigenous communities in eight districts of West Bengal. Das et al. (2015) reported 16 wild edible mushrooms with ethno-medical value from tropical dry deciduous forest of Eastern *Chota Nagpur* plateau. Deshmukh et al. (2006) reported that, around 40 species found from all over India were lethal. Singha et al. (2017b) explored the nutritional and antibacterial potentiality of some wild edible mushrooms from Gurguripal Eco-forest, Paschim Medinipur, West Bengal, India. Thus, the studies on mushroom diversity are often significant and contribute to the knowledge of the ecosystem of a forest.

The forest region of Bankura district is one of the enriched forest areas of West Bengal. The district possesses dense forest dominated by Sal (*Shorea robusta*). Other trees found in the forests include *Azadirachta indica* (Neem), *Dillenia indica* (Chalta), *Syzygium cumini* (Jam) study area (Mueller et al. 2004). After finding a colony or a single species of mushroom, the fruiting bodies were collected with the help of knife. Their habitat conditions and occurrence frequency were recorded. The samples were photographed (Nikon D5300 camera), both in their natural habitats and with the reference of a scale or coin, for identification. The samples were then taken in a container, labelled and kept for further study.

Identification of the specimens

The collected samples were examined in laboratory by observing the formation of the cap, arrangements of the gills, presence of pores on the under surface of the fruit bodies or not, presence of stipe and volva or not, the type of the surface (smooth or rough), etc. Then according to their characteristics, they were then identified with the help of standard literatures (Pradhan et al. 2010; Pushpa and Purushothama 2012; Acharya and Pradhan 2017).

better conserved forests (Pradhan et al. 2016). Bankura is surrounded with low-lying alluvial-laterite soil (Das and Paul 2015) with an average annual rainfall of 1329 mm (Majumder and Patra 1993). Overall, the biogeological environment provide favourable climatic zone for fungal growth. However, there is no valid documentation on diversity of mushrooms in this area till date. Hence, the present study is focused on the diversity and distribution of mushrooms in Bishnupur and adjacent forest areas of Bankura district, West Bengal.

Materials and Methods

Study area

Five major forest areas namely Bishnupur (23°04′48″N, 87°19′12″E; Altitude 59 m), Joypur (23°02′N, 87°27′E; Alt.74 m), Sonamukhi (23°18′11.5848″N, 87°24′56.4948″E; Alt. 66 m), Taldangra (23°01′1.092″N, 87°06′29.3688″E; Alt. 74 m), and Bankadaha (22°58′03.64″N 87°21′05.43″E; Alt. 74 m) of Bankura district were selected as the study area (Fig. 1). These forest areas have a tropical climate with dry and rainy season (annual average rainfall: 11000-15000 mm), dominated by 'Sal' trees with a laterite and alluvial type soil. The average temperature of this locations ranges between 20-30 °C during rainy season. The field study was conducted from August 2019 to October 2020 to obtain the maximum outcome.

Collection of samples

Opportunistic sampling method was being performed and conspicuous specimens were collected precisely from the preservative (25:5:70 ml rectified alcohol + formalin + distilled water) for further studies (Hawksworth et al. 1995).

Data analysis

The frequency of occurrence for each species was calculated by following formula as suggested by Aung et al. (2008).

$$\frac{\text{Occurrence frequency of species A}}{\text{Total number of all species}} \times 100$$

Simpson Index of Diversity was calculated as suggested by Simpson (1949).

Simpson Index of Diversity =1-D; where,

$$D = \frac{\Sigma n\,(n-1)}{N\,(N-1)}\text{; where,}$$

n = total number of organisms of a particular species
N = total number of organisms of all species

Shannon diversity index for mushroom was calculated as suggested by Margalef (2008).

$$H = -\Sigma\,(n/N)\log(n/N)\text{; where,}$$

H = diversity index
N = total number of individuals of all the species
n = total number of individuals of a particular species

Citations (2) References (56)

Three New Species of Genus Russula Pers. from Sal Dominated Forests of Tropical India Based on Morphotaxonomy and Multigene Phylogenetic Analysis

Article

Mar 2023 · CRYPTOGAMIE MYCOL

Aniket Ghosh · Bart Buyck · Dyutiparna Chakraborty · Kanad Das

A checklist of wild mushrooms in three urban parks in Kolkata, India

Article Full-text available

Jan 2023

Tarak Samanta · Lina Chatterjee · Saswati Sinha · Arjan Basu Roy

View Show abstract

DR. SABYASACHI CHATTERJEE

Research Article | Open Access
Volume 3 | Issue 2 | https://doi.org/10.3923/ajerpk.2021.109.113

Effect of Arsenic on Growth and Cell Division in Root Tip Cells of (*Allium sativum L.*)

Sabyasachi Chatterjee
PG Department of Botany, Ramananda College, Bishnupur- 722122, Bankura, West Bengal, India

Soumik Chatterjee
PG Department of Botany, RamanandaCollege, Bishnupur- 722122, Bankura, West Bengal, India

Received	Accepted	Published
26 Feb. 2021	26 Apr. 2021	15 Jun. 2021

ABSTRACT

Background and Objectives: Arsenic trioxide is a toxic element and effect on human health and as well as plants

Original Article | Published: 22 January 2022

In vitro regeneration of *Piper longum* L. and comparative RP-HPLC analysis of piperine production of in vitro and in vivo grown plants

Mousumi Chatterjee, Sabyasachi Chatterjee & Indrani Chandra

Plant Cell, Tissue and Organ Culture (PCTOC) 149, 205–212 (2022) | Cite this article

275 Accesses | 2 Altmetric | Metrics

Abstract

Piper longum L. is a well known spice plant belonging to the family Piperaceae with high pharmacognosy potential, but it is becoming threatened due to overexploitation. Thus, this investigation aims to standardize a cost effective protocol for in vitro propagation of this economically important plant. Internodal segments were used as explant for callogenesis in Murashige and Skoog medium with 3% sucrose and 0.8% agar, with NAA or 2,4 D. Optimum callus induction was observed in MS medium with 5.0 mg/L NAA. Calli were subcultured on shoot regeneration media containing different concentrations of cytokinin (KIN/BAP) along with 0.1 mg/L NAA. Best shoot regeneration was obtained on MS media supplemented with 2.0 mg/L KIN and 0.1 mg/L NAA. Induced shoots were rooted in either NAA or IBA and

DR. Chiranjit Pal

Journal of the Indian Chemical Society 98 (2021) 100145

Contents lists available at ScienceDirect

Journal of the Indian Chemical Society

journal homepage: www.editorialmanager.com/JINCS/default.aspx

Molecular selectivity of indenopyridines for fullerenes: A comparative study

Chiranjit Pal [a], Tandrima Chaudhuri [b,*], Chhanda Mukhopadhyay [c], Manas Banerjee [d]

[a] Department of Chemistry, Ramananda College, Bishnupur, Bankura, 722 122, India
[b] Department of Chemistry, Dr.Bhupendranath Dutta Smriti Mahavidyalaya, Burdwan, 713 407, India
[c] Department of Chemistry, University of Calcutta, 92 APC Road, Kolkata, 700 009, India
[d] Department of Chemistry, University of Burdwan, Burdwan, 713 104, India

ARTICLE INFO

Keywords:
Indenopyridines /[70]-Fullerene
Isosbestic formation
DFT
Electrochemical indices
[60]-fullerene - [70]-fullerene comparative study

ABSTRACT

Selectivity of [60]-Fullerene (C_{60}) over its [70]-analogue (C_{70}) is ably established for N-containing polynuclear aromatic planar indenopyridines (I) in organic media for the first time. The present work envisages the chemical physics behind non-covalent interaction between [70]-fullerene (C_{70}) and indenopyridines (I: I1, I3 and I4) in toluene alongwith a comparative analysis of previously studied interaction of C_{60} (Pal et al., 2019) via formation of multiple absorption isosbestic points and isoemissive point in UV–Vis and steady state fluorescence studies respectively, stable ground state equilibrium between C_{70} and I is recognized and is purely non-covalent in nature. All three indenopyridines showed high formation constant ($\sim 10^5$) with [70]-fullerene though the selectivity of binding favours [60]-fullerene. Experimental findings are well supported within *vacuo* DFT based computation. Loss of planarity of indenopyridines in the optimized adducts, FMO features, electrochemical indices and finally TD-DFT calculation validates the strong complexation. Taut wrapping of C_{70} by indenopyridines is most conspicuous for I4 among others as that of C_{60}.

1. Introduction

Huge studies has already been made in the field of charge transfer or electron donor-acceptor type weak interaction captivating Fullerenes viz. C_{60} and or C_{70} as electron acceptor [1–12]. The exploration of the emission and optical properties of fullerenes and their derivatives is a central topic among the dynamic research fields of fullerenes to study charge separation recombination phenomena in energy storage devices [12]. These studies are gently related to "donor-acceptor" molecular systems in polynuclear aromatic compounds [13–23]. Varieties of donors are available in literature for which comparative efficiency of charge transfer interaction reported in organic media for Fullerenes [1–6].

N-containing polynuclear aromatic donor indenopyridine [18–21] plays noteworthy chemical and biological consequence. The efficiency of indenopyridines to form a weak binding complex with C_{60} has already been reported by our group [9]. To the best of our knowledge, there is no report of its comparative interaction with other fullerenes as electron acceptors till date. So the purpose of this study is to investigate the mode and efficiency of interaction of indenopyridine donors with [70]-fullerene acceptor in comparison with its [60]-analogue.

In this study better selectivity of C_{60} for indenopyridine donors are established through the formation of reaction equilibrium between [70]-fullerene and three different indenopyridines viz., I1, I3 & I4 (Fig. 1). As that of C_{60}/I interactions reported earlier [9] all these are well established via the formation of both absorption isosbestic and isoemissive in toluene medium. Furthermore the interaction in the complex is modelled with density based change in global minimum geometry, Frontier orbital features, electrochemical indices and finally by TD-DFT transition estimation.

2. Experimental

2.1. Materials

Toluene HPLC (Merck India) grade is used as solvent. I1, I3 & I4, Indenopyridines are synthesized as reported [24], used in this study. Aldrich made [70]-fullerene (C_{70}) is used. The concentration range of 10^{-5} M -10^{-6} M of indenopyridines (I1, I3 & I4) is taken and the range of 10^{-6} M are taken for C_{70} in all the spectral measurements.

2.2. Instruments used

The UV–Vis spectral measurements are performed using Shimadzu UV 2400 series PC spectrophotometer fitted with an electronic

* Corresponding author.
E-mail address: tanchem_bu@yahoo.co.in (T. Chaudhuri).

https://doi.org/10.1016/j.jics.2021.100145
Received 28 June 2021; Received in revised form 20 August 2021; Accepted 28 August 2021

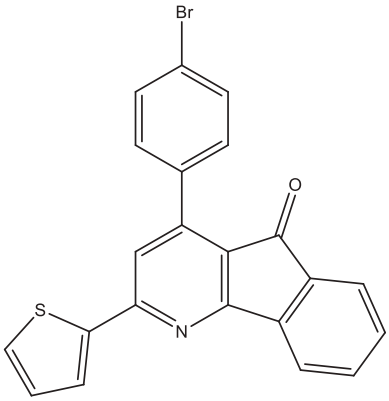

4-(4-Bromo-phenyl)-2-thiophen-2-yl-indeno[1,2-*b*]pyridin-5-one

I1

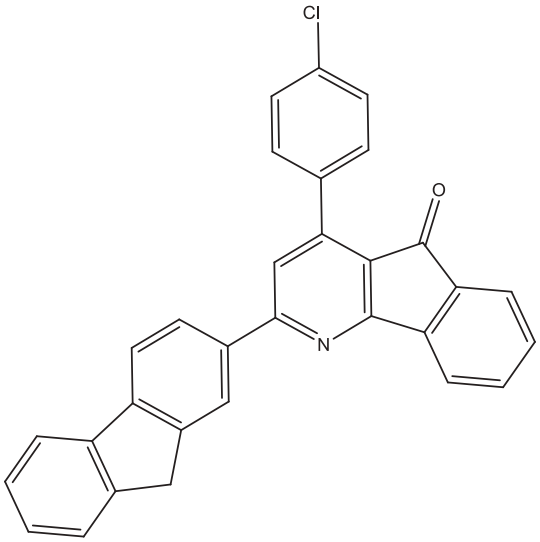

4-(4-chlorophenyl)-2-(9*H*-fluoren-2-yl)-5*H*-indeno[1,2-*b*]pyridin-5-one

I4

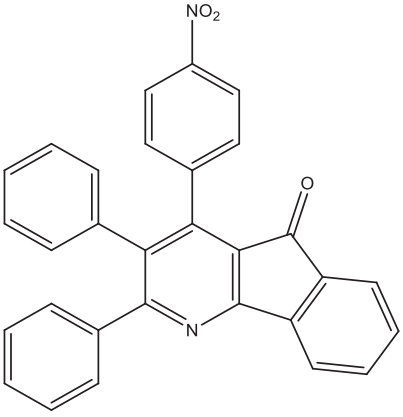

4-(4-Nitro-phenyl)-2,3-diphenyl-indeno[1,2-*b*]pyridin-5-one

I3

Fig. 1. Structures of the indenopyridines (I) used.

temperature controller unit (TCC –240 A). The emission and excitation spectra are recorded with a spectrofluorometer (Hitachi F-4500) equipped with a temperature controlled cell holder. Temperature is guarded to within ±0.1 K, by water circulation from a constant temperature bath (Heto Holten, Denmark).

Molecular simulations are performed using Spartan'14 molecular modelling software of Wavefunction Inc. (Irvine, CA, USA). The searches of global minima for all the three optimized complexes are done by the Monte Carlo simulation in vacuum using Merck molecular force-field calculations (MMFF). Gaussian 09 (Linux), Gaussian, Inc. (USA), software is used for DFT and TD-DFT theoretical calculations. For all the free systems and their complexes, MPW1PW91/6-31G functional is chosen for calculating single point geometries and frontier orbitals.

3. Results and discussion

3.1. Ground state interactions

The photon induced interaction processes of the electron deficient fullerene to indenopyridines (I1, I3 & I4) are scrutinized both by visible absorption and fluorescence spectroscopy. The three solutions of indenopyridines (I1, I3 & I4), are titrated separately with a stock C_{70} solution, in toluene. Titration process is as described earlier for C_{60} interaction [9]. Fig. 2 shows appearance of a set of three isosbestic points for all the three indenopyridine systems, for which intensity of maximum absorption of indenopyridine decreased by adding solutions of C_{70}. Table 1 listed the multiple isosbestic points in different regions of the spectra on interaction of I1, I3 and I4 with C_{70} in toluene. Thus all the three indenopyridine (I1, I3 & I4) systems form ground state steady equilibria with C_{70} in toluene medium.

Comparing with C_{60} isosbestic points, are red shifted for C_{70} interaction, irrespective of all three indenopyridines (shown in Table 1).

3.2. Excited state interaction

The excited state C_{70} – indenopyridine association has not yet been well established. The fluorescence maxima of indenopyridines systematically quenches without any remarkable shift. Still give rise to an isoemissive point in lower wavelength region with the increasing concentration of C_{70} in the solution, as shown in Fig. 3.

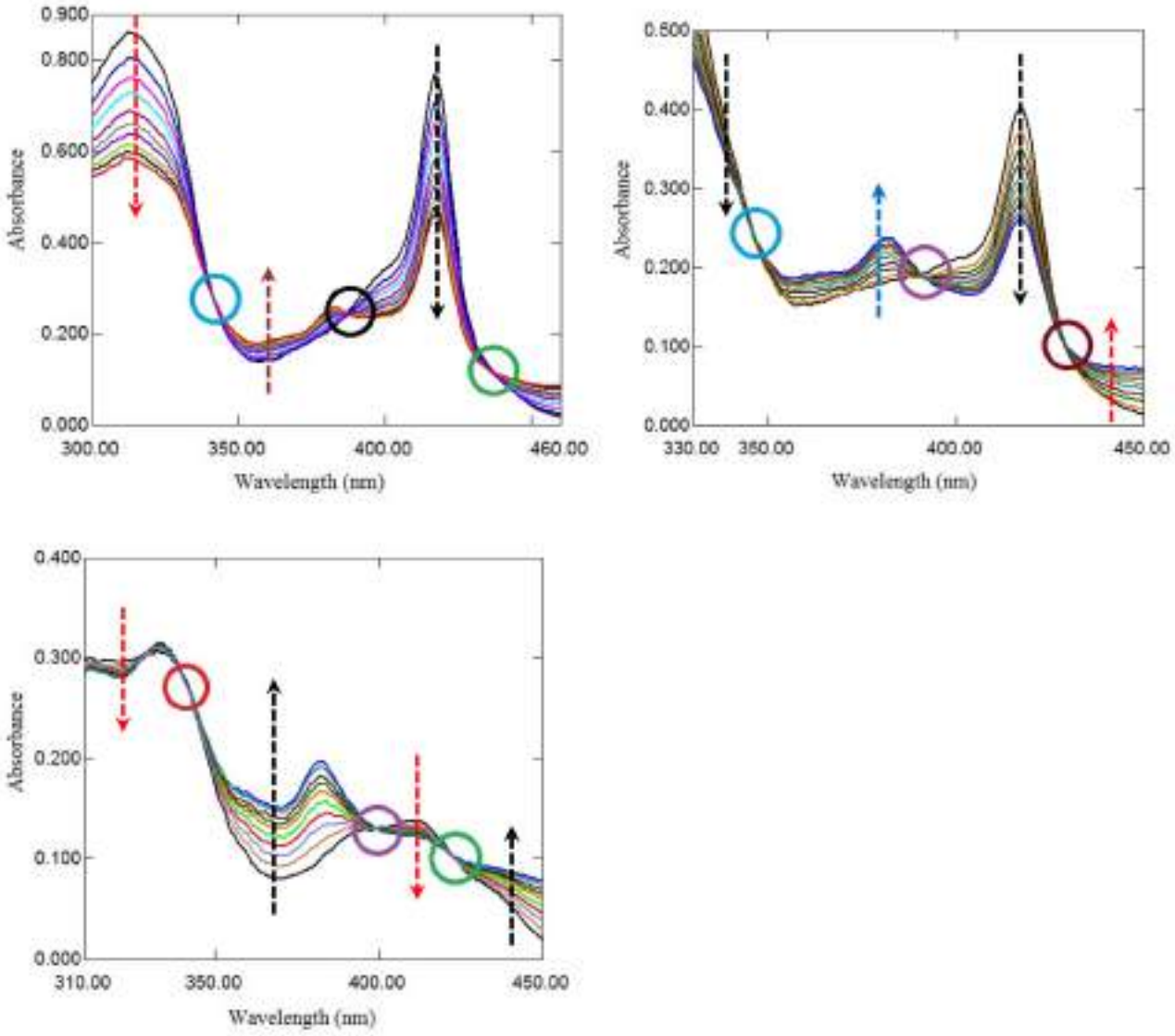

Fig. 2. Absorption isosbestic appearedin toluene medium due to interaction of (a) I1 (2.50×10^{-5} mol/dm^3) with [70]-fullerene, concentration of [70]-fullerene: 0.00, 6.88×10^{-7}, 1.26×10^{-6}, 1.75×10^{-6}, 2.16×10^{-6}, 2.52×10^{-6}, 2.84×10^{-6}, 3.12×10^{-6}, 3.36×10^{-6}, 3.58×10^{-6} mol/dm^3 (b) I3 (3.80×10^{-6} mol/dm^3), with [70]-fullerene, concentration of [70]-fullerene: 0.00, 6.88×10^{-7}, 1.26×10^{-6}, 1.75×10^{-6}, 2.16×10^{-6}, 2.52×10^{-6}, 2.84×10^{-6}, 3.12×10^{-6}, 3.36×10^{-6}, 3.58×10^{-6} mol/dm^3 (c) I4 (7.31×10^{-6} mol/dm^3), with [70]-fullerene, concentration of [70]-fullerene: 0.00, 6.88×10^{-7}, 1.26×10^{-6}, 1.75×10^{-6}, 2.16×10^{-6}, 2.52×10^{-6}, 2.84×10^{-6}, 3.12×10^{-6}, 3.36×10^{-6}, 3.58×10^{-6} mol/dm.^{3}.

Table 1
Isosbestic and isoemissive points appear upon interaction of indenopyridines (I1, I3 and I4) with two fullerenes in toluene. The excited state association constants for the corresponding three complexes.

Indenopyridine	Interaction with [60]-fullerene [9]			Interaction with [70]-fullerene			K_{C60}/K_{C70}
	Absorption isosbestic point at wavelength (nm)	Isoemissive point at wavelength (nm)	Stern-Volmer constant (K_{SV}) $\times 10^{-5}$ (M^{-1})	Absorption isosbestic point at wavelength (nm)	Isoemissive point at wavelength (nm)	Stern-Volmer constant (K_{SV}) $\times 10^{-5}$ (M^{-1})	
I1	369.8, 330.7	450.8	9.5 ± 0.18	435.60, 387.52, 341.03	446.6	1.90 ± 0.11	5.0
I3	369.5, 329.3	471.6	10.7 ± 0.24	428.23, 391.50, 345.32	446.1	2.06 ± 0.15	5.19
I4	381.4, 318.3, 300.5	440.2, 627.8	11.0 ± 0.30	421.85, 399.41, 340.76	431.2	2.35 ± 0.13	4.68

Thus with the appearance of isoemissive point static interaction between the fluorophore indenopyridines (I1, I3 & I4) and the fluorescence quencher (C_{70}) is well established as earlier [9]. On contrary, isoemissive points are blue shifted (shown in Table 1) on switching from C_{60} to C_{70}.

3.3. Determination of equilibrium constant

Stern-Volmer equation [25] is used to determine the association constant values (Fig. 4) and is listed in Table 1. I4 binds most efficiently with C_{70} among the indenopyridines used; reflects massive charge

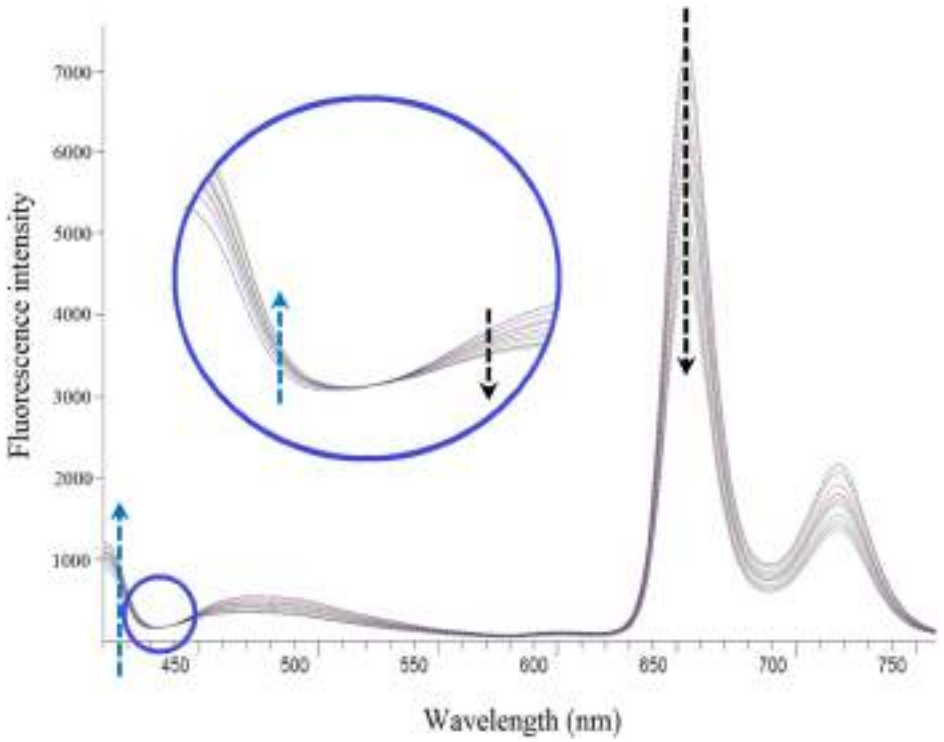

Fig. 3. Fluorescence spectra appeared on excitation at wavelength 436 nm in toluene medium due to interaction of I1 (2.50×10^{-5} mol/dm^3) with [70]-fullerene, concentration of [70]-fullerene: 0.00, 6.88×10^{-7}, 1.26×10^{-6}, 1.75×10^{-6}, 2.16×10^{-6}, 2.52×10^{-6}, 2.84×10^{-6}, 3.12×10^{-6}, 3.36×10^{-6}, 3.58×10^{-6} mol/dm.^{3}.

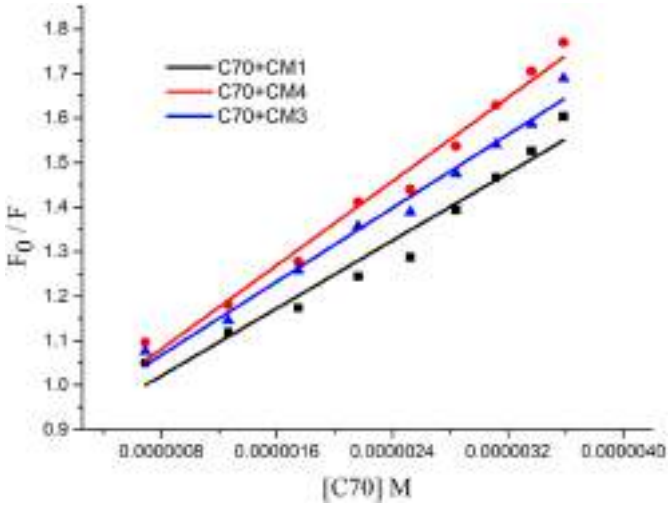

Fig. 4. Stern-Volmer plot of the three C_{70}/I interacting systems.

transfer of I4 with [70]-Fullerene amongst others. The order of excited state equilibrium constants follows $K_{C70/I4} > K_{C70/I3} > K_{C70/I1}$. Similar order of the binding is observed earlier in case of C_{60} also. However the association capability between fullerene and indenopyridines are 5 fold less in C_{70} in contrast to that of C_{60} might be due to lack of planarity [70]-analogue.

3.4. Theoretical analysis

A precise Monte Carlo (MC) conformational search protocol [25,26] is used for these associated complexes also. For studying weak intermolecular interactions such as CT, van der Waals, H-bonding, and hydrophobic [27–30], normally DFT optimization calculations of the adduct structures are employed. Fig. 5 presents best possible geometries of the three complexes. The donor (I) and the acceptor (C_{70}) intermolecular distances (shown in Table 2) are within 3.44 Å – 3.55 Å which is in the charge transfer range of interaction. This intermolecular distances are slightly higher compared to that of [60]-fullerene analogue (shown in Table 2) [9]. Between the interacting molecules strong π-π interaction originated due to π-parallel orientation as shown in Fig. 5. The angle between pyridine and indeno moiety of each indenopyridines in the fullerene adduct increases as reported earlier [9]. The interaction is more pronounced in case of C_{60} than C_{70} as evident from intermolecular distances and the angle between pyridine and fluorenyl moiety of I's, might be due to spherical symmetric structure of [60]-analogue. The aforesaid angle of I4 changes from 10.64° to 46.42° to create a suitable cavity for C_{70} and among the indenopyridines, I4 has the greatest binding constant with both the Fullerenes. The similar order as that of [60]-fullerene [9], the ability to wrap up [70]-fullerene in the opening of different indenopyridines and the distance between three sets of the interacting moieties, are followed.

The order of the equilibrium constant (K) depends directly on the amount of charge transfer taking place. Here the amount of charge transfer decreases with increase in distance between the interacting molecules. Consequently the K values follow the order.

The electronic chemical potential (μ) [31], the global electrophilicity index [32,33] (ω) and the global nucleophilicity N index [34] values are determined for donor-acceptor interaction as earlier [9]. Electronic chemical potential (μ) of Fullerenes (>-5.00eV) are found lower than that of indenopyridine derivatives (−4.39 to −4.70eV). Electrophilicity index (ω) of both [60]- and [70]-fullerene have higher values (4.06eV and 4.18eV) in compare to indenopyridine derivatives (2.77eV–2.95eV). Thus, in presence of Fullerene, indenopyridines act as donor and evidently fullerenes serves as acceptor during charge transfer process. The global nucleophilicity N index [34] value of indenopyridine derivatives are in the range (N > 3.0 eV) of a donor during charge transfer as shown earlier [9].

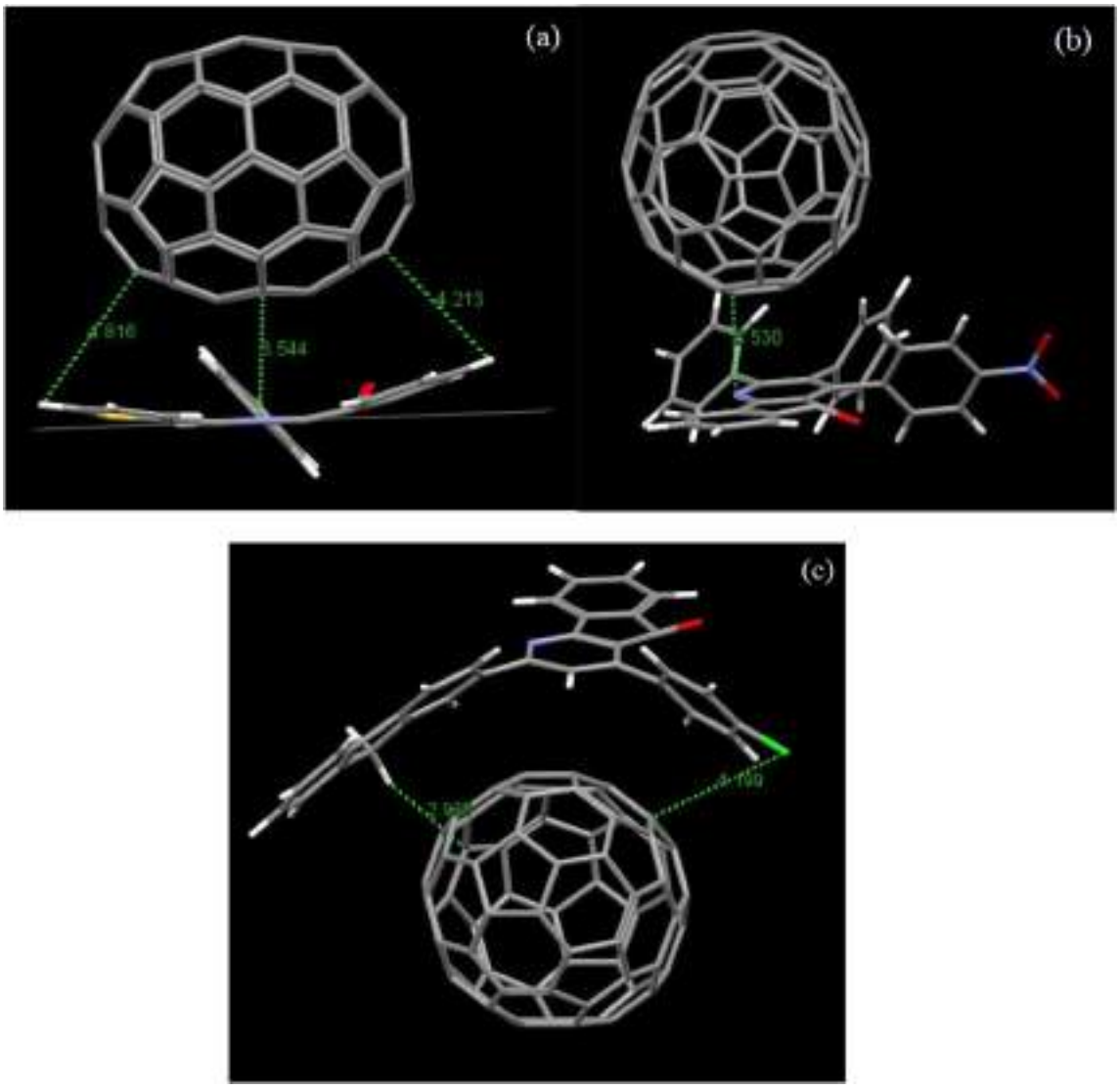

Fig. 5. The orientation of the adduct of (a) C_{70}/I1 (b) C_{70}/I3 and (c) C_{70}/I4 interacting systems in optimized groundstate geometry showing the intermolecular distances in Å.

Table 2
Parameters of the optimized ground state geometry of adducts.

Indenopyridines	Interaction with [60]-fullerene [9]			Interaction with [70]-fullerene		
	Minimum distance between the Fullerene-60 (C_{60}) and indenopyridine moieties (in Å)	Number of conformers	Dipole moment (D)	Minimum distance between the Fullerene-70 (C_{70}) and indenopyridine moieties (in Å)	Number of conformers	Dipole moment (D)
I1	3.109	2	4.6029	3.54443	2	4.2342
I3	3.424	1	7.7364	3.52999	1	8.7120
I4	3.417	2	4.7734	3.46302	2	4.7159

3.4.1. TD-DFT calculation

TD-DFT/MPW1PW91/6-31G calculation are done and reported in Table 3. Few of the possible transitions listed in Table 3 are there having little contribution in compare to others. The HOMO to (LUMO+1), HOMO to LUMO and (HOMO-1) to LUMO are the most prominent transitions in case of I/C_{70}.

3.4.2. HOMO-LUMO interactions

Investigating the interaction between the frontier HOMO/LUMO orbitals of the donor-acceptor adducts, the intermolecular type of interaction is conveniently interpreted. The FMO interactions between C_{70} and indenopyridines are studied through DFT/MPW1PW91/6-31G level calculation. Fig. 6 depicted that the HOMO, (HOMO-1) and (HOMO-2) orbitals of the complexes reside mainly on indenopyridine moiety and LUMO and (LUMO+1) mostly dwell on acceptor [70]-fullerene as that reported in case of C_{60} [9]. However, the direction of charge transfer from TD-DFT data in the CT transition is better explained. Thus the clear corroboration of charge transfer interaction between fullerene and indenopyridines are granted by frontier molecular orbital pictures.

Table 3
TD-DFT calculated percentage contribution of transitions of C_{70}/I1 adduct.

Excited state 1 Oscillator strength (f) = 0.0039		Excited state 2 Oscillator strength (f) = 0.0006		Excited state 3 Oscillator strength (f) = 0.0093	
Possible Transition	Percentage contribution	Possible Transition	Percentage contribution	Possible Transition	Percentage contribution
HOMO to LUMO	27.03%	HOMO to LUMO	54.87%	HOMO to LUMO	5.05%
HOMO to (LUMO+1)	15.92%	HOMO to (LUMO+1)	13.66%	HOMO to (LUMO+1)	25.12%
(HOMO-1) to LUMO	12.69%	(HOMO-2) to (LUMO+1)	2.11%	(HOMO-1) to LUMO	21.78%
(HOMO-2) to LUMO	16.80%	(HOMO-3) to LUMO	14.35%	(HOMO-2) to LUMO	31.05%
(HOMO-3) to (LUMO+1)	19.93%	(HOMO-3) to (LUMO+1)	6.92%	(HOMO-2) to (LUMO+1)	6.089%
–	–	(HOMO-1) to (LUMO+1)	2.24%	(HOMO-1) to (LUMO+1)	3.57%

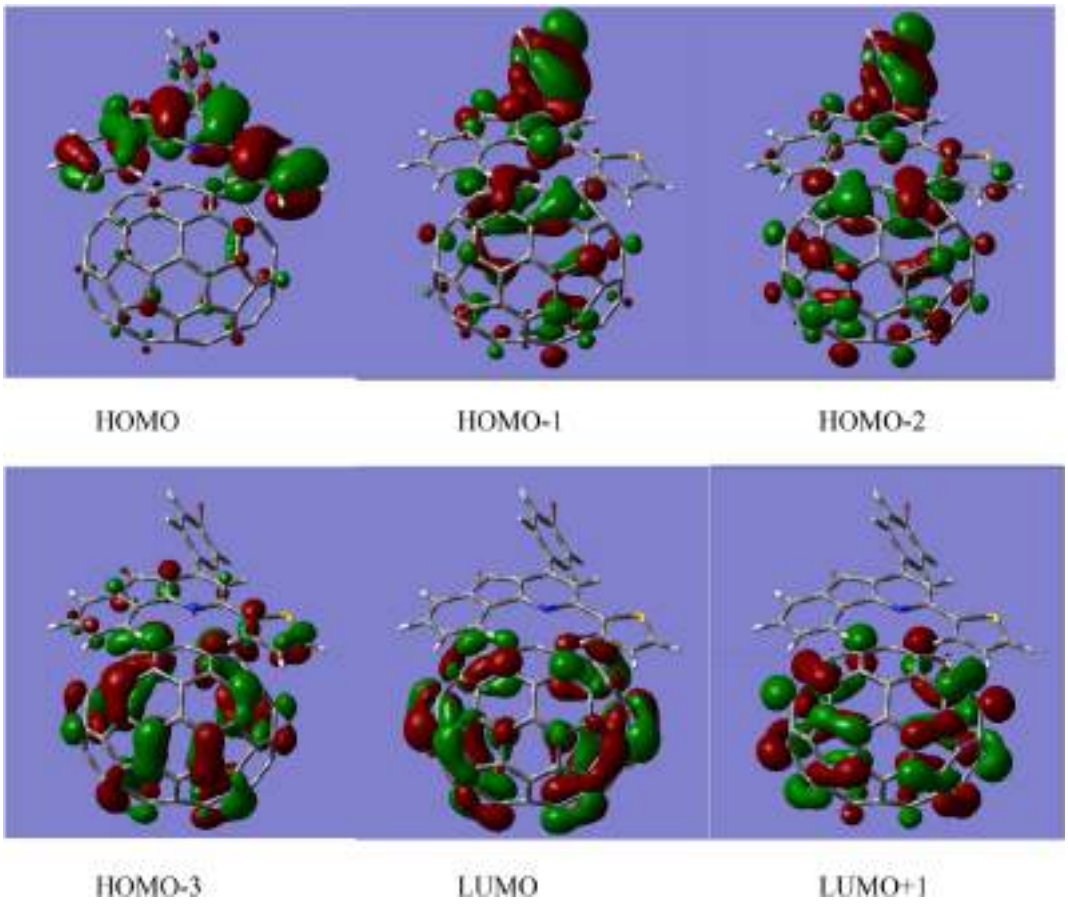

Fig. 6. Frontier Molecular orbital pictures of C_{70}/I1 interacting system.

4. Conclusion

However the electrophilicity index (ω) suggest C_{70} as better acceptor in comparison with C_{60}, still better spherical symmetry of C_{60} confirmed higher binding complexes with all three Indenopyridines used in this study. Not only both [60]- and [70]-Fullerenes form stable ground state equilibrium but also both distorted the planarity of N-based heterocyclic aromatic donor indenopyridines. Though angle of distortion of planarity is higher to accommodate coconut shaped C_{70}, still Stern-Volmer association constant ratio shows 5 fold higher selectivity of spherical C_{60} on interacting with Indenopyridines in Toluene.

Declaration of competing interest

The authors declare that they have no known competing financial interests or personal relationships that could have appeared to influence the work reported in this paper.

Acknowledgements

Author C. Pal acknowledges UGC for sanctioning FDP and The University of Burdwan for the infrastructural facilities and support.

References

[1] Chaudhuri T, Ghosh K, Mula S, Chattopadhyay S, Benerjee M. Molecular recognition of C_{70}-fullerene by meso-phenyl bodipy dye. J. Lumin. 2014;147:253–8. https://doi.org/10.1016/j.jlumin.2013.11.014.
[2] Mukherjee S, Bauri AK, Bhattacharya S. Spectroscopic and theoretical insights on non-covalent binding of Py-C_{60} with a designed diporphyrin in solution. J. Solut. Chem. 2013;42:111–24. https://doi.org/10.1007/s10953-012-9948-7.
[3] Ichiki T, Matsuo Y, Nakamura E. Photostability of a dyad of magnesium porphyrin and fullerene and its application to photocurrent conversion. Chem. Commun. 2013;49:279–81. https://doi.org/10.1039/C2CC36988E.
[4] Chaudhuri T, Nath S, Chattopadhyay S, Banerjee M, Nayak SK. Supramolecular interactions of meso-tetra-2-chlorophenylporphyrin with fullerenes: a luminescence study. J. Lumin. 2010;130:507–11. https://doi.org/10.1016/j.jlumin.2009.10.022.
[5] Karmakar A, Chaudhuri T, Mula S, Chattopadhyay S. Charge transfer in the electron

donor-acceptor complexes of a meso-phenol BODIPY dye with chloranils and fullerenes. Spectrochim. Acta A 2015;137:1258–64. https://doi.org/10.1016/j.saa.2014.09.037.
[6] Chaudhuri T, Goswami D, Banerjee M, Chattapadhya S, Nayak SK. Supramolecular selectivity of [60]-fullerene among equivalently photoactive porphyrins. J. Lumin. 2010;130:1750–5. https://doi.org/10.1016/j.jlumin.2010.04.004.
[7] Chaudhuri T, Santra S, Jana S, Hajra A. Determination of vertical ionization potential of nitroso-benzoimidazothiazole using charge transfer interaction with a series of acceptors. Spectrochim. Acta A 2018;204:403–8. https://doi.org/10.1016/j.saa.2018.06.083.
[8] Bandi V, Das SK, Awuah SG, You Y, D'Souza F. Thieno-pyrrole-fused 4, 4-Difluoro-4-bora-3a,4a-diaza-s-indacene–Fullerene dyads: utilization of near-infrared sensitizers for ultrafast charge separation in donor–acceptor systems. J. Am. Chem. Soc. 2014;136:7571–4. https://doi.org/10.1021/ja503015f.
[9] Pal C, Chaudhuri T, Mukhopadhyay C, Banerjee M. Interaction of Indenopyridines with [60]-fullerene: a spectroscopic and computational study. Indian J. Chem. 2019;58A:561–6. http://nopr.niscair.res.in/handle/123456789/47299.
[10] Rudolf M, Kirner S, Guldi D. A multicomponent molecular approach to artificial photosynthesis–the role of fullerenes and endohedralmetallofullerenes. Chem. Soc. Rev. 2016;45:612–30. https://doi.org/10.1039/C5CS00774G.
[11] Wang B, Zheng S, Saha A, Bao L, Lu X, Guldi DM. Understanding charge-transfer characteristics in crystalline nanosheets of fullerene/(metallo) porphyrincocrystals. J. Am. Chem. Soc. 2017;139:10578–84. https://doi.org/10.1021/jacs.7b06162.
[12] García-Simón C, Garcia-Borràs M, Gómez L, Parella T, Osuna S, Juanhuix J, Imaz I, Maspoch D, Costas M, Ribas X. Sponge-like molecular cage for purification of fullerenes. Nat. Commun. 2014;5:1–9. https://doi.org/10.1038/ncomms6557.
[13] Scurlock RD, Ogilby PR. Excited-state charge-transfer complexes formed between C_{60} and substituted naphthalenes. J. Photochem. Photobiol. Chem. 1995;91:21–5. https://doi.org/10.1016/1010-6030(95)04123-W.
[14] Sibley SP, Nguyen YT, Campbell RL, Silber HB. Spectrophotometric studies of complexation of C_{60} with aromatic hydrocarbons. Spectrochim. Acta, Part A 1997;53:679–84. https://doi.org/10.1016/S1386-1425(96)01843-4.
[15] Bhattacharya S, Nayak SK, Chattopadhyay S, Banerjee M, Mukherjee AK. Study of ground state EDA complex formation between [70]-fullerene and a series of polynuclear aromatic hydrocarbons. Spectrochim. Acta, Part A 2002;58:289–98. https://doi.org/10.1016/S1386-1425(01)00543-1.
[16] Sarova G, Berberan-Santos MN. Stable charge-transfer complexes versus contact complexes. Application to the interaction of fullerenes with aromatic hydrocarbons. J. Phys. Chem. B 2004;108:17261–8. https://doi.org/10.1021/jp047019z.
[17] Bhattacharya S, Ghosh K, Bauri AK, Chattopadhyay S, Banerjee M. Electronic structures and ionicity in [60]-fullerene/polycyclic aromatic hydrocarbon charge transfer complexes studied by UV–Vis and NMR spectroscopic techniques. J. Mol. Struct. 2006;784:124–37. https://doi.org/10.1016/j.molstruc.2005.08.021.
[18] Heintzelman GR, Averill KM, Dodd JH, Demarest KT, Tang Y, Jackson PF. PCT Int. Appl. 2003 WO 2003088963 A1 20031030.
[19] Safak C, Simsek R, Altas Y, Boydag S, Erol K. 2-methyl-3-acetyl-4-aryl-5-oxo-1,4-dihydro-5H indeno(1,2-b) pyridine derivatives studies and their calcium antagonistic activities. Boll. Chim. Farm. 1997;136:665–9.
[20] Chaudhuri T, Salampuria S, Mukhopadhyay C, Tapaswi PK, Chattopadhyay S, Banerjee M. Molecular recognition of anthracene and indeno-pyridine by (dibenzoylmethanato)boron difluoride in ethanol. J. Photochem. Photobiol. Chem. 2012;248:55–62. https://doi.org/10.1016/j.jphotochem.2012.08.017.
[21] Chaudhuri T, Salampuria S, Mukhopadhyay C, Tapaswi PK, Chattopadhyay S, Banerjee M. Charge transfer energies of the complexes of (dibenzoylmethanato) boron difluoride with indeno-pyridines and polynuclear aromatic hydrocarbons. Spectrochim. Acta, Part A 2013;108:181–5. https://doi.org/10.1016/j.saa.2013.01.089.
[22] Minameyer MB, Xu Y, Frühwald S, Görling A, von Delius M, Drewello T. Investigation of cycloparaphenylenes (CPPs) and their noncovalent ring-in-ring and fullerene-in-ring complexes by (Matrix-Assisted) laser desorption/ionization and density functional theory. Chem. Eur J. 2020;26:8729–41. https://doi.org/10.1002/chem.202001503.
[23] Li M-M, Wang Y-B, Zhang Y, Wang W. The nature of the noncovalent interactions between benzene and C_{60} fullerene. J. Phys. Chem. A 2016;120(28):5766–72. https://doi.org/10.1021/acs.jpca.6b06492.
[24] Pal C, Chaudhuri T, Banerjee M, Tapaswi P, Mukhopadhyay C. Non-covalent interaction between tetraphenylporphyrin and indenopyridine. Int. J. Photon. Optic. Technol. 2016;2(2):32–8.
[25] Lakowicz JR. Principles of Fluorescence Spectroscopy. third ed. New York: Springer; 2006.
[26] Chang G, Guida WC, Still WC. An internal-coordinate Monte Carlo method for searching conformational space. J. Am. Chem. Soc. 1989;111:4379–86. https://doi.org/10.1021/ja00194a035.
[27] Kong J, White CA, Krylov AI, Sherrill CD, Adamson RD, Furlani TR, Lee MS, Lee AM, Gwaltney SR, Adams TR, Ochsenfeld C, Gilbert ATB, Kedziora GS, Rassolov VA, Maurice DR, Nair N, Shao Y, Besley NA, Maslen PE, Dombroski JP, Daschel H, Zhang W, Korambath PP, Baker J, Byrd EFC, VanVoorhis T, Oumi M, Hirata S, Hsu CP, Ishikawa N, Florian J, Warshel A, Johnson BG, Gill PMW, Head-Gordon M, Pople JA. Q-Chem 2.0: a high-performance ab initio electronic structure program package. J. Comput. Chem. 2000;21:1532–48. https://doi.org/10.1002/1096-987X(200012)21:16%3C1532::AID-JCC10%3E3.0.CO;2-W.
[28] Cantrill SJ, Pease AR, Stoddart JF. A molecular meccano kit. J. Chem. Soc. Dalton Trans. 2000;21:3715–34. https://doi.org/10.1039/B003769I.
[29] Bhasikuttan AC, Mohanty J, Nau WM, Pal H. Efficient fluorescence enhancement and cooperative binding of an organic dye in a supra-biomolecular host–Protein assembly. Angew. Chem. Int. Ed. 2007;46:4120–2. https://doi.org/10.1002/anie.200604757.
[30] Baer R, Livshits E, Salzner U. Tuned range-separated hybrids in density functional theory. Annu. Rev. Phys. Chem. 2010;61:85–109. https://doi.org/10.1146/annurev.physchem.012809.103321.
[31] Velu SS, DiMeo F, Trouillas P, Sancho-Garcia J-C, Weber JFF. Regio- and stereo controlled synthesis of oligostilbenoids: theoretical highlights at the supramolecular level. J. Nat. Prod. 2013;76:538–46. https://doi.org/10.1021/np300705p.
[32] Chattaraj PK, Sarkar U, Roy DR. ElectrophilicityIndex. Chem. Rev. 2006;106:2065–91. https://doi.org/10.1021/cr040109f.
[33] Pérez P, Domingo LR, Aurell MJ, Contreras R. Quantitative characterization of the global electrophilicity pattern of some reagents involved in 1,3-dipolar cycloadditionreactions. Tetrahedron 2003;59:3117–25. https://doi.org/10.1016/S0040-4020(03)00374-0.
[34] Domingo LR, Chamorro E, Pérez P. Understanding the reactivity of captodative ethylenes in polar cycloaddition reactions. A theoretical study. J. Org. Chem. 2008;73:4615–24. https://doi.org/10.1021/jo800572a.

Prof. Rahul Dev Mukhopadhyay

ScienceDirect

Chem

Volume 8, Issue 8, 11 August 2022, Pages 2192-2203

Article

Out-of-equilibrium chemical logic systems: Light- and sound-controlled programmable spatiotemporal patterns and mechanical functions

Seoyeon Choi [2], Rahul Dev Mukhopadhyay [1 4], Shovan Kumar Sen [1], Ilha Hwang [1], Kimoon Kim [1 2 3 5]

Show more

Share Cite

https://doi.org/10.1016/j.chempr.2022.04.020

Get rights and content

The bigger picture

The complexity of biological processes and their programmability has kindled the imagination of researchers since decades. Exact mimicking of these complex processes to execute life-like functions still remains a distant goal. However, constant efforts are being dedicated to develop artificial life based on the limited knowledge that we have gained on various biological systems and intercellular processes. Among these, the exploration of out-of-equilibrium chemical systems has gained special attention in recent years. Nevertheless, the control over such systems with multiple input signals and programming them using basic Boolean logic for the execution of smart functions remain a challenging task. The present use of light, sound, and chemical inputs in out-of-equilibrium chemical logic systems addresses the aforementioned challenges. The long-term goal in this direction is to increase the complexity of such chemical logic systems and perform more complicated functions.

Summary

Living systems at different scales function through the sensing of multiple external signal inputs, which are further processed based on binary or more complicated computational models and networks. Inspired by such behavior, here, we show that the information processing in out-of-equilibrium chemical systems utilizing binary Boolean logic can be exploited to obtain transient functions such as spatiotemporally controlled chemical gradients and patterns in response to specific combination of multiple physical or chemical inputs (light, audible sound, and O_2). We further explore systems that are able to execute highly

complicated functions such as guiding a cargo through a maze by processing the information from multiple external stimuli. Our approach of integrating and encoding binary Boolean logic within out-of-equilibrium chemical systems for the extraction of mechanical work to execute transient biomimicking functions can expand the realms of systems chemistry and related research and help us design smart materials.

Graphical abstract

Download : Download high-res image (129KB)

Download : Download full-size image

Introduction

Living systems ranging from the size of a single cell to higher organisms such as animals and human beings obtain specific information (physical or chemical input signals) through their sensory systems, which is thereafter processed based on basic binary logic as well as complex computational algorithms to program much more complicated spatiotemporal functions, e.g., cell division, cell motility, cargo transport, etc. (FigureS1A).[1,2] In the recently passed epoch, the pursuit of making programmable life-like systems in the lab has therefore led to the exploration of complex chemical or biological networks that operate out of equilibrium, where different components interact with each other following a certain logic or program to give rise to a collective emergent behavior.3, 4, 5, 6, 7, 8, 9, 10, 11, 12, 13, 14 However, the possibility of integrating such binary Boolean logic in programming out-of-equilibrium chemical systems (CSs) to obtain transiently functional materials has so far been a daunting task.[3,]15, 16, 17 If such modules can be created utilizing chemical logic systems (**CLSs**) that encode binary logic and carry out information processing, it may pave the way toward smart systems capable of executing complex biomimicking functions.

Among other physical stimuli, the use of audible sound in controlling chemical processes is still in its infancy.18, 19, 20, 21, 22 Very recently, our group utilized audible sound to control redox-sensitive and pH-sensitive out-of-equilibrium CSs.[23] We anticipated that our approach can offer an alternate strategy to control the spatiotemporal distribution of out-of-equilibrium chemical network systems through the participation of various chemical (reducing agents, acid, atmospheric gases, etc.) and physical stimuli (sound, light, etc.), maintaining the rules of binary logic to mimic biological processes such as spatiotemporally controlled chemical gradients, patterns, etc. In a seminal work,[24] Hermans and coworkers

have demonstrated such features with out-of-equilibrium functional supramolecular polymers.[25,26] We thought of taking this challenge a step ahead by controlling the spatiotemporal location of nanoaggregates of such supramolecular polymers in solution to execute even higher level complex functions under out-of-equilibrium conditions.[27,28] We anticipated that the presence of nanoaggregates having different physical and chemical properties within different locations in a solution can segregate a solution into property-specific spatiotemporal domains, which would be useful in the execution of macroscopic functions such as extraction of mechanical work.29, 30, 31, 32 The topography of liquid surface generated by standing waves has previously been used as a template to assemble floating beads in programmable patterns.[33] We therefore thought of utilizing audible sound generated concentric surface waves as templated tracks for the programmed movement of a floating cargo.

Among the vast examples of mechanical work by systems exhibiting life-like behavior that involves collective intelligence,[32] solving a maze involves locating and reaching a specific target avoiding collisions with physical hurdles encountered along the way.[34] So far, maze solving has been explored using both active (self-propelled) and passive (that needs to be guided) particles through chemotaxis, phototaxis, magnetotaxis, etc.35, 36, 37, 38, 39 Nevertheless, the use of audible sound to guide a passive cargo through a maze is hitherto unknown.

Herein, we demonstrate that the concerted participation of various physical and chemical stimuli, which follows the rules of Boolean math, can be utilized to obtain a programmed spatiotemporal distribution of out-of-equilibrium CSs to program spatiotemporal patterns, chemical gradients, and most importantly, transient mechanical functions (FigureS1B). For instance, the pH-responsive nanoaggregates of a peptide-based gelator can be controlled with light in the presence of a photoacid, leading to a spatiotemporal change in the surface tension of the solution, which further induces motion in a passive floater (cargo) due to the Marangoni effect. The application of audible sound provides specific tracks for cargo movement through the generation of surface waves. An algorithm based on binary logic is further set up to successfully navigate the floating cargo through a maze.

Section snippets

Design of multistimuli-responsive redox chemical system for pattern formation: Chemical system 1 (CS1)

As a model multiple stimuli-responsive system, we chose the redox chemistry of methyl viologen ($\mathbf{MV^{2+}}$/$\mathbf{MV^{\cdot+}}$), which is known to form spatiotemporal patterns upon dissolution of atmospheric oxygen in solution under normal conditions. Such spatiotemporal patterns can be reproducibly obtained by controlling the dissolution of oxygen in water using audible sound-induced vibration of the air-water interface.[23] $\mathbf{MV^{2+}}$ is known to get reduced to its radical cationic ($\mathbf{MV^{\cdot+}}$) form through photoinduced…

Lead contact

Further information and requests for resources should be directed to and will be fulfilled by the lead contact Kimoon Kim (kkim@postech.ac.kr↗)….

Materials availability

All unique/stable reagents generated in this study are available from the lead contact with a completed Materials Transfer Agreement….

Acknowledgments

This work was supported by the Institute for Basic Science (IBS, IBS-R007-D1), Republic of Korea. We thank I.S. Kang (POSTECH) for helpful discussions.…

Author contributions

R.D.M. and K.K. conceived the idea. S.C. performed most of the experiments under supervision of R.D.M. S.K.S. and I.H. participated in the pattern experiments. R.D.M., S.C., and K.K. wrote the manuscript and all authors discussed the results, analyzed the data, and commented on the manuscript. K.K. supervised the overall research.…

Declaration of interests

The authors…

References (51)

A. Perrot *et al.*
Extraction of mechanical work from stimuli-responsive molecular systems and materials
J. Trends Chem. (2021)

Y. Benenson
Biomolecular computing systems: principles, progress and potential
Nat. Rev. Genet. (2012)

T. Kitada *et al.*
Programming gene and engineered-cell therapies with synthetic biology
Science (2018)

N. Wagner *et al.*
Systems chemistry: logic gates, arithmetic units, and network motifs in small networks
Chem. Eur. J. (2009)

R. Merindol *et al.*
Materials learning from life: concepts for active, adaptive and autonomous molecular systems
Chem. Soc. Rev. (2017)

B.A. Grzybowski *et al.*
From dynamic self-assembly to networked chemical systems
Chem. Soc. Rev. (2017)

G. Ashkenasy *et al.*
Systems chemistry
Chem. Soc. Rev. (2017)

G. Ragazzon *et al.*
Energy consumption in chemical fuel-driven self-assembly
Nat. Nanotechnol. (2018)

A. Jain *et al.*

Chemical fuel-driven living and transient supramolecular polymerization
Nat. Commun. (2019)

S. Choi *et al.*
Fuel-driven transient crystallization of a cucurbit[8]uril-based host-guest complex
Angew. Chem. Int. Ed. Engl. (2019)

View more references

Cited by (3)

Short-term plasticity, multimodal memory, and logical responses mimicked in stretchable hydrogels
2023, Matter

Show abstract

Out-of-equilibrium chemical logic systems
2022, Chem

Show abstract

Self-Regulatory Micro- and Macroscale Patterning of ATP-Mediated Nanobioconjugate
2023, ACS Nano

Recommended articles (6)

Research article

Tractable molecular adaptation patterns in a designed complex peptide system
Chem, Volume 8, Issue 7, 2022, pp. 1894-1905

Show abstract

Research article

Hydrogen-bonded organic frameworks: Chemistry and functions
Chem, Volume 8, Issue 8, 2022, pp. 2114-2135

Show abstract

Research article

Delocalized Li@Mn_6 superstructure units enable layer stability of high-performance Mn-rich cathode materials
Chem, Volume 8, Issue 8, 2022, pp. 2163-2178

Show abstract

Research article

Cross-reactive binding versus selective phosphate sensing in an imine macrocycle sensor

Chem, Volume 8, Issue 8, 2022, pp. 2228-2244

Show abstract

Research article

Transition-metal-catalyzed reactions promoted by cyclic (alkyl or aryl)(amino)carbene ligands

Chem, Volume 8, Issue 8, 2022, pp. 2082-2113

Show abstract

Research article

Anion chemistry enabled positive valence conversion to achieve a record high-voltage organic cathode for zinc batteries

Chem, Volume 8, Issue 8, 2022, pp. 2204-2216

Show abstract

4 Present address: Department of Chemistry, Ramananda College, Bankura University, Bishnupur 722122, West Bengal, India

5 Lead contact

View full text

nature COMMUNICATIONS

ARTICLE

https://doi.org/10.1038/s41467-022-30124-x OPEN

Cascade reaction networks within audible sound induced transient domains in a solution

Prabhu Dhasaiyan[1], Tanwistha Ghosh[1], Hong-Guen Lee[2], Yeonsang Lee[2], Ilha Hwang[1✉], Rahul Dev Mukhopadhyay[1,6✉], Kyeng Min Park[3], Seungwon Shin[4], In Seok Kang[5] & Kimoon Kim[1,2✉]

Spatiotemporal control of chemical cascade reactions within compartmentalized domains is one of the difficult challenges to achieve. To implement such control, scientists have been working on the development of various artificial compartmentalized systems such as liposomes, vesicles, polymersomes, etc. Although a considerable amount of progress has been made in this direction, one still needs to develop alternative strategies for controlling cascade reaction networks within spatiotemporally controlled domains in a solution, which remains a non-trivial issue. Herein, we present the utilization of audible sound induced liquid vibrations for the generation of transient domains in an aqueous medium, which can be used for the control of cascade chemical reactions in a spatiotemporal fashion. This approach gives us access to highly reproducible spatiotemporal chemical gradients and patterns, in situ growth and aggregation of gold nanoparticles at predetermined locations or domains formed in a solution. Our strategy also gives us access to nanoparticle patterned hydrogels and their applications for region specific cell growth.

[1] Center for Self-assembly and Complexity (CSC), Institute for Basic Science (IBS), Pohang 37673, Republic of Korea. [2] Department of Chemistry, Pohang University of Science and Technology (POSTECH), Pohang 37673, Republic of Korea. [3] Department of Biochemistry, Daegu Catholic University School of Medicine, Daegu 42472, Republic of Korea. [4] Department of Mechanical and System Design Engineering, Hongik University, Seoul 04066, Republic of Korea. [5] Department of Chemical Engineering, Pohang University of Science and Technology (POSTECH), Pohang 37673, Republic of Korea. [6] Present address: Department of Chemistry, Ramananda College, Bankura University, Bishnupur 722122 West Bengal, India. ✉email: ihwang1@ibs.re.kr; rdevmukherjee@gmail.com; kkim@postech.ac.kr

The coexistence of different chemical domains in which various chemical cascade reaction networks operate with spatiotemporal control is one of the fundamental principles of operation in living systems, particularly in eukaryotic cells[1–7]. Cells have developed mechanisms for the precise sensing of positional information of biochemical and for regulating the cascade processes in which they are involved. Intracellular gradients of biomolecules arise from the spatial separation of opposing reactions in biochemical reaction cycles. These gradients provide positional cues for executing vital transiently active cellular functions. To understand and mimic such localization and control over biochemical networks in living systems, various artificial counterparts such as liposomes, vesicles, polymersomes, etc. have been developed[8–18]. For instance, amphiphilic block copolymer-based semipermeable polymersomes were synthesized by van Hest and co-workers[12–15]. More recently, coacervate-based biomimetic systems were also extensively studied by Mann and others[19–23]. These systems provide specific domains that allow spatiotemporal control of various cascade reaction networks akin to biological systems. In a different strategy to execute such localization and control over chemical reactions, Pickering emulsions have also been explored[24]. A recent development in this area is the concentric liquid reactors formed under centrifugal force induced out-of-equilibrium conditions and utilized for sequential chemical synthesis and separation by Grzybowski and co-workers[25]. Given the requirements of a prudent molecular design that often leads to cumbersome synthetic steps in the case of the membrane-based systems, and the need for an astute choice of pairwise immiscible liquids in liquid-liquid phase separating membraneless systems, there are large demands for the development of novel straightforward strategies for the creation of programmable domains within a solution where specific chemical reaction networks can be spatiotemporally controlled. Among chemical reactions, enzymatic networks especially have biological significance and possess unique advantages. In general, enzyme cascades can be regulated either by tuning the abundance or activity of the enzymes or by perturbing the enzymatic reaction network with small molecules acting as inhibitors or competitors. However, it remains a central objective of synthetic biologists and chemists to explore alternate strategies to spatiotemporally control such enzymatic reaction networks, to program the predictable formation of chemical gradients through the spatiotemporal control of their reaction kinetics.

An external physical stimulus like light energy, which can be locally applied and can be remotely controlled, has been a useful tool to control the spatiotemporal assembly of organic molecules and that of nanoparticles within a matrix where chemical gradients are generally controlled by diffusion rather than by convection. In a recent work, Prins and co-workers demonstrated that kinetic asymmetry could emerge even at the macroscopic level within a gold nanoparticle embedded hydrogel matrix stimulated by a spatial delivery of light energy thereby installing a non-equilibrium state[26]. Nevertheless, controlling the kinetics of nanoparticle formation and their self-assembly utilizing localized energy delivery in a solution still remains challenging due to the uncontrolled diffusion and convectional currents operating within the system.

Sound energy, which can induce vibrations within a medium while traveling through it and has found wide applications in physics, medical science, materials science and other fields[27–29]. However, the use of sound energy in chemistry is mostly limited to ultrasound-induced cavitation effects that can efficiently execute several chemical reactions[30–32]. Nevertheless, utilizing audible sound (in the range of 20–20,000 Hz) to control any molecular or supramolecular events and synthesis is still in its infancy, most likely due to its low intensity, which is unable to induce chemical transformations[33]. However, it has been long known that vertical shaking of a liquid-filled dish using audible sound (or a vibration generator) can generate a standing wave pattern on the liquid surface (Faraday instability), and the patterns change significantly depending on the frequency of the applied sound and the shape of the dish[34–38]. Based on this phenomenon, very recently we have developed a facile strategy that utilizes audible sound to control the spatiotemporal distribution of chemical components in out-of-equilibrium systems resulting in the formation of predictable chemical patterns[39]. We specifically utilized the audible sound-induced vibration of the air-water interface to promote the dissolution of atmospheric gases (e.g., oxygen and carbon dioxide) to obtain spatiotemporal control over redox or pH-specific chemical reactions, which were easily visualized as predicable and programmable spatiotemporal patterns. The patterns consisted of distinct redox-specific and/or pH-specific domains, which were visualized from the color of the chemical indicators present in the solution. These domains although transiently generated, retained their position and distinct boundary features for a specific time period[40]. Therefore, we anticipated that redox or pH-responsive chemical reactions can favorably occur within these transient domains during the pattern formation process. The spatiotemporal execution of more complex reaction systems such as multistep enzymatic cascade reactions and controlling their kinetics within these transient domains was another interesting challenge that we considered exploring.

Herein, we report spatiotemporal control of enzyme-mediated cascade reactions within audible sound-induced transient domains created in a solution without utilizing any structure inducing molecules (Fig. 1). This is further extended to the spatiotemporal control over the in situ growth and self-assembly of nanoparticles within predictable domains present in the solution. Additionally, the preparation of nanoparticle-patterned hydrogels and their utilization for region-specific growth of cells is also explored. Our approach will offer a promising strategy to control chemical processes within predictable yet transiently generated domains within a solution. The strategy can be further utilized to gain control over the region-specific reaction kinetics of enzyme cascade reactions and other complex chemical network systems in solution. The present findings will be significant in the development and control over cascade reaction networks in a solution.

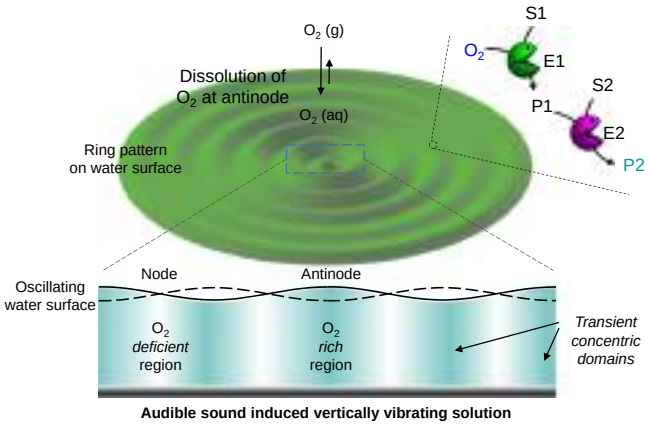

Fig. 1 Audible sound induced generation of transient domains and spatiotemporally controlled cascade reaction networks. Schematic of the audible sound induced surface standing wave and generation of corresponding concentric rings (cross-sectional view). Spatiotemporally controlled cascade reaction of substrate S1 with an oxygen responsive enzyme E1 is facilitated at the antinodal domains due to the region-specific dissolution of oxygen. The final product P2 is generated by the reaction of product P1 and substrate S2 with enzyme E2, which is observed as a color pattern.

Results

Cascade reactions within audible sound induced transient domains. Among enzyme cascade reactions, we chose the widely studied glucose oxidase (GOx) and horseradish peroxidase (HRP) cascade combination with glucose and a redox responsive colorimetric dye. Dyes such as 2,2'-azino-bis(3-ethylbenzothiazoline-6-sulfonic acid) (ABTS) and *o*-dianisidine are typically utilized as substrates in the aforementioned cascade. Recently, Hess and co-workers have reported the spontaneous generation of colored spatiotemporal patterns of ABTS radical utilizing the same enzymatic cascade system that arose from reaction-driven Rayleigh–Bernard convection[41]. Although the overall nature of the resulting patterns was rather similar in each trial, the patterns were not exactly the same in general. Nevertheless, predictable pattern generation depends on the region-specific control of oxygen (substrate) dissolution into the solution, which as mentioned before can be efficiently controlled by audible sound induced liquid vibrations[39].

As shown in Fig. 1, during the audible sound induced vertical vibration of the liquid, the atmospheric oxygen molecules undergo region-specific dissolution and diffusion into the solution. Specifically, the nodes where the vibration is minimum show lesser gas dissolution (oxygen deficient region) while at the antinodal positions where the vibration is maximum the gas dissolves more efficiently into the solution (oxygen rich region). The nodal and antinodal positions are reproducibly obtained at the same places in the solution for all trials and as a consequence, the colored spatiotemporal patterns of ABTS radical obtained by this strategy should be the same or predictable over several repeated cycles. The overall solution in the dish is in a way isolated into domains differing in their oxygen concentration (oxygen rich: intense bluish cyan and oxygen deficient: pale cyan). These distinctly colored chemical gradients are generated due to the regional expedited dissolution of atmospheric gases such as oxygen into certain concentric domains within the solution, which retain their identity, position and boundary features transiently in solution and can be utilized to execute enzymatic cascade reactions within a single phase with much more precision.

The experimental setup used in the present study is shown in Supplementary Fig. 1. A schematic representation of the GOx-HRP enzymatic cascade is portrayed in Fig. 2a. The typical reaction involves the ping-pong mechanism of GOx where the first step is the reduction of GOx-FAD to GOx-$FADH_2$ by glucose. The recovery of reduced GOx-$FADH_2$ was initially taken care of by oxygen and produces H_2O_2, which is further used by HRP in order to oxidize ABTS (colorless) to $ABTS^{+\bullet}$ (cyan)[41]. The pattern experiments were performed after optimizing the concentration of the cascade ingredients with a solution (5.0 mL) containing GOx (3.6 U/mL), HRP (2.2 U/mL), ABTS (1.0 mM), and glucose (50 mM) taken in a well-cleaned glass Petri dish, which was tightly covered. The dish was then placed on a loudspeaker connected to a function generator and waited until the solution became colorless. When the solution was exposed to air, in the absence of any external sound input, a randomly shaped cyan-colored pattern was generated as shown in Fig. 2b. The same pattern was not reproducibly obtained in the subsequent trials. In contrast, when the solution was exposed to air in the presence of an audible sound input (40 Hz), a "target" (or concentric ring) pattern was formed, as shown in Fig. 2c. Within a few seconds of audible sound induced vibration of the enzyme-substrate mixture, a concentric ring pattern with cyan and colorless domains was generated due to the region-specific preference in the dissolution of oxygen and subsequent enzymatic cascade reactions. More specifically, the cyan-colored regions correspond to the oxygen rich antinodes where H_2O_2 is produced by the O_2/glucose/GOx reaction, followed by the generation of $ABTS^{+\bullet}$ by the H_2O_2/ABTS/HRP reaction. On the other hand, the colorless regions correspond to the nodes where the formation of $ABTS^{+\bullet}$ is limited due to the minimal vibration of liquid and less oxygen uptake. In the present case, since the cyan-colored regions are separated by the colorless regions, the contents of each cyan-colored region are not mixed with those of the adjacent regions. Accordingly, the cyan-colored domains can be considered as "pseudo-compartments", while the colorless regions can be thought of as "pseudo-barriers" as they spatially separate transient domains in the solution. Although the boundaries of the transient pseudo-compartments generated in this way are less clearly defined than traditional permanent compartments based on lipids or other structure inducing molecules, they could be utilized to generate regional chemical concentration gradients and successfully control chemical reactions.

The strategy also works well in the case of other substrates as evident from a similar pattern with orange and colorless domains that were generated in case we used *o*-dianisidine as a colorimetric indicator (Supplementary Fig. 2). The effect of atmospheric oxygen concentration, which plays a key role in the aforementioned pattern generation process was also tested. For example, no pattern was generated under inert conditions, while the pattern generation was faster in the presence of an oxygen rich atmosphere than under normal atmospheric conditions. (Supplementary Fig. 3).

The formation of the target pattern here is presumably due to the viscous nature of the solution with weaker vibration, which suppresses the lateral flow thereby generating a concentric ring-based pattern rather than a two-vortex pattern as previously observed[39,42]. The cyan-colored concentric domains remain transiently stable in the solution. However, after ~30 min, most of the solution turns into a cyan color, which can be ascribed to the slow diffusion of H_2O_2 throughout the solution. Since the standing wave generated in the dish is highly dependent on the applied audible sound frequency, we could control the pitch of the colored ring pattern as shown in Supplementary Fig. 4, thereby we can specifically change the distance between the concentric domains, which can be a useful strategy to affect the chemical diffusion or communication between these domains. In addition, the number of domains increases with an increase in the diameter of the dish as shown in Supplementary Fig. 5. The shape of the transient domain, that is, the cyan-colored features in the pattern, can also be changed by changing the shape of the dish. For example, a target pattern is observed in a circular dish, while a checkerboard pattern was observed in a square dish (Supplementary Fig. 6). To further establish the predictability and reproducibility of patterns developed by our strategy, we performed the pattern formation experiments by varying the depth of the solution with and without applying audible sound (Supplementary Fig. 7). Thereby, we surmised that under the typical experimental conditions, only concentric ring domains were generated in the presence of audible sound, and we could clearly suppress the effects of the reaction-driven Rayleigh–Bernard convection usually observed in these systems under normal circumstances. We observed that during the pattern formation experiments, once a random pattern is generated in the absence of audible sound, it is difficult to reorganize the chemical gradients to obtain a pure concentric pattern even if the sound is applied later, as shown in Supplementary Fig. 8. The resultant pattern is therefore a mixture of random maze-like and concentric ring-shaped chemical gradients.

Another way of interpreting the patterns is through the rate of the enzyme cascade reaction, which is comparatively much faster at the antinodes than at the nodal positions. The rate of reaction even varied at the individual antinodal domains. Image analysis

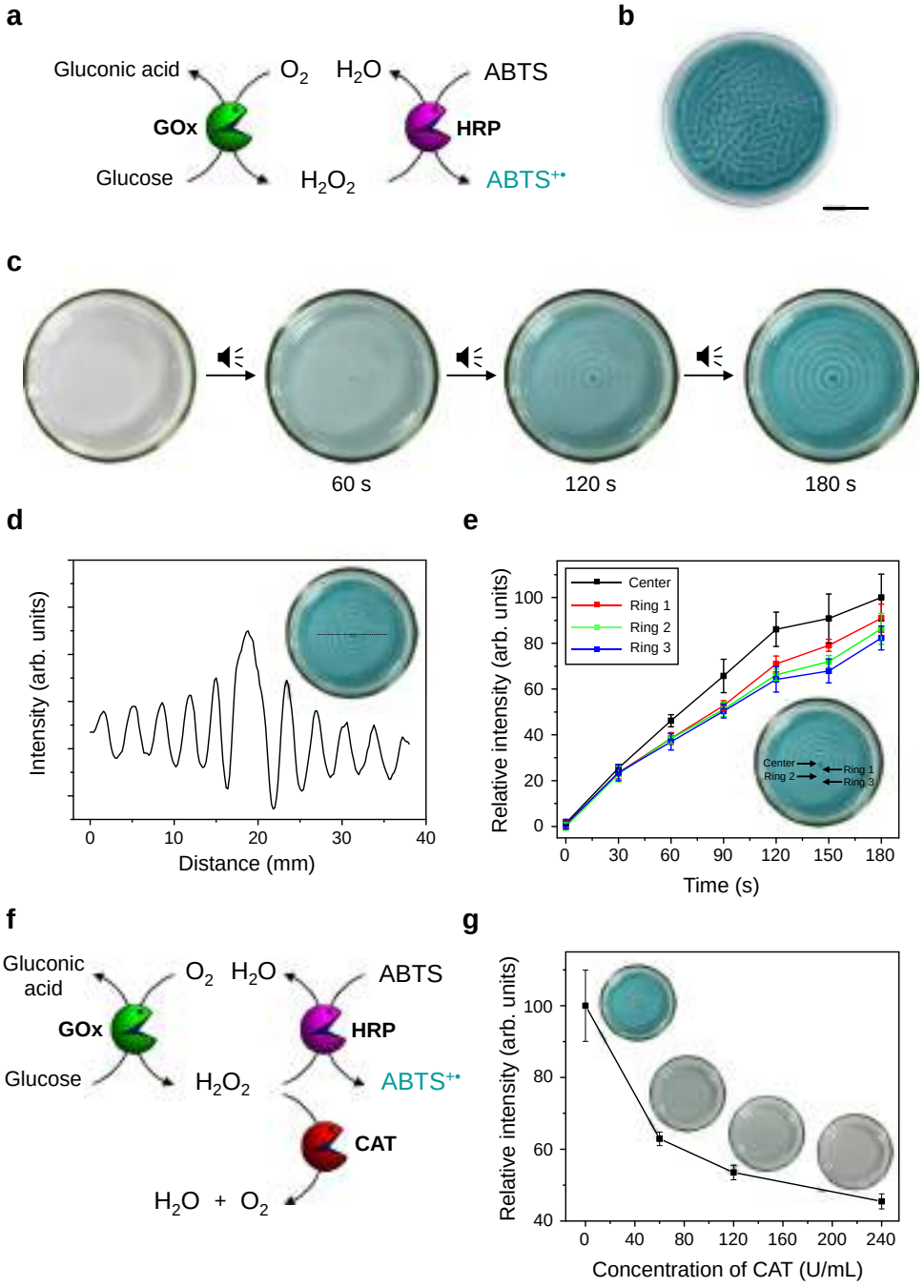

Fig. 2 Audible sound mediated spatiotemporal control over glucose/GOx/HRP/ABTS cascade reaction. a Schematic representation of glucose/GOx/HRP/ABTS cascade reaction. Here the color pattern is generated from production of the cyan-colored $ABTS^{+\bullet}$. GOx: glucose oxidase, HRP: horseradish peroxidase, ABTS: 2,2′-azino-bis(3-ethylbenzothiazoline-6-sulfonic acid). **b** Random shaped pattern generated without applying audible sound (scale bar is 1.5 cm). **c** Time-dependent changes of a concentric ring pattern obtained by applying an audible sound input (40 Hz). **d** A line profile of image color intensity for the color pattern taken at 3 min. **e** Time-dependent changes in the image color intensity with standard deviation ($N = 10$) at the central region of the pattern and the first three antinodal concentric domains. **f** Schematic of the enzymatic cascade reaction with catalase as a competitive scavenger for H_2O_2. CAT: catalase. **g** Effect of catalase for the circular $ABTS^{+\bullet}$ pattern generation. The color intensities with standard deviation ($N = 10$) at the center of the patterns were compared. Inset: pattern images taken after 3 min of reaction.

of the patterns at any particular instant during the pattern generation showed that the color intensity corresponding to the amount of $ABTS^{+\bullet}$ formation showed a steady decrease as one moved from the center to the periphery (Fig. 2d). This observation can be attributed to the rate of oxygen dissolution being affected by the concomitant decrease in the amplitude of the vibrations at the antinodal positions from the center towards the periphery, which is well established in the literature[43]. As a matter of fact, we monitored the time-dependent changes in the $ABTS^{+\bullet}$ formation at the center and at the first three concentric ring-shaped domains (at the antinodes), where we clearly observed that the rate of progression of the enzyme cascade reaction is different at the different concentric rings being highest at the center and shows a gradual decline as the rings are placed towards the periphery (Fig. 2e). The overall rate of pattern formation or the rate of the enzyme cascade reaction in the

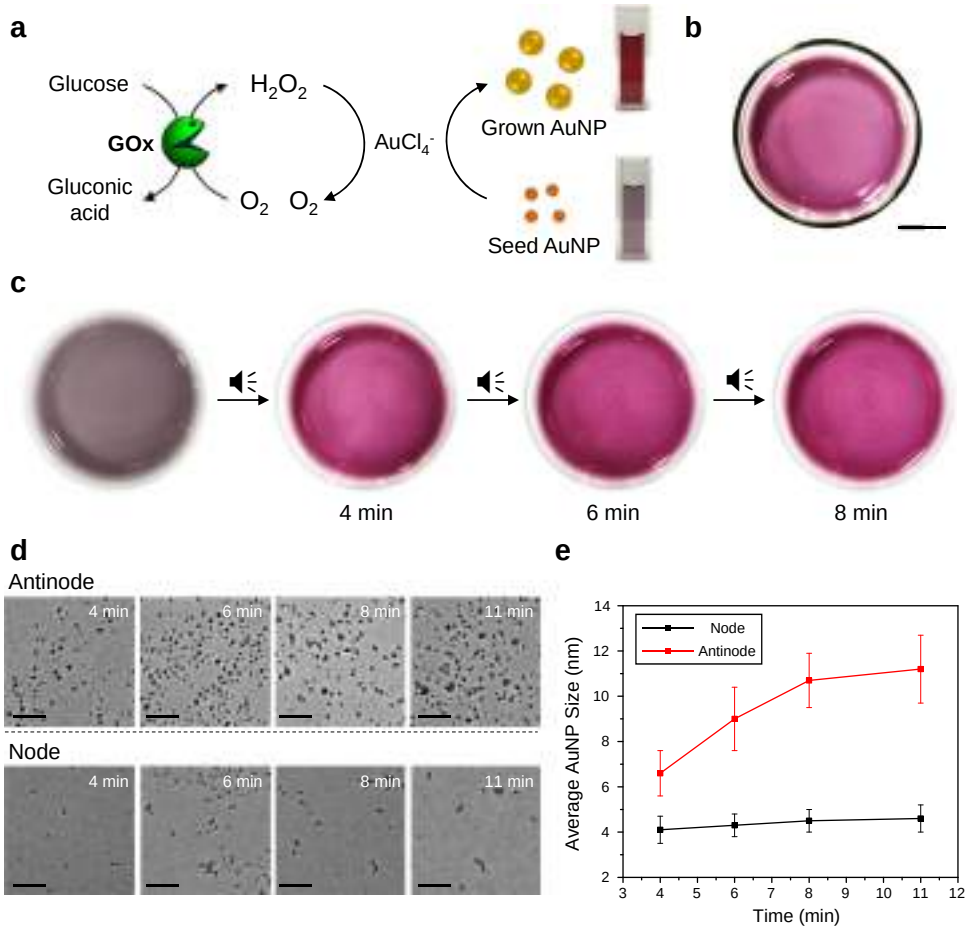

Fig. 3 Audible sound mediated spatiotemporal control over glucose/GOx/$AuCl_4^-$/seed AuNP cascade reaction. a Schematic representation of glucose/GOx/$AuCl_4^-$/seed AuNP cascade reaction. Here the colored pattern is generated from the in suit grown AuNPs. GOx: glucose oxidase, AuNP: gold nanoparticle. **b** Pattern generated without applying audible sound (scale bar is 1.5 cm). **c** Time-dependent changes of circular pattern generation with applying 30 Hz of audible sound. **d** TEM images of AuNP solutions taken at the antinodal (top) and nodal (bottom) positions of the colored pattern at 4, 6, 8, and 11 min, respectively (scale bar is 50 nm). **e** Plots for the time-dependent changes in the average size with standard deviation ($N = 100$) of the nanoparticles obtained from the TEM images from samples at the antinodal and nodal positions of the solution, respectively.

specified domains can also be manipulated by the addition of a competitor. For instance, the addition of catalase leads to the fast decomposition of H_2O_2 and thereby affects the rate of $ABTS^{+\bullet}$ formation (Fig. 2f)[44]. We observed that the rate of enzyme cascade reaction at the concentric rings was significantly decreased and the pattern formation was largely delayed as we increased the catalase concentration in solution (Fig. 2g).

In situ growth of gold nanoparticles within audible sound induced transient domains. After the successful control of the GOx-HRP enzymatic cascade, we decided to expand our strategy to spatiotemporally control the in situ seeded growth of gold nanoparticles (AuNPs) (Fig. 3a) within the audible sound generated transient domains within the same solution. Here, we utilized the growth of small sized AuNPs (~4 nm, acting as seed) in a cascade with the biocatalytic reaction between glucose, GOx and O_2 as schematically represented in Fig. 3a[45–47]. Seed AuNPs were prepared by literature procedure and characterized by transmission electron microscopy (TEM) and UV–Vis spectroscopy. The UV–Vis spectra of the as synthesized seed AuNPs showed characteristic surface plasmon peak at 513 nm, which supported the formation of small sized seed and the TEM experiments further confirmed the formation of spherical seed AuNPs with an average size of 4.1 nm (Supplementary Fig. 10). For the in situ growth of AuNPs, we varied different parameters and optimized a suitable condition for executing the audible sound experiments (Supplementary Fig. 11). When an aqueous solution (5.0 mL) containing seed AuNP (8 nM), GOx (35 U/mL), glucose (50 mM), and $AuCl_4^-$ (0.6 mM) was placed in a Petri dish, the solution turned wine red in color within 10 min (Fig. 3b), indicating the formation of larger AuNPs (average size ~ 11 nm) due to the reduction of Au^{3+} to Au^0 on the seed AuNP surface by the reaction byproduct H_2O_2. The results obtained from time-dependent UV–Vis spectra corroborates the AuNP growth process in the solution state (Supplementary Fig. 12).

When the same cascade biocatalytic nanoparticle growth mixture was subjected to audible sound and exposed to the air, we observed the appearance of red-colored concentric ring pattern within a few minutes, indicating the spatiotemporal expedited growth of AuNPs at the antinodal regions, as shown in Fig. 3c. We observed that the more oxygen supplied antinode regions turned wine red within a few minutes owing to the accelerated production of H_2O_2 that promoted the growth of the seed AuNPs, while the nodal positions where the supply of oxygen was limited appeared as thin concentric lines with a comparatively less intense wine red color. From the time-dependent TEM images obtained from aliquots extracted from each area, we further confirmed the facilitated growth of the AuNPs at the transiently generated domains placed at the antinodal positions of the standing wave.

Whereas, a time-dependent TEM analysis of samples extracted from the nodal positions showed minimal changes in the size of AuNPs (Fig. 3d, e). Although our audible sound method allowed us to control the in situ regional growth of AuNPs within transiently generated domains in a solution, a sharp boundary between the concentric ring-shaped domains (at the antinodal positions) as in the case of ABTS/ABTS$^{+\bullet}$ pattern was not achieved in this case, which can be ascribed to relatively small differences in molar extinction coefficients (~100-fold) as well as surface plasmon peaks (~20 nm) between seed and fully grown AuNPs[48]. Therefore, we aimed towards exploring a nanoparticle-based cascade reaction with a clear contrast between the concentric ring-shaped domains. We anticipated that the large difference in solution color between dispersed and aggregated AuNPs may be useful in obtaining such results. It may also simultaneously provide an easy route for the spatiotemporal self-assembly of specifically surface functionalized AuNPs.

Gold nanoparticle aggregation within audible sound induced transient domains. On demand control of metal nanoparticle assembly is important as the physical properties of metal nanoparticles are largely dependent on the aggregation or stacking of individual nanoparticles. Controlling such nanoparticle assembly in a spatiotemporal fashion is challenging and has so far been achieved using external stimuli such as chemicals, biomolecules, light, magnetic field, etc[49–52]. To apply our audible sound method to spatiotemporally program a nanoparticle assembly, we prepared carboxylic acid-functionalized gold nanoparticles (AuNPs) because their aggregation tendency and the resulting vivid color changes in acidic pH have been well-known for decades. We first synthesized 13 nm AuNPs capped with citric acid and the surface capping agent of these AuNPs was further exchanged with thioctic acid by ligand exchange reaction as the latter provides better stability and pH response in water[53,54]. As shown in Supplementary Fig. 13, the thioctic acid-functionalized AuNPs (TA-AuNP) were well dispersed in basic and neutral aqueous solution and exhibited a red-wine color. However, it turned blue below pH 4, indicating AuNP aggregation. Therefore, based on the color changes, we can easily recognize the formation of TA-AuNP aggregates under acidic conditions (Fig. 4a).

Following the previous ABTS pattern experiment, here we used the glucose/GOx reaction again because the reaction produces gluconic acid that lowers the pH of the solution. Firstly, TA-AuNP was mixed with glucose/GOx and the solution was exposed to air without applying sound. As the enzymatic reaction proceeds, the pH of the solution decreases and thus TA-AuNP aggregation occurs, resulting in randomly positioned blue regions in the red-colored solution as shown in Fig. 4b. The time-dependent UV–Vis spectra of this solution are given in Supplementary Fig. 14, which establishes the gradual self-assembly of the AuNPs. In contrast, the application of audible sound to the above solution produced a concentric ring pattern with blue and red concentric rings as shown in Fig. 4c. Such a ring pattern was evolved because of the enzymatic reaction, which proceeded preferentially at the antinodal regions transiently generated in the solution. In this pattern, small portions of the red and blue regions were extracted and analyzed by time-dependent TEM analysis. As shown in Fig. 4d, the TA-AuNPs in the red-colored nodal positions of the standing wave, mostly existed as individual particles, while the nanoparticles in the blue-colored concentric regions located at the antinodal positions exhibited the formation of larger nanoparticle aggregates and clusters with time as we expected. Since the color of the dispersed and aggregated nanoparticles was distinctly different, we could track the relative rates of TA-AuNP aggregation at the various antinodal regions through analysis of pattern images exhibited in Fig. 4c. The obtained results clearly corroborated that the TA-AuNP aggregation follows a much faster kinetics at the center and the rate of aggregation gradually decreases as one shifts to the antinodal regions (ring 1 to ring 3) towards the periphery (Supplementary Fig. 15) as observed in the case of the ABTS$^{+\bullet}$ pattern (Fig. 1e). These results confirm that our audible sound method provides an innovative strategy to program the self-assembly of gold nanoparticles within transient domains generated in a solution.

Nanoparticle-patterned hydrogels for region-specific cell growth. Region-specific growth of cells on specifically designed or patterned substrates can be exploited in a variety of biomedical applications, including regenerative medicine, tissue engineering, development of biosensors, and elucidation of cell-matrix interactions, etc[55,56]. To explore such applications, patterned surfaces of functional polymer or hydrogels have been often utilized as platforms for cell growth[57]. Similarly, the scope of studying the interaction of cells with patterned substrates containing materials such as carbon nanotubes[58], metal nanoparticles[59], etc. remains open for investigation. For instance, inhibition of cell growth has been reported in the presence of dispersed AuNPs. Whereas, an increase in the growth rate of cells has been observed in the presence of large AuNP aggregates[59]. The patterns obtained in the aforementioned cases mostly utilize chemical vapor deposition or techniques such as inkjet printing. We thought that using our audible sound-based strategy it may be possible to obtain patterns of AuNPs and AuNP aggregates, which can be further immobilized within a hydrogel matrix. We anticipated that these patterned substrates can be utilized as a platform to obtain region-selective cell growth, which in a way can extend the cascade chemical processes to the next higher level of biological applications. Figure 5a shows a schematic illustration of the nanoparticle-patterned hydrogel preparation and its application as a platform for selective cell growth. When 40 Hz of audible sound was applied to a solution containing TA-AuNP (8 nM), GOx (80 U/mL), glucose (50 mM), poly(ethylene glycol)-diacrylate (PEG-DA) ($M_n = 700$, 10 wt%) and a photo-initiator (Irgacure 2959, 1 wt%), spatiotemporal patterns consisting of blue concentric rings of aggregated AuNPs were developed within 3 min as shown in Fig. 5b. The fully developed pattern was fixed by irradiating the solution with 365 nm UV light. Figure 5c shows a photograph of the resulting nanoparticle-patterned hydrogel material. The hydrogel comprising of aggregated (blue region) and non-aggregated (pink region) nanoparticles containing domains was further utilized as a scaffold for region-selective growth of HeLa cells. To improve cell adhesion and proliferation, the hydrogel surface was treated with a cyclic RGDyK peptide and poly-L-lysine conjugate (c(RGDyK)-PLL) (see Methods section)[60,61], and the resulting hydrogel was incubated overnight after being treated with HeLa cells. When the patterned hydrogel was observed under a fluorescent microscope after 24 h, patterned cell growth is observed as shown in Fig. 5d, and the corresponding three-dimensional (3D) fluorescence image intensity plot of the cells (Fig. 5e) was found to be prominent along with alternate concentric rings as observed in the hydrogel pattern (See also Supplementary Fig. 16). Additionally, cells in the antinodal region show well spread morphology, whereas those in the nodal region do not (Supplementary Fig. 17). Analyzing these images, we could confirm a region-specific cell growth over the AuNP aggregated domains, which coincide with the antinodal positions of the pattern. As a control experiment, we carried out the same study using a hydrogel, random-patterned with AuNPs and AuNP aggregates that was prepared without applying sound. This resulted in random cell growth over the hydrogel surface, as

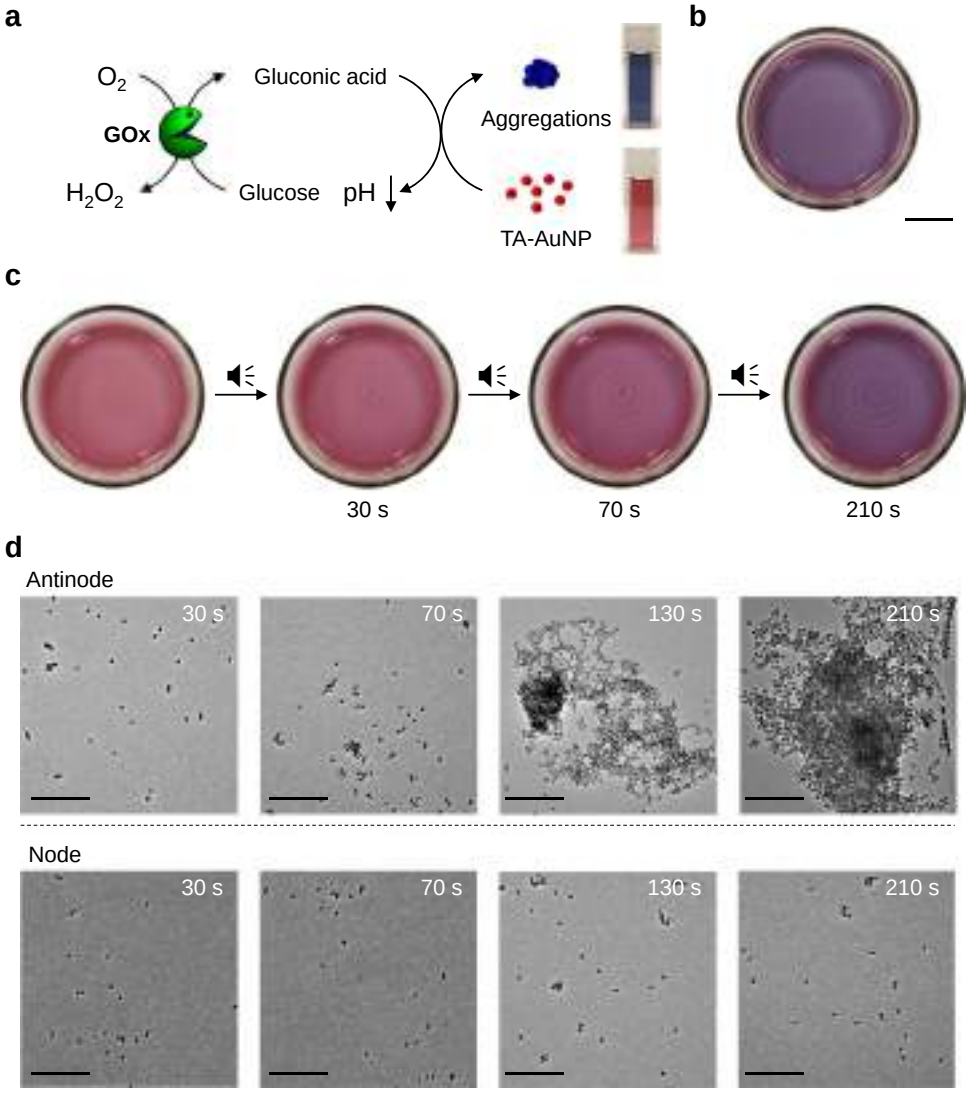

Fig. 4 Audible sound mediated spatiotemporal control over glucose/GOx/TA-AuNP cascade reaction. a Schematic representation of glucose/GOx/TA-AuNP cascade reaction. Here the color pattern is generated from the blue-colored aggregates of TA-AuNPs. GOx: glucose oxidase, TA-AuNP: thioctic acid-functionalized gold nanoparticle. **b** Random shaped pattern generated without applying audible sound (scale bar is 1.5 cm). **c** Time-dependent changes of a concentric ring pattern generated with applying 30 Hz of audible sound. **d** Time-dependent TEM images of TA-AuNP solution taken at the antinodal (top) and nodal (bottom) positions of the colored pattern at 30, 70, 130, and 210 s, respectively (scale bar is 200 nm).

shown in Supplementary Fig. 18. We further confirmed that our strategy of obtaining region-selective cell growth can be extended to other cells, such as human umbilical vein endothelial cells (HUVECs) (Supplementary Fig. 19).

Discussion

We have demonstrated the utilization of audible sound induced liquid vibration to generate transient domains within a solution wherein enzyme-mediated cascade chemical reactions can be spatiotemporally controlled to obtain predictable and reproducible spatiotemporal chemical gradients and colored patterns. Our approach further provided a way to gain spatiotemporal control over the in situ growth or aggregation of AuNPs in an aqueous solution. Finally, we prepared nanoparticle-patterned hydrogels and showed their utilization for region-specific cell growth. The uniqueness and expandability of our strategy of using audible sound to generate transient domains, which act as pseudo-compartments within a solution, may provide more insights for gaining better control over complex chemical reaction networks at the macroscopic level and in the development of smart materials or systems that can be controlled by such cascade chemical reaction networks.

Methods

Materials and general methods. All the reagents and solvents employed were commercially available and used as supplied without further purification. Cyclic RGDyk peptide was obtained from PEPTRON (Daejeon, Republic of Korea). HeLa and HUVEC were purchased from ATCC. Deionized water with a resistivity of 18.2 MΩ cm^{-1} was used to prepare aqueous solutions. UV–visible absorption spectra were collected on a Cary series UV–Vis–NIR spectrophotometer, Agilent Technologies. TEM images were recorded on an FEI Titan Themis electron microscope operating at 300 kV. A function generator (AFG-2005, GW Instek) and a speaker (PC83-8 or DS135-8, Dayton Audio) were used to generate and control vertical vibrations. Vibrational acceleration was measured by a vibration meter (ST-140, Tenmars). Photos of the experiments were taken by a smartphone or a digital camera. A fluorescence microscope (Eclipse Ti-E, Nikon) was used for the imaging of cells.

Protocol for sound induced transient domains and colored pattern generation experiments. A circular glass Petri dish was mounted on top of a loudspeaker with a flat acrylic tray and the loudspeaker was connected to a function generator to generate vertical sinusoidal vibration. The typical experimental set up is shown in Supplementary Fig. 1. The ranges of frequency and amplitude of vibration were

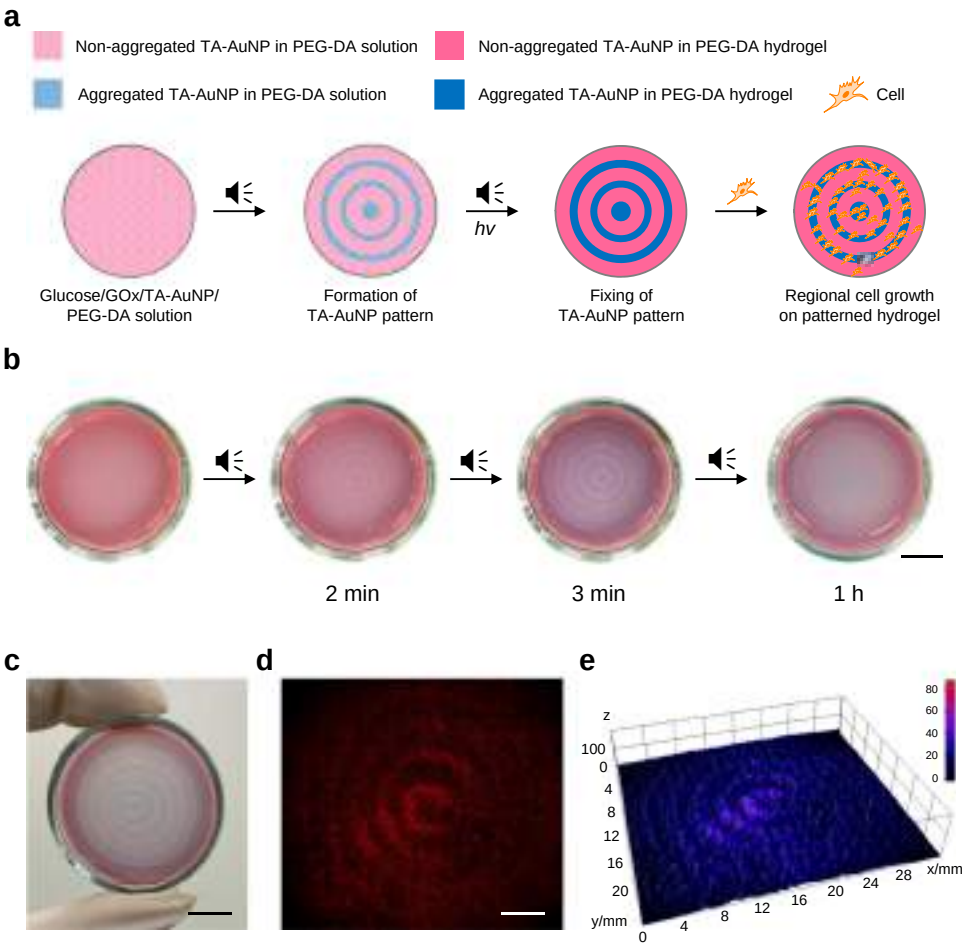

Fig. 5 Preparation of TA-AuNP-patterned hydrogel and its application to region-specific cell growth. a Schematic representation of sound assisted patterned hydrogel formation and selective cell growth. GOx: glucose oxidase, TA-AuNP: thioctic acid-functionalized gold nanoparticle, PEG-DA: poly(ethylene glycol)-diacrylate. **b** Time-dependent images during the formation of a concentric ring pattern obtained by applying 40 Hz of audible sound and preparation of patterned hydrogel (scale bar is 10 mm). **c** A photograph of the patterned hydrogel (scale bar is 10 mm). **d** HeLa cell growth pattern on the hydrogel (scale bar is 5 mm). **e** 3D fluorescence intensity plot of the region-specific cell growth pattern.

controlled by a function generator and the amplitude of vibration was measured with a vibration meter. For the audible sound-induced transient domains and color pattern generation experiments, frequency in the range of 30−90 Hz with an amplitude of the vibration in the range of 0.20−0.25 g were found to be suitable. Unless otherwise noted, a 56 mm-sized (inner diameter) circular glass Petri dish was used for pattern generation experiments. Each pattern generation experiment was repeated more than 10 times to confirm the reproducibility of the pattern formation process.

Glucose/GOx/HRP/ABTS cascade reaction without applying sound. A 5.0 mL solution containing 3.6 U/mL GOx, 2.2 U/mL HRP, 1.0 mM ABTS, and 50 mM glucose in PBS (pH 7.1) was purged with nitrogen gas for 1 h and then gently poured into a Petri dish placed on a tray, and covered with a piece of plastic wrap. After the solution turned colorless, the Petri dish was gently shaken to ensure that the solution was homogenous. After waiting for several seconds for further stabilization, the Petri dish was uncovered and exposed to the air to initiate pattern generation. The pattern generation in the dish was recorded with a smartphone.

Glucose/GOx/HRP/ABTS cascade reaction with applying sound. A 5.0 mL solution containing 3.6 U/mL GOx, 2.2 U/mL HRP, 1.0 mM ABTS, and 50 mM glucose in PBS (pH 7.1) was purged with nitrogen gas for 1 h, and then gently poured into a Petri dish placed on an acrylic tray over the loudspeaker, and covered with a piece of plastic wrap. After the solution turned colorless, the Petri dish was gently shaken to ensure that the solution was homogenous. After waiting several seconds for further stabilization, the Petri dish was uncovered and exposed to the air and the function generator connected to the loudspeaker was turned on to initiate pattern generation. The pattern generation in the dish was recorded with a smartphone. In experiments to study the effect of catalase on color pattern generation, catalase was additionally added to the initial reaction mixture at different concentrations. Pattern experiments were carried out at different concentrations of atmospheric oxygen; a 5 L glass beaker (filled with pure oxygen or argon gas) was used as a reaction chamber for such a purpose (Supplementary Fig. 3). For the pattern generation experiments with different sized or shaped dishes, the solution volume was adjusted in such a way that the height of the solution remain 2 mm, taking into account the size of the dish (Supplementary Figs. 5 and 6).

Glucose/GOx/HRP/dianisidine cascade reaction with applying sound. A 5.0 mL solution containing 7.2 U/mL GOx, 4.5 U/mL HRP, 2.0 mM *o*-dianisidine, and 50 mM glucose in PBS (pH 7.1) was purged with nitrogen gas for 1 h, gently poured into the Petri dish on a tray. After waiting several seconds for stabilization, the function generator was turned on to initiate the color pattern generation. The reaction scheme and colored pattern in the dish were shown in Supplementary Fig. 2.

Colored pattern analyses. The images obtained from the pattern experiments were analyzed using ImageJ software. Firstly, the RGB color pattern images were converted into grayscale representation, then the gray values were collected using the multi-point/point tool. For each image at a particular time, 10 data points were collected from the region of interest. Finally, the mean and standard deviations were calculated and plotted. Since the gray value at $t = 0$ s is considered as a background, the initial gray value was subtracted and a percentage change in gray value was calculated. The error bars in the line profile figures represent the standard deviation of the pattern image intensity.

Effect of applying frequency. To ascertain the effect of frequency on the transient domain formation, experiments were performed by varying the frequency of the applied audible sound. Throughout the frequency range investigated (30−90 Hz), the shape of the domain was found to be similar but the thickness of the concentric ring-shaped domain became narrow with an increase in the frequency of the applied sound as shown in Supplementary Fig. 4.

Preparation of seed AuNPs. Seed gold nanoparticles (AuNPs) were prepared according to the literature[62]. In a typical experiment, a 20 mL aqueous solution containing 0.25 mM $HAuCl_4$ and 0.25 mM trisodium citrate was prepared in a glass sample vial. Next, freshly prepared ice-cold $NaBH_4$ (0.1 M, 0.6 mL) was added under vigorous stirring. Stirring was continued for 30 s and the solution was kept undisturbed for 4 h. The seed AuNP was characterized by UV–Vis spectroscopy and TEM (Supplementary Fig. 10).

Optimizing the conditions for the growth of seed AuNPs. In order to optimize the concentration of various components in the growth of seed AuNPs, UV–Vis experiments were performed with different concentrations of each component. When we varied the concentration of GOx from 35–85 U/mL (keeping the concentration of glucose = 50 mM, $AuCl_4^-$ = 0.60 mM, seed AuNP = 8 nM), there was a blue shift in the surface plasmon peak (530−538 nm), also the generation of red color was faster in case of using a high concentration of GOx (Supplementary Fig. 11a). This indicated that the growth of seed AuNPs could be tuned by changing the GOx concentration. Upon changing the concentration of glucose from 10 to 50 mM (keeping the concentration of GOx = 85 U/mL, $AuCl_4^-$ = 0.60 mM, seed AuNP = 8 nM), the resulting spectra remained the same, suggesting that the changes in glucose concentration in this region had no significant effect on the growth of seed AuNPs (Supplementary Fig. 11b). Then, the concentration of $AuCl_4^-$ was varied 0.2 − 1.0 mM and keeping concentration of glucose = 50 mM, GOx = 50 U/mL, and seed AuNP = 8 nM. As shown in the Supplementary Fig. 11c, the surface plasmon peak value for higher concentration (1 mM) showed a red shift, revealing the formation large sized nanoclusters (surface plasmon peak at 550 nm). Finally, the concentration of seed AuNPs was also varied (2−8 nM) keeping the concentration of glucose = 50 mM, GOx = 50 U/mL, and $AuCl_4^-$ = 0.60 mM, respectively (Supplementary Fig. 11d). Since the high concentration of seed AuNP produced a red color within a few minutes (surface plasmon peak at 533 nm), it was confirmed that it is suitable for sound-induced pattern experiments. At a low concentration of seed AuNPs, the spectra were broad and the surface plasmon peaks appeared at higher wavelengths as shown in Supplementary Fig. 11d. The corresponding average particle sizes were calculated from the TEM images (Supplementary Figs. 11e–h). By combining all the results, we conclude that 50 mM of glucose, 35 U/mL of GOx, 8 nM of seed AuNPs, and 0.60 mM of $AuCl_4^-$ was an appropriate condition for the spatiotemporal in situ growth of AuNPs using our protocol. Time-dependent UV–Vis spectral changes corresponding to the seeded growth of AuNP are presented in Supplementary Fig. 12.

Sound-controlled in situ growth of AuNPs. Before the experiment, the cascade components (glucose/GOx/seed AuNPs/$AuCl_4^-$) were degassed individually with nitrogen gas for 1 h. Then, 5.0 mL solution containing 50 mM of glucose, 35 U/mL of GOx, 8 nM of seed AuNPs, and 0.6 mM of $AuCl_4^-$ were quickly transferred into a Petri dish on top of the loudspeaker. After waiting several seconds for stabilization, the function generator connected to the loudspeaker was turned on. Within a few minutes, the mauve colored solution was segregated into two domains due to sound-induced liquid vibrations, and the red-colored pattern generated in the dish was recorded with a smartphone.

Synthesis and characterization of TA-AuNP. After synthesizing 13 nm-sized gold nanoparticles according to the literature, thioctic acid-functionalized gold nanoparticles (TA-AuNPs) were prepared by ligand exchange method[49,50]. For the ligand exchange of the citrate stabilized AuNPs, an ethanolic solution of thioctic acid (10 mM, 4.0 mL) was added to the citrate stabilized AuNPs solution (40 mL) whose basicity was preadjusted to pH 11, the mixture was then stirred for 18 h in the dark. The solution was then centrifuged for 20 min (at 18,000 × *g*, 10 °C), followed by decantation of supernatants. The precipitated TA-AuNPs were redispersed in water and centrifuged again two times more under the same conditions. The resulting TA-AuNPs were characterized by TEM (Supplementary Fig. 13a), and pH-dependent UV–Vis spectral changes were also observed (Supplementary Fig. 13b). Time-dependent UV–Vis spectral changes with glucose/GOx reaction system are presented in Supplementary Fig. 14.

Sound-controlled TA-AuNP pattern experiments. Prior to the experiments, all the required ingredient solutions were thoroughly degassed with N_2 gas for 1 h. Then, 5.0 mL solution containing 40 U/mL GOx, 8 nM TA-AuNP, 50 mM NaCl, and 50 mM glucose was taken into a Petri dish. Once the solution became steady, the function generator connected to the loudspeaker was turned on. The pattern generation in the dish was recorded with a smartphone.

Preparation of gold nanoparticle-patterned hydrogels. Prior to the experiments, all the required ingredient solutions were thoroughly degassed with N_2 gas for 1 h. Then, 1.5 mL solution containing 80 U/mL GOx, 8 nM TA-AuNP, 75 mM NaCl, 50 mM glucose, 10 wt% PEG-DA (M_n = 700), and 1 wt% Irgacure 2959 was taken into a 36 mm-sized Petri dish. Once the solution became steady, the function generator connected to the loudspeaker was turned on and a frequency of 40 Hz was applied to this solution. The pattern generation in the dish was recorded with a smartphone. The fully developed pattern was fixed by irradiating the solution in the Petri dish with a handheld UV lamp (365 nm) for 1 h.

Preparation of c(RGDyK)-PLL. A cyclic RGDyK peptide and poly-L-lysine conjugate (c(RGDyK)-PLL) was prepared by following the previous work[60,61]. To a solution of poly-L-lysine (PLL) (50 mg) in deionized (DI) water (5 mL), a solution of dibenzocyclooctyne-*N*-hydroxysuccinimidyl ester (100 µL, 0.2 mM in DMSO) was added and the mixture was stirred at room temperature for 1 h. Followed by the addition of cyclo[Arg-Gly-Asp-D-Phe-Lys(Azide)] (c(RGDyK-azide), 100 µL, 0.2 mM in DI water) to the reaction mixture and stirred at room temperature for 12 h. After the reaction mixture was purified by dialysis against water using a membrane with a molecular weight cut-off of 10000, the sample was lyophilized to give c(RGDyK)-PLL (45 mg). The product was dissolved in DI water (1 mg/mL) and used in the following experiments.

Cell culture experiments with a patterned hydrogel. The patterned hydrogel was thoroughly washed with PBS buffer to remove any unreacted residues. Subsequently, the hydrogel was coated with the solution of c(RGDyK)-PLL for 1 h. A solution of live cells (4 mL, 2×10^6 cells, HeLa in DMEM), which was stained with DiIC18(3), was transferred to the hydrogel. In the case of HUVECs, a solution of live cells (4 mL, 2×10^6 cells, HUVEC in F-12K), which was stained with SP-DiOC18(3). The cells were incubated at 37 °C in a humidified incubator under standard culture conditions for 1 to 3 days. The cells were imaged under a fluorescence microscope and the images were manually arranged to make an overview image of the hydrogel.

Reporting summary. Further information on research design is available in the Nature Research Reporting Summary linked to this article.

Data availability

The authors declare that all the data supporting the findings of this study are available within the paper and its Supplementary Information file or from the corresponding authors upon request.

Received: 1 April 2021; Accepted: 7 April 2022;
[illegible]

References

1. Chen, A. H. & Silver, P. A. Designing biological compartmentalization. *Trends Cell Biol.* **22**, 662–670 (2012).
2. Trantidou, T. et al. Engineering compartmentalized biomimetic micro- and nanocontainers. *ACS Nano* **11**, 6549–6565 (2017).
3. Zhao, Y. G. & Zhang, H. Phase separation in membrane biology: the interplay between membrane-bound organelles and membraneless condensates. *Dev. Cell* **55**, 30–44 (2020).
4. Szostak, J. W., Bartel, D. P. & Luisi, P. L. Synthesizing life. *Nature* **409**, 387–390 (2001).
5. Dzieciola, A. J. & Mann, S. Designs for life: protocell models in the laboratory. *Chem. Soc. Rev.* **41**, 79–85 (2012).
6. Buddingh, B. C. & van Hest, J. C. M. Artificial cells: synthetic compartments with life-like functionality and adaptivity. *Acc. Chem. Res.* **50**, 769–777 (2017).
7. Shin, Y. & Brangwynne, C. P. Liquid phase condensation in cell physiology and disease. *Science* **357**, eaaf4382 (2017).
8. Marguet, M., Bonduelle, C. & Lecommandoux, S. Multicompartmentalized polymeric systems: towards biomimetic cellular structure and function. *Chem. Soc. Rev.* **42**, 512–529 (2013).
9. Küchler, A., Yoshimoto, M., Luginbühl, S., Mavelli, F. & Walde, P. Enzymatic reactions in confined environments. *Nat. Nanotechnol.* **11**, 409–420 (2016).
10. Rideau, E., Dimova, R., Schwille, P., Wurm, F. R. & Landfester, K. Liposomes and polymersomes: a comparative review towards cell mimicking. *Chem. Soc. Rev.* **47**, 8572–8610 (2018).
11. Vázquez-González, M., Wang, C. & Willner, I. Biocatalytic cascades operating on macromolecular scaffolds and in confined environments. *Nat. Catal.* **3**, 256–273 (2020).
12. Che, H. & van Hest, J. C. M. Adaptive polymersome nanoreactors. *ChemNanoMat* **5**, 1092–1109 (2019).
13. Vriezema, D. M. et al. Positional assembly of enzymes in polymersome nanoreactors for cascade reactions. *Angew. Chem. Int. Ed.* **46**, 7378–7382 (2007).
14. Peters, R. J. R. W. et al. Cascade Reactions in Multicompartmentalized Polymersomes. *Angew. Chem. Int. Ed.* **53**, 146–150 (2014).
15. van Oppen, L. M. P. E. et al. Biodegradable synthetic organelles demonstrate ros shielding in human-complex-I-deficient fibroblasts. *ACS Cent. Sci.* **4**, 917–928 (2018).
16. Dewey, D. C., Strulson, C. A., Cacace, D. N., Bevilacqua, P. C. & Keating, C. D. Bioreactor droplets from liposome-stabilized all-aqueous emulsions. *Nat. Commun.* **5**, 4670 (2014).

17. Liu, X., Formanek, P., Voit, B. & Appelhans, D. Functional cellular mimics for the spatiotemporal control of multiple enzymatic cascade reactions. *Angew. Chem. Int. Ed.* **56**, 16233–16238 (2017).
18. Chen, Z. et al. Synthetic beta cells for fusion-mediated dynamic insulin secretion. *Nat. Chem. Bio.* **14**, 86–93 (2018).
19. Koga, S., Williams, D. S., Perriman, A. W. & Mann, S. Peptide-nucleotide microdroplets as a step towards a membrane-free protocell model. *Nat. Chem.* **3**, 720–724 (2011).
20. Qiao, Y., Li, M., Booth, R. & Mann, S. Predatory behaviour in synthetic protocell communities. *Nat. Chem.* **9**, 110–119 (2017).
21. Martin, N. et al. Antagonistic chemical coupling in self-reconfigurable host-guest protocells. *Nat. Commun.* **9**, 3652 (2018).
22. Kojima, T. & Takayama, S. Membraneless compartmentalization facilitates enzymatic cascade reactions and reduces substrate inhibition. *ACS Appl. Mater. Interfaces* **10**, 32782–32791 (2018).
23. Chen, Y. et al. Construction of coacervate-in-coacervate multicompartment protocells for spatial organization of enzymatic reactions. *Chem. Sci.* **11**, 8617–8625 (2020).
24. Yang, H., Fu, L., Wei, L., Liang, J. & Binks, B. P. Compartmentalization of incompatible reagents within Pickering emulsion droplets for one-pot cascade reactions. *J. Am. Chem. Soc.* **137**, 1362–1371 (2015).
25. Cybulski, O. et al. Concentric liquid reactors for chemical synthesis and separation. *Nature* **586**, 57–63 (2020).
26. Chen, R., Neri, S. & Prins, L. J. Enhanced catalytic activity under non-equilibrium conditions. *Nat. Nanotechnol.* **15**, 868–874 (2020).
27. Marzo, A. & Drinkwater, B. W. Holographic acoustic tweezers. *Proc. Natl Acad. Sci. USA* **116**, 84–89 (2019).
28. Wiklund, M., Green, R. & Ohlin, M. Acoustofluidics 14: applications of acoustic streaming in microfluidic devices. *Lab Chip* **12**, 2438–2451 (2012).
29. Martorell, A. J. et al. Multi-sensory gamma stimulation ameliorates Alzheimer's-associated pathology and improves. *Cell* **177**, 256–271 (2019).
30. Suslick, K. S. Sonochemistry. *Science* **247**, 1439–1445 (1990).
31. Mason, T. J. Ultrasound in synthetic organic chemistry. *Chem. Soc. Rev.* **26**, 443–451 (1997).
32. Bang, J. H. & Suslick, K. S. Applications of ultrasound to the synthesis of nanostructured materials. *Adv. Mater.* **22**, 1039–1059 (2010).
33. Tsuda, A. et al. Spectroscopic visualization of sound-induced liquid vibrations using a supramolecular nanofiber. *Nat. Chem.* **2**, 977–983 (2010).
34. Douady, S. Experimental study of the Faraday instability. *J. Fluid Mech.* **221**, 383–409 (1990).
35. Périnet, N., Juric, D. & Tuckerman, L. S. Numerical simulation of Faraday waves. *J. Fluid Mech.* **635**, 1–26 (2009).
36. Wright, P. H. & Saylor, J. R. Patterning of particulate films using Faraday waves. *Rev. Sci. Instrum.* **74**, 4063–4070 (2013).
37. Chen, P. et al. Microscale assembly directed by liquid-based template. *Adv. Mater.* **26**, 5936–5941 (2014).
38. Guex, A. G., Di Marzio, N., Eglin, D., Alini, M. & Serra, T. The waves that make the pattern: a review on acoustic manipulation in biomedical research. *Mater. Today Bio.* **10**, 100110 (2021).
39. Hwang, I. et al. Audible sound-controlled spatiotemporal patterns in out-of-equilibrium systems. *Nat. Chem.* **12**, 808–813 (2020).
40. Périnet, N., Gutiérrez, P., Urra, H., Mujica, N. & Gordillo, L. Streaming patterns in Faraday waves. *J. Fluid Mech.* **819**, 285–310 (2017).
41. Zhang, Y., Tsitkov, S. & Hess, H. Complex dynamics in a two-enzyme reaction network with substrate competition. *Nat. Catal.* **1**, 276–281 (2018).
42. Bazilevskii, A. V., Kalinichenko, V. A. & Rozhkov, A. N. Effect of fluid viscosity on the Faraday surface waves. *Fluid Dyn.* **53**, 750–761 (2018).
43. Hong, S.-H. et al. Surface waves control bacterial attachment and formation of biofilms in thin layers. *Sci. Adv.* **6**, eaaz9386 (2020).
44. Zhang, Y., Tsitkov, S. & Hess, H. Proximity does not contribute to activity enhancement in the glucose oxidase-horseradish peroxidase cascade. *Nat. Commun.* **7**, 13982 (2016).
45. Willner, I., Baron, R. & Willner, B. Growing metal nanoparticles by enzymes. *Adv. Mater.* **18**, 1109–1120 (2006).
46. Chen, M., Zeng, G., Xu, P., Lai, C. & Tang, L. How do enzymes 'meet' nanoparticles and nanomaterials? *Trends Biochem. Sci.* **42**, 914–930 (2017).
47. Liu, D. et al. Glucose oxidase-catalyzed growth of gold nanoparticles enables quantitative detection of attomolar cancer biomarkers. *Anal. Chem.* **86**, 5800–5806 (2014).
48. Link, S. & El-Sayed, M. A. Spectral properties and relaxation dynamics of surface plasmon electronic oscillations in gold and silver nanodots and nanorods. *J. Phys. Chem. B* **103**, 8410–8426 (1999).
49. Boles, M. A., Engel, M. & Talapin, D. V. Self-assembly of colloidal nanocrystals: from intricate structures to functional materials. *Chem. Rev.* **116**, 11220–11289 (2016).
50. Nie, Z., Petukhova, A. & Kumacheva, E. Properties and emerging applications of self-assembled structures made from inorganic nanoparticles. *Nat. Nanotechnol.* **5**, 15–25 (2019).
51. Grzelczak, M., Liz-Marzán, L. M. & Klajn, R. Stimuli-responsive self-assembly of nanoparticles. *Chem. Soc. Rev.* **48**, 1342–1361 (2019).
52. Huang, C., Chen, X., Xue, Z. & Wang, T. Effect of structure: A new insight into nanoparticle assemblies from inanimate to animate. *Sci. Adv.* **6**, eaba1321 (2020).
53. Hill, H. D. & Mirkin, C. A. The bio-barcode assay for the detection of protein and nucleic acid targets using DTT-induced ligand exchange. *Nat. Protoc.* **1**, 324–336 (2006).
54. Lin, S.-Y., Tsai, Y.-T., Chen, C.-C., Lin, C.-M. & Chen, C.-H. Two-step functionalization of neutral and positively charged thiols onto citrate-stabilized Au nanoparticles. *J. Phys. Chem. B* **108**, 2134–2139 (2004).
55. Li, W., Yan, Z., Ren, J. & Qu, X. Manipulating cell fate: dynamic control of cell behaviors on functional platforms. *Chem. Soc. Rev.* **47**, 8639–8684 (2018).
56. Ye, K. et al. Advanced Cell and Tissue Biomanufacturing. *ACS Biomater. Sci. Eng.* **4**, 2292–2307 (2018).
57. Chen, L., Yan, C. & Zijian, Z. Functional polymer surfaces for controlling cell behaviors. *Mater. Today* **21**, 38–59 (2018).
58. Béduer, A. et al. Elucidation of the role of carbon nanotube patterns on the development of cultured neuronal cells. *Langmuir* **28**, 17363–17371 (2012).
59. Cui, W. et al. Effects of aggregation and the surface properties of gold nanoparticles on cytotoxicity and cell growth. *Nanomed.: NBM* **8**, 46–53 (2012).
60. Ardjomandi, N. et al. Indirect coating of RGD peptides using a poly-L-lysine spacer enhances jaw periosteal cell adhesion, proliferation, and differentiation into osteogenic tissue. *J. Biomed. Mater. Res.* **8**, 2034–2044 (2012).
61. Kim, S. W., Hur, M. Y., Kim, J., Park, K. M. & Kim, K. Strong host-guest interaction enables facile and controllable surface modification of cucurbit[6] uril-based polymer nanocapsules for in vivo cancer targeting. *Supramol. Chem.* **31**, 289–295 (2019).
62. Jana, N. R., Gearheart, L. & Murphy, C. J. Seeding growth for size control of 5-40 nm diameter gold nanoparticles. *Langmuir* **17**, 6782–6786 (2001).

Acknowledgements

This work was supported by the Institute for Basic Science (IBS) [IBS-R007-D1].

Author contributions

I.H., R.D.M., and K.K. conceived the idea. P.D. performed most of the experiments under supervision of I.H. Y.L. and T.G. supported TEM and nanoparticle experiments, respectively. T.G. prepared hydrogels and H.-G.L. and K.M.P. performed cell experiments, respectively. S.S. and I.S.K. contributed to understanding the audible sound-induced fluid dynamics and pattern formation mechanism. P.D., T.G., I.H., R.D.M., and K.K. wrote the manuscript and all authors discussed the results, analyzed the data and commented on the manuscript. K.K. supervised the overall research.

Competing interests

The authors declare no competing interests.

Additional information

Supplementary information The online version contains supplementary material available at https://doi.org/10.1038/s41467-022-30124-x.

Correspondence and requests for materials should be addressed to Ilha Hwang ,Rahul Dev Mukhopadhyay or Kimoon Kim.

Peer review information *Nature Communications* thanks Henry Hess and the other anonymous reviewers for their contribution to the peer review of this work.

JOURNAL OF CHEMICAL EDUCATION

pubs.acs.org/jchemeduc

Communication

Audible Sound Controlled Blue Bottle Experiment

Ilbong Lee, Ilha Hwang,* Rahul Dev Mukhopadhyay, and Kimoon Kim*

Cite This: https://doi.org/10.1021/acs.jchemed.1c01146

Read Online

ACCESS | Metrics & More | Article Recommendations | Supporting Information

ABSTRACT: The formation of chemical patterns is in general difficult to control due to the random diffusive motions of the reacting chemical species in solution. In this paper, we present a new method using audible sound to control the formation of chemical patterns obtained in blue bottle experiments. The waves generated on the surface of the solution by applying audible sound result in the nonuniform dissolution of atmospheric gases such as oxygen at the nodal and antinodal positions. On the basis of this phenomenon, the shapes of the patterns could be tuned according to the characteristics of the applied sound input, such as frequency and amplitude. This is an easy way for students to follow and control redox-responsive and pH-responsive chemical reactions in solution. The experiments involve chemicals that are mostly nontoxic and are easy to demonstrate since they involve common electronic gadgets (e.g., smartphones, Bluetooth speakers, etc.). These experiments provide interesting demonstration activities as well as a new understanding of utilizing audible sound for controlling chemical reactions.

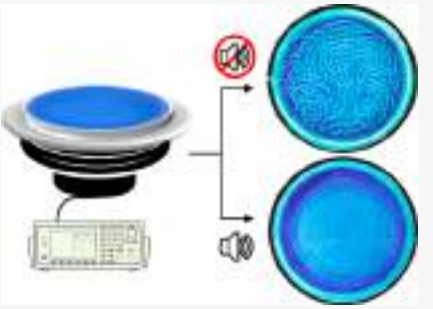

KEYWORDS: *Graduate Education/Research, Upper-Division Undergraduate, Demonstrations, Interdisciplinary/Multidisciplinary, Mechanisms of Reactions, Acids/Bases, Dyes/Pigments, Oxidation/Reduction*

INTRODUCTION

Since Alan Turing first proposed the theory of chemical pattern generation using a reaction-diffusion model in 1952,[1] many studies have been conducted to study the generation of spatiotemporal patterns through chemical reactions.[2−13] Representative examples include the patterns formed during the Belousov−Zhabotinsky reaction[5,6] and the "blue bottle" reaction[7−9] reported in the 1960s. In particular, the latter has been frequently used for the demonstration of colored chemical pattern generation because it is nontoxic and easy for students to follow. Later, on the basis of the blue bottle experiment, various other colored chemical pattern generation systems have also been developed using different dyes and reducing agents.[10−12] However, since it is difficult to control the diffusive behavior of chemical species in these reactions, the nature of the generated chemical patterns is rather inconsistent and unpredictable.

Sound is a series of pressure waves propagating through the medium, and it is not well-utilized in chemistry except for sonochemistry where high-power ultrasound is used.[14,15] In particular, audible sound (typically 20−20,000 Hz) has very low energy, which is insufficient to induce chemical reactions. However, it is known that audible sound can affect the surface waves and internal flow in a fluid, which is similar to a physical phenomenon known as Faraday waves. The Faraday waves were first reported by Michael Faraday in 1831, where the waves occur at the air−liquid interface when a low-frequency vertical vibration is applied to a liquid placed in a dish.[16−18] The same phenomenon can be executed when the dish is placed over a loudspeaker generating audible sound. Here, the waves generated in the liquid are determined according to the frequency and amplitude of the sound, the shape of the dish, etc. On the basis of the above methods, various applications have been reported in the literature. This includes self-assembly of floating beads on the liquid surface and precipitation patterns of bacteria, cells, microscale beads, etc.[19−22] In addition, we have recently demonstrated a novel method of generating chemically different domains in a solution using audible sound.[23] The waves generated on the surface of the solution by applying audible sound resulted in the nonuniform dissolution of atmospheric gases such as oxygen at the antinodal and nodal positions, because the former come into frequent contact with air, while the latter did not (Scheme 1a). On the basis of this phenomenon, we have shown that redox reactions can be performed with region specific control in a solution, and the progress of the reaction can be visualized through the formation of a colored spatiotemporal pattern. The same principle was applied to the region specific dissolution of carbon dioxide and the achievement of spatiotemporal control over an acid−base reaction. Interestingly, the patterns generated through this method could be programmed on the basis of the frequency of the applied sound.

Received: November 11, 2021
Revised: January 14, 2022

Scheme 1. (a) Schematic Cross Sectional View of Region Specific Dissolution of Gases into a Vertically Vibrating Solution,[a] (b) Schematic of the Experimental Setup for Audible Sound Controlled Blue Bottle Pattern Generation Experiment,[b] (c) Redox Equilibrium in Methylene Blue Based Pattern Experiment,[c] and (d) Acid−Base Equilibrium in Phenolphthalein Based Pattern Experiment[d]

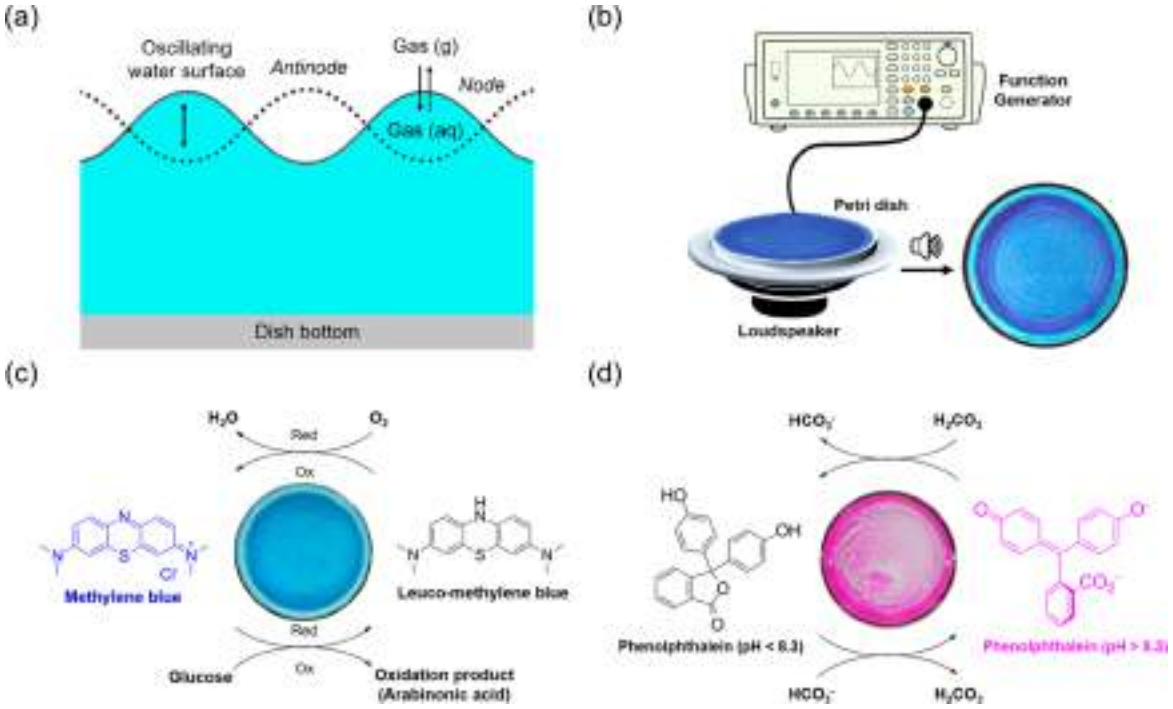

[a]More gases are dissolved at the antinode regions under the standing wave conditions. [b]A representative pattern figure that can be obtained in the presence of audible sound is also presented. [c]A typical pattern image obtained using methylene blue reaction in the absence of audible sound is also presented in the center. [d]A typical pattern image obtained using phenolphthalein reaction in the absence of audible sound is also presented in the center.

Herein, we extend our audible sound strategy to the traditional blue bottle reaction, which is known to generate spatiotemporal patterns. In addition, we show the generation of phenolphthalein based patterns using carbon dioxide and sound. Lastly, in order to increase the ease of demonstration of our strategy, we also verified that the same experiment is possible with a freely available smartphone based function generator application and a Bluetooth speaker.

MATERIALS AND METHODS

Chemicals

Methylene blue, resazurin sodium salt, D-glucose, sodium hydroxide, phenolphthalein, and dimethyl sulfoxide (DMSO) were purchased from commercial vendors and used as purchased.

Preparing Stock Solutions

Sodium hydroxide stock solution (5 M), glucose stock solution (1 M), and methylene blue stock solution (1 mg/mL) were prepared by dissolving the corresponding amounts of solutes in deionized water. Phenolphthalein stock solution (2 mg/mL) was prepared in DMSO.

Pattern Experiment with Methylene Blue

Solutions for the pattern experiment using methylene blue were prepared by mixing 3.85 mL of deionized water, 0.25 mL of methylene blue stock solution, 0.55 mL of glucose stock solution, 0.25 mL of DMSO, and 0.10 mL of sodium hydroxide stock solution in a 20 mL vial, in the listed order. The final molar concentrations of each species in the solution were as follows: 0.15 mM methylene blue, 110 mM glucose, 100 mM sodium hydroxide. The mixture was gently shaken, and the vial was kept undisturbed for 5 min with the lid closed. Then, 5 mL of the mixture was poured into a 56 mm sized (inner diameter) glass Petri dish placed on a loudspeaker and gently shaken again until it did not show any haze (see Scheme 1b and Supporting Information Figure S1a for experimental setup). Pattern generation was started as soon as we turned on the function generator connected to the loudspeaker, and the pattern images were recorded on a smartphone.

Pattern Experiment with Phenolphthalein under Carbon Dioxide Atmosphere

Solutions for the phenolphthalein experiment were prepared by mixing 4.15 mL of deionized water, 0.60 mL of sodium hydroxide (pH 12) solution, and 0.25 mL of phenolphthalein stock solution in a 20 mL vial, in the listed order. The final molar concentrations of each species in the solution were as follows: 0.32 mM phenolphthalein, 1.2 mM sodium hydroxide. The mixture was gently shaken and poured to a 56 mm sized glass Petri dish. The dish was then covered with a carbon dioxide filled glass beaker (see Supporting Information Figure S1b for experimental setup). Pattern generation was started as soon as we turned on the function generator connected to the loudspeaker, and the pattern images were recorded on a smartphone.

https://doi.org/10.1021/acs.jchemed.1c01146
J. Chem. Educ. XXXX, XXX, XXX−XXX

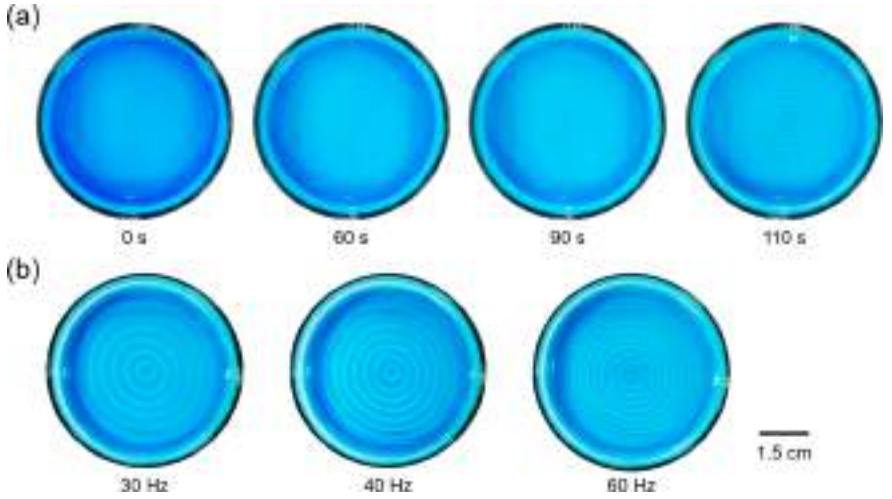

Figure 1. (a) Photographs showing pattern generation over time in a methylene blue based pattern experiment with 60 Hz sound. See Figure S2 for larger and detailed images. (b) Changes in patterns obtained at different audible sound frequencies (30−60 Hz).

HAZARDS

Sodium hydroxide is a highly corrosive chemical, so participants should remain cautious while handling sodium hydroxide. DMSO is classified as a class 3 solvent (low toxic potential) by the United States Food and Drug Administration. However, DMSO penetrates well into the skin and causes irritation. Therefore, the participants should wear proper protective equipment such as gloves, lab coats, and safety goggles during the experiment. The experiment can be carried out outside a fume hood because of the low vapor pressure of DMSO.

RESULTS AND DISCUSSION

Pattern Experiment with Methylene Blue

Among the various pattern generation experiments, the methylene blue based blue bottle experiment was selected as the main experiment in consideration of its wide representativeness, accessibility, and safety. The chemical reaction related to the blue bottle experiment is shown in Scheme 1c. In a typical blue bottle experiment, we usually observe the process of color change of a blue methylene blue solution to its colorless leuco form in an oxygen-deficient environment, such as inside the closed bottle. However, in this paper, we tried to observe the process of changing the blue colored pattern using a Petri dish in an open space. The schematic of the experimental setup for the audible sound controlled blue bottle reaction and corresponding pattern generation is shown in Scheme 1b.

We checked the nature of the patterns generated in the Petri dish depending on the presence or absence of audible sound. The pattern obtained in the absence of audible sound is given in Scheme 1c. The pattern generated without sound showed a "worm-like" shape, which is probably caused by the density-driven chemical convections of glucose and its oxidation products, but the exact mechanism is not yet known.[9,24] Here, the oxidation product was initially identified as gluconic acid, but recent studies have indicated the formation of arabinonic acid as a major oxidation product.[12,25,26] In contrast, in the presence of 60 Hz audible sound, a spatiotemporal pattern consisting of well-defined concentric rings was observed as shown in Figure 1a. The pattern formation started with the appearance of a blue dot at the center of a Petri dish after ∼60 s; this was followed by the development of the concentric rings from the center to the side wall of the Petri dish (see also Supporting Information Video S1). The pattern was most vivid at ∼110 s and lasted until ∼3 min. After this time, the rings gradually broadened, and the distinction between the rings became ambiguous; the overall color of the solution became brighter.

The concentric ring pattern is generated due to the standing wave on the surface of the solution present in the Petri dish generated by audible sound. As the antinodal regions vibrate up and down more than adjacent surface areas, there exists more chance for the solution in these regions to come in contact with the atmosphere. This process results in a greater absorption of oxygen at the antinodal regions. On the other hand, the nodal regions remain relatively static and absorb less oxygen. The regions with higher oxygen concentration remain blue as leuco-methylene blue readily reacts with oxygen and produces methylene blue, whereas the regions with lower oxygen concentration turn colorless. Therefore, the resulting colored ring pattern in a Petri dish is a visualization of the concentration gradient of methylene blue and leuco-methylene blue in a Petri dish. The nature of the formed spatiotemporal pattern depends on the size of the Petri dish. As the size of the dish increases, the number of concentric rings increases while maintaining the spacing between them (see Figure S3).

Since we use audible sound as an external stimulus, we also studied the changes in pattern formation by varying the frequency of the audible sound input. As shown in Figure 1b, it was confirmed that the distance between the ring patterns narrowed when the frequency was increased. As a representative example, here we present the results of three frequencies from 30 to 60 Hz, but this method of obtaining reproducible spatiotemporal patterns worked well when the audible sound frequency was varied between 25 and 100 Hz. At frequencies lower than 25 Hz, it was difficult to obtain a stable sound using ordinary loudspeakers, and frequencies higher than 100 Hz caused surface waves and patterns that were too narrow to recognize with the naked eye. Sound intensity is also an important factor for stable and reproducible pattern formation. A method for determining the appropriate sound intensity is described in the Supporting Information (see Figure S4).

https://doi.org/10.1021/acs.jchemed.1c01146
J. Chem. Educ. XXXX, XXX, XXX−XXX

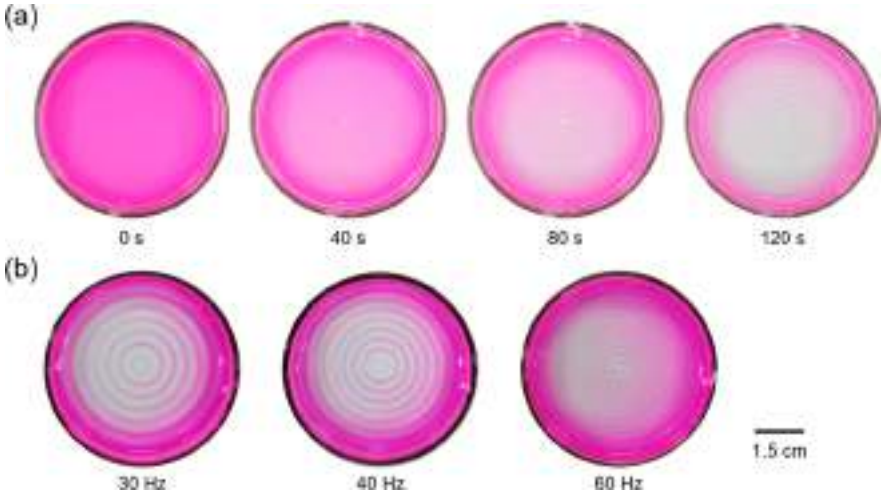

Figure 2. (a) Photographs showing pattern generation over time in a phenolphthalein based pattern experiment with 60 Hz sound. See Figure S6 for larger and detailed images. (b) Changes in patterns obtained at different audible sound frequencies (30−60 Hz).

The audible sound controlled pattern generation method can also be applied to other types of blue bottle experiments, such as in the case of resazurin based pattern experiments. As shown in Figure S5, it was confirmed that the resazurin also forms sound dependent patterns as in the case of methylene blue. A detailed explanation of the pattern generation experiments with resazurin is described in the Supporting Information.

Pattern Experiment with Phenolphthalein under Carbon Dioxide Atmosphere

As mentioned in the pattern experiments above, the application of audible sound causes regional dissolution of oxygen into the solution in a Petri dish. The same principle applies to a carbon dioxide rich environment, and we have already demonstrated the formation of pH gradients in a solution induced by the audible sound assisted CO_2 dissolution in our previous report. Herein, we propose another variation of pattern generation experiment using a phenolphthalein solution and a carbon dioxide filled chamber. Phenolphthalein is an indicator that remains colorless in acidic and neutral environments (pH < 8.3) and turns to pink in basic solution (Scheme 1d). Therefore, the solution for the pattern generation experiment was designed to have an initial pH around 11, so that carbon dioxide absorption and carbonic acid generation could be expressed as a color change (pink to colorless).[27] The carbon dioxide rich atmosphere was prepared with a 5 L glass beaker and a high-pressure carbon dioxide tank or dry ice (see Supporting Information Figure S1b for experimental setup).

First, we tested the pattern generation using a phenolphthalein solution and a carbon dioxide chamber. As shown in Scheme 1d, we obtained a worm-like pattern as in other cases shown above. Instead of the density-driven convection in the case of the blue bottle reaction, the heat generated during the inhomogeneous exothermic reaction between carbonic acid and phenolphthalein in solution is presumed to be the plausible reason for random pattern generation. After confirming that the pattern can also be generated by this method, the effect of audible sound on the phenolphthalein pattern was also investigated. In the presence of audible sound, a pink concentric ring pattern was obtained using a carbon dioxide rich atmosphere and a phenolphthalein solution (Figure 2). This time, the pattern was developed in a way that the antinodal regions lost their pink color due to the dissolution of carbon dioxide, which led to a decrease in solution pH, and phenolphthalein's colorless form became dominant. Figure 2a shows the time-dependent development of a pattern obtained by applying 60 Hz sound. Antinodal regions turned colorless starting from the center to the side wall, and the ring pattern was fully developed at around 80 s. As time passed, the remaining pink nodes also turned colorless from the center, and eventually, the pattern disappeared after 200 s (see Figure S6). As in the case of the oxygen experiments, the higher frequency of sound led to narrower concentric lines present in the patterns obtained in the carbon dioxide experiments (see Figure 2b).

Pattern Experiments with an Easily Accessible Experimental Setup

Since we also aimed this experiment to be versatile and accessible in various lab conditions, we considered substituting a readily available counterpart for a less accessible component such as a function generator. In this regard, we confirmed the possibility of utilizing a smartphone application instead of a typical function generator. A function generator and a wired speaker were substituted with a free smartphone application and a Bluetooth speaker as given in Figure 3a (see Supporting Information for details). Even though the commercial Bluetooth speakers exhibited a limitation in generating consistent sound in the low-frequency regions, it was possible to obtain a decent ring pattern using the substituted setup as shown in Figure 3b.

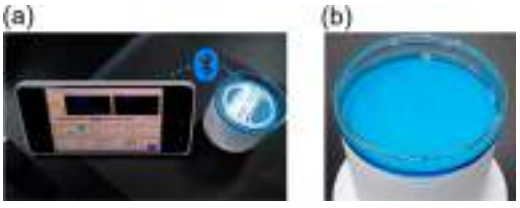

Figure 3. (a) Photograph taken during the pattern experiment with an alternative setup. (b) A photograph of a methylene blue concentric ring pattern generated at 40 Hz on a Bluetooth speaker.

https://doi.org/10.1021/acs.jchemed.1c01146
J. Chem. Educ. XXXX, XXX, XXX−XXX

CONCLUSION

We have demonstrated a novel method to generate well-defined color patterns using audible sound induced liquid vibrations. The waves generated on the surface of the solution by audible sound cause the inhomogeneous dissolution of atmospheric gases in the solution. For example, antinodes come into frequent contact with air, while nodes do not. Using this phenomenon, we successfully demonstrated various pattern generation experiments using reactions sensitive to oxygen or carbon dioxide. The shapes of the resulting patterns were determined by the frequency of the applied sound. This study will provide better control of the blue bottle reaction and open new perspectives on the spatiotemporal regulation of redox- and pH-sensitive chemical reactions using audible sound. Finally, using audible sound for regional regulation of chemical reactions could make students interested in physics and fluid dynamics as well as in chemistry.

ASSOCIATED CONTENT

Supporting Information

The Supporting Information is available at https://pubs.acs.org/doi/10.1021/acs.jchemed.1c01146.

Detailed descriptions on the audible sound controlled pattern generation experiments, supplementary figures for the experiment, a student worksheet, and an instructor manual including the model answers for the student worksheet and expected questions from students (PDF)

Video clip showing the pattern experiment with methylene blue under 60 Hz sound (MP4)

AUTHOR INFORMATION

Corresponding Authors

Ilha Hwang − *Center for Self-Assembly and Complexity, Institute for Basic Science, Pohang 37673, Republic of Korea;* orcid.org/0000-0002-0627-6011; Email: ihwang1@ibs.re.kr

Kimoon Kim − *Department of Chemistry, Pohang University of Science and Technology, Pohang 37673, Republic of Korea; Center for Self-Assembly and Complexity, Institute for Basic Science, Pohang 37673, Republic of Korea;* orcid.org/0000-0001-9418-3909; Email: kkim@postech.ac.kr

Authors

Ilbong Lee − *Department of Chemistry, Pohang University of Science and Technology, Pohang 37673, Republic of Korea*

Rahul Dev Mukhopadhyay − *Department of Chemistry, Ramananda College, Bankura University, Bishnupur 722122 West Bengal, India*

Complete contact information is available at: https://pubs.acs.org/10.1021/acs.jchemed.1c01146

Notes

The authors declare no competing financial interest.

ACKNOWLEDGMENTS

This work was supported by the Institute for Basic Science (IBS) [IBS-R007-D1].

REFERENCES

(1) Turing, A. M. The Chemical Basis of Morphogenesis. *Philos. Trans. R. Soc. London B* **1952**, *237*, 37−72.

(2) Johnson, B. R.; Scott, S. K. New Approaches to Chemical Patterns. *Chem. Soc. Rev.* **1996**, *25*, 265−273.

(3) Sagués, F.; Epstein, I. R. Nonlinear Chemical Dynamics. *Dalton Trans.* **2003**, 1201−1217.

(4) Horváth, J.; Szalai, I.; De Kepper, P. An Experimental Design Method Leading to Chemical Turing Patterns. *Science* **2009**, *324*, 772−775.

(5) Winfree, A. T. The Prehistory of the Belousov-Zhabotinsky Oscillator. *J. Chem. Educ.* **1984**, *61*, 661−663.

(6) Field, R. J.; Kóros, E.; Noyes, R. M. Oscillations in Chemical Systems. I. Detailed Mechanism in a System Showing Temporal Oscillations. *J. Am. Chem. Soc.* **1972**, *94*, 1394−1395.

(7) Dutton, F. B. Methylene Blue - Reduction and Oxidation. *J. Chem. Educ.* **1960**, *37*, A799.

(8) Campbell, J. Kinetics-Early and Often. *J. Chem. Educ.* **1963**, *40*, 578−583.

(9) Limpanuparb, T.; Areekul, C.; Montriwat, P.; Rajchakit, U. Blue Bottle Experiment: Learning Chemistry without Knowing the Chemicals. *J. Chem. Educ.* **2017**, *94*, 730−737.

(10) Staiger, F. A.; Peterson, J. P.; Campbell, D. J. Variations on the "Blue-Bottle" Demonstration Using Food Items That Contain FD&C Blue #1. *J. Chem. Educ.* **2015**, *92*, 1684−1686.

(11) Rajchakit, U.; Limpanuparb, T. Greening the Traffic Light: Air Oxidation of Vitamin C Catalyzed Redox Indicators. *J. Chem. Educ.* **2016**, *93*, 1486−1489.

(12) Rajchakit, U.; Limpanuparb, T. Rapid Blue Bottle Experiment: Autoxidation of Benzoin Catalyzed by Redox Indicators. *J. Chem. Educ.* **2016**, *93*, 1490−1494.

(13) Li, Z.; Yuan, L.; Liu, M.; Cheng, Z.; Zheng, J.; Epstein, I. R.; Gao, Q. The Briggs-Rauscher Reaction: A Demonstration of Sequential Spatiotemporal Patterns. *J. Chem. Educ.* **2021**, *98*, 665−668.

(14) Suslick, K. S. Sonochemistry. *Science* **1990**, *247*, 1439−1445.

(15) Cravotto, G.; Cintas, P. Molecular Self-Assembly and Patterning Induced by Sound Waves. The Case of Gelation. *Chem. Soc. Rev.* **2009**, *38*, 2684−2697.

(16) Faraday, M. On a Peculiar Class of Acoustical Figures, and on Certain Forms Assumed by Group of Particles upon Vibrating Elastic Surfaces. *Philos. Trans. R. Soc. London* **1831**, *121*, 299−340.

(17) Douady, S. Experimental Study of the Faraday Instability. *J. Fluid Mech.* **1990**, *221*, 383−409.

(18) Périnet, N.; Gutiérrez, P.; Urra, H.; Mujica, N.; Gordillo, L. Streaming Patterns in Faraday Waves. *J. Fluid Mech.* **2017**, *819*, 285−310.

(19) Wright, P. H.; Saylor, J. R. Patterning of Particulate Films Using Faraday Waves. *Rev. Sci. Instrum.* **2003**, *74*, 4063−4070.

(20) Chen, P.; Luo, Z.; Güven, S.; Tasoglu, S.; Ganesan, A. V.; Weng, A.; Demirci, U. Microscale Assembly Directed by Liquid-Based Template. *Adv. Mater.* **2014**, *26*, 5936−5941.

(21) Hong, S.; Gorce, J.; Punzmann, H.; Francois, N.; Shats, M.; Xia, H. Surface Waves Control Bacterial Attachment and Formation of Biofilms in Thin Layers. *Sci. Adv.* **2020**, *6*, No. eaaz9386.

(22) Guex, A. G.; Di Marzio, N.; Eglin, D.; Alini, M.; Serra, T. The Waves That Make the Pattern: A Review on Acoustic Manipulation in Biomedical Research. *Mater. Today Bio.* **2021**, *10*, 100110.

(23) Hwang, I.; Mukhopadhyay, R. D.; Dhasaiyan, P.; Choi, S.; Kim, S.; Ko, Y. H.; Baek, K.; Kim, K. Audible Sound-Controlled Spatiotemporal Patterns in Out-of-Equilibrium Systems. *Nat. Chem.* **2020**, *12*, 808−813.

(24) Pons, A.; Sagués, F.; Bees, M.; Sørensen, P. G. Pattern Formation in the Methylene-Blue Glucose System. *J. Phys. Chem. B* **2000**, *104*, 2251−2259.

(25) Anderson, L.; Wittkopp, S. M.; Painter, C. J.; Liegel, J. J.; Schreiner, R.; Bell, J. A.; Shakhashiri, B. Z. What Is Happening When the Blue Bottle Bleaches: An Investigation of the Methylene Blue-

Catalyzed Air Oxidation of Glucose. *J. Chem. Educ.* **2012**, *89*, 1425−1431.
(26) Limpanuparb, T.; Roongruangsree, P.; Areekul, C. A DFT investigation of the blue bottle experiment: $E^{\circ}_{\text{half-cell}}$ analysis of autoxidation catalysed by redox indicators. *R. Soc. Open Sci.* **2017**, *4*, 170708.
(27) Sweeder, R. D.; Jeffery, K. A. A Comprehensive General Chemistry Demonstration. *J. Chem. Educ.* **2013**, *90*, 96−98.

https://doi.org/10.1021/acs.jchemed.1c01146
J. Chem. Educ. XXXX, XXX, XXX−XXX

Chem

CellPress

Article

Remotely controllable supramolecular rotor mounted inside a porphyrinic cage

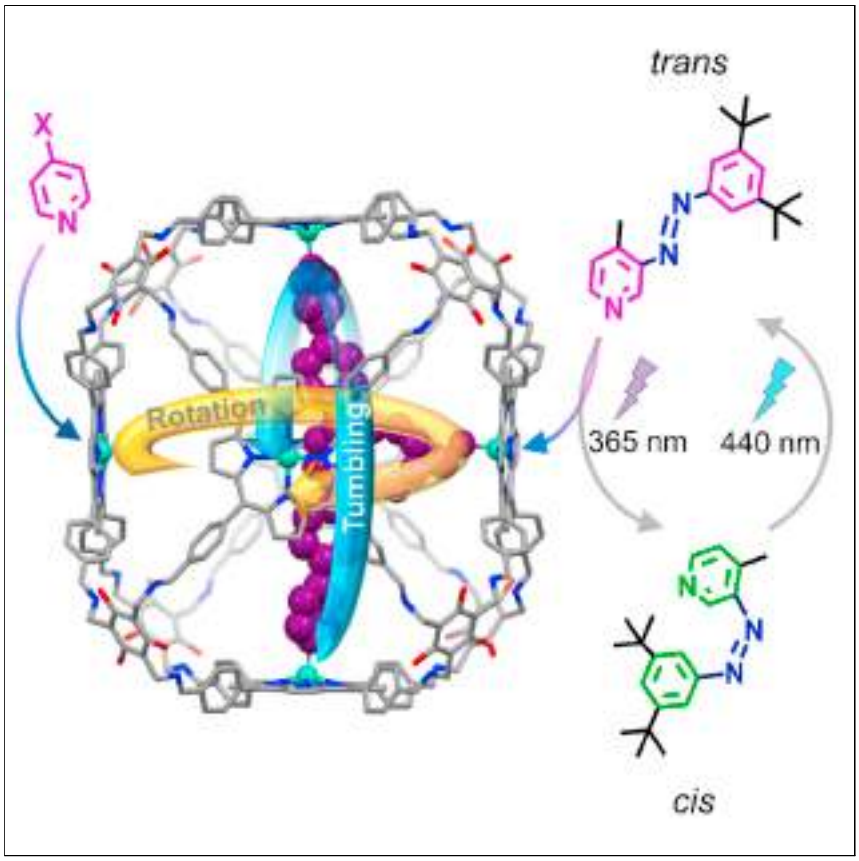

The confinement of molecular machines into nanostructured cages and controlling their functions by external stimuli holds great potential for the creation of smart functional materials that imitate the embodied intelligence of biological machineries. Here, we report the synthesis and confinement of a supramolecular rotor inside a porous Zn–porphyrinic cage. The supramolecular rotor exhibits dual mechanical motions upon the addition of chemical stimuli (pyridine derivatives), and reversible control over the dual motions is achieved by using a photo-dissociable ligand.

Avinash Dhamija, Chandan K. Das, Young Ho Ko, ..., In-Chul Hwang, Lars V. Schäfer, Kimoon Kim

kkim@postech.ac.kr

Highlights

Design and synthesis of a supramolecular rotor within a porous Zn–porphyrinic cage

High-yielding IEDDA reaction enables facile construction of the rotor inside the cage

Initiation of both rotary and tumbling motions of the rotor with chemical stimuli

Reversible control of the dual mechanical motions by a photo-dissociable ligand

Dhamija et al., Chem *8*, 1–14
February 10, 2022
https://doi.org/10.1016/j.chempr.2021.12.008

Please cite this article in press as: Dhamija et al., Remotely controllable supramolecular rotor mounted inside a porphyrinic cage, Chem (2021), https://doi.org/10.1016/j.chempr.2021.12.008

Chem

CellPress

Article

Remotely controllable supramolecular rotor mounted inside a porphyrinic cage

Avinash Dhamija,[1] Chandan K. Das,[3] Young Ho Ko,[1] Younghoon Kim,[1] Rahul Dev Mukhopadhyay,[1,4] Anilkumar Gunnam,[1] Xiujun Yu,[1] In-Chul Hwang,[1] Lars V. Schäfer,[3] and Kimoon Kim[1,2,5,*]

SUMMARY

The confinement of molecular machines into nanostructured cages and controlling their functions by external stimuli holds great potential for the creation of smart functional materials that imitate the embodied intelligence of biological processes. Herein, we report the construction of a supramolecular rotor in a porous Zn-metallated porphyrinic cage (1) by encapsulation of a tetrazine-based linear axle (LA) via metal-ligand coordination bond, followed by post-assembly modification to append a controllable side arm to LA via inverse electron demand Diels-Alder (IEDDA) reaction. While the rotor alone shows nearly no motion, the addition of pyridine derivatives as a zinc coordinating ligand results in both 90° jump-like rotary motion of the rotor and slow tumbling motion of the rotor axle in a stochastic manner. Interestingly, the dual motions of the rotor can be reversibly controlled by the UV and visible light-induced coordination and dissociation of an azopyridine-based ligand with Zn centers as a signal transducer.

INTRODUCTION

"Confinement effect" at various length scales is believed to play an indispensable role in evolution of life,[1,2] stabilization of biomolecules,[3,4] and in controlling the reactivity and functions of chemical systems.[5–7] The physical and chemical properties of a molecule can be astutely altered once confined within a suitable nanoscopic domain.[6,7] Among other complex macromolecular or supramolecular systems, the confinement of biological machineries within specific nanoscopic domains inside the cellular matrix, which provides an environment that is electronically and sterically different from the extracellular matrix, is the very basis for their remarkable precision and programmed mechanical motion of their constituent components and associated functions.[8–10] Most of these biomolecular machines are controlled by various chemical or physical stimuli and transform their energy to perform a specific biological function.[8] One of the most celebrated examples is adenosine triphosphate (ATP) synthase, where the rotatory motion of the enzyme subunits is controlled by chemical processes, such as proton (or Na^+) flux or ATP hydrolysis.[11,12] In some cases, transmembrane proteins remotely control the mechanical motion of biomolecules, such as bacteriorhodopsin or halorhodopsin in light-driven ion pumps.[13–15] Inspired by such natural systems, numerous stimuli-controlled artificial molecular machines have been developed.[16–21] One approach to further explore the potential of artificial molecular machines for practical applications and to gain a better control over their functions is to confine them inside a 3D nanoscopic environment.[22–28] These nanoporous confinements can serve as a stable scaffold to anchor the molecular machines in a specific orientation so that a collective effect of the functioning of individual

The bigger picture

The confinement of biological molecular machines, which are controlled by various chemical or physical stimuli within the cytoskeleton matrix, endows them with remarkable precision and programmable mechanical motions. Biological molecular machines are far more complex than any artificial molecular machine ever built. To mimic the intricate behavior of biological machinery, strategies need to be developed for embedding and confining artificial molecular machines within nanoscopic domains in which their functions can be specifically controlled by external stimuli. One such approach is the confinement of molecular machines inside porous organic cages. The high porosity of the organic cages provides ample room for uninterrupted movement, and its shape-persistent and interactive framework provides a high degree of control over the mechanical motion triggered by external stimuli. Our strategy may lay the foundation for the development of tunable molecular devices using porous organic cages.

Please cite this article in press as: Dhamija et al., Remotely controllable supramolecular rotor mounted inside a porphyrinic cage, Chem (2021), https://doi.org/10.1016/j.chempr.2021.12.008

machines can be harnessed to execute a predetermined function, a long-cherished goal in the area of amphidynamic materials.[29–31] Nevertheless, there always exists a tradeoff between controlling the orientation of the machines through rigid confinement and maintaining the required flexibility to carry out the specific motion as efficiently as in the solution state. In this regard, porous molecular cages are particularly interesting for encapsulating guest molecules as molecular machines via non-covalent interactions and to study the effect of molecular confinement on their functions. Due to their accessible internal cavities for nanoscale confinement, shape persistence, and their molecular solubility, the molecular machines can retain their solution-state efficiency even after being confined inside the cages.[32–35] Such an alliance of molecular machines and porous organic cages can, in principle, serve as a functional nanoscale unit for the controlled manipulation (via catalysis) and transport of other chemical species (such as ions).[36,37] Despite these inherent advantages, it still remains synthetically challenging to install molecular machines inside the nano-sized porous organic cages and to control the molecular motion by chemical or/and physical stimuli.

Of particular interest is controlling confined molecular machines remotely by an external stimulus, which may unlock new properties of these systems with spatiotemporal precision. In comparison with other remotely controlled stimuli, light has unique advantages of being a clean energy source and having the ability to be transiently delivered at a precise location in a solution.[38,39] These benefits have led to the development of a large number of photoresponsive molecular machines, self-assemblies, smart materials, drug delivery systems, etc.[40–43] Usually, a molecular machine consists of a light-responsive component, such as azobenzenes,[44,45] dithienylethenes,[46,47] spiropyranes,[48–50] etc.,[51] to control its mechanical motion by light in the confinement. However, using a light source to control a molecular machine that is devoid of any photoresponsive component can be very interesting considering its resemblance with the biological machines, e.g., light-driven ion pumps.

We have recently reported cube-shaped porous organic cages self-assembled from six square-shaped porphyrins and eight triangular linkers by dynamic covalent chemistry.[52–54] Shape-persistent porphyrinic cages, due to their well-defined receptor cavities, are ideal platforms to install molecular machines in a precise and predictable manner. Previously, a number of Zn–porphyrins-based dynamic molecular machines have been reported.[55–58] However, the establishment of a rational and high-yielding synthetic strategy to precisely organize molecular machines inside Zn–porphyrin-based porous organic cages with a 3D encompassed intrinsic nanoscopic cavity and to control their functions with multiple external stimuli requires further exploration. Herein, we report the synthesis of a supramolecular rotor built inside a porous Zn–porphyrinic cage (**1**) by insertion of a tetrazine-based **LA** followed by post-assembly modification to append a controllable side arm to the axle. The ^{1}H and 2D EXSY NMR studies reveal a 90° jump-like random rotary motion of the rotor arm and a slow tumbling motion of the rotor axle upon the addition of pyridine derivatives, which compete with the rotor for zinc–porphyrin coordination. Computational calculations confirm the stochastic nature of the molecular motions. Moreover, the rotation rates of these two motions can be adjusted by varying the amounts of pyridine derivatives. The reversible control over the dual motions of the rotor is achieved by UV and visible light-induced coordination and dissociation of azopyridine-based photo-dissociable ligand (PDL), which acts as a signal transducer. The nanoscale hydrophobic cavity of the Zn–porphyrinic cage and the remotely controllable functions of the rotor may collectively lead to the development of tunable

[1]Center for Self-Assembly and Complexity (CSC), Institute for Basic Science (IBS), Pohang 37673, Republic of Korea

[2]Department of Chemistry, Pohang University of Science and Technology (POSTECH), Pohang 37673, Republic of Korea

[3]Center for Theoretical Chemistry, Ruhr University Bochum, 44780 Bochum, Germany

[4]Present address: Department of Chemistry, Ramananda College, Bankura University, Bishnupur, 722122, West Bengal, India

[5]Lead contact

*Correspondence: kkim@postech.ac.kr

https://doi.org/10.1016/j.chempr.2021.12.008

Please cite this article in press as: Dhamija et al., Remotely controllable supramolecular rotor mounted inside a porphyrinic cage, Chem (2021), https://doi.org/10.1016/j.chempr.2021.12.008

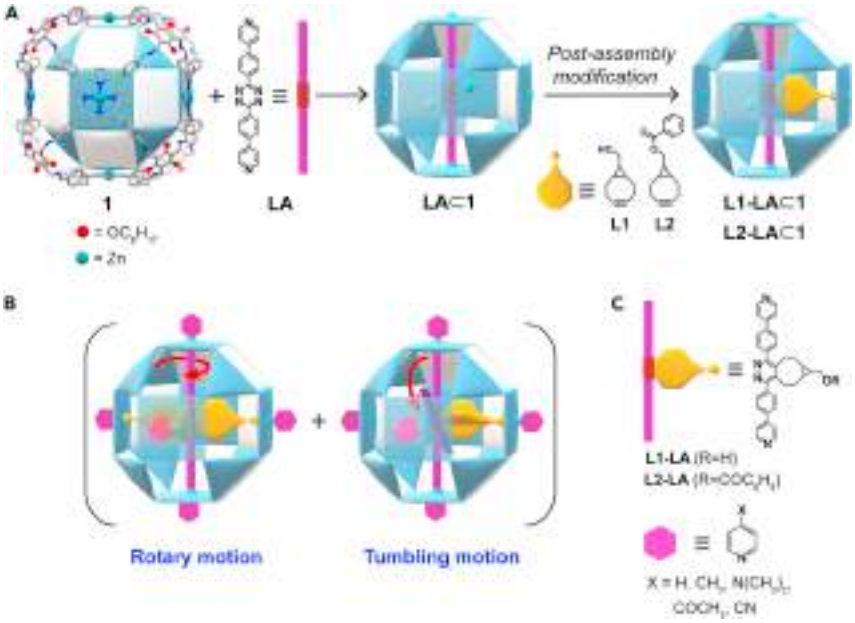

Figure 1. Synthesis and functioning of the supramolecular rotor

(A) Schematic representation of encapsulation of tetrazine-based **LA** inside **1** and its post-assembly modification with **L1** and **L2** substrates.

(B) Schematic representation of rotary and tumbling motions of the rotor in the presence of pyridine derivatives.

(C) Schematic representation of **L1-LA**, **L2-LA**, and *para*-substituted pyridine derivatives.

molecular devices with potential applications in reversible on-off ion channels, switchable catalysis, and drug delivery.

RESULTS AND DISCUSSION

Synthesis and characterization

At the outset of this work, we synthesized a pyridine terminated **LA** (length, ~1.9 nm, see synthesis in Scheme S1), which can coordinate to two Zn metal centers of **1** (distance, ~2.3 nm), across the cavity (Figure S1). **LA** consists of a central tetrazine moiety that can react efficiently with alkenes or alkynes dienophiles via inverse electron demand Diels-Alder (IEDDA) reaction to attach a new functionality on **LA**. By using the remarkably high-yielding IEDDA reactions for post-assembly modification, a number of different rotor moieties can be precisely incorporated into the cage. We envisaged that post-assembly modification of **LA** inside **1** with (1*R*,8*S*,9*s*)-bicyclo[6.1.0]-non-4-yn-9-ylmethanol (**L1**) may provide a controllable side arm for the freely rotating axle as **L1** contains a hydroxy group (–OH) at the terminal position, which can coordinate with the "equatorial" Zn–porphyrins of **1** (Figure 1). The mechanical motion of the resulting assembly **L1-LA**⊂**1** can be triggered in the presence of chemical stimuli, such as pyridine derivatives, which can coordinate with the Zn–porphyrinic faces of **L1-LA**⊂**1** from outside the hydrophobic cavity, thus initiating the motion by inhibiting the formation of coordination bonds between the Zn centers of **1** and the rotor **L1-LA** (Figure 1B).

The axle insertion experiment was performed by adding a stoichiometric amount of **LA** to the chloroform solution of **1**, yielding **LA**⊂**1** (Figure 1A). The binding affinity (K_a) of **1** for **LA** was determined to be 3.8 ± 0.1 × 10^7 M^{-1} by UV-vis titration (Figure S2), confirming a strong host-guest interaction between **1** and **LA**. In the ^{1}H

Please cite this article in press as: Dhamija et al., Remotely controllable supramolecular rotor mounted inside a porphyrinic cage, Chem (2021), https://doi.org/10.1016/j.chempr.2021.12.008

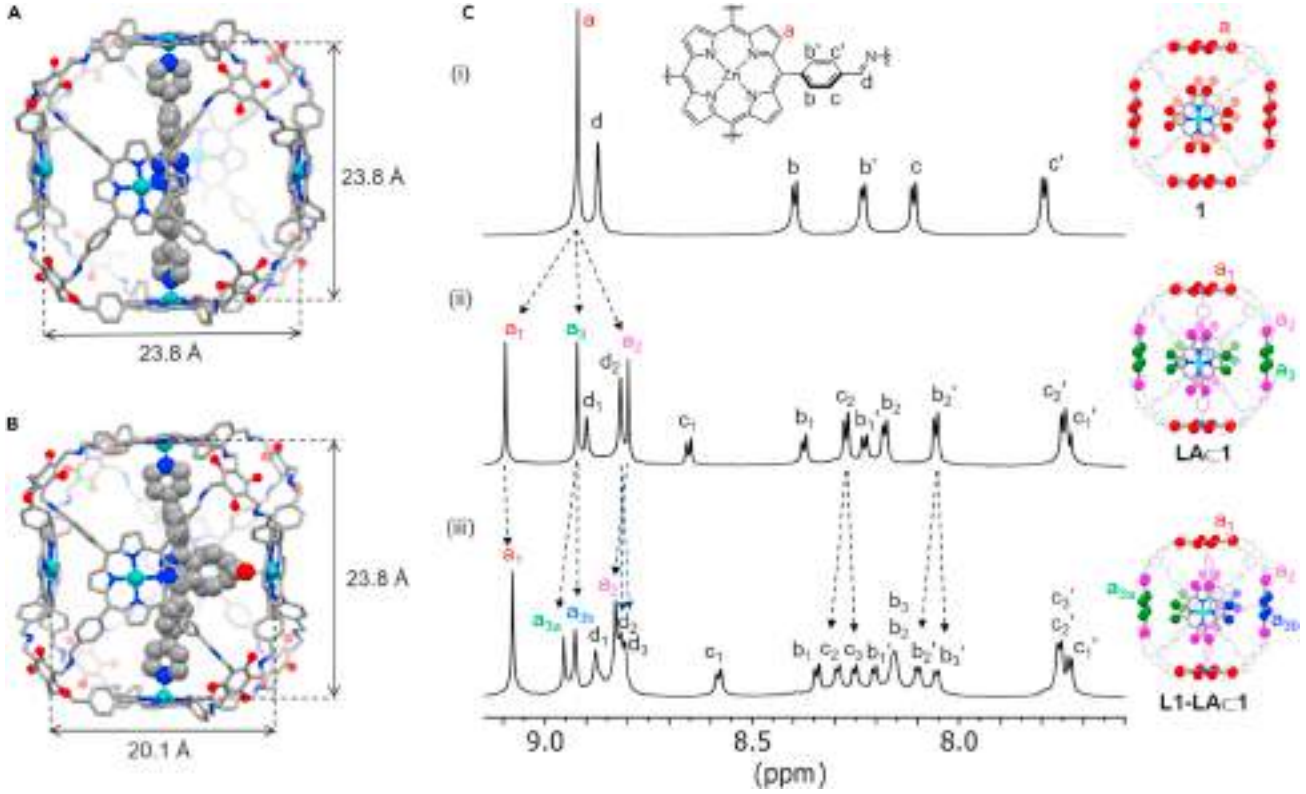

Figure 2. Characterization of the supramolecular rotor by single-crystal X-ray diffraction and ^{1}H NMR spectroscopy

(A and B) X-ray crystal structures of (A) **LA⊂1** and (B) **L1-LA⊂1** (disordered octyloxy chains and hydrogen atoms have been omitted for clarity).

(C) Partial ^{1}H NMR of (Ci) **1**, (Cii) **LA⊂1**, and (Ciii) **L1-LA⊂1** in toluene-d_8 at 298 K. Color-coded spheres (right) represent chemically non-equivalent pyrrolic protons.

NMR spectrum of **LA⊂1** in toluene-d_8, **LA** protons showed a large upfield shift compared with their free state, due to the strong ring current of the porphyrin units. In particular, the α-py protons that are closest to the porphyrin ring showed the largest upfield shift (8.84 to 1.88 ppm), indicating that **LA** is precisely positioned inside **1** (Figure S3). Moreover, the insertion of **LA** into the cavity of **1** splits the identical pyrrolic protons (a) of all six porphyrins of **1** into three sets: a_1 protons for two "axial" porphyrins (connecting to the axle) and a_2 and a_3 protons for four "equatorial" porphyrins (parallel to the axle). The a_2 and a_3 protons show different chemical shifts as they are directed toward the axial and equatorial porphyrins, respectively (Figure 2). The NMR splitting pattern of the cage protons suggests the $O \rightarrow D_4$ desymmetrization of the cage structure. All peaks were assigned by several 2D NMR experiments (^{1}H–^{13}C HSQC [heteronuclear single quantum coherence spectroscopy], ^{1}H–^{1}H COSY [homonuclear correlation spectroscopy], and ROESY [rotating-frame nuclear overhauser effect spectroscopy]; Figures S4–S7). A single trace in the DOSY (diffusion-ordered spectroscopy) spectrum confirmed the presence of a single species (**LA⊂1**) in the solution (Figure S8). Finally, X-ray structure analysis of **LA⊂1** (for crystallization conditions, see **supplemental information**) confirmed the coordination of the py moieties of **LA** to the Zn metal centers of the opposite faces of **1** ($Zn–N_{py}$ = 2.081(5) Å). In the crystal structure, **LA⊂1** maintained an overall cube-shape with the same opposite Zn•••Zn distance (23.8 Å) in all three directions despite the insertion of **LA** (Figure 2A).

Please cite this article in press as: Dhamija et al., Remotely controllable supramolecular rotor mounted inside a porphyrinic cage, Chem (2021), https://doi.org/10.1016/j.chempr.2021.12.008

To demonstrate facile post-assembly modification of **LA⊂1**, norbornadiene was chosen as a model compound for IEDDA reaction that quantitatively converts the tetrazine-based axle (**LA**) to a pyridazine-based axle (**PLA**) inside **1** (**PLA⊂1**) within 4 h at room temperature, which is manifested by the disappearance of ^{1}H NMR signals of **LA** and the appearance of **PLA** signals (Figures S9 and S10). The formation of **PLA⊂1** was confirmed by 2D NMR and DOSY analysis (Figures S11–S13).

The post-assembly modification of **LA⊂1** with **L1** substrate (1 equiv per tetrazine) by IEDDA reaction proceeded almost instantly at room temperature to furnish a ring-fused pyridazine-based axle inside **1** (**L1-LA⊂1**), as verified by ^{1}H NMR, MALDI-TOF, and elemental analysis (EA) (Figures S14 and S15). Thermal stability was confirmed by thermogravimetric analysis (TGA) (Figures S16 and S17). In the ^{1}H NMR spectrum of **L1-LA⊂1** in toluene-d_8, the **L1** protons are shifted in the upfield region (appeared between 0 to −5 ppm), which may be due to their close proximity with one of the "equatorial" Zn–porphyrin from inside the cavity. In addition, the pyrrolic protons a_3 of the equatorial Zn–porphyrins of **LA⊂1** are divided into two sets a_{3a} and a_{3b}, indicating further desymmetrization of the cage structure (Figure 2C). The splitting of phenyl and imine protons also suggests the lowering of cage symmetry. All peaks were assigned by several 2D NMR experiments (Figures S18–S21). Moreover, DOSY experiment confirmed the single species in solution (Figure S22). Unexpectedly, the pyrrolic protons a_1 and a_2 of **L1-LA⊂1** showed no splitting, the reason for which is currently not fully understood. On the other hand, upon directly mixing the 1:1 ratio of **L1-LA** and **1**, a non-symmetrical pattern of **LA** protons was observed in the ^{1}H NMR spectrum, indicating that **L1-LA** coordinates to **1** from outside the cage in a monodentate fashion (Figure S23), probably due to small-sized windows of the cage and long alkyl chains blocking the cage windows. After numerous attempts, the structure of **L1-LA⊂1** has been finally confirmed by single-crystal X-ray crystallography (Figure 2B). The molecular structure revealed that **L1-LA** resides inside **1** by the coordination of the py groups of **L1-LA** to the "axial" Zn–porphyrins (Zn–N_{py} = 2.129(5) Å) and the hydroxy group (–OH) to the "equatorial" Zn–porphyrin (Zn–OH = 2.379(5) Å). As shown in Figure 2B, the slightly bent axle **LA** (bent angle, ∼167°) and curved shape of the side arm **L1** assist in the coordination of the hydroxy group (–OH) with one of the "equatorial" Zn–porphyrins. The opposite Zn•••Zn distances in the a and b axes are both 23.7 Å, whereas that in the c axis is 20.1 Å. The shorter Zn•••Zn distance may be ascribed to the coordination of the –OH group of **L1-LA** to the equatorial Zn–porphyrin. The bent shape of **LA** and the curved shape of **L1** were also observed in the X-ray crystal structure of **L1-LA** (Figure S24).

Rotary motion of the supramolecular rotor

Next, we investigated the operation of the supramolecular rotor **L1-LA⊂1**. In the absence of external stimulus, upon cooling the solution of **L1-LA⊂1** (in toluene-d_8) down to 243 K, no splitting of pyrrolic protons peaks was observed in the ^{1}H NMR spectrum (Figure S25), which suggests that **L1-LA** is either rotating too slowly on the NMR timescale or no rotation at all, possibly due to the Zn–$OH_{L1\text{-}LA}$ coordination bond. It is known that Zn–porphyrins bind more strongly to pyridine than to alcohols.[59] In fact, coordination of pyridine to the Zn center can replace the Zn–OH coordination bond for maintaining a five-coordinate binding mode. The coordination of pyridine to **L1-LA⊂1** is borne out by the upfield shift of the pyridine protons peaks in the ^{1}H NMR spectrum. However, in the presence of excess pyridine, the peaks shifted back to the downfield region due to the establishment of a fast equilibrium between coordinated and free pyridine molecules (Figure S26).

Please cite this article in press as: Dhamija et al., Remotely controllable supramolecular rotor mounted inside a porphyrinic cage, Chem (2021), https://doi.org/10.1016/j.chempr.2021.12.008

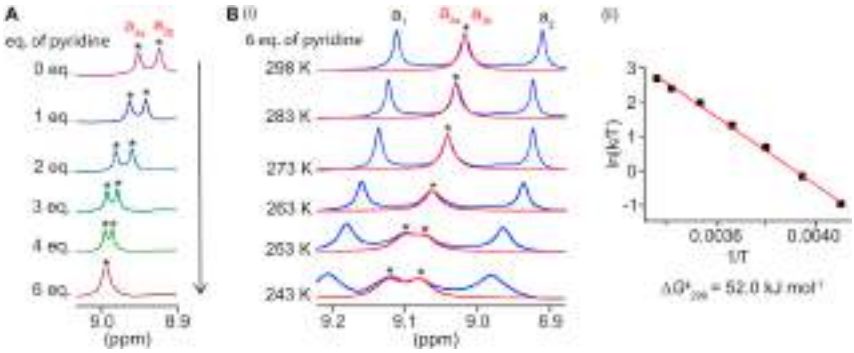

Figure 3. Rotary motion of the supramolecular rotor in the presence of pyridine

(A) ^{1}H NMR titration of **L1-LA⊂1** upon stepwise addition of pyridine (0–6 equiv) in toluene-d_8 at 298 K. (B) (Bi) Variable temperature ^{1}H NMR spectra of a mixture of **L1-LA⊂1** and 6 equiv of pyridine at various temperatures in toluene-d_8 (blue trace, experimental; red trace, simulated) and (Bii) Eyring plot of the variable-temperature data (red line, best linear fit) used to determine the activation energy barrier (52.0 kJ mol^{-1}).

Thereafter, the effect of the addition of the chemical stimulant (pyridine) to **L1-LA⊂1** was studied in detail by ^{1}H NMR spectroscopy. Upon stepwise addition of pyridine (up to 6 equiv) to **L1-LA⊂1**, the pyrrolic protons a_{3a} and a_{3b} of the four equatorial porphyrins merged into a sharp singlet at 8.98 ppm (Figure 3A). The imine protons and the phenyl protons that correspond to the equatorial porphyrins also merged, indicating the symmetrization of the cage framework (Figure S26A). Additionally, the side arm (**L1**) protons that appear between 0 to −5 ppm due to their close proximity with one of the equatorial Zn–porphyrins broadened and shifted slightly downfield (Figure S26B). The symmetrical structure of the cage framework as derived from the ^{1}H NMR spectroscopic studies and broadened resonances of the side arm protons suggested that the coordination of pyridine molecules to the Zn centers dissociated the Zn–OH coordination bond, and, as a result, the side arm started jumping rapidly around all four equatorial Zn–porphyrin stations at room temperature by using the rotor axle as a hinge (Figure 1B). To confirm that the mixing of the peaks is due to the rotary motion and not to pyridine coordination, ^{1}H NMR titration between pyridine (0–6 equiv) and **1** was performed, which showed that the coordination of pyridine does not affect the protons signals of cage **1** due to its relatively rapid association/dissociation equilibrium with the Zn–porphyrins of **1** on the NMR timescale (Figure S27).

Further insight into the rotor dynamics was obtained from variable-temperature (VT) ^{1}H NMR studies. While the a_{3a} and a_{3b} protons of **L1-LA⊂1** appeared as a single peak in the presence of 6 equiv of pyridine at 298 K, the peak was broadened at 263 K and emerged as two distinct peaks at 9.05 and 9.09 ppm at 243 K (Figure 3B). The ^{1}H NMR could not be recorded below 243 K due to poor solubility of **L1-LA⊂1** in toluene-d_8 at the low temperatures. Upon raising the temperature back to 298 K, the peaks again merged into a single peak at 8.99 ppm (Figure S28). These experiments further corroborated the notion that the rotor exhibits a fast rotary motion in the presence of the chemical stimulant pyridine, whereas the rotation decelerates at low temperatures. Line shape analysis of the VT ^{1}H NMR data in the presence of 6 equiv of pyridine provided rotation rates (k) of 4.0×10^3 and 1.0×10^2 Hz at 298 and 243 K, respectively, from which an activation energy barrier ($\Delta G^{\ddagger}_{298}$) of 52.0 kJ mol^{-1} is estimated (Figure 3Bii). Whereas, in the presence of 10 equiv of pyridine, rotation rates (k) of 6.0×10^3 and 2.0×10^2 Hz are obtained at 298 and 243 K, respectively (Figure S29). Similarly, *para*-substituted pyridine derivatives, 4-

Please cite this article in press as: Dhamija et al., Remotely controllable supramolecular rotor mounted inside a porphyrinic cage, Chem (2021), https://doi.org/10.1016/j.chempr.2021.12.008

(dimethylamino)pyridine, 4-methylpyridine, 4-acetylpyridine, and 4-cyanopyridine were also used as chemical stimuli for the initiation of the rotary motion. Depending on the electronic effect of the substituent at the *para*-position, different equivalents of pyridine derivatives were required to start the rotary motion, which is shown by merging of the a_{3a} and a_{3b} peaks of **L1-LA**⊂**1**. 4-(dimethylamino)pyridine and 4-methylpyridine start the rotary motion at 4 and 6 equiv, respectively, due to the presence of strong electron-donating substituents at the *para*-positions (Figures S30 and S31). However, 16 equiv of 4-acetylpyridine was required to initiate the rotary motion because of the electron-withdrawing acetyl group (Figure S32). In the case of 4-cyanopyridine, the peaks did not merge even after the addition of a large excess (30 equiv) due to the presence of a strong electron-withdrawing cyano group at the *para*-position (Figure S33). The equivalents of substituted pyridine derivatives required to initiate rotary motion showed a decent linear correlation with the Hammett substituent constants, proving that the addition of pyridine derivative is the key factor in initiating the rotary motion (Figure S34).

To further probe the proposed operation of the rotor, we synthesized another model system, **L2-LA**⊂**1** (Figures 1A and S35–S41), in which the coordination site (–OH) is hindered by the benzoyl group (Scheme S2). In the ^{1}H NMR spectrum of **L2-LA**⊂**1** in toluene-d_8, the pyrrolic protons (a_3) corresponding to the equatorial porphyrins appeared as a single peak at 8.92 ppm without pyridine and did not split upon the addition of pyridine, which suggests that the rotor **L2-LA** does not behave as static but rotates freely inside the cavity (Figure S42). Furthermore, the VT NMR experiments of **L2-LA**⊂**1** showed that the pyrrolic protons signal broadened but did not split upon reducing the temperature up to 243 K (Figure S43). A quantum chemical calculation suggests that despite the large size of the side arm **L2**, the space inside **1** is large enough for free rotation of the rotor, which is consistent with the results mentioned earlier (Figure S44).

To better understand the mode of operation of the rotor at the atomic level, we carried out quantum chemical calculations and molecular dynamics (MD) simulations. First, in a model system consisting of the rotor **L1-LA** and two axial Zn–porphyrins, relaxed potential energy surface scans (PES) were computed for the rotation of **L1-LA** around the Zn–pyridyl bond (Zn–N_{py} bond), pyridyl–phenyl bond (C–C bond), and phenyl–pyridazinyl bond (C–C bond), which revealed that the rotation around the Zn–N bond is energetically most favorable in comparison with the C–C bonds along the axle backbone (Figure S45). After that, relaxed PES scans were performed for the rotation of **L1-LA** inside cage **1**, both in the absence and in the presence of pyridine molecules bound to the "equatorial" Zn centers. As a reaction coordinate, the distance between the O atom of **L1-LA** and the bonded Zn center was used. The resulting energy profiles (Figure S46) suggest that the binding of pyridine from outside of the cage lowers the activation barrier by ca. 15–20 kJ/mol, in line with the experimental observation that the addition of pyridine induces the rotational motion of the rotor. Interestingly, coordination of a pyridine molecule to the Zn center to which the rotor is bound from the inside already leads to a substantial lengthening, or even partial dissociation, of the Zn–$OH_{L1\text{-}LA}$ coordination bond (Figure S46), supporting the notion that the lowering of the activation energy barrier is due to weakening of the Zn–OH bond.

To investigate the dynamics of the rotational motion, MD simulations of **L1-LA**⊂**1** in explicit toluene solvent were carried out. In total, 100 MD simulation trajectories of length 200 ns were generated (50 each in the canonical and microcanonical ensembles, see methods in supplemental information), yielding a total of 20 μs of simulation time. MD simulations were carried out in the absence of pyridine, but the

Please cite this article in press as: Dhamija et al., Remotely controllable supramolecular rotor mounted inside a porphyrinic cage, Chem (2021), https://doi.org/10.1016/j.chempr.2021.12.008

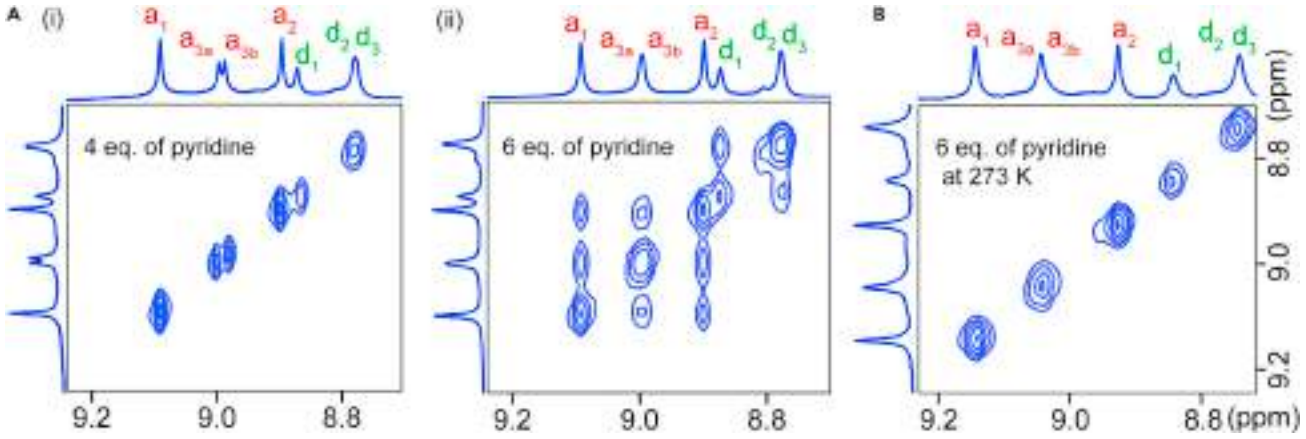

Figure 4. Tumbling motion of the supramolecular rotor in the presence of pyridine
(A) 2D-EXSY plots of **L1-LA⊂1** with (Ai) 4 equiv, (Aii) 6 equiv of pyridine at 298 K in toluene-d_8.
(B) 2D-EXSY plot of **L1-LA⊂1** with 6 equiv of pyridine at 273 K in toluene-d_8.

interaction strength of the Zn–$OH_{L1\text{-}LA}$ coordination bond in the force field was weak enough to observe a statistically significant number of rotation events within the simulation timescale (Video S1). The dihedral angle time trace shown in Figure 5 reveals that the rotational motion of **L1-LA** inside **1** is jump-like in nature, in the sense that rotations by +90° or −90°, which occur spontaneously, are fast but followed by long dwell times in the symmetry equivalent energy minima. This observation is in line with the energy profiles shown in Figure S46, which suggests that rotation of **L1-LA** is an activated process. Because of the curved shape of the rotor arm **L1** and the preferred orientation of hydroxy group (–OH), we thought that the rotation might be unidirectional in nature. However, out of the total number of 259 rotation events observed in the MD simulations, forward (+90°) and backward (−90°) direction of rotation were found in 140 (54%) and 119 (46%) of the cases, respectively. The results from the canonical and microcanonical simulations were similar, with 55% forward and 45% backward rotations. Given the uncertainties of about 12%, as obtained from the jump statistics, it can be concluded that the rotor **L1-LA** undergoes jump-like random rotation inside **1**. Overall, the MD simulation data concluded that the direction of the rotary motion is random for every 90° event.

Tumbling motion of the supramolecular rotor

Apart from the fast rotary motion of the supramolecular rotor, surprisingly, a slow mechanical motion was also detected by 2D-EXSY (exchange spectroscopy) experiments. Upon addition of 6 equiv of pyridine to **L1-LA⊂1**, off-diagonal peaks were observed between the pyrrolic protons (a_1, a_2, a_{3a}, and a_{3b}) and also between the imine protons (d_1, d_2, and d_3) of the axial and equatorial Zn–porphyrins in the 2D-EXSY experiment (mixing time, 0.3 s), indicating a slow exchange of the rotor axle between the axial and equatorial Zn–porphyrins through dissociation and re-association of Zn–$N_{L1\text{-}LA}$ coordination bonds (Figure 1B). This finding supports a model that, in the presence of 6 equiv of pyridine at room temperature, rotor **L1-LA** not only performs rotary motion but also simultaneously executes tumbling motion in a stochastic manner. Interestingly, no off-diagonal peak was recorded when up to 4 equiv of pyridine was added to **L1-LA⊂1** (Figures 4A and S47), which suggests that at low concentration, pyridine molecules only coordinate with the "equatorial" four-coordinated or weakly five-coordinated Zn–porphyrins to trigger the rotary motion. However, in the presence of 6 equiv of pyridine, the free pyridine molecules attack the "axial" five-coordinated Zn–porphyrins from outside the cavity, destabilizing the internal Zn–$N_{L1\text{-}LA}$ coordination bonds and

Please cite this article in press as: Dhamija et al., Remotely controllable supramolecular rotor mounted inside a porphyrinic cage, Chem (2021), https://doi.org/10.1016/j.chempr.2021.12.008

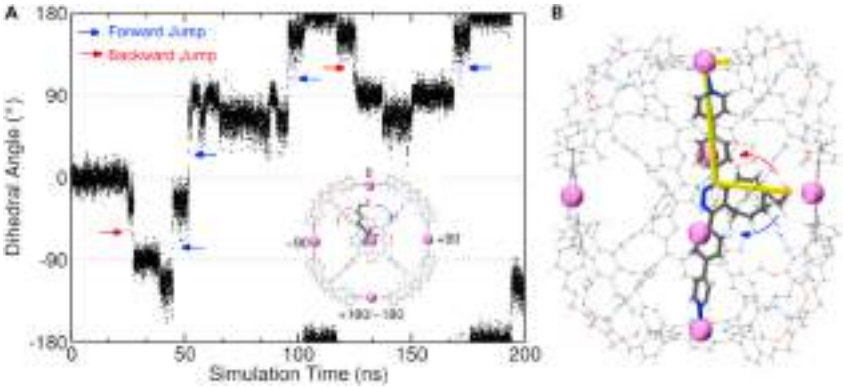

Figure 5. Molecular dynamics (MD) simulation of rotary motion of L1-LA inside 1
(A and B) (A) Time evolution of the dihedral angle describing the rotation (see B) during a representative MD simulation trajectory. Forward (+90°, "clockwise") and backward (−90°, "counterclockwise") jumps are indicated by blue and red arrows, respectively.

triggering the tumbling motions also. The exchange rate of the tumbling motion of **L1-LA⊂1** with 6 equiv of pyridine was estimated from the 2D-EXSY spectrum as 1.1 Hz per 90° rotation ($\Delta G^{\ddagger}_{298}$ = 72.8 kJ mol^{-1}, see methods in supplemental information). Even upon the addition of 10 equiv of pyridine to **L1-LA⊂1**, the tumbling rate is only slightly increased to 1.6 Hz per 90° rotation (Figure S47). Slow tumbling rate can be attributed to the high binding affinity of **1** for the rotor axle (**LA**) (3.8 ± 0.1 × 10^{7} M^{-1}), due to which free pyridine molecules can only destabilize the rotor but cannot replace it.[60] Furthermore, the VT 2D-EXSY experiment of **L1-LA⊂1** with 6 equiv of pyridine showed that the tumbling motion is completely quenched at 273 K (Figure 4B), whereas the rotary motion is retained up to 243 K (Figure 3B), confirming that the rotary motion and the tumbling motion are two separate processes completely uncorrelated to each other. Since the rate of the tumbling motion is slower (1.1 Hz per 90° rotation) than the rotary motion (4,000 Hz), the rotor's axis of rotation changes depending on the tumbling of the axle, and, as a result, the rotor performs multi-directional motion inside the cage in a random manner. A similar tumbling motion was also observed when 6 equiv of pyridine was added to **L2-LA⊂1**, yielding a tumbling rate of 1.3 Hz per 90° rotation ($\Delta G^{\ddagger}_{298}$ = 70.8 kJ mol^{-1}, Figure S48).

Light-induced reversible control of the rotary and tumbling motions of the supramolecular rotor

To reversibly control the rotary and tumbling motions of the supramolecular rotor by light, we utilized an azopyridine-based ligand 3-((3,5-di-tert-butylphenyl)diazenyl)-4-methylpyridine (PDL),[61,62] which can coordinate to the Zn–porphyrinic faces of **L1-LA⊂1** in the *trans* form to trigger the motions, while dissociating in the *cis* form to stop the motions (Figure 6A). To check our proposition, we performed a photoirradiation experiment of PDL in the presence of a model compound, zinc tetraphenylporphyrin (ZnTPP). In UV-visible spectroscopy, upon the addition of increasing amounts of *trans*-PDL (0–400 equiv) to ZnTPP (1 × 10^{-6} M), the Soret band of ZnTPP at 418 nm decreased and a new band appeared at 428 nm. The binding affinity (K_{trans}) of ZnTPP for *trans*-PDL was estimated as 5.8 ± 0.3 × 10^{3} M^{-1}. Upon UV (365 nm) light irradiation of the solution mentioned earlier, the absorption band at 428 nm decreased, whereas the Soret band of free ZnTPP reappeared because the steric hindrance between the porphyrin ring and the *t*-Bu groups of *cis*-PDL restricted the Zn–$N_{cis\text{-PDL}}$ coordination (Figure S49). In ^{1}H NMR spectroscopy, UV (365 nm) irradiation of a 1:1 mixture of ZnTPP and *trans*-PDL achieves a photostationary (PS) *cis*/*trans* ratio of 65:35, which is

Please cite this article in press as: Dhamija et al., Remotely controllable supramolecular rotor mounted inside a porphyrinic cage, Chem (2021), https://doi.org/10.1016/j.chempr.2021.12.008

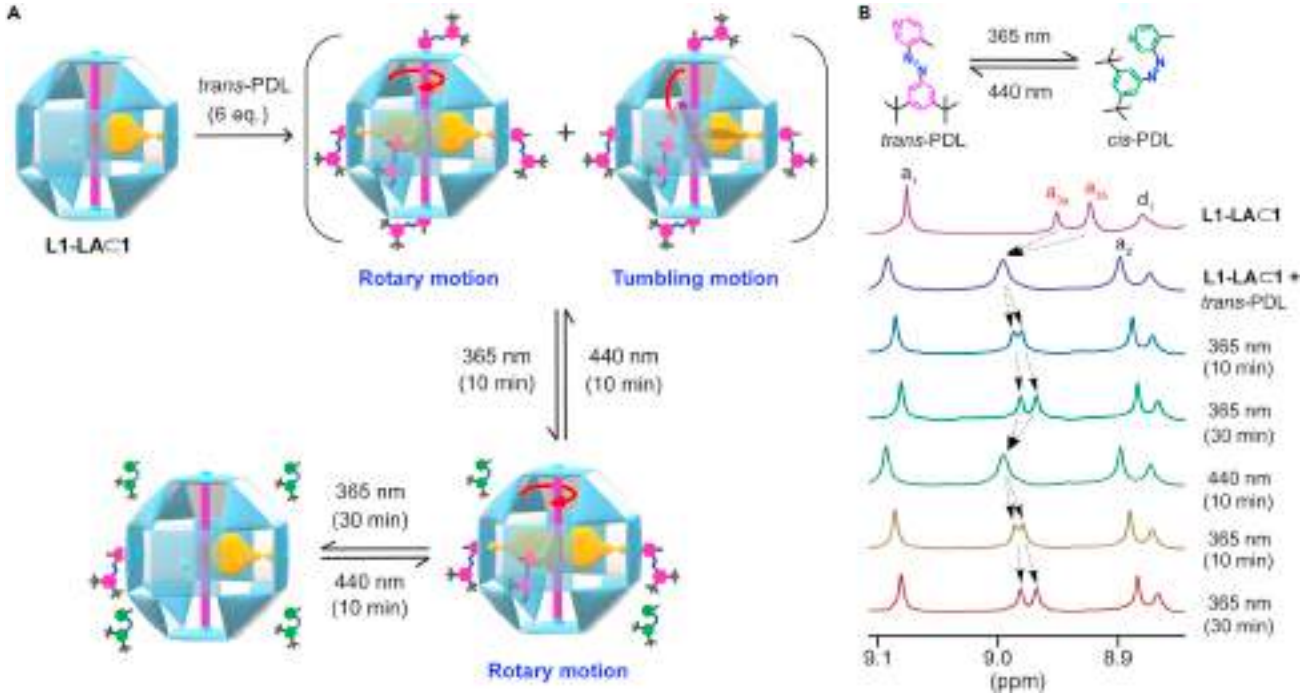

Figure 6. Reversible control of the rotary and tumbling motions by a photo-dissociable ligand (PDL)

(A) Schematic representation of reversible control of rotary and tumbling motions of **L1-LA⊂1** by the addition and photoisomerization of azopyridine-based ligand (PDL).

(B) ^{1}H NMR spectra of **L1-LA⊂1**/*trans*-PDL (6 equiv) upon UV (365 nm) and visible (440 nm) light irradiation in an alternate sequence in toluene-d_8 at 298 K.

much lower than the PS ratio of isolated PDL (*cis*/*trans* = 91:9),[61] most likely due to the stabilization of the *trans*-PDL upon coordination with ZnTPP (Figure S50).

The "modus operandi" of PDL in controlling the mechanical motion of the rotor was investigated by ^{1}H NMR and 2D EXSY experiments. Upon addition of the *trans*-PDL (6 equiv) to **L1-LA⊂1**, the pyrrolic protons a_{3a} and a_{3b} corresponding to the equatorial porphyrins merged into a single peak in the ^{1}H NMR spectrum (Figures 6B and S51), as well as the off-diagonal peaks appeared between the axial and equatorial porphyrins protons in the 2D-EXSY experiment (Figure S52A), which confirmed the outset of both rotary and tumbling motions. However, UV (365 nm) light irradiation of the solution mentioned earlier for a short time (10 min) caused isomerization of *trans*-PDL molecules that were weakly coordinated to the "axial" Zn–porphyrins. At this point, the off-diagonal peaks disappeared (Figure S52B), and the pyrrolic protons split slightly (Figure 6B), indicating that the tumbling motion had stopped completely. Further irradiation with UV light for a long time (30 min) increased the separation between the pyrrolic protons a_{3a} and a_{3b} peaks, reflecting that the rotation rate is substantially reduced on the NMR timescale. No further splitting of the peaks was observed even upon prolonged irradiation, because the UV light irradiation on 6 equiv of *trans*-PDL can only achieve up to 3.9 equiv of *cis*-PDL (65:35 *cis*/*trans*) in the presence of Zn–porphyrins (see earlier). The rotary and tumbling motions resumed upon visible (440 nm) light irradiation of the sample for a short time (10 min). No observable fatigue was observed in ^{1}H NMR spectra after several cycles of irradiation by 365 and 440 nm light under ambient conditions. In UV-vis spectroscopy, UV and visible light irradiation on a mixture of **L1-LA⊂1** and *trans*-PDL switched the Soret band of **L1-LA⊂1** between two photostationary states (PSS), PSS_{trans} at 431 nm and PSS_{cis}

Please cite this article in press as: Dhamija et al., Remotely controllable supramolecular rotor mounted inside a porphyrinic cage, Chem (2021), https://doi.org/10.1016/j.chempr.2021.12.008

at 426 nm (Figure S53). The results mentioned earlier suggest that PDL is an effective stimulus to fully control the tumbling motion and partially control the rotary motion of the rotor in an on/off fashion through exposure to UV or visible light, respectively.

Organization of supramolecular rotor in solid state

Organization of such rotors in the solid state by simple crystallization may provide amphidynamic crystals,[29–31] which are a promising platform for the development of tunable molecular devices. In particular, the precise organization of such rotors in a specific orientation in the crystalline state may allow a synchronized motion of the rotors. Therefore, we decided to take a close look at the packing structures of **LA**⊂**1** and **L1**-**LA**⊂**1**. We found that the cube-shaped **LA**⊂**1** molecules crystallized in the cubic space group *Pn*-3n with the **LA** axles randomly oriented in all three (a, b, and c) axes (Figure S54A). In contrast, the square prism-shaped **L1**-**LA**⊂**1** molecules are packed in such a way that the rotor axles (**LA**) are aligned in the a and b axes with the lateral side arm (**L1**) pointing toward the c axis (Figure S54B). The rotor molecules arrange themselves in the same orientation in the solid state, which offers the opportunity to explore various properties of this system. Therefore, we performed preliminary ^{13}C magic-angle spinning (MAS) solid-state NMR experiments to study the dynamics in the solid state. However, without labeling with ^{13}C isotope, spectra of **L1**-**LA**⊂**1** in the absence and presence of pyridine were very broad and the shifting of the rotor or cage peaks was not clear (Figure S55). Therefore, we concluded that to explore the solid-state properties of the rotor, ^{13}C or ^{2}H isotope labeling of the cage or rotor or both is needed. Work along these lines is in progress.

CONCLUSIONS

We have developed a rational high-yielding synthetic strategy to confine a supramolecular rotor inside the cavity of Zn–porphyrinic cage (**1**) by encapsulation of a tetrazine-based **LA** by metal-ligand coordination bond, followed by its post-assembly modification with bulky cycloalkyne substrates. By using the exceptionally high-yielding IEDDA reactions for the post-assembly modification, a variety of rotor moieties can be precisely incorporated into the cage, and at the same time, the tedious bottom-up synthetic strategies conventionally adopted for the synthesis of complex molecular rotors can be avoided. The ^{1}H and 2D EXSY NMR studies revealed that, whereas the rotor alone displays little or no motion, the addition of pyridine derivatives results in both 90° jump-like random rotary motion of the rotor arm and slower tumbling motion of the central rotor axle in a stochastic manner. Since the rate of the tumbling motion is slower than the rotary motion, the rotor's axis of rotation changes depending on the tumbling of the axle, and as a result, the rotor performs multidirectional motion inside the cage in a random manner. The nature of the molecular motions was supported by quantum chemical calculations and MD simulations. A reversible control over the aforementioned dual motions was achieved by the irradiation of UV and visible light, which induced the coordination and dissociation of an azopyridine-based ligand with the cage.

The concept of confining molecular machines inside a molecular cage and remotely controlling their functions is beneficial not only for understanding the operation of biological machines confined within the intracellular matrix but also for the development of functional nanoscale units for the controlled manipulation (via catalysis) and transportation of other chemical species (such as ions) through their 3D nanocavities. To the best of our knowledge, this is the first experimental demonstration of two different motions in a single-rotor system confined within a molecular cage that can be remotely controlled by chemical stimulus and light. At present, the dual motions are stochastic

in nature, further design and understanding of the complementary role of rotary and tumbling motions is needed, and efforts in this direction are currently in progress.

EXPERIMENTAL PROCEDURES

Resource availability

Lead contact

Correspondence should be addressed to K.K. (kkim@postech.ac.kr).

Materials availability

All unique/stable reagents generated in this study are available from the lead contact with a completed materials transfer agreement.

Data and code availability

The authors declare that all data supporting the findings of this study are available within this article and supplemental information files. Crystallographic data for the structures reported in this article have been deposited at the Cambridge Crystallographic Data Centre, under deposition numbers "CCDC: 2127747, 2092616, 2092617". These data can be obtained free of charge via www.ccdc.cam.ac.uk/getstructures.

SUPPLEMENTAL INFORMATION

Supplemental information can be found online at https://doi.org/10.1016/j.chempr.2021.12.008.

ACKNOWLEDGMENTS

This work was supported by the Institute for Basic Science (IBS) (IBS-R007-D1), Republic of Korea. X-ray crystallography experiments with synchrotron radiation were performed at the Pohang Accelerator Laboratory (2D-SMC, 6D, and 11C beamlines), Republic of Korea. We thank beamline managers Drs. D. Moon, T.J. Shin, and S.-Y. Park for single-crystal X-ray diffraction measurements. This project received funding from the European Union's Horizon 2020 research and innovation program, Marie Sklodowska-Curie grant agreement no. 801459, Germany; Deutsche Forschungsgemeinschaft (DFG), Germany's Excellence Strategy–EXC 2033–390677874–RESOLV, Germany; and the Research Training Group Confinement-controlled Chemistry–GRK 2376/331085229, Germany.

AUTHOR CONTRIBUTIONS

A.D. and K.K. conceived and designed the experiments. A.D., Y.H.K., I.-C.H., A.G., and Y.K. performed the experiments and analyzed the data. A.D., X.Y., and I.-C.H. carried out single-crystal X-ray analyses. C.K.D. and L.V.S. performed and analyzed the MD simulations. A.D., R.D.M., I.-C.H., and K.K. wrote the paper. All authors discussed the results and commented on the manuscript.

DECLARATION OF INTERESTS

The authors declare no competing interests.

Received: June 28, 2021
Revised: August 5, 2021
Accepted: December 9, 2021
Published: January 18, 2022

Please cite this article in press as: Dhamija et al., Remotely controllable supramolecular rotor mounted inside a porphyrinic cage, Chem (2021), https://doi.org/10.1016/j.chempr.2021.12.008

REFERENCES

1. Szostak, J.W., Bartel, D.P., and Luisi, P.L. (2001). Synthesizing life. Nature *409*, 387–390.
2. Hansma, H.G. (2014). The power of crowding for the origins of life. Orig. Life Evol. Biosph. *44*, 307–311.
3. Zhou, H.-X., and Dill, K.A. (2001). Stabilization of proteins in confined spaces. Biochemistry *40*, 11289–11293.
4. Panganiban, B., Qiao, B., Jiang, T., DelRe, C., Obadia, M.M., Nguyen, T.D., Smith, A.A.A., Hall, A., Sit, I., Crosby, M.G., et al. (2018). Random heteropolymers preserve protein function in foreign environments. Science *359*, 1239–1243.
5. Grommet, A.B., Feller, M., and Klajn, R. (2020). Chemical reactivity under nanoconfinement. Nat. Nanotechnol. *15*, 256–271.
6. Rebek, J. (2009). Molecular behavior in small spaces. Acc. Chem. Res. *42*, 1660–1668.
7. Yoshizawa, M., Klosterman, J.K., and Fujita, M. (2009). Functional molecular flasks: new properties and reactions within discrete, self-assembled hosts. Angew. Chem. Int. Ed. Engl. *48*, 3418–3438.
8. Kinbara, K., and Aida, T. (2005). Toward intelligent molecular machines: directed motions of biological and artificial molecules and assemblies. Chem. Rev. *105*, 1377–1400.
9. Schliwa, M., and Woehlke, G. (2003). Molecular motors. Nature *422*, 759–765.
10. Vale, R.D., and Milligan, R.A. (2000). The way things move: looking under the hood of molecular motor proteins. Science *288*, 88–95.
11. Stock, D., Leslie, A.G., and Walker, J.E. (1999). Molecular architecture of the rotary motor in ATP synthase. Science *286*, 1700–1705.
12. Noji, H., Yasuda, R., Yoshida, M., and Kinosita, K. (1997). Direct observation of the rotation of F1-ATPase. Nature *386*, 299–302.
13. Jia, Y., and Li, J. (2019). Reconstitution of FoF1-ATPase-based biomimetic systems. Nat. Rev. Chem. *3*, 361–374.
14. Lanyi, J.K., and Pohorille, A. (2001). Proton pumps: mechanism of action and applications. Trends Biotechnol *19*, 140–144.
15. Richard, P., Pitard, B., and Rigaud, J.-L. (1995). ATP synthesis by the FoF1-ATPase from the thermophilic *Bacillus* PS3 co-reconstituted with bacteriorhodopsin into liposomes. Evidence for stimulation of ATP synthesis by ATP bound to a noncatalytic binding site. J. Biol. Chem. *270*, 21571–21578.
16. Kottas, G.S., Clarke, L.I., Horinek, D., and Michl, J. (2005). Artificial molecular rotors. Chem. Rev. *105*, 1281–1376.
17. Erbas-Cakmak, S., Leigh, D.A., McTernan, C.T., and Nussbaumer, A.L. (2015). Artificial molecular machines. Chem. Rev. *115*, 10081–10206.
18. Kassem, S., van Leeuwen, T., Lubbe, A.S., Wilson, M.R., Feringa, B.L., and Leigh, D.A. (2017). Artificial molecular motors. Chem. Soc. Rev. *46*, 2592–2621.
19. Baroncini, M., Silvi, S., and Credi, A. (2020). Photo- and redox-driven artificial molecular motors. Chem. Rev. *120*, 200–268.
20. Coskun, A., Banaszak, M., Astumian, R.D., Stoddart, J.F., and Grzybowski, B.A. (2012). Great expectations: can artificial molecular machines deliver on their promise? Chem. Soc. Rev. *41*, 19–30.
21. Astumian, R.D., Kay, E.R., Leigh, D.A., and Zerbetto, F. (2006). Design principles for Brownian molecular machines: how to swim in molasses and walk in a hurricane. Proc. Natl. Acad. Sci. USA *46*, 10771–10776.
22. Wilson, B.H., Vojvodin, C.S., Gholami, G., Abdulla, L.M., O'Keefe, C.A., Schurko, R.W., and Loeb, S.J. (2021). Precise spatial arrangement and interaction between two different mobile components in a metal-organic framework. Chem *7*, 202–211.
23. Su, Y.-S., Lamb, E.S., Liepuoniute, I., Chronister, A., Stanton, A.L., Guzman, P., Pérez-Estrada, S., Chang, T.Y., Houk, K.N., Garcia-Garibay, M.A., and Brown, S.E. (2021). Dipolar order in an amphidynamic crystalline metal-organic framework through reorienting linkers. Nat. Chem. *13*, 278–283.
24. Danowski, W., van Leeuwen, T., Abdolahzadeh, S., Roke, D., Browne, W.R., Wezenberg, S.J., and Feringa, B.L. (2019). Unidirectional rotary motion in a metal-organic framework. Nat. Nanotechnol. *14*, 488–494.
25. Orlova, T., Lancia, F., Loussert, C., Iamsaard, S., Katsonis, N., and Brasselet, E. (2018). Revolving supramolecular chiral structures powered by light in nanomotor-doped liquid crystals. Nat. Nanotechnol. *13*, 304–308.
26. Kaleta, J., Chen, J., Bastien, G., Dračínský, M., Mašát, M., Rogers, C.T., Feringa, B.L., and Michl, J. (2017). Surface inclusion of unidirectional molecular motors in hexagonal Tris(o-phenylene)cyclotriphosphazene. J. Am. Chem. Soc. *139*, 10486–10498.
27. Li, Q., Fuks, G., Moulin, E., Maaloum, M., Rawiso, M., Kulic, I., Foy, J.T., and Giuseppone, N. (2015). Macroscopic contraction of a gel induced by the integrated motion of light-driven molecular motors. Nat. Nanotechnol. *10*, 161–165.
28. Seo, J., Matsuda, R., Sakamoto, H., Bonneau, C., and Kitagawa, S. (2009). A pillared-layer coordination polymer with a rotatable pillar acting as a molecular gate for guest molecules. J. Am. Chem. Soc. *131*, 12792–12800.
29. Roy, I., and Stoddart, J.F. (2019). Amphidynamic crystals key to artificial molecular machines. Trends Chem *1*, 627–629.
30. Colin-Molina, A., Karothu, D.P., Jellen, M.J., Toscano, R.A., Garcia-Garibay, M.A., Naumov, P., and Rodríguez-Molina, B. (2019). Thermosalient amphidynamic molecular machines: motion at the molecular and macroscopic scales. Matter *1*, 1033–1046.
31. Karlen, S.D., and Garcia-Garibay, M.A. (2005). Amphidynamic crystals: structural blueprints for molecular machines. In Molecular Machines, T.R. Kelly, ed. (Springer), pp. 179–227.
32. Rizzuto, F.J., Ramsay, W.J., and Nitschke, J.R. (2018). Otherwise unstable structures self-assemble in the cavities of cuboctahedral coordination cages. J. Am. Chem. Soc. *140*, 11502–11509.
33. Löffler, S., Lübben, J., Wuttke, A., Mata, R.A., John, M., Dittrich, B., and Clever, G.H. (2016). Internal dynamics and guest binding of a sterically overcrowded host. Chem. Sci. *7*, 4676–4684.
34. Mugridge, J.S., Szigethy, G., Bergman, R.G., and Raymond, K.N. (2010). Encapsulated Guest-Host dynamics: guest rotational barriers and tumbling as a probe of host interior cavity space. J. Am. Chem. Soc. *132*, 16256–16264.
35. Kitagawa, H., Kobori, Y., Yamanaka, M., Yoza, K., and Kobayashi, K. (2009). Encapsulated-guest rotation in a self-assembled heterocapsule directed toward a supramolecular gyroscope. Proc. Natl. Acad. Sci. USA *106*, 10444–10448.
36. Elemans, J.A.A.W., and Nolte, R.J.M. (2019). Porphyrin cage compounds based on glycoluril—from enzyme mimics to functional molecular machines. Chem. Commun. *55*, 9590–9605.
37. Gilissen, P.J., White, P.B., Berrocal, J.A., Vanthuyne, N., Rutjes, F.P.J.T., Feringa, B.L., Elemans, J.A.A.W., and Nolte, R.J.M. (2020). Molecular motor-functionalized porphyrin macrocycles. Nat. Commun. *11*, 5291.
38. van Leeuwen, T., Lubbe, A.S., Štacko, P., Wezenberg, S.J., and Feringa, B.L. (2017). Dynamic control of function by light-driven molecular motors. Nat. Chem. Rev. *1*, 96.
39. Kundu, P.K., Samanta, D., Leizrowice, R., Margulis, B., Zhao, H., Börner, M., Udayabhaskararao, T., Manna, D., and Klajn, R. (2015). Light-controlled self-assembly of non-photoresponsive nanoparticles. Nat. Chem. *7*, 646–652.
40. Ube, H., Yasuda, Y., Sato, H., and Shionoya, M. (2017). Metal-centred azaphosphatriptycene gear with a photo- and thermally driven mechanical switching function based on coordination isomerism. Nat. Commun. *8*, 14296.
41. Qu, D.H., Wang, Q.C., Zhang, Q.W., Ma, X., and Tian, H. (2015). Photoresponsive host-guest functional systems. Chem. Rev. *115*, 7543–7588.
42. Klajn, R. (2014). Spiropyran-based dynamic materials. Chem. Soc. Rev. *43*, 148–184.
43. Russew, M.M., and Hecht, S. (2010). Photoswitches: from molecules to materials. Adv. Mater. *22*, 3348–3360.
44. Moosa, B., Alimi, L.O., Shkurenko, A., Fakim, A., Bhatt, P.M., Zhang, G., Eddaoudi, M., and Khashab, N.M. (2020). A polymorphic azobenzene cage for energy-efficient and highly selective p-xylene separation. Angew. Chem. Int. Ed. Engl. *59*, 21367–21371.
45. Wang, Z., Knebel, A., Grosjean, S., Wagner, D., Bräse, S., Wöll, C., Caro, J., and Heinke, L.

(2016). Tunable molecular separation by nanoporous membranes. Nat. Commun. *7*, 13872.

46. Zheng, Y., Sato, H., Wu, P., Jeon, H.J., Matsuda, R., and Kitagawa, S. (2017). Flexible interlocked porous frameworks allow quantitative photoisomerization in a crystalline solid. Nat. Commun. *8*, 100.

47. Li, R.J., Tessarolo, J., Lee, H., and Clever, G.H. (2021). Multi-stimuli control over assembly and guest binding in metallosupramolecular hosts based on dithienylethene photoswitches. J. Am. Chem. Soc. *143*, 3865–3873.

48. Williams, D.E., Martin, C.R., Dolgopolova, E.A., Swifton, A., Godfrey, D.C., Ejegbavwo, O.A., Pellechia, P.J., Smith, M.D., and Shustova, N.B. (2018). Flipping the switch: fast photoisomerization in a confined environment. J. Am. Chem. Soc. *140*, 7611–7622.

49. Mondal, B., Ghosh, A.K., and Mukherjee, P.S. (2017). Reversible multi-stimuli switching of a spiropyran-functionalized organic cage in solid and solution. J. Org. Chem. *82*, 7783–7790.

50. Kundu, P.K., Olsen, G.L., Kiss, V., and Klajn, R. (2014). Nanoporous frameworks exhibiting multiple stimuli responsiveness. Nat. Commun. *5*, 3588.

51. Castiglioni, F., Danowski, W., Perego, J., Leung, K.-C.F., Sozzani, P., Bracco, S., Wezenberg, S.J., Comotti, A., and Feringa, B.L. (2020). Modulation of porosity in a solid material enabled by bulk photoisomerization of an overcrowded alkene. Nat. Chem. *12*, 595–602.

52. Mukhopadhyay, R.D., Kim, Y., Koo, J., and Kim, K. (2018). Porphyrin boxes. Acc. Chem. Res. *51*, 2730–2738.

53. Benke, B.P., Aich, P., Kim, Y., Kim, K.L., Rohman, M.R., Hong, S., Hwang, I.-C., Lee, E.H., Roh, J.H., and Kim, K. (2017). Iodide-selective synthetic ion channels based on shape-persistent organic cages. J. Am. Chem. Soc. *139*, 7432–7435.

54. Hong, S., Rohman, M.R., Jia, J., Kim, Y., Moon, D., Kim, Y., Ko, Y.H., Lee, E., and Kim, K. (2015). Porphyrin boxes: rationally designed porous organic cages. Angew. Chem. Int. Ed. Engl. *54*, 13241–13244.

55. Goswami, A., and Schmittel, M. (2020). Double rotors with fluxional axles: domino rotation and azide–alkyne Huisgen cycloaddition catalysis. Angew. Chem. Int. Ed. Engl. *59*, 12362–12366.

56. Gaikwad, S., Goswami, A., De, S., and Schmittel, M. (2016). A Metalloregulated four-state nanoswitch controls two-step sequential catalysis in an eleven-component system. Angew. Chem. Int. Ed. Engl. *55*, 10512–10517.

57. Liu, S., Kondratuk, D.V., Rousseaux, S.A.L., Gil-Ramírez, G., O'Sullivan, M.C., Cremers, J., Claridge, T.D.W., and Anderson, H.L. (2015). Caterpillar track complexes in template-directed synthesis and correlated molecular motion. Angew. Chem. Int. Ed. Engl. *54*, 5355–5359.

58. Muraoka, T., Kinbara, K., and Aida, T. (2006). Mechanical twisting of a guest by a photoresponsive host. Nature *440*, 512–515.

59. Olsson, S., Dahlstrand, C., and Gogoll, A. (2018). Design of oxophilic metalloporphyrins: an experimental and DFT study of methanol binding. Dalton Trans *47*, 11572–11585.

60. Samanta, S.K., Samanta, D., Bats, J.W., and Schmittel, M. (2011). DABCO as a dynamic hinge between cofacial porphyrin panels and its tumbling inside a supramolecular cavity. J. Org. Chem. *76*, 7466–7473.

61. Thies, S., Sell, H., Bornholdt, C., Schütt, C., Köhler, F., Tuczek, F., and Herges, R. (2012). Light-driven coordination-induced spin-state switching: rational design of photodissociable ligands. Chemistry *18*, 16358–16368.

62. Hirose, T., Helmich, F., and Meijer, E.W. (2013). Photocontrol over cooperative porphyrin self-assembly with Phenylazopyridine ligands. Angew. Chem. Int. Ed. Engl. *52*, 304–309.

Dr. Shyamasish Das

THE JOURNAL OF PHYSICAL CHEMISTRY C
A JOURNAL OF THE AMERICAN CHEMICAL SOCIETY

pubs.acs.org/JPCC

Article

Structure and Electronic Effects from Mn and Nb Co-doping for Low Band Gap $BaTiO_3$ Ferroelectrics

Published as part of The Journal of Physical Chemistry virtual special issue "D. D. Sarma Festschrift".

Soham Mukherjee,* Dibya Phuyal, Carlo U. Segre, Shyamashis Das, Olof Karis, Tomas Edvinsson, and Håkan Rensmo*

Cite This: *J. Phys. Chem. C* 2021, 125, 14910−14923

Read Online

ACCESS | Metrics & More | Article Recommendations | Supporting Information

ABSTRACT: We have investigated the doping-induced local structural and electronic effects in the recently developed low band gap room temperature ferroelectric Mn−Nb co-doped $BaTiO_3$. Experimental and theoretical Raman spectroscopies are utilized to quantify the Ti off-centering, identified to be the intrinsic origin of ferroelectricity in these systems. Mn and Nb exhibit contrasting doping behaviors that have remarkable effects on $BaTiO_3$ functionality. Jahn−Teller distorted Mn^{3+} is primarily associated with lowering of the bulk band gap, while charge-compensating Nb^{5+} off-centers within the O_6 octahedra, creating a polar mode that stabilizes the ferroelectric ground state. The charge neutral aliovalent Mn^{3+}−Nb^{5+} pair effectively couples to the inherent ferroelectric instability of the $BaTiO_3$ lattice, restoring some spontaneous polarization lost by doping Mn^{3+} (d^4) ions at Ti^{4+} (d^0) sites.

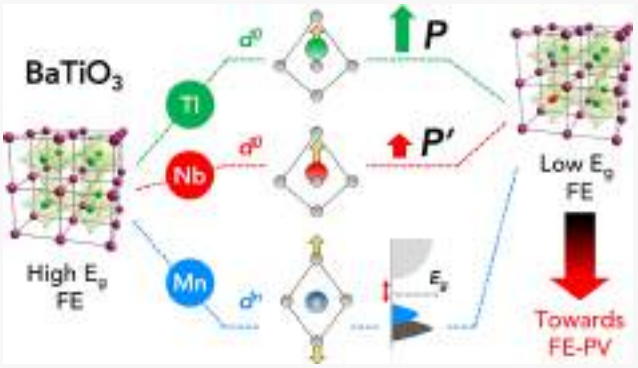

INTRODUCTION

Research on ferroelectric materials has come a long way since the discovery of the perovskite oxide $BaTiO_3$ as a ferroelectric in 1946,[1] finding a wide array of applications[2,3] in the modern age such as capacitors,[4,5] actuators,[6] sensors,[7,8] waveguide modulators,[9,10] and ferroelectric memories.[11] Ferroelectrics typically exhibit high dielectric constants and carry spontaneous lattice polarization (P) that can be reversed by using an external electric field greater than the coercive field. This intrinsic polarization can be utilized to sustain efficient separation of photogenerated electron−hole pairs, thereby generating a steady-state photocurrent. The high electric field in ferroelectrics is capable of producing above band gap voltages,[12] with controllable voltage output.[13] This fundamental advantage over conventional p−n junctions explains the tremendous interest in ferroelectric photovoltaics.[14−17]

In the classical ferroelectric $BaTiO_3$, the lowest unoccupied energy states (3d) of d^0 ion Ti^{4+} strongly hybridize with O 2p states, thus largely driving the ferroelectric distortion.[18] The Ti^{4+} ion off-centers from its centrosymmetric position in the unit cell, resulting in large inherent polarization (P = 24.1 $\mu C/cm^2$). In addition to such a high P value, $BaTiO_3$ exhibits a rich structural phase diagram, high chemical stability, and wide doping tunability of the perovskite structure ABO_3 which provides an ideal framework for tuning and exploring multifunctionalities.[19−22] However, the biggest challenge in realizing $BaTiO_3$ ferroelectrics as photovoltaics stems from its typically large bulk band gap (3.2 eV) which limits its access mostly to the UV range, as commonly observed[23,24] for all d^0-ferroelectric perovskites (e.g., $KNbO_3$ and $BaZrO_3$). This is primarily due to the requirement of partial d-occupancy on the B-site cation to reduce the optical band gap that tends to remove the ferroelectric distortion, eventually stabilizing the prototypical high-symmetry phase.[25−27] Work on improving overall performance focuses mainly on narrowing the band gap through modification in compositions and the connection between polar order and photovoltaic effect.[15] Band gap engineering via chemical substitution such as A-site La-doped $BiFeO_3$[15] and B-site Cr-doped in $BiFeO_3$ has shown remarkable overall efficiencies of nearly 8%.[24] Another route is to make solid solutions such as $[KNbO_3]_{1-x}[BaNi_{1/2}Nb_{1/2}O_{3-\delta}]_x$ which show a wide tunability with enhanced photovoltaic properties under visible light.[16] Furthermore, the

Received: March 21, 2021
Revised: June 15, 2021
Published: July 1, 2021

competing structural distortions associated with a remnant polarization are dramatically reduced as a function of doping. This complicates the trade-off between a narrow gap and large remnant polarization.

This goal was, however, recently accomplished[28] by co-doping equimolar amounts of Mn^{3+} (d^4) and Nb^{5+} (d^0) at Ti^{4+} sites in $BaTiO_3$. This doping strategy allowed for substantial band gap tunability (1.5−3.2 eV), suitable for visible light absorption, and sufficiently high P values. A P value of 1.66 eV was reported for 7.5% doping (P = 15.1 $\mu C/cm^2$), which retained ∼70% polarization of $BaTiO_3$. DFT+U calculations[28,29] revealed the doping induced midgap states to be of predominantly Mn 3d character, as was also concluded from enhancement of the Mn 3d states detected by resonant photoelectron spectroscopy,[29] identifying Jahn−Teller (JT) active Mn^{3+} (d^4) to be responsible for reduction of the observed band gap. Nb^{5+} (d^0), on the other hand, acted as a charge compensator, also capable of stabilizing ferroelectric ground states similar to ferroelectric niobates.[30−32] The Mn−Nb dopant pair dipole was argued to effectively couple to the $BaTiO_3$ lattice, thereby retaining the electric polarization to a large extent. Domain switching was observed through piezoresponse force microscopy (PFM)[33] measurements on epitaxial thin films of Mn−Nb co-doped $BaTiO_3$ (hereafter termed BTMNO) grown by pulsed later deposition, validating good ferroelectric response in films, a key step toward $BaTiO_3$-based PV[34,35] device fabrication.

While the electronic properties of the BTMNO are being investigated currently, experimental studies on the local geometric structure about the dopant ions and how they link to the electronic structure have been less explored. This is of fundamental importance, as local structural distortions operative beneath a well-defined periodic lattice[36−39] can often significantly influence material functionalities. The present work uses X-ray absorption fine structure (XAFS) with support from Raman and DFT calculations to elucidate the dopant environment: position of dopants, formal valence states, modes of distortion, and their link to the material functionality. We find Mn and Nb residing at Ti sites to be an effective charge neutral pair exhibiting fundamentally different modes of local distortions, which leads them to assume characteristic roles in the band gap engineering and retention of electrical polarization in BTMNO. The ability to control such local structures is fundamental to formulate strategies for making ferroelectric perovskites efficient solar harvesters.

METHODS

Experiments. BTMNO with x = 0.0, 0.025, 0.05, 0.075, and 0.1 were prepared by using previously reported methods.[28] Raman spectroscopy measurements were performed by using a Renishaw inVia Raman spectrometer equipped with a 633 nm wavelength laser and an edge filter for Rayleigh scattering rejection. A sharp cut of the edge filter designed for 633 nm wavelength allowed the measurements of soft modes to as low as 40 cm^{-1}.

X-ray absorption spectroscopy (XAS) measurements at the K-edges of Ti (4966 eV), Mn (6539 eV), and Nb (18986 eV) were performed at the Materials Research Collaborative Access Team (MRCAT) Sector 10 bending magnet line of the Advanced Photon Source, Argonne National Laboratory, with high photon flux (6.4×10^9 at 10 keV) and high resolution ($\Delta E/E \sim 10^{-4}$). The incident photon beam was monochromatized by using a Si (111) double-crystal monochromator detuned by 50% to remove harmonics. A mixture of N_2 and He gas was optimized to absorb ∼5−10% of the incident photons. Polycrystalline samples were first ground into a fine powder, mixed with boron nitride and PVDF, and then pressed into 7 mm diameter pellets. Samples were oriented at 45° with respect to the incident X-ray beam, thereby allowing simultaneous measurement of a reference foil using the transmitted beam intensity. Flourescence data were collected by using a four-element Vortex (Hitachi) SDD detector with xMap (XiA) digital pulse processing electronics. The step size corresponding to selected XAS energy ranges for each metal edge is provided in the Supporting Information (Table S1). The fluorescence mode data were found to be free from significant amplitude loss due to self-absorption effects. During data collection multiple scans were recorded for each sample. Comparing these individual scans against their average gives an idea about the noise level and the reliability of the data. All XAS data sets were processed and analyzed by using the Athena-Artemis software suite, a front end to FEFF and IFEFFIT.[40] The subtracted background was calculated by using the AUTOBK algorithm implemented in the software.[41]

EXAFS Analyses. The XAS data were first converted to absorption versus energy, followed by energy scale calibration, pre-edge background removal using a linear fit, and post-edge background removal using a third-order polynomial. All the spectra were normalized to have an edge step of 1. The amplitude reduction factor (S_0^2) values for Mn (0.85) and Nb (0.98) were first extracted individually and thereafter retained as constant values while performing simultaneous fits to Mn K and Nb K-edge data for all BTMNO compositions. Coordination numbers, bond distances, energy offsets, and pseudo-Debye−Waller factors (σ^2) were extracted as local structural parameters. For Ti K-edge data, strong interference with the Ba L_3 (5247 eV) edge limits usable k_{max} to ∼8.2 $Å^{-1}$, rendering EXAFS resolution too poor to account for Ti off-centering in terms of three different Ti−O bond lengths. Thus, the modulus of Fourier transforms of $\chi(k)$ over the range 2.0−8.0 $Å^{-1}$ for the Ti K-edge data (Figure 2d) has been interpreted qualitatively and compared to results obtained from the pre-edge fine structure analyses. For both dopant K-edges (Mn and Nb), longer k ranges could be extracted: 2.0−9.0 $Å^{-1}$ for Mn and 3.0−13.5 $Å^{-1}$ for Nb. Fits to Mn K and Nb K data sets were performed over these k-ranges by using the standard EXAFS equation[40] and a Hanning window (Δk = 2 $Å^{-1}$, ΔR = 0.2 Å). We calculated the EXAFS for undoped tetragonal $BaTiO_3$ from the available crystal structure information (Inorganic Crystal Structure Database ICSD-67520) as the starting model. A second calculation was performed, where the neighboring Ti atoms were replaced by Mn and Nb. In both calculations, the central Ti atom was replaced with Mn (or Nb) while fitting the Mn K (or Nb K) edge data. While this approach allows us to estimate the Ti:(Mn + Nb) ratio at B-sites, the observed uncertainty limits were ∼5%, higher than the doping interval (2.5%). Thus, the final fits were performed by fixing the Ti:(Mn + Nb) ratio to their nominal values. A minimum of two metal (M)−O (M = Mn, Nb) paths were required to describe the O-shell, two M−Ba paths for the Ba-shell and two paths for the next-neighbor B-site: one Ti−Ti single scattering and one Ti−Ti−O multiple scattering path, which amounts to a large number of free parameters. Therefore, the number of free parameters were minimized by four approaches: (1) estimating the S_0^2 values for Mn and Nb individually and by using them as constant

https://doi.org/10.1021/acs.jpcc.1c02539
J. Phys. Chem. C 2021, 125, 14910−14923

values for simultaneous fits, (2) choosing a single ΔE_0 parameter (to align the energy grid of the calculation to that of the data) for all the FEFF paths for a given BTMNO composition, (3) independently estimating the coordination numbers (N) for first shell (N = 6 for O), second shell (N = 8 for Ba), third shell (N = 6 for M = Ti, Mn, Nb), and multiple scattering paths (N = 8) and fixing them; (4) using one isotropic expansion factor (α_1) for the two M−Ba distances (M−Ba1 and M−Ba2) and a second isotropic expansion factor (α_2) for Ti−Ti single scattering and Ti−Ti−O multiple scattering paths. The α_1 and α_2 parameters have been translated into the corresponding bond distances and tabulated. The estimated bond distances and coordination numbers tally very well with the reported crystallographic data on tetragonal $BaTiO_3$ structure (ICSD-67520), which gives us confidence about the high data quality in the present case. The errors were estimated by a standard Levenberg−Marquardt, nonlinear minimization of the statistical χ^2 parameter, built within the Artemis program.[40] Fits to all data in k and R (real part and magnitude) space, extracted EXAFS parameters and their associated error limits are detailed in the Supporting Information.

Theory. Density functional theory (DFT) calculations were performed within two contexts: to extract the theoretical ground state geometries by using three different functionals (PBE, PBE0, and B3LYP) and to assist in the assignment of Raman bands by applying linear response DFT. The phonon modes in $BaTiO_3$ were obtained with periodic calculations in Crystal17[42,43] using the general gradient approximation (GGA) functional PBE and hybrid DFT with the PBE0 and B3LYP functionals. Consistent Gaussian basis sets of triple-zeta valence with polarization quality[44] were utilized for Ti and O, while a scalar relativistic Hay and Wadt small core effective potential[45] and 10 electron valence description[46] were used for Ba. A mesh of 12 × 12 × 12 k points in reciprocal space was generated according to the Monkhorst−Pack method[47] and used for both the geometry optimizations and linear response calculations. The geometry optimizations were performed for both the cell and atoms by using a SCF energy convergence limit of 10^{-8} hartree. Linear response DFT calculations were subsequently performed on the geometry-optimized structures where both the dielectric tensor and vibrational modes were extracted. The Raman intensities were calculated by a coupled-perturbed Kohn−Sham calculation up to fourth order before the calculation of the frequencies as implemented in Crystal17.[48]

RESULTS AND DISCUSSION

Modeling BTO. To provide a thorough basis for the discussion, we performed density functional theory (DFT) calculations of the parent compound ($BaTiO_3$) using three different functionals: one with a pure generalized gradient approximation, GGA (PBE), and two hybrid-functionals (PBE0 and B3LYP). The theoretical ground state was fully geometry-optimized for both cubic and tetragonal cell dimensions and internal atomic coordinates, while subsequent linear response DFT calculations provided the dielectric tensor (Table 1) with naturally slightly lower value along the polar direction in comparison to the less polar directions. To faithfully assign experimental effects arising from asymmetries, such as off-centering, full vibrational assignments were performed by analyzing the displacement vectors and their relative amplitudes. The linear response DFT calculations and the Raman-active vibrational modes can be seen in Table 2. The Raman intensities were extracted by using the Berry phase method using a coupled-perturbed Kohn−Sham calculation approach to fourth order before the calculation of the frequencies.

Table 1. Ground State Structure, Dielectric Tensor, and Band Gap of Cubic (*Pm*-3*m*) and Tetragonal (*P*4*mm*) $BaTiO_3$ Obtained in This Work

	PBE	PBE0	B3LYP	exp[a,b]
		cubic (*Pm*-3*m*)		
a (Å)	4.019	3.978	4.021	4.006
ε_{11}, ε_{22}, ε_{33}	6.476	5.184	5.337	(5.4)
E_g (eV)	1.71	3.79	3.33	3.3
		tetragonal (*P*4*mm*)		
a (Å)	3.997	3.959	3.983	4.000[a] (3.986)[b]
c (Å)	4.136	4.092	4.225	4.018 (4.026)
c/a	1.035	1.034	1.061	1.005 (1.010)
δ_z(Ti)	0.025	0.025	0.016	0.018 (0.015)
ε_{11}, ε_{22}	6.057	4.906	5.188	5.19[c]
ε_{33}	5.169	4.456	4.879	5.05[c]
E_g (eV)	1.76	3.89	3.39	3.4[d]

[a]*Acta Crystallogr., Sect. B: Struct. Sci.* **1992**, *48*, 764. [b]Shirane, G.; Danner, H.; Pepinsky, R. *Phys. Rev.* **1957**, *105*, 856. [c]Hermet, P.; Veithen, M.; Ghosez, Ph. *J. Phys. Condens. Matter* **2009**, *21*, 215901. [d]Wemple, S. H. *Phys. Rev. B* **1970**, *2*, 2679.

Table 2. Calculated and Experimental Raman Active Γ-Point Phonon Frequencies and Dominating LO Phonons from the TO-LO Split for the Tetragonal (*P*4*mm*) Phase of $BaTiO_3$ (in cm^{-1})

Raman mode	PBE	PBE0	B3LYP	exp[a]	exp[this work]
$1A_1/2E$	165	180	187	168	
2E	170	196	187	168	
$2A_1$	291	376[b]	258	270	270
3E	297	313	310	270−320[c]	270−320[c]
B_1	291	313	315	304	308
4E	466	499	494	470	515
$3A_1$	546	569	512	515	515
E TO−LO split	658	717	709	715	720
A_1 TO−LO split	725	777	733	715	720

[a]Raman spectrum of $BaTiO_3$. Parsons, J. L.; Rimai, L. *Solid State Commun.* **1967**, *5*, 423−427. [b]This mode was found at unusually high wavenumbers by using the PBE0 functional. [c]Peak hidden by other stronger vibration modes in the region noted.

All functionals give the well-known overdetermination along the c-axis and thus a slight elongated tetragonal structure in agreement with previous theoretical calculations.[49] Incorporation of exchange via hybrid functionals enables theoretical description that match the experimental situation better than the pure GGA. In addition, the relative off-centering of Ti in the unit cell and the dielectric tensor is best described by B3LYP. The general trends and main conclusions, however, can without loss of generality also be performed from the vibration modes found for the other functionals (Table 2). By use of the B3LYP functional, cubic $BaTiO_3$ exhibits a triply degenerate Ti-displacement mode with compensating Ti−O

https://doi.org/10.1021/acs.jpcc.1c02539
J. Phys. Chem. C 2021, 125, 14910−14923

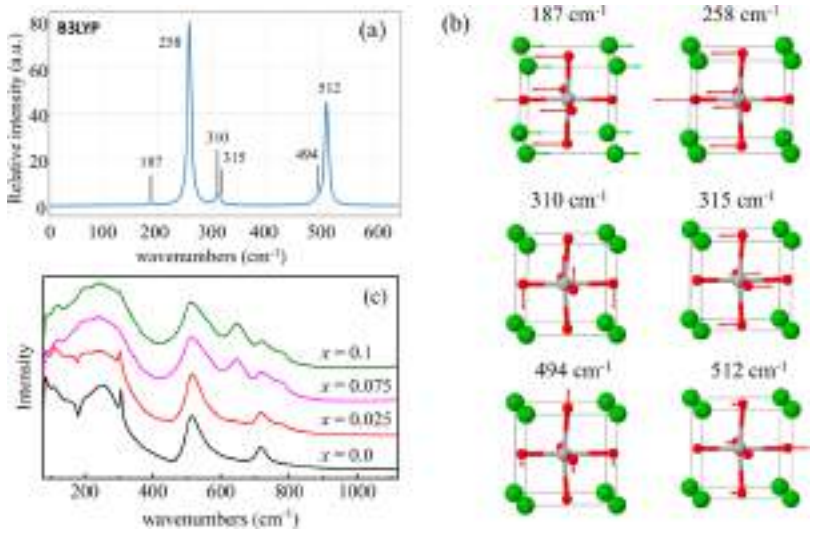

Figure 1. (a) Calculated Raman spectra for tetragonal (*P4mm*) $BaTiO_3$ with the theoretical wavenumbers with the B3LYP functional. (b) Schematic representation of the eigenvectors of the Raman active phonon modes shown in the Ti-centered $BaTiO_3$ perovskite unit. (c) Experimental Raman spectra for the BTMNO series: x = 0.0 (black), 0.025 (red), 0.075 (magenta), and 0.1 (olive).

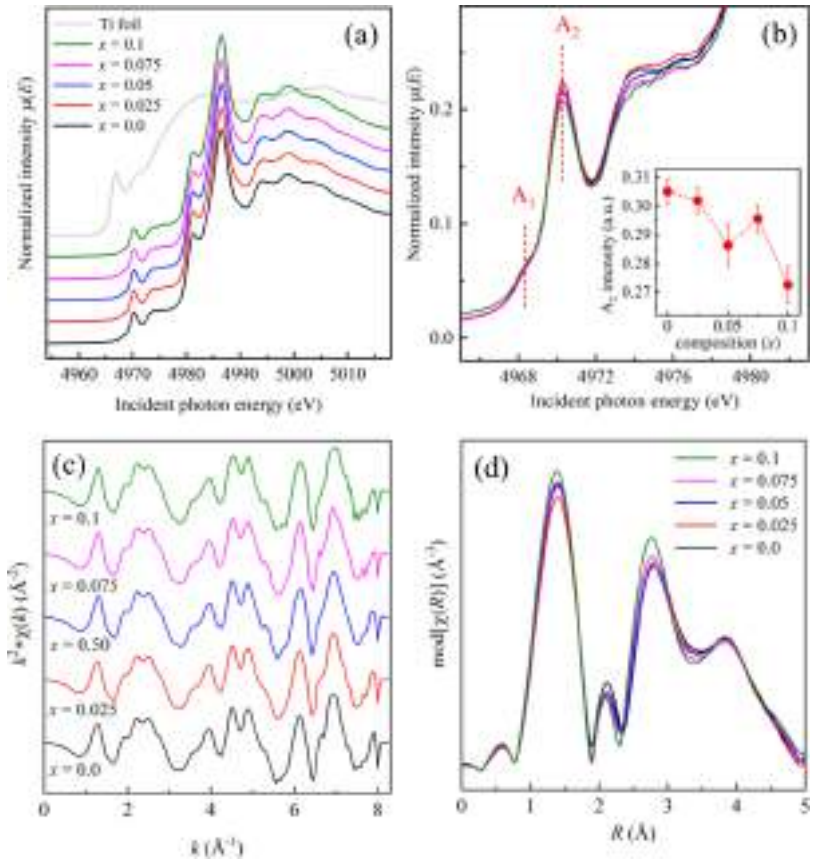

Figure 2. (a) Ti K XANES for the BTMNO series: x = 0.0 (black), 0.025 (red), 0.05 (blue), 0.075 (magenta), and 0.1 (olive), showing Ti^{4+} oxidation states. (b) Pre-edge region showing intense p−d peaks (A_2) in BTMNO samples due to Ti off-centering within O_6 octahedra; the inset shows A_2 peak intensities decreasing with doping, suggesting loss of polarization. (c) k^2-weighted $\chi(k)$ functions and (d) modulus of the $\chi(R)$ functions for Ti data, showing remarkable similarities in Ti local environments in BTMNO systems.

asymmetric stretch at 92 cm^{-1} and a triply degenerate Ti-displacement with more or less constant Ti−O distance but instead compensating Ti−O bending and Ba displacement at 180 cm^{-1}. Two triply degenerate vibrations are found at 326 and 508 cm^{-1} which correspond to asymmetric O−Ti−O bending and symmetric bending, respectively, where the latter is coupled to an asymmetric O−Ti−O stretch. The vibrations at 92, 180, and 508 cm^{-1} are IR-allowed with the first mode having high intensity. The 180 cm^{-1} mode has more or less negligible intensity due to the small change in dipole during the vibration, while the 508 cm^{-1} vibration should have a small but detectable intensity due to the induced dipole change upon

https://doi.org/10.1021/acs.jpcc.1c02539
J. Phys. Chem. C 2021, 125, 14910−14923

the Ti−O vibration coupling. Neither of the modes are Raman-active, however, due to the cancellation of changes in polarizability during the vibration from the selection rules of a cubic perovskite system.

The off-centering of Ti in the transition to a tetragonal system activates several of the vibrations due to the broken symmetry. For the tetragonal phase, the 180 cm^{-1} mode in the cubic system is translated to 187 cm^{-1}, and the triply degenerate 326 cm^{-1} mode in the cubic system splits into a high intensity 258 cm^{-1} mode and a doubly degenerate mode at 310 cm^{-1}. The triply degenerate 508 cm^{-1} mode in the cubic system is transformed into a doubly degenerate mode at 494 cm^{-1} and a nondegenerate mode at 512 cm^{-1}. The theoretical Raman spectrum with the B3LYP functional and the displacement for the eigenvectors of the elements in the unit cell for the tetragonal phase ($P4mm$) is shown in Figure 1a,b. As is well-known, the dipoles that are created with long-wave longitudinal phonons in polar crystals are responsible for the removal of degeneracy between the LO and TO phonons at the Brillouin zone center and thus the phenomenon of LO−TO splitting. Because the magnitude of the TO−LO split is dependent on the dielectric constant, a hybrid functional is here preferred due to the inclusion of more exact exchange and thus closer correspondence between the experimental and theoretical dielectric properties. By use of the Born effective charges and the theoretical dielectric tensor, subsequent linear response calculations were utilized to obtain LO phonons. Using the B3LYP functional, we calculated the LO modes to 184 cm^{-1} (E(LO)), 196 cm^{-1} (A_1(LO)), 310 cm^{-1} (E(LO)), 482 cm^{-1} (E(LO)), 486 cm^{-1} (A_1(LO)), 709 cm^{-1} (E(LO)), and 733 cm^{-1} (A_1(LO)), where only the latter two have high intensities. For the comparison of the vibrational modes using different DFT functionals and experimental modes, see Table 2.

Experimental Raman Spectra. Figure 1c shows the Raman spectra of $BaTiO_3$ (x = 0.0) and BTMNO samples for x = 0.025, 0.075, and 0.1. Upon comparison with the theoretical spectra for the tetragonal structure with that of the experimental $BaTiO_3$, it is clear that the experimental spectrum is more complex and contains more asymmetric as well as broader modes. Moreover, the complexity of the spectra increases further with doping. The Raman spectrum shows broad peaks centered around 270 cm^{-1} ($2A_1$, E(TO)), a sharp peak at 308 cm^{-1} (B_1, E(LO + TO)), an asymmetric broad peak at 515 cm^{-1} (A_1, E(TO)), and a broad weak peak at 720 cm^{-1} (A_1(LO), E(LO)), where phonon mode assignments are given inside parentheses. A_1 modes are related to Ti ion displacements relative to O and Ba ions along the c-axis and E modes to Ti ion displacements along the a/b-axis, while B_1 modes are related to O ion displacement along the c-axis.[50] The presence of the E(1TO) soft mode is a fundamental criterion for spontaneous polarization to exist through long-range phenomenon, which indicates the existence of ferroelectric properties in BTMNO samples. It increases in relative intensity as x increases; that is, the volume fraction of the B-site exhibiting an asymmetric breathing mode increases with x, which provides direct evidence[51] of B-site doping of Mn and Nb. One can note that the asymmetric shoulder of the 515 cm^{-1} band develops with increased doping. Recalling the mode assignment from DFT (Figure 1a), the JT distorted Mn−O_6 octahedra and off-centered Nb−O_6 octahedra are seen to distort the symmetric bending modes in the Ti−O_6 octahedra in the doped samples compared to pure $BaTiO_3$.

One can also note a new band emerging at around 645 cm^{-1} with an accompanying band at around 800 cm^{-1} with intensity at the expense of the intermediate band at 720 cm^{-1} (Figure 1c), further supporting the broken symmetry modifying the TO−LO split upon Ti replacement. The origin of this is due to incorporation of heavier B-site cations and changed bond strength of the metal−O bond. The line shapes at lower wavenumbers also become visibly broader at higher concentrations (7.5% and 10%), as more Ti sites are being substituted by Mn and Nb ions.

Ti K XAS. The absolute absorption energy (E_0) for a specific X-ray edge can be used to fingerprint the mean valence for an element when compared to well-known standards. Figure 2a shows the normalized Ti K XANES for the BTMNO series and Ti foil. The E_0 positions, as estimated from the position of the inflection point in the main part of the absorption Ti K-edges for all BTMNO samples, show extremely consistent values close to 4987 eV, indicating a Ti^{4+} oxidation state. Figure 2b shows the pre-edge region of the Ti K XANES for BTMNO samples, exhibiting multiple peaks,[52,53] of which the first two peaks (A_1 and A_2) are marked. While peak A_1 is explained by a quadrupolar 1s → 3d transition, peak A_2 has contributions from both quadrupolar (1s → 3d) and dipolar (1s → 4p) transitions, the quadrupolar transition being the more dominant one.[52,53] In tetragonal $BaTiO_3$, Ti atoms are displaced from the center of O_6 octahedra, thereby breaking the centrosymmetry and affecting p−d mixing. A_2 peak intensity is therefore an indicator of the degree of orbital hybridization between the two atomic states and is directly proportional to the mean-squared displacements of Ti from the centers of the surrounding O_6 octahedra. The A_2 peak is difficult to model with a single Gaussian over a narrow window due to significant overlap with the intense peaks beyond 4972 eV (Figure 2b). Thus, a much wider pre-edge region (∼15 eV) is needed to be modeled for a more accurate estimate of A_2 peak intensity variations as a function of doping (x). Pre-edge fine structure fits over −20 to −5 eV across the Ti K absorption edge of the BTMNO series were performed, after proper background subtraction using a linear baseline and a Lorentzian function. The background subtracted data, corresponding total fits, and contributions of individual Gaussian components to the total fit for all BTMNO samples are plotted in Figure S1, and the fit parameters are tabulated in Table S2. A_2 peak intensities derived from the fits are plotted in the inset of Figure 2b. We find A_2 intensities to decrease with co-doping Mn and Nb at Ti sites, suggesting reduced p−d mixing.

Increased doping systematically decreases tetragonality and, hence, the polarization in $BaTiO_3$. The largest drop is noticed going from x = 0.075 to x = 0.1, where the system becomes a paraelectric (cubic). Nonetheless, Figure 2b clearly establishes that in BTMNO Ti ions remain off-centered within the Ti−O_6 octahedral environment in $BaTiO_3$ for all doping concentrations; the extent of this distortion decreases with x.

Figure 2c shows the k^2-weighted $\chi(k)$ functions for Ti. We find remarkable similarities in Ti local environments, suggesting the Mn and Nb dopants to have little influence on the overall Ti environment. Ba L_3 (5247 eV) XAS interferes strongly with Ti K (4966 eV) XAS, limiting reliable data for Ti K only up to k_{max} ∼ 8.2 $Å^{-1}$. The number of independent variables (n) that could be extracted is defined by the resolution of EXAFS as $\approx 2\Delta k \Delta R/\pi$. For Ti K, n gets reduced to only 3, far short of minimum requirement n = 7 to estimate

https://doi.org/10.1021/acs.jpcc.1c02539
J. Phys. Chem. C 2021, 125, 14910−14923

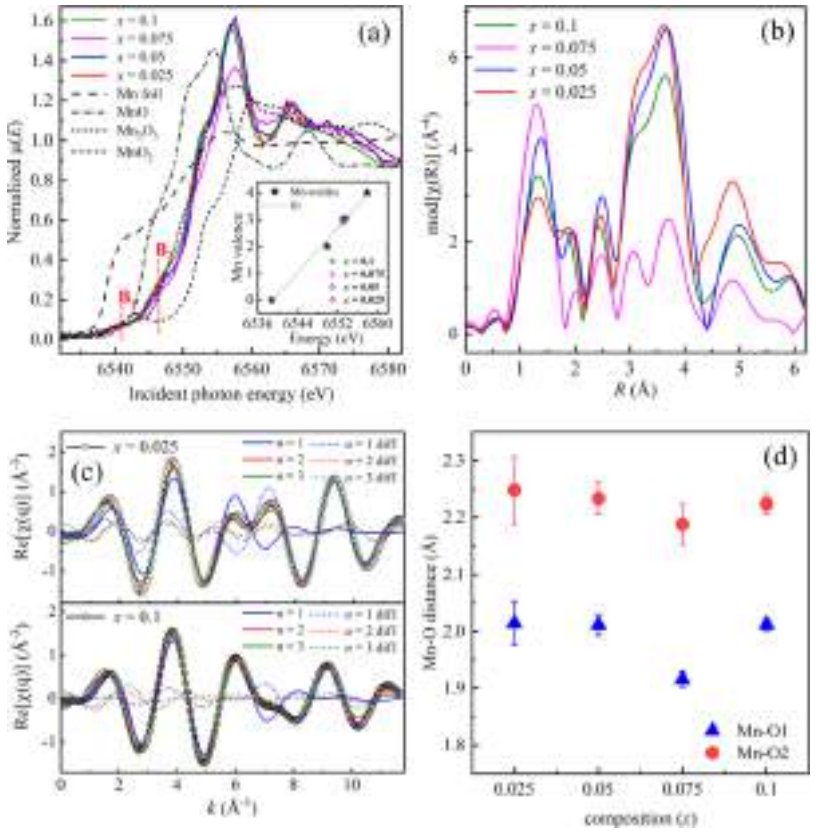

Figure 3. (a) Mn K XANES for the BTMNO series: x = 0.025 (red), 0.05 (blue), 0.075 (magenta), 0.1 (olive), and well-known Mn standards; inset shows Mn in BTMNO systems to assume 3+ formal valence. (b) Modulus of the k^3-weighted $\chi(R)$ functions for Mn data. (c) Mn−O shell modeled with different numbers (n) of Mn−O distances: 1 (blue), 2 (red), and 3 (olive) and corresponding differences plotted in dotted lines. (d) Mn−O distances within $Mn-O_6$ octahedra, showing four short Mn−O1 (blue triangles) and two long Mn−O2 (red circles) bonds, suggesting JT distortion within the $Mn^{3+}-O_6$ octahedra.

Ti off-centering in the $Ti-O_6$ octahedra. The modulus of Fourier transforms of $\chi(k)$ over the range 2.0−8.0 $Å^{-1}$ for the Ti K-edge data is shown in Figure 2d. A small increase of amplitude is noticeable for the x = 0.1 (olive) sample, suggestive of somewhat lower extent of distortion in the Ti local environment. This increase is be expected from decreasing tetragonality of the system with doping (Figure 2b), which eventually becomes cubic at x = 0.1.

Mn K XAS. Figure 3a shows the normalized Mn K XANES for the BTMNO series in comparison with reference Mn oxides [MnO(II), Mn_2O_3(III), and MnO_2(IV)] and Mn foil. A linear fit to the estimated E_0 positions of the Mn standards was used to extract the Mn valence states by mapping the E_0 positions of the BTMNO system: 6553.66 ± 0.11 eV for x = 0.025, 6553.73 ± 0.07 eV for x = 0.05, 6552.98 ± 0.11 eV for x = 0.075, and 6553.35 ± 0.03 eV for x = 0.1. The E_0 values for all BTMNO samples show a narrow spread around the Mn_2O_3 standard (6553.02 ± 0.03 eV), indicating a Mn^{3+} oxidation state (Figure 3a, inset). The E_0 value also agrees well with the reported[54] E_0 value for the Mn K-edge in $LaMnO_3$, another perovskite structure with Mn^{3+} residing in an octahedral O environment. The leading Mn K-edge for the 7.5% sample is slightly broader. While mixed valence states are known to induce such broadening, the leading edge is still positioned significantly apart from MnO and MnO_2. The observed broadening therefore is related to the higher disorder present in the x = 0.075 sample.

The quadrupolar transitions (Mn 1s → 3d (t_{2g}) and 3d (e_g) states) in the Mn K pre-edge appear as a broad feature in the region B_1 which could not be resolved experimentally due to core-hole lifetime broadening. The intensity of feature B_1 for Mn is much lower compared to the corresponding quadrupolar intensities observed for Ti (Figure 2a) for any given x value. The $Mn-O_6$ octahedra, therefore, are expected to be relatively more symmetrically distorted than $Ti-O_6$ octahedra. The feature in region B_2 (Figure 2a) corresponds to the d-states of neighboring metal (M) sites through oxygen-mediated intersite hybridization of Mn(4p)−O(2p)−M(3d). Feature B_2 shows small, non-monotonic changes with doping, which might be a consequence of disorder associated with B-site doping, to be discussed later.

Figure 3b shows the Fourier transform of $\chi(k)$ (2.0−9.0 $Å^{-1}$) for the Mn K-edge data in the BTMNO series. The first split peak at ∼1.5 Å corresponds to nearest O neighbors, and the multipeak at ∼3.2 Å corresponds to second (Ba) and third near neighbors (Ti, Mn, and Nb), including multiple scattering contributions from Mn−Ti−O paths. The apparently lower values of the distances are due to phase shifts for different atom-pair correlations and were accounted for during the fitting procedure. The Mn−O peak amplitude tends to decrease with doping, indicating that the oxygen environment around the manganese is becoming more distorted, except for the x = 0.075 sample. The multipeak corresponds to a weighted sum of contributions from Mn−Ti, Mn−Mn, and Mn−Nb. This peak appears much smoother, which suggests

https://doi.org/10.1021/acs.jpcc.1c02539
J. Phys. Chem. C 2021, 125, 14910−14923

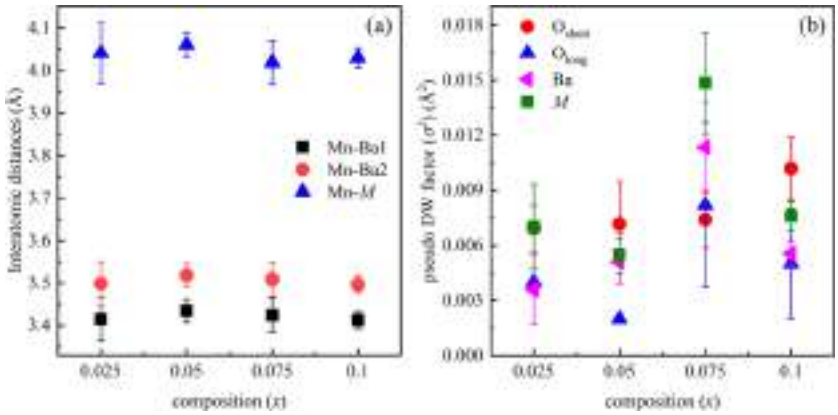

Figure 4. (a) Mn−Ba (2NN) short (black squares), Mn−Ba long (red circles), and Mn−*M* (*M* = Ti, Mn, Nb) (3NN) (blue triangles) interatomic distances in BTMNO samples. (b) Pseudo-Debye−Waller factors (σ^2) associated with each sublattice: O (short: red circles, long: blue triangles), Ba (magenta left triangle), and *M* (olive squares), revealing high σ^2 values and the largest scatter for the $x = 0.075$ composition.

that the distribution of Mn−Ti, Mn−Mn, and Mn−Nb interatomic distances is possibly more disordered. Hence, no large changes are observable in the local structure in this bond length range for this peak with doping. The $x = 0.075$ sample breaks this trend, with a very different higher shell environment and possibly higher disorder.

We found the optimal number of O atoms surrounding Mn to be 6 for all *x*, clearly establishing B-site doping of Mn. The split peak on Mn−O prompts us to check for multiple Mn−O distances within the $Mn-O_6$ octahedra in a perovskite structure. In this framework, the quality of preliminary fits with different Mn−O distances ($n = 1, 2, 3$) and one σ^2 parameter was compared (Table S3) and presented in Figure 3c for the lowest and highest doping concentrations (2.5% and 10%). The residuals (dotted lines) obtained considering multiple Mn−O distances ($n = 2, 3$) were significantly lower (by a factor between 20% and 30%) (Figure 3c) than the residuals calculated with a single Mn−O bond distance ($n = 1$), as reflected in lower fit quality of the $n = 1$ models. Also, the $n = 1$ models consistently yielded higher σ^2 values (Table S3) compared to $n = 2, 3$ models, suggesting the O_6 environment surrounding Mn to be nonisotropic. The systematic lower residual for $n = 2$ compared to $n = 3$ indicates that the $Mn-O_6$ octahedra in BTMNO systems support the model with two different values of the Mn−O distance: four short (Mn−O1) and two long Mn−O (Mn−O2) bonds. Formation of such distorted O shell due to B-site doping was evidenced in our Raman experiments (Figure 1c) as well. The two different Mn−O bonds are plotted in Figure 3d which does not show any noticeable composition dependence. Fits to the Mn K-edge data over the range $\Delta k = 2.0-9.0$ Å^{-1} and $\Delta R = 1.05-4.0$ Å for the BTMNO series are provided in the Supporting Information (Figure S2a,b). EXAFS parameters corresponding to first shell (Mn−O) fits are provided in Table S4.

Different types of distortions could be prevalent in the $Mn-O_6$ octahedra: JT effect, Mn off-centering within O_6 octahedra, charge disproportionation, and occurrence of multiple Mn^{3+} sites. Each of these effects would have a different manifestation on the structure, as mentioned below:

- The Jahn−Teller (JT) effect would (e.g., similar to $LaMnO_3$) generate a 2 + 2 + 2 distribution of Mn−O distances at ∼1.9, ∼1.97, and ∼2.15 Å along three different crystallographic axes in an orthorhombic[54] structure, represented as JT-(*o*). In a tetragonal[55] structure, JT distortion (JT-(*t*)) is expected to generate a 4 + 2 distribution of Mn−O distances (∼1.9 and ∼2.15 Å): two along the axis of distortion and four in the plane perpendicular to the axis of distortion.
- Off-centering (OC) distortion[56] of Mn along the polar *c*-axis like Ti would create a 1 + 4 + 1 distribution of Mn−O distances: one short and one long Mn−O axial bond (along *c*) and four Mn−O bonds (in the *ab*-plane) assuming intermediate values.
- Charge disproportionation (CD) of a fraction (*y*) of Mn^{3+} into Mn^{2+} and Mn^{4+} would create $y \times Mn^{3+}-O$ distances ∼2 Å, $(1 - y/2) \times Mn^{2+}-O$ (∼2.14 Å) and $(1 - y/2) \times Mn^{4+}-O$ bonds at ∼1.87 Å.[57]
- Mn^{3+} can exist as multiple sites (MS), where the short and long Mn−O bonds are associated with two different sites.[58] EXAFS can be effectively employed to resolve such local distortions, as revealed by the simulations provided in Figure S3.

The bond lengths used in the bullets above are based on sum of atomic radii[57] and ignores doping-induced lattice effects. However, for BTMNO these approximations are not too crucial due to rather comparable ionic radii of the dopants (Mn^{3+}: 0.72 Å and Nb^{5+}: 0.78 Å) replacing Ti^{4+} (0.745 Å) and low doping concentrations.

Both OC and CD effects would necessarily require the ratio of long and short Mn−O bonds to be 1:1, which is in sharp contrast to ratio (1:2) we found find from optimized fits ($n = 2$) to the Mn-EXAFS (Figure 3d). MS are known to occur in solid solutions with large ionic radii differences between the substituted and substituting ions and at high doping limits. Such ionic radii mismatch induces strain that can yield locally heterogeneous phases, often tracked by isosbestic points[58,59] in the metal K absorption edges. No signature of isosbestic points could be detected in the Mn K XANES (Figure 3a), thereby making the MS model rather unlikely as well. This is not surprising, considering similar ionic radii of the host (Ti^{4+}) and the dopant (Mn^{3+} and Nb^{5+}) ions and such low doping concentrations, as the EXAFS would be dominated by scattering from Ba and Ti, which predominantly form the matrix. Our results in Figure 3d with $n = 2$ (four short and two long Mn−O bonds) therefore can be best related to a Jahn−Teller distortion (JT-(*t*)). The Mn−O environment in BTMNO is in marked contrast with the Mn−O arrangement

https://doi.org/10.1021/acs.jpcc.1c02539
J. Phys. Chem. C 2021, 125, 14910−14923

in orthorhombic $LaMnO_3$ which experiences a JT-(o) distortion. This is primarily due to tetragonal symmetry of $BaTiO_3$, having identical Ti−O−Ti angles along a- and b-axes (∼180°). At low doping limits of Mn, the B-site is mostly Ti, leading to more regular arrangement of Mn−O bonds along the a- and b-axes.

For a tetragonal structure one expects a bimodal distribution of the second shell (Mn−Ba) and third shell (Mn−M; M = Ti/Mn/Nb) distances. Scattering factors of Mn and Ti are rather similar, while Nb has a significantly different scattering factor. However, the dopant concentration limit is too low to independently estimate the (Mn + Nb):Ti concentration. Therefore, the nominal (Mn + Nb):Ti ratio was used as a constraint to model the higher neighboring shells. Details of the corresponding Mn K EXAFS parameters are provided in the Supporting Information (Table S5). Figure 4a shows the variation of Mn−Ba and Mn−M distances with x. The distances remain roughly similar, with no appreciable composition dependence. The σ^2 values corresponding to all the different sublattices are shown in Figure 4b across the entire composition window. Clearly the σ^2 parameters assume higher values and reveal the maximum scatter among different sublattices for the x = 0.075 sample. The σ^2 for Mn−M is rather large, suggesting high disorder at the B-sites. Also, we find that the x = 0.075 sample experiences the largest JT splitting (Figure 3d) and broadening of the Mn K absorption edge (Figure 3a). All these observations are clearly suggestive of a unique, more disordered Mn local environment for the x = 0.075 sample.

Nb K XAS. Figure 5a shows the normalized Nb K XANES for the BTMNO series. Similar to the Mn co-dopant, we find that the E_0 positions (white line energy absorption feature due to the 1s → 4p transition) stay more or less constant for all doping concentrations. The BTMNO samples show similar values (∼18903 eV), closest to the reported value[60] for Nb_2O_5, indicating Nb to exist predominantly as Nb^{5+} at these time scales (10^{-15} s). A single broad, intense pre-edge shoulder feature (labeled C) around 18990 eV is noticeable, but the fine structure cannot be resolved due to the large intrinsic width of the Nb core level. Nonetheless, considerable intensity of the p−d peak indicates the niobium atoms to be displaced from the centers of the NbO_6 octahedra.[32,61,62] The baseline-subtracted Nb K absorption edge of the BTMNO series over −15 to −5 eV is shown in the inset of Figure 5a. The peak intensity is maximum for the x = 0.075 sample, suggesting Nb distortion within the O_6 octahedra is expected to be largest for this composition.

Figure 5b shows the modulus of $\chi(R)$ obtained by Fourier transformation over the k-range 3.0−13.5 $Å^{-1}$. Direct comparison of first peak (O shell) in $\chi(R)$ suggests that the oxygen polyhedra around Nb ions remain similar regardless of the doping concentrations, except for x = 0.075. The Nb−O peak distribution is narrower compared to the distribution for the co-dopant Mn (Figure 3b), suggesting that the oxygen environment around the Nb is possibly less distorted compared to Mn when occupying a Ti site. The intense multipeak at ∼3.2 Å corresponds to combined scattering from Ba, Ti, Mn, and Nb and a significant multiple scattering path Nb−Ti−O described already. No significant changes in the peak profile can be noticed in this bond length range with x, except for the x = 0.075 sample which exhibits higher disorder.

The coordination number for O atoms was found to be 6, indicating that Nb acts as substitutional impurity at Ti sites in

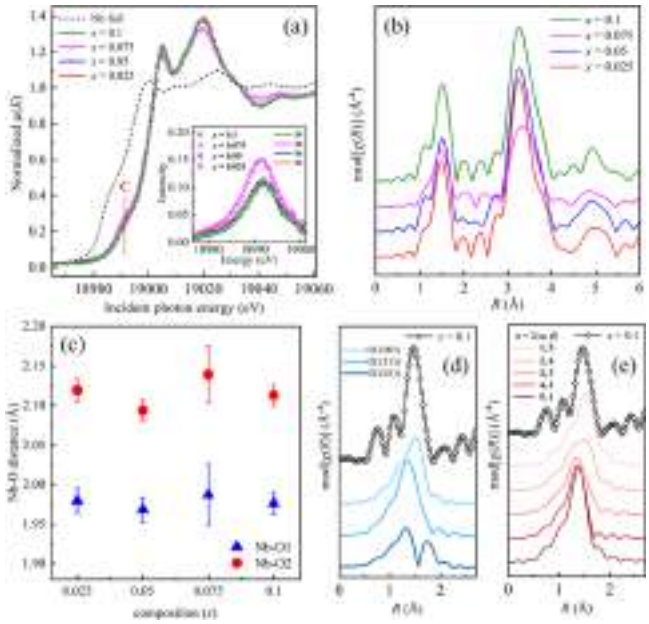

Figure 5. (a) Nb K XANES for the BTMNO series: x = 0.025 (red), 0.05 (blue), 0.075 (magenta), and 0.1 (olive); inset shows the baseline-subtracted pre-edge feature C related to local distortion of Nb within the O_6 octahedra. (b) Modulus of $\chi(R)$ for the BTMNO series (c) Distribution of Nb−O bond distances within Nb−O_6 octahedra, showing one short Nb−O1 (blue triangles) and five long Nb−O2 bonds (red circles). (d) Nb−O shell for 10% Mn-Nb-doped $BaTiO_3$ compared with different models: Nb off-centering models along (001), (111), and (011) directions. (e) All possible combinations for the n = 2 (α, β) model, revealing closest proximity of the (α = 5, β = 1) model to the OC(001) model, i.e., off-centering distortion of Nb within the Nb^{5+}−O_6 octahedra.

BTMNO. The intense p−d peak (Figure 5a) and Nb−O peak structure (Figure 5b) prompt us to check for possible distortions within the Nb−O_6 octahedra. As observed with Mn−O_6, the n = 1 model (single Nb−O distance) could not provide a satisfactory description of the Nb−O_6 octahedra. The Nb−O octahedron was therefore modeled with multiple distinct Nb−O paths (n = 2, 3). Both models yielded similar quality fits, but the results were not unique. This is because all three-path models (n = 3) approached a five short Nb−O and one long Nb−O bond combination of the two-path (n = 2) model. Optimal fits were thus concluded by using two Nb−O distances, five short (Nb−O1), and one long (Nb−O2). This unusual bonding arrangement Nb−O_6 octahedra persists for all doping compositions up to x = 0.1, as plotted in Figure 5c. Fits to the Nb K-edge data over the range Δk = 3.0−13.5 $Å^{-1}$ and ΔR = 1.05−4.0 Å for the BTMNO series are provided in Figures S4a,b. EXAFS parameters corresponding to first shell (Nb−O) fits are provided in Table S6.

Nb^{5+} being a d^0 ion is JT-inactive; therefore, the Nb−O environment was checked for plausible distortions other than JT:

- Off-centering (OC) distortion[30−32,63] of Nb along (001), (011), or (111) directions.
- OC (001) would create a 1 + 4 + 1 Nb−O bond distribution, as explained previously.
- OC (011) would create three sets of Nb−O distances, two small, two intermediate, and two large Nb−O bonds (2 + 2 + 2 distribution) typical of an orthorhombic distortion in a perovskite.

https://doi.org/10.1021/acs.jpcc.1c02539
J. Phys. Chem. C 2021, 125, 14910−14923

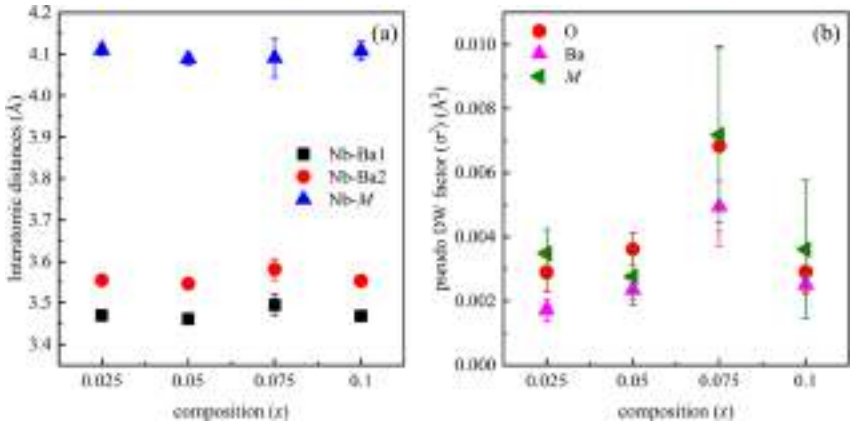

Figure 6. (a) Nb−Ba (2NN) short (black squares), Nb−Ba long (red circles), and Nb−*M* (*M* = Ti, Mn, Nb) (3NN) (blue triangles) interatomic distances in BTMNO samples. (b) Pseudo-Debye−Waller factors (σ^2) associated with each sublattice: O (red circles), Ba (magenta left triangle), and *M* (olive squares), showing high σ^2 values and largest scatter for the x = 0.075 composition.

- OC (111) would create two sets of Nb−O distances each involving three bonds (3 + 3 distribution), typical of a rhombohedral distortion in a perovskite.
- Charge disproportionation (CD) would have a different interpretation for Nb than Mn. This is because Nb is already presumably at its maximum valence (+5), but it can assume a range of lower formal valence states. This would be reflected as a weighted sum of different fractions of Nb^{n+}−O bonds at different distances (e.g., Nb oxides).
- Multiple sites (MS)[58] can exist, one site associated with only short Nb−O bonds and the other site with only long Nb−O bonds.

To fit a five short and one long Nb−O bond length description, a CD model would require assigning 83.3% of Nb−O bonds to Nb^{5+} and 16.7% to Nb^{4+}, resulting in nonstoichiometry effects. No appreciable broadening of the main Nb K absorption edge has been observed for BTMNO samples to support this claim. Rather, the absorption profiles are almost overlapping, suggesting the fraction of Nb^{5+} in Nb sites has no dependence on concentration. For a MS model, a similar case can be argued as with Mn that this mode of distortion, even if operative, would be rather weak at such low doping levels. We also find no evidence for isosbestic points in the Nb K XANES to support the CD or the MS model. Moreover, these models cannot explain the intense pre-peak in Nb K XANES. The Nb−O_6 distortion must therefore be related to some form of OC distortion in the Nb−O_6 octahedra.

Figure 5d compares all OC three-path models (n = 3). The OC (011) model is simply too broad to describe the Nb−O_6 environment, The OC (111) model, too, yielded a poor description with largely offset Nb−O bond distances. Thus, Nb is not likely to be displaced toward any of the Nb−O_6 octahedral faces or edges. The OC (001) model improves the description reasonably, hinting that the Nb−O_6 comprises of a considerable fraction of shorter Nb−O bonds, assuming values close to the Ti−O distances in the *ab*-plane for $BaTiO_3$. In undoped $BaTiO_3$, an ideal Ti off-centering along (001) gives rise to three Ti−O distances of 1.84, 1.98, and 2.14 Å. If we simply replace the Ti by Nb and use a single expansion factor (retaining proportional variation of the Ti−O bond lengths in $BaTiO_3$), the corresponding Nb−O distances occur around 1.84, 1.97, and 2.11 Å, with poor fit quality. The short Nb−O bond, when relaxed, immediately converges to a value ∼1.98 Å, and a high fit quality is achieved. Interestingly, this value is almost identical to the four equatorial Ti−O distances. So essentially, one sees a distribution of five short and one long Nb−O distance within the Nb−O_6 octahedra. Interestingly, the longer Nb−O bond also assumes a value close to the longer axial Ti−O bond in $BaTiO_3$. This implies that although Nb distorts the O_6 cage locally, some portion of the intrinsic tetragonal (001) distortion of the O_6 cage (Ti−O_6 octahedra in pure $BaTiO_3$) is still preserved. Neither of the other two OC models—OC (011) (2 + 2 + 2 distribution) and OC (111) (3 + 3 distribution)—could be reduced similarly to a five short + one long Nb−O distance distribution. The Nb−O_6 distortion we observe, therefore, can be regarded as a structural variant of the OC (001) distortion model.

We check the validity of this observation in Figure 5e by comparing all two-path (n = 2(α, β)) Nb−O bond combinations, where α and β represent the number of short and long Nb−O bonds. One can clearly see that how the Nb−O description could be approached by systematically replacing longer Nb−O bonds (β) with shorter Nb−O (α) bonds. Thus, Nb when doped at the Ti site does remain off-centered within the O_6 octahedra being displaced roughly along the polarization axis. This finding emphasizes the natural tendency of d^0 ions in perovskites to create a polar distortion at the B-site, a fundamental criterion for stabilizing a ferroelectric ground state.[18,25] Thus, apart from being a charge compensator ion, Nb^{5+} also is likely to contribute to the total polarization of the system, although the extent of off-centering is relatively lower as compared to Ti. We note here that local structure about Nb is in marked contrast with Nb−O arrangement in $KNbO_3$ and similar reported structures of Nb in perovskite ferroelectrics. This again is related to the tetragonal symmetry of the $BaTiO_3$ lattice, which drives the directionality of Nb displacement within the Nb−O_6 octahedra.

Figure 6a shows the interatomic distances for second shell (Nb−Ba) and third shell (Nb−*M*; *M* = Ti/Mn/Nb). The (Mn + Nb):Ti ratio was constrained close to the nominal (Mn + Nb):Ti ratio to model the higher neighboring shells, as in the Mn K-edge fits. Details of the corresponding Nb K EXAFS parameters are provided in Table S7. The Nb−Ba and Nb−*M* distances do not reveal any significant changes with increasing doping concentration. The σ^2 values for the different sublattices are shown in Figure 6b for all x values. Like Mn,

https://doi.org/10.1021/acs.jpcc.1c02539
J. Phys. Chem. C 2021, 125, 14910−14923

here also we notice the largest σ^2 values for the x = 0.075 sample, also exhibiting the largest spread of σ^2. The spread of σ^2 among different sublattices, however, is considerably lower compared to the Mn results (Figure 4b).

Doping Comparison and Links to Material Functionality. Comparing the local environments about Mn and Nb reveal several interesting facts. First, the distortions associated with Mn and Nb doping at Ti sites are fundamentally different from each other: Mn at Ti sites show JT distortion, while Nb at Ti sites show off-center distortion. This has important implications on material properties as will be discussed below. Second, doping effects of Mn/Nb are extremely local in nature. Most pronounced structural changes are observed for the nearest neighboring O shell, while the higher shell (Ba, Ti) environments show smaller lattice effects regardless of doping composition, with interatomic distances for Nb being slightly larger (~0.05 Å) than Mn. This suggests that local structural descriptions about dopants in BTMNO samples start conforming toward more uniform description within 4 Å, where the next B-sites occur. The changes in the O environments thus are accommodated by the lattice through cooperative rotation with neighboring Ti−O_6 octahedra, preserving the overall lattice periodicity. Third, the σ^2 values for all sublattices in the Mn local environment are systematically higher compared to the corresponding σ^2 values in the Nb local environment, which explains why the $\chi(k)$ oscillations for Mn are comparatively less structured than Nb-$\chi(k)$ (Figure S5). This can be understood from the changes in the O−O interatomic distances in a Ti−O_6 octahedra when the Ti is replaced by a Mn or Nb. The long O−O interatomic distance for Ti in $BaTiO_3$ is ~4.0 Å. When doped with Mn, the O−O interatomic distance increases to ~4.4 Å, much higher compared to O−O interatomic distance (~4.2 Å) when Ti is replaced with Nb. The larger octahedral volume of Mn−O_6 compared to Nb−O_6 is expected to be compensated through greater adjustment of the Mn−O−Ti bond angles and hence larger σ^2 values. This is not surprising, as JT is known to be a stronger lattice distortion compared to OC.

Incorporation of Mn in $BaTiO_3$ supplies a finite number of d electrons (d^n) that create new midgap states with predominantly Mn 3d character.[28] Our O K XAS studies[29] have also identified newly formed doped states appearing below the conduction band to be primarily of Mn 3d character. By removing the 3d degeneracy, the JT distortion governs the splitting of the midgap states, eventually lowering the bulk band gap. Mn doping, therefore, is primarily associated with improving the photovoltaic functionality of BTMNO. On the other hand, exchanging Ti with Mn is believed to be detrimental to ferroelectricity, as exchanging d^0 ions by d^n ions typically decreases the inherent polarization. However, larger polarization loss (25%) was reported by Das *et al.*[28] when the co-dopant to Nb^{5+} was a JT-inactive Fe^{3+} ($3d^5$) ion. This indicates that strong JT distortions about Mn^{3+} aid effective coupling of Mn^{3+}−O_6 octahedra to the surrounding corner-shared tetragonally distorted Ti−O_6 octahedra, minimizing loss of overall $BaTiO_3$ polarization.

The other dopant, Nb, plays a very different role when doped at Ti sites. An equimolar amount of Nb^{5+} acts as a charge compensator to Mn^{3+}, maintaining overall charge neutrality in BTMNO. The "d^0-ness"[25] of metals occupying B-sites (e.g., Ti^{4+}, Nb^{5+}, and Zr^{4+}) in perovskites is well-known to generate off-centered displacement of the d^0 ion within the O_6 octahedra which stabilizes a ferroelectric phase. We find similar off-centering distortion for Nb^{5+} within the O_6 octahedra for the BTMNO systems. Because of this innate asymmetry, Nb could retain some portion of the polarization of $BaTiO_3$ lost due to Mn doping. However, being a d^0 system, Nb^{5+} is not expected to have any appreciable influence on band gap engineering. Incorporation of Nb, therefore, is primarily associated with the ferroelectric functionality of BTMNO.

The above discussion highlights the effectiveness of co-doping aliovalent ions Mn^{3+} and Nb^{5+} over isovalent doping in broadening the absorption in the visible region for ferroelectric $BaTiO_3$. Isovalent Mn doping alone in $BaTiO_3$ results in a hexagonal structure with no ferroelectricity.[26] Also, an electronically degenerate Mn^{4+} ion would be JT-inactive. Isovalent doping of only Nb in $BaTiO_3$, on the other hand, is synthetically challenging due to slow kinetics of Nb incorporation.[64] It is also known to suffer from charge imbalance and requires high temperature conditions for reproducible electrical properties.[65] In contrast, aliovalent doping of Mn^{3+}−Nb^{5+} pair could behave as a dipole that can effectively couple to the tetragonally distorted $BaTiO_3$ lattice and help retain the overall electric polarization. This explains the efficacy of the co-doping strategy to strike the right balance between good solar absorption and good polarization to be able to function as a potential ferroelectric photovoltaic material.

Figure 7 shows the local structure−property correlation between distortions (δ) within the local octahedra associated

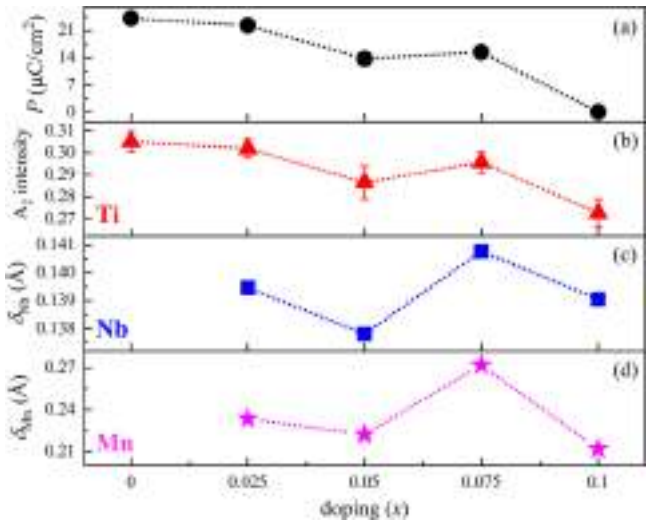

Figure 7. Correlation of (a) polarization (P) (black circles) in BTMNO to structural distortions associated with the B-sites: (b) Ti^{4+} off-centering distortion indicated by A_2 intensities (red triangles), (c) off-centering distortion of Nb^{5+} (blue squares), and (d) Jahn−Teller distortion of Mn^{3+} (magenta stars) ions.

with each B-site in BTMNO and the polarization (P) values reported by Das et al.[28] Using high-energy resolution fluorescence detected X-ray absorption (HERFD-XAS) at the Ti K-edge, we have already elucidated[29] how evolution of the A_2 peak intensities (∝ Ti off-centering) correlates strongly with evolution of P values over the doping window ($0.0 \leq x \leq 0.1$). For the dopants, we define distortion (δ) from the difference of short (M−O1) and long (M−O2) bonds within the respective M−O_6 octahedra (M = Mn, Nb): thus, $\delta M = \Delta M$−O = M−O2 − M−O1. Surprisingly enough, we find that the doping dependence for δ_{Mn} and δ_{Nb} roughly parallels the

https://doi.org/10.1021/acs.jpcc.1c02539
J. Phys. Chem. C 2021, 125, 14910−14923

variation of A_2 intensities and P values. This observation indicates strong coupling of Mn and Nb to the inherent Ti distortion in BTMNO. Replacing Ti^{4+} with Nb^{5+} keeps the number of d^0 ions maximum to retain the ferroelectric distortion, while strong JT distortion enables Mn^{3+} to effectively couple to the $BaTiO_3$ lattice. Also, the δ_{Mn} values are noticeably larger than the corresponding δ_{Nb} values for a given composition, revealing stronger distortion (JT-induced) about Mn ions compared to Nb (off-center displaced). This explains why the local environment about Mn exhibits higher disorder (σ^2) as compared to Nb. It is important to remember that even though some level of distortion persists locally for all x, doping systematically leads to reduction of tetragonality, eventually making the system cubic at $x = 0.1$. Ferroelectricity in $BaTiO_3$ is driven by long-range ordered displacement of Ti. Mn−Nb co-doping disrupts the Ti−O covalent bonding, limiting long-range polar ordering. The P value, therefore is determined by the balance between these long-range Coulombic forces and doping induced short-range interatomic forces. Beyond a critical doping threshold ($x \geq 0.1$), the macroscopic polarization eventually goes to 0 and the system becomes paraelectric.[28]

Figure 7 also highlights the anomalous behavior of the $x = 0.075$ sample, showing an increase of polarization (P) and distortion effects. We recall here that for the $x = 0.075$ sample the $\chi(R)$ functions for both Mn (Figure 3b) and Nb (Figure 5b) data reveal severe dampening effects, especially visible for the higher order peak (~3.2 Å). We also found maximum spread of σ^2 values associated with different sublattices (Figures 4b and 6b), with unusually high values for the Mn−M and Nb−M pairs. This typically happens as EXAFS cannot fully resolve multiple local structures closely resembling each other and therefore accounts for it by a single broad bond distribution. One common origin for such multiple environments is local chemical inhomogeneities at the B-site, for example, dopant clustering effects. In such a scenario, the dopant-rich small fraction of the sample would exhibit high disorder and low polarization, whereas the Ti-rich major fraction would essentially behave as a pure undisrupted $BaTiO_3$ lattice, eventually resulting in higher P values. Thus, one cannot rule out the possibility that $x = 0.075$ experiences dopant clustering effects. Such local effects, as often observed, remain intimately connected to the overall lattice, thereby affecting the bulk band gap. The structural peculiarity of $x = 0.075$ possibly stems from the fact that tetragonal to cubic phase transition point in BTMNO lies in the vicinity of $x = 0.075$. This region is hence sensitive since small composition changes can affect major structural changes. Still, however, the $x = 0.075$ sample was, in fact, fairly reproducible. A more accurate description of such unique structural anomalies requires detailed calculations. Nonetheless, Figure 7 implies that co-doping of Mn^{3+} and Nb^{5+} can induce strong electron−lattice coupling, which in turn is capable of sustaining the ferroelectric distortion prevalent in tetragonal BTMNO. This explains how the inherent $BaTiO_3$ polarization is preserved to a considerable extent even in the presence of a non-d^0 system like Mn^{3+}. Such coupling remains effective up to an optimal doping limit, beyond which the system would assume a higher symmetry cubic phase, as we see for $x = 0.1$.

CONCLUSIONS

We have studied how the local structural effects about B-sites (dopants: Mn and Nb; host: Ti) can influence material functionality in the room temperature low band gap ferroelectric system BTMNO, where Mn is primarily responsible for reducing the band gap and Nb acts as a charge compensator ion. Calculated Raman modes clearly identify Ti off-centering to be the driving force for such spontaneous polarization in the system. The intensity of the 1s → 3d quadrupolar transition, a measure of the extent of displacement of the B-site (Ti) from the O_6 octahedral center, correlates well with reported polarization values for a given composition. Our XAS studies reveal Mn^{3+} and Nb^{5+} to be the dominant charge states of the dopant species. Both dopants experience strong local structural distortions at the Ti sites, but the modes of distortion associated with the two dopants have fundamentally different origins. The Mn^{3+}−O_6 distortion could be related to the Jahn−Teller effect, while the Nb^{5+}−O_6 distortion could be associated with off-center displacement of Nb within the O_6 octahedra. A d^4 Mn^{3+} ion replacing Ti^{4+} helps to improve the photovoltaic functionality of $BaTiO_3$ through bulk band gap reduction and partial loss of polarization. However, the loss is significantly minimized by strong JT distortions about Mn^{3+} that adequately couple the Mn^{3+}−O_6 octahedra to the overall ferroelectric $BaTiO_3$ lattice. A d^0 Nb^{5+} ion replacing Ti^{4+}, in contrast, partially compensates for this small loss of polarization by replenishing the number of d^0 ions but barely participates in band gap tunability. The relatively stronger extent of distortion of Mn^{3+} within the O_6 octahedra introduces higher disorder in $BaTiO_3$ compared to Nb^{5+}. We find the Mn and Nb residing at Ti sites to be an effective charge neutral pair with insignificant charge disproportionation effects. Rather, the Mn^{3+}−Nb^{5+} pair has the ability to integrate with the tetragonal $BaTiO_3$ lattice, preserving the intrinsic polarization to a considerable extent. Our findings reveal how BTMNO material functionality can be correlated to complex B-site local distortions, thereby highlighting the effectiveness of controlled co-doping strategies in making promising ferroelectric photovoltaics and other optoelectronic applications in the future.

ASSOCIATED CONTENT

Supporting Information

The Supporting Information is available free of charge at https://pubs.acs.org/doi/10.1021/acs.jpcc.1c02539.

Ti K pre-edge fine structure fits, EXAFS data analyses, fits to Mn K and Nb K data for BTMNO in $\chi(k)$, real part of $\chi(R)$ and modulus of the $\chi(R)$ functions, Mn K and Nb K EXAFS parameters, simulations for distortion models within O6 octahedra, $\chi(k)$ functions for (a) Mn and (b) Nb in BTMNO systems (PDF)

AUTHOR INFORMATION

Corresponding Authors

Håkan Rensmo − *Department of Physics and Astronomy, Molecular and Condensed Matter Physics, Uppsala University, SE-75120 Uppsala, Sweden;* orcid.org/0000-0001-5949-0997; Email: hakan.rensmo@physics.uu.se

Soham Mukherjee − *Department of Physics and Astronomy, Molecular and Condensed Matter Physics, Uppsala University, SE-75120 Uppsala, Sweden;* Email: soham.mukherjee@physics.uu.se

Authors

Dibya Phuyal − *Division of Material and Nano Physics, Department of Applied Physics, KTH Royal Institute of Technology, 114 28 Stockholm, Sweden;* orcid.org/0000-0003-0351-3138

Carlo U. Segre − *CSRRI and Department of Physics, Illinois Institute of Technology, Chicago, Illinois 60616, United States;* orcid.org/0000-0001-7664-1574

Shyamashis Das − *Department of Chemistry, Ramananda College, Bishnupur 722122 West Bengal, India*

Olof Karis − *Department of Physics and Astronomy, Molecular and Condensed Matter Physics, Uppsala University, SE-75120 Uppsala, Sweden;* orcid.org/0000-0001-6406-217X

Tomas Edvinsson − *Department of Engineering Sciences − Solid State Physics, Uppsala University, 75121 Uppsala, Sweden;* orcid.org/0000-0003-2759-7356

Complete contact information is available at: https://pubs.acs.org/10.1021/acs.jpcc.1c02539

Notes

The authors declare no competing financial interest.

■ ACKNOWLEDGMENTS

The authors especially want to thank Prof. DD Sarma for very inspirational collaboration over the years and for introducing us into the research area. We thank STandUP for Energy, the Swedish Research Council (Grants VR 2018-06465, 2018-04330, and 2019-05591), the Swedish Foundation for Strategic Research (Project RMA15-0130), and the Swedish Energy Agency (Grants P43549-1, P50626-1) for financial support. D.P. acknowledges the Swedish Research Council (Grant 2020-00681). T.E. acknowledges use of computational resources provided by the Swedish National Infrastructure for Computing (SNIC) under Projects snic2019-3-542 and snic2019-3-461. We thank DST CSIR, NSF, and DFG for funding this investigation. MRCAT operations are supported by the Department of Energy and the MRCAT member institutions. This research used resources of the Advanced Photon Source, a U.S. Department of Energy (DOE) Office of Science User Facility operated for the DOE Office of Science by Argonne National Laboratory under Contract DE-AC02-06CH11357. Support for C.U.S. was provided in part by the National Science Foundation under Grant DMR-086935.

■ ABBREVIATIONS

BTMNO, $BaTi_{1-x}(Mn_{0.5}Nb_{0.5})_xO_3$; XAS, X-ray absorption spectroscopy; XANES, X-ray absorption near-edge structure; EXAFS, extended X-ray absorption fine structure; JT, Jahn−Teller; JT-(*o*), Jahn−Teller (orthorhombic); JT-(*t*), Jahn−Teller (tetragonal); OC, off-centering; CD, charge disproportionation; MS, multiple sites.

■ REFERENCES

(1) von Hippel, A.; Breckenridge, R. G.; Chesley, F. G.; Tisza, L. High Dielectric Constant Ceramics. *Ind. Eng. Chem.* **1946**, *38* (11), 1097−1109.

(2) Scott, J. F. Applications of Modern Ferroelectrics. *Science (Washington, DC, U. S.)* **2007**, *315* (5814), 954−960.

(3) Dawber, M.; Rabe, K. M.; Scott, J. F. Physics of Thin-Film Ferroelectric Oxides. *Rev. Mod. Phys.* **2005**, *77* (4), 1083−1130.

(4) Hennings, D.; Klee, M.; Waser, R. Advanced Dielectrics: Bulk Ceramics and Thin Films. *Adv. Mater.* **1991**, *3* (7), 334−340.

(5) Wang, S.-F.; Dayton, G. O. Dielectric Properties of Fine-Grained Barium Titanate Based X7R Materials. *J. Am. Ceram. Soc.* **1999**, *82* (10), 2677−2682.

(6) Bhattacharya, K.; Ravichandran, G. Ferroelectric Perovskites for Electromechanical Actuation. *Acta Mater.* **2003**, *51*, 5941−5960.

(7) Su, L.; Zou, L.; Fong, C.-C.; Wong, W.-L.; Wei, F.; Wong, K.-Y.; Wu, R. S. S.; Yang, M. Detection of Cancer Biomarkers by Piezoelectric Biosensor Using PZT Ceramic Resonator as the Transducer. *Biosens. Bioelectron.* **2013**, *46*, 155−161.

(8) Damjanovic, D.; Muralt, P.; Setter, N. Ferroelectric Sensors. *IEEE Sens. J.* **2001**, *1* (3), 191−206.

(9) Tang, P.; Towner, D. J.; Meier, A. L.; Wessels, B. W. Low-Loss Electrooptic $BaTiO_3$ Thin Film Waveguide Modulator. *IEEE Photonics Technol. Lett.* **2004**, *16* (8), 1837−1839.

(10) Petraru, A.; Schubert, J.; Schmid, M.; Buchal, Ch Ferroelectric $BaTiO_3$ Thin-Film Optical Waveguide Modulators. *Appl. Phys. Lett.* **2002**, *81* (8), 1375−1377.

(11) Scott, J. F.; Paz De Araujo, C. A. Ferroelectric Memories. *Science (Washington, DC, U. S.)* **1989**, *246* (4936), 1400−1405.

(12) Spanier, J. E.; Fridkin, V. M.; Rappe, A. M.; Akbashev, A. R.; Polemi, A.; Qi, Y.; Gu, Z.; Young, S. M.; Hawley, J.; Imbrenda, D.; et al. Power Conversion Efficiency Exceeding the Shockley-Queisser Limit in a Ferroelectric Insulator. *Nat. Photonics* **2016**, *10*, 611−616.

(13) Huang, H. Ferroelectric Photovoltaics. *Nat. Photonics* **2010**, *4* (3), 134−135.

(14) Hu, Y.; Florio, F.; Chen, Z.; Phelan, W. A.; Siegler, M. A.; Zhou, Z.; Guo, Y.; Hawks, R.; Jiang, J.; Feng, J.; et al. A Chiral Switchable Photovoltaic Ferroelectric 1D Perovskite. *Sci. Adv.* **2020**, *6* (9), 1−10.

(15) You, L.; Zheng, F.; Fang, L.; Zhou, Y.; Tan, L. Z.; Zhang, Z.; Ma, G.; Schmidt, D.; Rusydi, A.; Wang, L.; Chang, L.; Rappe, A. M.; Wang, J. Enhancing Ferroelectric Photovoltaic Effect by Polar Order Engineering. *Sci. Adv.* **2018**, *4* (7), 1−10.

(16) Grinberg, I.; West, D. V.; Torres, M.; Gou, G.; Stein, D. M.; Wu, L.; Chen, G.; Gallo, E. M.; Akbashev, A. R.; Davies, P. K.; et al. Perovskite Oxides for Visible-Light-Absorbing Ferroelectric and Photovoltaic Materials. *Nature* **2013**, *503* (7477), 509−512.

(17) Paillard, C.; Bai, X.; Infante, I. C.; Guennou, M.; Geneste, G.; Alexe, M.; Kreisel, J.; Dkhil, B. Photovoltaics with Ferroelectrics: Current Status and Beyond. *Adv. Mater.* **2016**, *28*, 5153−5168.

(18) Cohen, R. E. Origin of Ferroelectricity in Perovskite Oxides. *Nature* **1992**, *358*, 136−138.

(19) Krawczyk, P. A.; Jurczyszyn, M.; Pawlak, J.; Salamon, W.; Baran, P.; Kmita, A.; Gondek, L.; Sikora, M.; Kapusta, C.; Strączek, T.; et al. High-Entropy Perovskites as Multifunctional Metal Oxide Semiconductors_ Synthesis and Characterization of $(Gd_{0.2}Nd_{0.2}La_{0.2}Sm_{0.2}Y_{0.2})CoO_3$. *ACS Appl. Electron. Mater.* **2020**, *2*, 3211−3220.

(20) Wang, Y.; Wang, C.; Liang, W.; Song, X.; Zhang, Y.; Huang, M.; Jiang, H. Multifunctional Perovskite Oxide for Efficient Solar-Driven Evaporation and Energy-Saving Regeneration. *Nano Energy* **2020**, *70*, 104538.

(21) Jana, S.; Panda, S. K.; Phuyal, D.; Pal, B.; Mukherjee, S.; Dutta, A.; Kumar, P. A.; Hedlund, D.; Schött, J.; Thunström, P.; et al. Charge Disproportionate Antiferromagnetism at the Verge of the Insulator-Metal Transition in Doped $LaFeO_3$. *Phys. Rev. B: Condens. Matter Mater. Phys.* **2019**, *99* (7), 075106.

(22) Phuyal, D.; Mukherjee, S.; Panda, S. K.; Jana, S.; Segre, C. U.; Simonelli, L.; Butorin, S. M.; Rensmo, H.; Karis, O. Origin of Itinerant Carriers in Antiferromagnetic $LaFe_{1-x}Mo_xO_3$ Studied by X-Ray Spectroscopies. *Phys. Rev. Mater.* **2020**, *4* (3), 034405.

(23) Yuan, Y.; Xiao, Z.; Yang, B.; Huang, J. Arising Applications of Ferroelectric Materials in Photovoltaic Devices. *J. Mater. Chem. A* **2014**, *2*, 6027−6041.

(24) Nechache, R.; Harnagea, C.; Li, S.; Cardenas, L.; Huang, W.; Chakrabartty, J.; Rosei, F. Bandgap Tuning of Multiferroic Oxide Solar Cells. *Nat. Photonics* **2015**, *9*, 61−67.

(25) Hill, N. A. Why Are There so Few Magnetic Ferroelectrics? *J. Phys. Chem. B* **2000**, *104* (29), 6694−6709.

(26) Wang, S.-F.; Wu, Y.-C.; Hsu, Y.-C.; Chu, J.-P.; Wu, C.-H. Properties of Hexagonal $Ba(Ti_{1-x}Mn_x)O_3$ Ceramics: Effects of Sintering Temperature and Mn Content. *Jpn. J. Appl. Phys.* **2007**, *46* (5A), 2978−2983.
(27) Benedek, N. A.; Fennie, C. J. Why Are There So Few Perovskite Ferroelectrics? *J. Phys. Chem. C* **2013**, *117*, 13339−13349.
(28) Das, S.; Ghara, S.; Mahadevan, P.; Sundaresan, A.; Gopalakrishnan, J.; Sarma, D. D. Designing a Lower Bandgap Bulk Ferroelectric Material with a Sizable Polarization at the Room Temperature. *ACS Energy Lett.* **2018**, *3*, 1176−1182.
(29) Phuyal, D.; Mukherjee, S.; Das, S.; Jana, S.; Kvashnina, K. O.; Sarma, D. D.; Rensmo, H.; Buortin, S. M.; Karis, O. The Origin of Low Bandgap and Ferroelectricity of a co-doped $BaTiO_3$. *EPL (Europhysics Letters)* **2018**, *124* (2), 27005.
(30) Frenkel, A. I.; Wang, F. M.; Kelly, S.; Ingalls, R.; Haskel, D.; Stern, E. A.; Yacoby, Y. Local Structural Changes in $KNbO_3$ under High Pressure. *Phys. Rev. B: Condens. Matter Mater. Phys.* **1997**, *56* (17), 10869−10877.
(31) Lemeshko, M. P.; Nazarenko, E. S.; Gonchar, A. A.; Reznichenko, L. A.; Nedoseykina, T. I.; Novakovich, A. A.; Mathon, O.; Joly, Y.; Vedrinskii, R. V. EXAFS Studies of the Local Atomic Structure of the Lead-Free Piezoelectric Ceramics $K_xNa_{1-x}NbO_3$ over the Temperature Range 10 - 1023 K. *Phys. Rev. B: Condens. Matter Mater. Phys.* **2007**, *76*, 134106.
(32) Ivliev, M. P.; Raevskaya, S. I.; Raevskii, I. P.; Shuvaeva, V. A.; Pirog, I. V. Formation of Ferroelectric Phases in $KNbO_3$ and Other Niobates with Perovskite Structure. *Phys. Solid State* **2007**, *49* (4), 769−779.
(33) Phuyal, D.; Mukherjee, S.; Jana, S.; Denoel, F.; Kamalakar, M. V.; Butorin, S. M.; Kalaboukhov, A.; Rensmo, H.; Karis, O. Ferroelectric Properties of $BaTiO_3$ Thin Films co-doped with Mn and Nb. *AIP Adv.* **2019**, *9* (9), 095207.
(34) Kola, L.; Murali, D.; Pal, S.; Nanda, B. R. K.; Murugavel, P. Enhanced Bulk Photovoltaic Response in Sn Doped $BaTiO_3$ through Composition Dependent Structural Transformation. *Appl. Phys. Lett.* **2019**, *114* (18), 183901.
(35) Pal, S.; Muthukrishnan, S.; Sadhukhan, B.; Sarath, N. V.; Murali, D.; Murugavel, P. Bulk Photovoltaic Effect in $BaTiO_3$-based Ferroelectric Oxides: An Experimental and Theoretical Study. *J. Appl. Phys.* **2021**, *129* (084106), 1−9.
(36) Balzarotti, A.; Czyżyk, M.; Kisiel, A.; Motta, N.; Podgòrny, M.; Zimnal-Starnawska, M. Local Structure of Ternary Semiconducting Random Solid Solutions: Extended x-Ray-Absorption Fine Structure of $Cd_{1-x}Mn_xTe$. *Phys. Rev. B: Condens. Matter Mater. Phys.* **1984**, *30* (4), 2295−2298.
(37) Mukherjee, S.; Nag, A.; Kocevski, V.; Santra, P. K.; Balasubramanian, M.; Chattopadhyay, S.; Shibata, T.; Schaefers, F.; Rusz, J.; Gerard, C.; et al. Microscopic Description of the Evolution of the Local Structure and an Evaluation of the Chemical Pressure Concept in a Solid Solution. *Phys. Rev. B: Condens. Matter Mater. Phys.* **2014**, *89* (22), 224105.
(38) Pradhan, J.; Mukherjee, S.; Khan, A. H.; Dalui, A.; Satpati, B.; Segre, C. U.; Sarma, D. D.; Acharya, S. Two-Dimensional Hybrid Organohalide Perovskites from Ultrathin PbS Nanocrystals as Template. *J. Phys. Chem. C* **2017**, *121*, 6401−6408.
(39) Khan, A. H.; Dalui, A.; Mukherjee, S.; Segre, C. U.; Sarma, D. D.; Acharya, S. Efficient Solid-State Light-Emitting CuCdS Nanocrystals Synthesized in Air. *Angew. Chem., Int. Ed.* **2015**, *54* (9), 2643−2648.
(40) Ravel, B.; Newville, M. ATHENA, ARTEMIS, HEPHAESTUS: Data Analysis for X-Ray Absorption Spectroscopy Using IFEFFIT. *J. Synchrotron Radiat.* **2005**, *12*, 537−541.
(41) Zabinsky, S. I.; Rehr, J. J.; Ankudinov, A.; Albers, R. C.; Eller, M. J. Multiple-Scattering Calculations of x-Ray-Absorption Spectra. *Phys. Rev. B: Condens. Matter Mater. Phys.* **1995**, *52* (4), 2995−3009.
(42) Dovesi, R.; Saunders, V. R.; Roetti, C.; Orlando, R.; Zicovich-Wilson, C. M.; Pascale, F.; Civalleri, B.; Doll, K.; Harrison, N. M.; Bush, I. J.; et al. *CRYSTAL17 User's Manual*; University of Torino: Torino, 2017.
(43) Dovesi, R.; Erba, A.; Orlando, R.; Zicovich-Wilson, C. M.; Civalleri, B.; Maschio, L.; Rerat, M.; Casassa, S.; Baima, J.; Salustro, S.; Kirtman, B. Quantum-Mechanical Condensed Matter Simulations with CRYSTAL. *Wiley Interdiscip. Rev.: Comput. Mol. Sci.* **2018**, *8*, No. e1360.
(44) Peintinger, M. F.; Oliveira, D. V.; Bredow, T. Consistent Gaussian Basis Sets of Triple-Zeta Valence with Polarization Quality for Solid-State Calculations. *J. Comput. Chem.* **2013**, *34*, 451−459.
(45) Hay, P. J.; Wadt, W. R. *Ab initio* Effective Core Potentials for Molecular Calculations. Potentials for the Transition Metal Atoms Sc to Hg. *J. Chem. Phys.* **1985**, *82* (1), 270−283.
(46) Piskunov, S.; Heifets, E.; Eglitis, R. I.; Borstel, G. Bulk Properties and Electronic Structure of $SrTiO_3$, $BaTiO_3$, $PbTiO_3$ Perovskites: An *ab initio* HF/DFT Study. *Comput. Mater. Sci.* **2004**, *29*, 165−178.
(47) Monkhorst, H. J.; Pack, J. D. Special Points for Brillonin-Zone Integrations. *Phys. Rev. B* **1976**, *13* (12), 5188−5192.
(48) Maschio, L.; Kirtman, B.; Rérat, M.; Orlando, R.; Dovesi, R. *Ab Initio* Analytical Raman Intensities for Periodic Systems through a Coupled Perturbed Hartree-Fock/Kohn-Sham Method in an Atomic Orbital Basis. II. Validation and Comparison with Experiments. *J. Chem. Phys.* **2013**, *139*, 164101.
(49) Bilc, D. I.; Orlando, R.; Shaltaf, R.; Rignanese, G.-M.; Íñiguez, J.; Ghosez, Ph Hybrid Exchange-Correlation Functional for Accurate Prediction of the Electronic and Structural Properties of Ferroelectric Oxides. *Phys. Rev. B: Condens. Matter Mater. Phys.* **2008**, *77* (16), 165107.
(50) Freire, J. D.; Katiyar, R. S. Lattice Dynamics of Crystals with Tetragonal $BaTiO_3$ Structure. *Phys. Rev. B: Condens. Matter Mater. Phys.* **1988**, *37* (4), 2074−2085.
(51) Pokorńy, J.; Pasha, U. M.; Ben, L.; Thakur, O. P.; Sinclair, D. C.; Reaney, I. M. Use of Raman Spectroscopy to Determine the Site Occupancy of Dopants in $BaTiO_3$. *J. Appl. Phys.* **2011**, *109* (11), 114110.
(52) Yamamoto, T.; Mizoguchi, T.; Tanaka, I. Core-Hole Effect on Dipolar and Quadrupolar Transitions of $SrTiO_3$ and $BaTiO_3$ at Ti K Edge. *Phys. Rev. B: Condens. Matter Mater. Phys.* **2005**, *71* (24), 245113.
(53) Vedrinskii, R. V.; Kraizman, V. L.; Novakovich, A. A.; Demekhin, P. V.; Urazhdin, S. V. Pre-Edge Fine Structure of the 3d Atom K x-Ray Absorption Spectra and Quantitative Atomic Structure Determinations for Ferroelectric Perovskite Structure Crystals. *J. Phys.: Condens. Matter* **1998**, *10* (42), 9561−9580.
(54) Booth, C. H.; Bridges, F.; Kwei, G. H.; Lawrence, J. M.; Cornelius, A. L.; Neumeier, J. J. Lattice Effects in $La_{1-x}Ca_xMnO_3$ (x = 001): Relationships between Distortions, Charge Distribution, and Magnetism. *Phys. Rev. B: Condens. Matter Mater. Phys.* **1998**, *57* (17), 10440−10454.
(55) Tan, T.-Y.; Kennedy, B. J.; Zhou, Q.; Ling, C. D.; Miiller, W.; Howard, C. J.; Carpenter, M. A.; Knight, K. S. Impact of Jahn-Teller Active Mn^{3+} on Strain Effects and Phase Transitions in $Sr_{0.65}Pr_{0.35}MnO_3$. *Phys. Rev. B: Condens. Matter Mater. Phys.* **2012**, *85* (10), 104107.
(56) Lebedev, A. I.; Sluchinskaya, I. A.; Erko, A.; Kozlovskii, V. F. Direct Evidence for Off-Centering of Mn Impurity in $SrTiO_3$. *JETP Lett.* **2009**, *89* (9), 457−460.
(57) Shannon, R. D. Revised Effective Ionic Radii and Systematic Studies of Interatomie Distances in Halides and Chaleogenides. *Acta Crystallogr., Sect. A: Cryst. Phys., Diffr., Theor. Gen. Crystallogr.* **1976**, *A32*, 751−767.
(58) Mukherjee, S.; Ganegoda, H.; Kumar, A.; Pal, S.; Segre, C. U.; Sarma, D. D. Evolution of the Local Structure within Chromophoric Mn-O5 Trigonal Bipyramids in $YMn_{1-x}In_xO_3$ with Composition. *Inorg. Chem.* **2018**, *57* (15), 9012−9019.
(59) Hocking, R. K.; Brimblecombe, R.; Chang, L. Y.; Singh, A.; Cheah, M. H.; Glover, C.; Casey, W. H.; Spiccia, L. Water-Oxidation Catalysis by Manganese in a Geochemical-like Cycle. *Nat. Chem.* **2011**, *3* (6), 461−466.

https://doi.org/10.1021/acs.jpcc.1c02539
J. Phys. Chem. C 2021, 125, 14910−14923

(60) Cartier, C.; Hammouda, T.; Boyet, M.; Mathon, O.; Testemale, D.; Moine, B. N. Evidence for Nb^{2+} and Ta^{3+} in Silicate Melts under Highly Reducing Conditions: A XANES Study. *Am. Mineral.* **2015**, *100*, 2152−2158.
(61) Shuvaeva, V. A.; Pirog, I.; Azuma, Y.; Yagi, K.; Sakaue, K.; Terauchi, H.; Raevskii, I. P.; Zhuchkov, K.; Antipin, M. Yu. The Local Structure of Mixed-Ion Perovskites. *J. Phys.: Condens. Matter* **2003**, *15*, 2413−2421.
(62) Vedrinskii, R. V.; Kraizman, V. L.; Lemeshko, M. P.; Nazarenko, E. S.; Novakovich, A. A.; Reznichenko, L. A.; Fokin, V. N.; Shuvaeva, V. A. Local Atomic Structure of Niobates and Titanates from X-Ray Absorption Spectroscopic Data. *Phys. Solid State* **2009**, *51* (7), 1394−1398.
(63) Bugaev, L. A.; Shuvaeva, V. A.; Alekseenko, I. B.; Zhuchkov, K. N.; Vedrinskii, R. V. Determination of the Local Structure of NbO_6 Octahedra in the Orthorhombic Phase of a $KNbO_3$ Crystal Using EXAFS. *Phys. Solid State* **1998**, *40* (6), 1001−1005.
(64) Masó, N.; Beltrán, H.; Cordoncillo, E.; Flores, A. A.; Escribano, P.; Sinclair, D. C.; West, A. R. Synthesis and Electrical Properties of Nb-doped $BaTiO_3$. *J. Mater. Chem.* **2006**, *16*, 3114−3119.
(65) Kowalski, K.; Ijjaali, M.; Bak, T.; Dupre, B.; Nowotny, J.; Rekas, M.; Sorrell, C. C. Electrical Properties of Nb-doped $BaTiO_3$. *J. Phys. Chem. Solids* **2001**, *62*, 543−551.

https://doi.org/10.1021/acs.jpcc.1c02539
J. Phys. Chem. C 2021, 125, 14910−14923

Prof Ajit Debnath


Journal of Critical Reviews

2021, Vol: 8, Issue: 8

Current Issue (indexb02d.html?sec=cissue)

Online First

Archive (./archive.php)

Aims and Scope

Abstracting & Indexing

Most Accessed Articles

Most Downloaded Articles

Most Cited Articles

Required files to be uploaded

☐ **Copyright (https://www.ejmanager.com/mnstemps/197/stdfls/Copyright .doc)**

Focus and Scope

Journal of critical reviews (JCR) is peer reviewed open access journal published bimonthly (onward May 2017). **JCR** is designed to foster the exchange of ideas and transfer of knowledge between scientists and engineers involved in various Field that deal only with investigations or reviews in all fields . It is not limited to the specific details of science and engineering but is instead devoted to a very wide range of subfields in the all Engineering, sciences,Pharmacy,Management,Social Science and Humanities.

JCR accepts Review articles, Research Articles . The high standard of excellence for any of published papers will be ensured by peer-review procedure.

Submit Article (./submit_article.php)

About Publisher (./aboutpublisher.php)

Editorial Policies (./editorialpolicies.php)

Peer Review Policy (./peer.php)

Editorial & Peer Review Process (./editorialandpeer.php)

Author's Rights and Obligations (./authorright.php)

Publication Ethics and Publication Malpractice Statement (./publicationethics.php)

Conflict of Interest Policy (./conflict.php)

Plagiarism Policy (./plagiarism.php)

Protection of Research Participants (Statement On Human And Animal Rights) (./protectionof.php)

Privacy Policy (./privacypolicy.php)

Corrections, Retractions & Expressions of Concern (http://www.jcreview.com/?sec=correctionretractionconcern)

Self-Archiving Policies (./selfarchive.php)

Statement of Informed Consent (./statementof.php)

Advertising Policy (./advertising.php)

License Information (./license.php)

Contact Information

Journal of Critical Review,

Tower 23/4,

Jalan ampang,

Kuala Lumpur, malaysia

editorial.jcr@gmail.com

Dr. Mohammad Ali Khan

Journal of Information and Optimization Sciences ›
Volume 41, 2020 - Issue 8

Articles

Anti-synchronization phenomenon of discrete chaotic maps using linear transformations

Mohammad Ali Khan, Himadri Pai Mazumdar & Syeda Darakhshan Jabeen

Pages 1757-1769 | Received 01 Jan 2016, Published online: 18 Jun 2020

Download citation https://doi.org/10.1080/02522667.2017.1321766 Check for updates

References Citations Metrics Reprints & Permissions Get access

Abstract

This paper develops the theory of generalized anti-synchronization (GAS) of discrete chaotic Hénon maps via linear transformations. This anti-synchronization method is based on the stability criteria of the linear system. The necessary and sufficient condition of GAS of chaotic maps using linear transformation is established. T paper suggests a method to study GAS through linear transformation in drive response system. Our proposed method is able to find the relationship between the drive variables and response variables after anti-synchronization.

Subject Classification: 00A71 00A72 34C15 34C23 34C60 34D06 34D20 34D23 34D45 34H10 34H15 34H20 35B32 35B35 35B40 35B41 37G10 37G15 37G35 37G40 53Z05

Keywords: Chaos Chaotic system Generalized anti-synchronization(GAS) Hénon map

Related research

People also read | Recommended articles | Cited by 3

Adaptive method of linear programming problems with hybrid variables

Ahlem Zaarat et al.

Journal of Information and Optimization Sciences

Published online: 5 Aug 2020




Regular Article | Published: 12 September 2021

Design of multistability of chaotic systems via self and cross coupling

Mohammad Ali Khan, Gopal Mahapatra, Jayanta Kumar Sarkar & Syeda Darakhshan Jabeen

The European Physical Journal Plus **136**, Article number: 931 (2021)

Abstract

In this paper, we proposed general coupling conditions to the error dynamics of coupled dynamical systems for realizing multistability. The basic mechanism to propose multistability is to design partial synchronization of states between the coupled system and use to find some initial condition-dependent constants of motion. Here, we propose that i number of state variables are completely synchronized, and the remaining j number of state variables of two coupled systems are in constant difference to obtain multistable behaviour, where $1 \leq i, j \leq m-1$ and $i+j=m$. We interpret our scheme for coupled chaotic Lorenz, Rossler, and Van der Pol–Duffing oscillators. Further, we establish numerical simulation results with a bifurcation diagram,

phase diagram, and maximum Lyapunov exponent to show the desired results of our schemes.

References

1. F.M. Hilker, M. Langlais, H. Malchow, The Allee effect and infectious diseases: extinction, multistability, and the (dis-) appearance of oscillations. Am. Nat. **173**(1), 72–88 (2009)

2. G.P. Neverova, M.P. Kulakov, E. Ya Frisman, Changes in population dynamics regimes as a result of both multistability and climatic

fluctuation. Nonlinear Dyn. **97**(1), 107–122 (2019)

3. E. González-Olivares, et al. Bifurcations and multistability on the May-Holling-Tanner predation model considering alternative food for the predators. (2019)

4. E. Simonnet, J. Rolland, F. Bouchet. Multistability and rare spontaneous transitions between climate and jet configurations in a barotropic model of the Jovian mid-latitude troposphere.' arXiv preprint arXiv:2009.09913 (2020)

5. R. Arumugam et al., Dynamic environment-induced multistability and critical transition in a metacommunity ecosystem. Phys. Rev. E **99**(3), (2019)

6. P.S. Skardal, A. Arenas, Abrupt desynchronization and extensive multistability in globally coupled oscillator simplexes. Phys. Rev. Lett. **122**(24), (2019)

7. M.F.A. Rahim et al., Dynamics of a new hyperchaotic system and multistability. Eur. Phys. J. Plus **134**(10), 1–9 (2019)

8. M. Guo et al., Multistability in a physical memristor-based modified Chua‘s circuit. Chaos Interdiscip. J. Nonlinear Sci. **29**(4), (2019)

9. I. Bashkirtseva, A. Pankratov, Stochastic Higgins model with diffusion: pattern formation, multistability and noise-induced preference. Eur. Phys. J. B **92**(10), 1–9 (2019)

10. F. Parastesh, S. Jafari, H. Azarnoush, Traveling patterns in a network of memristor-based oscillators with extreme multistability. Eur. Phys. J. Spec. Top. **228**(10), 2123–2131 (2019)

11. P. Louodop et al., Extreme multistability in a Josephson-junction-based circuit. Phys. Rev. E **99**(4), (2019)

12. J.-L. Schwartz et al., Multistability in perception: binding sensory modalities, an overview. Philos. Trans. R. Soc. B Biol. Sci. **367.591**, 896–905 (2012)

13. G. Deco, V.K. Jirsa, Ongoing cortical activity at rest: criticality, multistability, and ghost attractors. J. Neurosci. **32**(10), 3366–3375 (2012)

14. A.A. Anzo-Hernández, H.E. Gilardi-Velázquez, E. Campos-Cantón, On multistability behavior of unstable dissipative systems. Chaos Interdiscip. J. Nonlinear Sci. **28**(3), (2018)

15. A.N. Pisarchik, U. Feudel, Control of multistability. Phys. Rep. **540**(4), 167–218 (2014)

16. C.N. Ngonghala, U. Feudel, K. Showalter, Extreme multistability in a chemical model system. Phys. Rev. E **83**(5), (2011)

17. J.C. Sprott, C. Li, Comment on How to obtain extreme multistability in coupled dynamical systems. Phys. Rev. E **89**(6), (2014)

18. P.R. Sharma et al., Control of multistability in hidden attractors. Eur. Phys. J. Special Top. **224**(8), 1485–1491 (2015)

19. Hn. Sun, S.K. Scott, K. Showalter, Uncertain destination dynamics. Phys. Rev. E **60**(4), 3876 (1999)

20. C.R. Hens et al., How to obtain extreme multistability in coupled dynamical systems. Phys. Rev. E **85**(3), (2012)

21. S. Pal, B. Sahoo, S. Poria, A generalized scheme for designing multistable continuous dynamical systems. Pramana **86**(6), 1183–1193 (2016)

22. S. Pal, B. Sahoo, Swarup Poria, Multistable behaviour of coupled Lorenz-Stenflo systems. Phys. Scr. **89**(4), (2014)

23. M.A. Khan, M. Nag, S. Poria, Design of multistable systems via partial synchronization. Pramana **89**(2), 1–8 (2017)

24. S. Pal, S. Poria, Uncertain destination dynamics of delay coupled systems. Phys. Scr. **90**(3), (2015)

25. P. Chakraborty, S. Poria, Extreme multistable synchronisation in coupled dynamical systems. Pramana **93**(2), 1–13 (2019)

26. M.A. Khan, M. Nag, S. Poria, Multistability in coupled different-dimensional dynamical systems. Pramana **91**(6), 1–7 (2018)

Author information

Authors and Affiliations

Department of Mathematics, Ramananda College, Bishnupur, Bankura, West Bengal, India

Mohammad Ali Khan & Gopal Mahapatra

Department of Mathematics, Raja N.L. Khan Womens College, Midnapore, West Bengal, India

Jayanta Kumar Sarkar

Department of Mathematics, Birla Institute of Technology, Mesra, Ranchi, India

Syeda Darakhshan Jabeen

Corresponding author

Correspondence to Syeda Darakhshan Jabeen.

Rights and permissions

About this article

Cite this article

Khan, M.A., Mahapatra, G., Sarkar, J.K. *et al.* Design of multistability of chaotic systems via self and cross coupling. *Eur. Phys. J. Plus* **136**, 931 (2021). https://doi.org/10.1140/epjp/s13360-021-01884-0

Received	Accepted	Published
03 August 2021	19 August 2021	12 September 2021

DOI

https://doi.org/10.1140/epjp/s13360-021-01884-0

Research Article | Published: 26 January 2021

Spatiotemporal Synchronization of Diffusively Coupled Modified Logistic Map Under Complex Network

Mohammad Ali Khan, Debjani Maity & Syeda Darakhshan Jabeen

Proceedings of the National Academy of Sciences, India Section A: Physical Sciences **92**, 147–156 (2022)

Abstract

We study spatiotemporal synchronization under complex network of diffusively coupled chaotic modified logistic map. In modified logistic map a new parameter is introduced such that nonlinear term is in fractional power. The complex network is dynamic whose coupling connections change stochastically in time. Here we investigate the spatiotemporal dynamics of coupled modified logistic maps whose coupling connections are rewired randomly, and we determine (1) the effects of variation of newly induced parameter β, (2) the effects of variation of low and high rewiring probability, (3) the effects of variation of growth rate r and (4) the effects of variation of different randomness and linear stability analysis of the synchronized steady-state solution. We have

calculated analytically the critical coupling coefficient for the transition to spatiotemporal regularity of the lattice. The analytical results match well with the numerical simulation results. The variation of the basin size with respect to coupling strength and rewiring probability with various randomness and coupling is plotted. The simulation results do not change significantly with the variation of lattice sizes.

References

1. Pecora LM, Carroll TL (1990) Synchronization in chaotic systems. Phys Rev Lett 64:821–824

2. Shooshtari BK, Forouzanfar AM, Molai MR (2016) Identical synchronization of a non-autonomous unified chaotic system with continuous periodic switch. Springer Plus. https://doi.org/10.1186/s40064-016-3299-6

3. Tarai A, Poria S, Chatterjee P (2009) Generalized synchronization of unified chaotic system. Chaos Solitions Fractals 40:885–892

4. Tarai A, Poria S, Chatterjee P (2009) Synchronization of bidirectionally of coupled chaotic Chen's system with delay. Chaos Solitions Fractals 41:190–197

5. Chung SJ, Bandyopadhyay S, Chang I, Hadaegh FY (2003) Phase synchronization control of complex networks of Lagrangian systems on adaptive digraphs. Automatica 49:1148–1161

6. Wang X, Zhang H, Lin X (2014) Module-phase synchronization in hyperchaotic complex Lorenz system after modified complex projection. Appl Math Comput 232:91–96

7. Khan MA, Poria S (2013) Projective synchronization of chaotic systems with bidirectional nonlinear coupling. Pramana J Phys 81:395–406

8. Bao HB, Cao JD (2015) Projective synchronization of fractional order memristor based neural networks. Neural Netw 63:1–9

9. Al-Sawalha M, Noorani M (2009) Anti-synchronization of two hyperchaotic systems via nonlinear control. Commun Nonlinear Sci Numer Simul 14:3402–3411

10. Sing PP, Sing JP, Roy BK (2014) Synchronization and anti-synchronization of Lu and Bhalekar–Gejji chaotic systems using nonlinear active control. Chaos Solitions Fractals 69:31–39

11. Ji DH, Jeong SE, Park JH, Lee SM, Won SC (2012) Adaptive lag synchronization for uncertain complex dynamical network with delayed coupling. Appl Math Comput 218:4872–4880

12. Huang J, Li C, Huang T, He X (2014) Finite time lag synchronization of delayed neural networks. Neurocomputing 139:145–149

13. Kaneko K (1993) Theory and application of coupled map lattices. Wiley, Hoboken

14. Casagrande V, Mikhailov AS (2005) Birhythmicity, synchronization and turbulence

in an oscillatory system with nonlocal inertial coupling. Phys D Nonlinear Phenom 205:154–169

15. Oppo GL, Yao AM, Prati F, Valcarcel GJ (2009) Long term spatiotemporal dynamics of solid state lasers and vertical cavity surface emitting lasers. Phys Rev A 79:033824

16. Kastrup CJ, Kastrup CJ, Runyon MK, Shen F, Ismagilov RF (2006) Modular chemical mechanism predicts spatiotemporal dynamics of initiation in the complex network of hemostasis. Proc Natl Acad Sci USA 103:15747–15752

17. Bascompte J, Sole RV (1995) Rethinking complexity: modelling spatiotemporal dynamics in ecology. Trends Ecol Evol 10:361–366

18. Sinha S (2005) Spatiotemporal consequence of random coupling. Proc Indian Natl Sci Acad 71:97–111

19. Poria S, Khan MA, Nag M (2013) Spatiotemporal synchronization of coupled Ricker maps over a complex network. Phys Scr 88:015004

20. Nag M, Poria S (2015) Synchronization in a network of delay coupled maps with stochastically switching topologies. Chaos Solitions Fractals. https://doi.org/10.1016/j.chos.2016.04.022

21. Khan MA, Sahoo B (2016) Temporospatial synchronization of discrete logistic map through complex network. Optik 127:1526–1531

22. Noymanee J, San-Um W (2015) A modified simple logistic chaotic map through exponential controller in nonlinear term. In: Science and information conference 2015, London UK, 28–30 July

Author information

Authors and Affiliations

Department of UG and PG Mathematics, Ramananda College, Bankura University, Bishnupur, Bankura, West Bengal, India
Mohammad Ali Khan

Department of Mathematics, Bankura University, Bankura, West Bengal, India
Debjani Maity

Department of Mathematics, Birla Institute of Technology, Mesra, Ranchi, India
Syeda Darakhshan Jabeen

Corresponding author

Correspondence to Mohammad Ali Khan.

Additional information

Publisher's Note

Springer Nature remains neutral with regard to jurisdictional claims in published maps and institutional affiliations.

Rights and permissions

Reprints and Permissions

About this article

Cite this article

Khan, M.A., Maity, D. & Jabeen, S.D. Spatiotemporal Synchronization of Diffusively Coupled Modified Logistic Map Under Complex Network. *Proc. Natl. Acad. Sci., India, Sect. A Phys. Sci.* **92**, 147–156 (2022). https://doi.org/10.1007/s40010-020-00726-5

Received	Revised	Accepted
02 August 2017	02 February 2019	02 December 2020

Published	Issue Date
26 January 2021	June 2022

DOI
https://doi.org/10.1007/s40010-020-00726-5

Keywords

Modified logistic map (MLM)

Coupled map lattice (CML)

Spatiotemporal synchronization (SS)

DESIGN OF MULTISTABLE SYSTEM OF COUPLED DIFFERENT LORENZ AND NUCLEAR SPIN GENERATOR SYSTEMS

June 2022 · Advances in Mathematics Scientific Journal 11(6):539-556
DOI:10.37418/amsj.11.6.3.

Authors:

Jayanta Kumar Sarkar **Mohammad Ali Khan**

Gour Chandra Mahata
Sidho Kanho Birsha University

Abstract

In this paper, we propose a new theoretical scheme design of multistable system of coupled Nuclear spin generator and Lorenz systems. In the system coupled Nuclear spin generator and Lorenz systems reduces to a single modified Lorenz system. We derive the existence conditions of fixed points and the conditions of local stability of the modified system is also derived. To obtain multistable behaviour maximum lyapunov exponent of the system and bifurcation analysis are analyzed. Dynamical behaviour with respect to multistable parameter using MATCONT software are also analyzed. The main observation is that: In coupling two m-dimensional dynamical systems multistable behaviour can be obtained if i number of variables of the two systems are completely synchronized and j number of variables keep a constant difference between them, where i + j = m and 1 ≤ i, j ≤ m−1. Numerical simulation results are presented to verify the proposed schemes.

Advances in Mathematics: Scientific Journal **11** (2022), no.6, 539–556
ISSN: 1857-8365 (printed); 1857-8438 (electronic)
https://doi.org/10.37418/amsj.11.6.3

DESIGN OF MULTISTABLE SYSTEM OF COUPLED DIFFERENT LORENZ AND NUCLEAR SPIN GENERATOR SYSTEMS

Jayanta Kumar Sarkar, Mohammad Ali Khan[1], and Gour Chandra Mahata

Jayanta Kumar Sarkar, Mohammad Ali Khan[1], and Gour Chandra Mahata

ABSTRACT. In this paper, we propose a new theoretical scheme design of multistable system of coupled Nuclear spin generator and Lorenz systems. In the system coupled Nuclear spin generator and Lorenz systems reduces to a single modified Lorenz system. We derive the existence conditions of fixed points and the conditions of local stability of the modified system is also derived. To obtain multistable behaviour maximum lyapunov exponent of the system and bifurcation analysis are analyzed. Dynamical behaviour with respect to multistable parameter using MATCONT software are also analyzed. The main observation is that: In coupling two m-dimensional dynamical systems multistable behaviour can be obtained if i number of variables of the two systems are completely synchronized and j number of variables keep a constant difference between them, where $i + j = m$ and $1 \leq i, j \leq m-1$. Numerical simulation results are presented to verify the proposed schemes.

1. INTRODUCTION

Multistability is the property whereby the solutions of a dynamical system can alternate between two or more exclusive lyapunov stable and convergent equilibrium states under asymptotically slowly changing inputs or system parameters.

[1]*corresponding author*
2020 *Mathematics Subject Classification.* 37 Dynamical systems and ergodic theory, 58 Global analysis, analysis on manifolds, 97 Mathematics education.
Key words and phrases. Multistability, Lorenz system, Nuclear spin generator system and Bifurcation analysis.
Submitted: 21.05.2022; *Accepted:* 05.06.2022; *Published:* 13.06.2022.

Citations (0) References (17)

Multistable behaviour of coupled Lorenz-Stenflo systems
Article Full-text available
Apr 2014 · PHYS SCRIPTA
Santinath Pal · Banshidhar Sahoo · Swarup Poria
View Show abstract

Design of multistable systems via partial synchronization
Article
Aug 2017
Mohammad Ali Khan · Mayurakshi Nag · Swarup Poria
View Show abstract

Hidden extreme multistability in memristive hyperchaotic system
Article
Jan 2017 · CHAOS SOLITON FRACT
Bocheng Bao · Han Bao · Ning Wang · Xu Quan
View Show abstract

Dynamical principles in neuroscience
Article
Nov 2006
Mikhail israel Rabinovich · Pablo Varona · Allen Selverston · Henry D. I. Abarbanel
View Show abstract

Deterministic non-periodic flow
Article
Jan 1963
Lorenz EN
View

Multistability in symmetric chaotic systems
Article
Jul 2015 · EUR PHYS J-SPEC TOP
Chunbiao Li · W. Hu · Julien Clinton Sprott · Xiong Wang
View Show abstract

Feedback control of bursting and multistability in chaotic systems
Article
Jul 2012 · Comm Nonlinear Sci Numer Simulat
Andrea Geltrude · Kais A. M. Al Naimee · Stefano Euzzor · Binoy Krishna Goswami
View Show abstract

Multistability and hysteresis in the climate-cryosphere system under orbital forcing
Article
Nov 2005
Reinhard Calov · Andrey Ganopolski

View Show abstract

Synchronization in chaotic systems

Article

Jun 1990

Louis M. Pecora · T. L. Carroll

View Show abstract

Experimental Evidence of Subharmonic Bifurcations, Multistability, and Turbulence in a Q-Switched Gas Laser

Article

Oct 1982

Tito Arecchi · R. Meucci · Gian Piero Puccioni · J. R. Tredicce

View Show abstract

Show more

Dr. Prasanta Das

A mathematical model for fluxes associated with internal gravity waves excited by a corner mountain

PRASANTA DAS
Department of Mathematics, Ramananda College, Bishnupur, Bankura – 722 122, West Bengal, India

SOMENATH DUTTA
India Meteorological Department (IMD), MoES, Pune – 411 005, India

DOI: https://doi.org/10.54302/mausam.v73i1.5091

Keywords: Corner mountain hills., Energy flux, Momentum flux

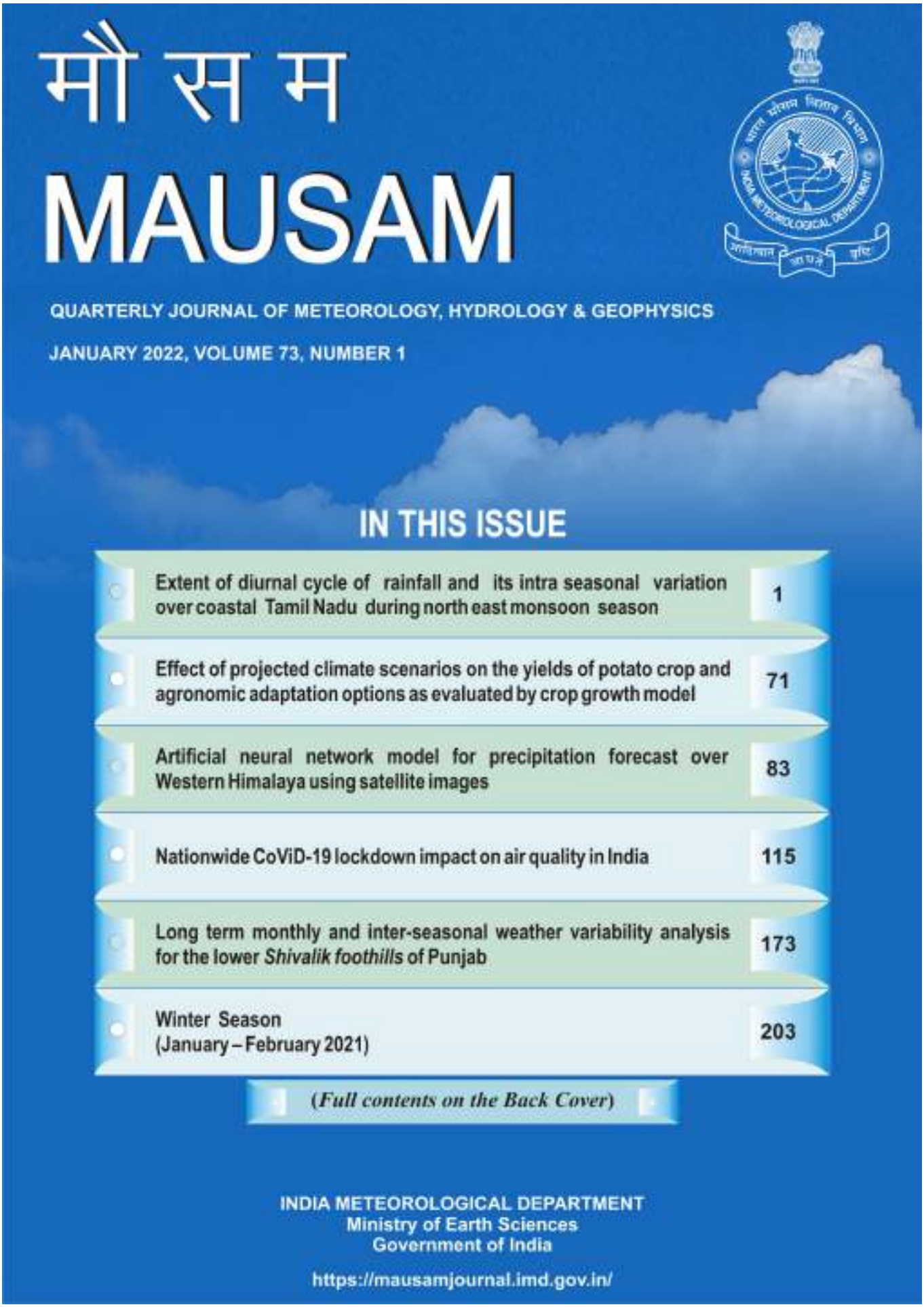
मौ स म
MAUSAM
QUARTERLY JOURNAL OF METEOROLOGY, HYDROLOGY & GEOPHYSICS
JANUARY 2022, VOLUME 73, NUMBER 1
IN THIS ISSUE
Extent of diurnal cycle of rainfall and its intra seasonal variation over coastal Tamil Nadu during north east monsoon season 1
Effect of projected climate scenarios on the yields of potato crop and agronomic adaptation options as evaluated by crop growth model 71
Artificial neural network model for precipitation forecast over Western Himalaya using satellite images 83
Nationwide CoViD-19 lockdown impact on air quality in India 115
Long term monthly and inter-seasonal weather variability analysis for the lower Shivalik foothills of Punjab 173
Winter Season (January – February 2021) 203
(Full contents on the Back Cover)
INDIA METEOROLOGICAL DEPARTMENT
Ministry of Earth Sciences
Government of India
https://mausamjournal.imd.gov.in/

pdf

Published
29-03-2022

How to Cite
P. . . DAS and S. . DUTTA, “A mathematical model for fluxes associated with internal gravity waves excited by a corner mountain”, *MAUSAM*, vol. 73, no. 1, pp. 181–188, Mar. 2022.

More Citation Formats

Issue
Vol. 73 No. 1 (2022): MAUSAM

Section
Shorter Contribution

Most read articles by the same author(s)

- SOMENATH DUTTA, R. BALASUBRAMANIAM, MAHENDRA JAGTAP, PRADEEP AWATE, NAHUSH KULKARNI, MD. DANISH, S. DESHPANDE, U. SATPUTE, R. WAYAL, P. BHAGBAT, BINDU NAMBIER, D. KULKARNI, L. BILE, P. V. KAMBLE, KRIPAN GHOSH, G. K. SAWAISARJE, SIRISH KHEDIKAR, CHETNA PATIL , OSAID ALAM , A. K. SAHAI, A pilot study on assessing the effect of climate on the incidence of vector borne disease at Pune and Pimpri-Chinchwad area, Maharashtra , MAUSAM: Vol. 72 No. 2 (2021): MAUSAM
- SOMENATH DUTTA, A. K. MUKHERJEE, A. K. SINGH, EFFECT OF PALGHAT GAP ON THE RAINFALL PATTERN TO THE NORTH & SOUTH OF ITS AXIS , MAUSAM: Vol. 57 No. 4 (2006): MAUSAM
- SOMENATH DUTTA, U. S. DE, SUNITHA DEVI , A diagnostic study on the energetics aspects of hiatus in the advance of southwest monsoon , MAUSAM: Vol. 60 No. 4 (2009): MAUSAM
- SOMENATH DUTTA, S.G. NARKHEDKAR, D.R. SIKKA, SUNITHA DEVI, A dynamical comparison between two recent drought southwest monsoon seasons 2002 and 2009 over India , MAUSAM: Vol. 62 No. 2 (2011): MAUSAM
- G. K. SAWAISARJE, SOMENATH DUTTA , S. JAGTAP, Role of Hamiltonian energy in thunderstorms , MAUSAM: Vol. 68 No. 3 (2017): MAUSAM
- SOMENATH DUTTA, AMIT P. KESARKAR, Diurnal and spatial variation of convective parameters over Bay of Bengal during BOBMEX 1999 , MAUSAM: Vol. 55 No. 2 (2004): MAUSAM
- SOMENATH DUTTA, D. M. RASE , SUNITHA DEVI, A diagnostic study on the energetic aspects of weak/strong spell of north east monsoon , MAUSAM: Vol. 67 No. 2 (2016): MAUSAM
- SOMENATH DUTTA, S. I. LASKAR, M. MAITI, Does the Western-Ghats play any dynamical role in the distance effect of vortex over the Bay of Bengal on the enhancement of monsoon rainfall over Pune? , MAUSAM: Vol. 57 No. 4 (2006): MAUSAM
- SOMENATH DUTTA, NARESH KUMAR, Parameterization of momentum and energy flux associated with mountain wave across the Assam - Burma hills , MAUSAM: Vol. 56 No. 3 (2005): MAUSAM
- SOMENATH DUTTA, PRAKASH KHARE, AVINASH TATHE, Isolated heavy rainfall over Sylhet, Bangladesh and convective instability , MAUSAM: Vol. 66 No. 4 (2015): MAUSAM

1 2 > >>

List of special issues

List of awards papers

Information

For Readers

For Authors

For Librarians

Impact Factor

Make a Submission

MAUSAM, the quarterly research journal brought out by the India Meteorological Department (IMD)

Follow MAUSAM Journal on:

About us

[About the Journal](#)

[Editorial Committee](#)

Other Publications

[NewsLetter](#)

[Annual Report](#)

Discover Content

[Search an Article](#)

New Entries

[Make a New Submission](#)

Privacy Policy

[Privacy statement](#)

Contact us:

Phone:

+911143824522, +911143824298

e-mail @ -
mausam.imd@imd.gov.in,
mausampublication@gmail.com

Dr. Bhaskar Chandra Sarkar

Journal of Scientific Research

Laminar Forced Convection MHD Couette-Poiseuille Flow with Viscous and Joule Dissipations

B. C. Sarkar
Department of Mathematics, Ramananda College, Bishnupur 722122, India

DOI: https://doi.org/10.3329/jsr.v14i3.58945

Abstract

The laminar forced convection MHD Couette-Poiseuille flow of a viscous incompressible fluid with the viscous and Joule dissipations has been studied. Two different orientations of the wall thermal boundary-conditions have been considered, namely: the constant heat-flux at the upper moving plate with the adiabatic stationary lower plate and the constant heat flux at the stationary lower plate with an adiabatic moving upper plate. The governing equations are solved analytically. It is observed that the fluid velocity increases near the stationary plate and it decreases near the moving plate with an increase in magnetic parameter. The temperature field is significantly affected by the modified Brinkman number. The fluid temperature increases when the lower plate is adiabatic and the upper plate is at positive constant heat flux while it decreases in case the lower plate is at negative constant heat flux and the upper plate is adiabatic with an increase in modified Brinkman number for the combined effects of viscous and Joule dissipations. Further, the fluid temperature decreases for positive heat flux case while it increases for negative heat flux case with an increase in either magnetic parameter or velocity parameter when the combined effects of viscous and Joule dissipations are taken into account.

Downloads

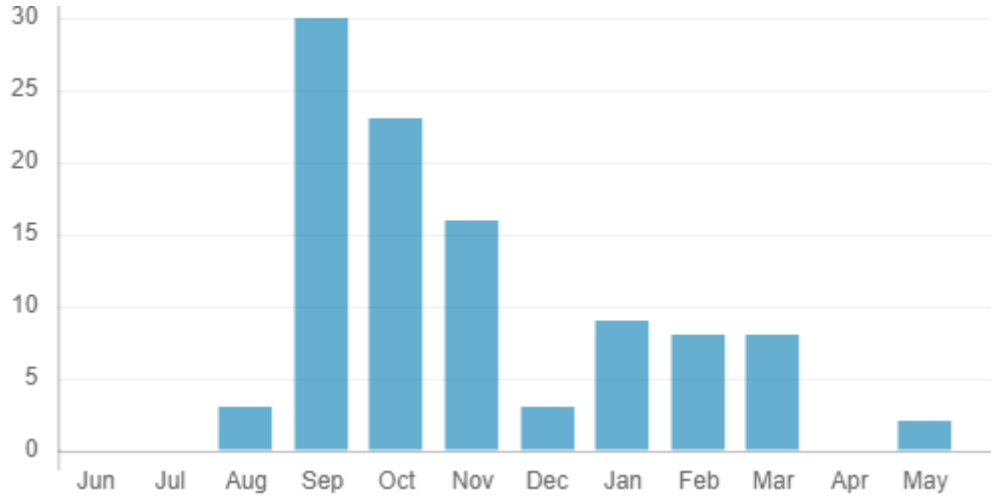

Information

For Readers

For Authors

Journal of Scientific Research
ISSN 2070-0237 eISSN 2070-0245

DR. Baibaswata Bhattacharjee

DR. DEEPAK KUMAR SINGH

Sports Scientists Views in
Indian Journal of Physical Education, Sports & Applied Sciences
I.J.P.E.S.A.S
Available Online
www.sportscientistsviews. com
Journal DOI-05-2016-44975451
Scientific Journal Impact Factor-5.684

A COMPARATIVE STUDY ON SELECTED FITNESS VARIABLES OF TRIBAL HANDBALL AND VOLLEYBALL PLAYERS

Argha Nayak[1] & Dr. Deepak Kumar Singh[2]

Affiliations:

1. State Aided College Teacher, Gobinda Prasad Mahavidyalaya, Bankura, West Bengal Email: arghanayak90@gmail.com
2. Assistant Professor Department of Physical Education Ramananda College Bishnupur, Bankura, West Bengal, Email: deepakpe2014@gmail.com Mobile 8918873871

ABSTRACT

Sports by their very nature an enjoyable, challenging, all absorbing and require a certain amount of skill and physical condition in order of human values. Ball games is one of the most popular of all the common games and sports. Handball is very fast by its nature and demands a high level of specific fitness. It is game of constant actions and requires continuous adaptations to the changing situation by the team as well as by individual players. Volleyball has a requirement for great deal of planned program to highly trained teams. The purpose of the study was to compare the selected fitness variables between tribal Handball and Volleyball players of Bankura district. Forty (40) male student players of Gobinda Prasad Mahavidyalaya and Ramananda College (20 Handball and 20 volleyball players) were selected as subjects. The average age of the subject was 19.2 years. The performance variables such as speed, strength, agility and cardiorespiratory endurance were measured with a standard test. Product moment correlation was used to established reliability. t-test was used in order to find out the significant differences between the selected variables of Handball and Volleyball players. The significant differences were observed at 0.05 level in speed, leg explosive strength, agility and cardiorespiratory endurance. No significant difference was seen in Arm and shoulder strength.

Keywords: Speed, Strength, Agility, Cardio respiratory, Variables.

DR. BAIBASWATA BHATTACHARJEE

Abstract

In recent trends, digital systems in the light of power dissipation are a crucial issue. In computing, the computational process of reversible logic is bijective and can decrease the rising issue of power dissipation. In reversible circuit design, Peres gate considered as one of the fundamental reversible gate. Therefore, a Peres gate using Add/Drop Multiplexer (ADM) and Reflective Semiconductor Optical Amplifier (RSOA) is proposed in this paper. Frequency encoding scheme and dibit-based logic are incorporated here. In long range transmission, frequency encoding bears huge benefits in respect with the other encoding techniques. This encoding technique may decrease the probability of bit error. Due to the high gain and low noise property of RSOA, the proposed design can perform operations like computation, data processing, etc. at ultra-high speed with low noise. MATLAB Simulink (R2018a) software has been used to verify the operation of the proposed design.

Keywords: Frequency encoding ▪ dibit-based logic ▪ Peres gate ▪ reflective semiconductor optical amplifier (RSOA) ▪ add/drop multiplexer (ADM)

Research Article | Published: 29 August 2022

A design of all-optical read-only memory using reflective semiconductor optical amplifier

Surajit Bosu & Baibaswata Bhattacharjee

Journal of Optics (2022)

Abstract

In recent times, any device should be designed with taken care of power consumption as well as speed. Photon has super-fast speed so it is very preferable to the researcher rather than the electron. So the researchers focus on the development of low-power-consuming devices. The reflective semiconductor optical amplifier (RSOA) is a suitable candidate for that purpose. It has a versatile gain medium and also it has huge application in passive optical networks. In this article, we have proposed a design of read-only memory using RSOA. To verify the practical feasibility, we have used MATLAB software to simulate the design. For all the memory outputs, the quality factor (Q), extinction ratio, contrast ratio, and also bit error rate have been calculated.

References

1. B. Ghosh, S. Hazra, N. Haldar, D. Roy, S.N. Patra, J. Swarnakar, P.P. Sarkar, S. Mukhopadhyay, A novel approach to realize of all optical frequency encoded dibit based XOR and XNOR logic gates using optical switches with simulated verification. Opt. Spectrosc. **124**(3), 337 (2018)

2. K. Mukherjee, K. Majhi, A. Raja, A novel approach to all-optical universal soliton logic gate NAND utilizing reflective semiconductor optical amplifiers. J. Opt. **49**(4), 516 (2020)

3. K. Mukherjee, K. Maji, A. Raja, M.K. Mandal, All-optical soliton based universal logic NOR utilizing a single reflective semiconductor optical amplifier (RSOA). Photon. Netw. Commun. **43**(2), 101 (2022). https://doi.org/10.1007/s11107-021-00956-6

4. A. Kotb, K.E. Zoiros, W. Li, C. Guo, Theoretical investigation of 120 Gb/s all-optical AND and OR logic gates using reflective semiconductor optical amplifiers. Opt. Eng. **60**(6), 066107 (2021)

5. A. Alquliah, A. Kotb, S.C. Singh, C. Guo, All-optical AND, NOR, and XNOR logic gates using semiconductor optical amplifiers-based Mach-Zehnder interferometer followed by a delayed interferometer. Optik **225**, 165901 (2021)

6. S. Mitra, S. Mukhopadhyay, An all-optical scheme for implementing a NAND logic by dibit representation of squeezed state of light. J. Nonlinear Opt. Phys. Mater. **24**(04), 1550048 (2015)

7. S. Saha, S. Mukhopadhyay, All optical frequency encoded quaternary memory unit using symmetric configuration of MZI-SOA. Opt. Laser Technol. **131**, 106386 (2020)

8. P.P. Sarkar, B. Ghosh, S.N. Patra, S. Mukhopadhyay, A new scheme of an all optical frequency encoded dibit based latch with its simulated result. J. Opt. Technol. **84**(9), 631–634 (2017)

9. S. Saha, S. Dey, & S. Mukhopadhyay, All optical wavelength encoded 1-bit memory unit exploiting the nonlinear character of asymmetric MZI-SOA switch, in *International Conference on Fibre Optics and Photonics* (Optical Society of America, Th3A-32, 2016)

10. A. Raja, K. Mukherjee, J.N. Roy, Design of dual semiconductor optical amplifier structure based all-optical standard quaternary inverter and quaternary clocked SR flip-flop. Opt. Quant. Electron. **54**(1), 1–23 (2022)

11. K. Mukherjee, A.K. Meikap, D. Kumbhakar, Frequency encoded all optical single bit memory unit using difference frequency generation alone. Opt. Quant. Electron. **43**(6), 101–107 (2012)

12. B. Chakraborty, S. Mukhopadhyay, A method of implementing all-optical clocked flip-flop with phase encoded optical logic. Optik **123**(16), 1432–1435 (2012)

13. G.K. Bharti, J.K. Rakshit, Design of all-optical JK, SR and T flip-flops using micro-ring resonator-based optical switch. Photon Netw. Commun. **35**(3), 381–391 (2018)

14. J.K. Rakshit, J.N. Roy, T. Chattopadhyay, A theoretical study of all optical clocked D flip flop using single micro-ring resonator. J. Comput. Electron. **13**(1), 278–286 (2014)

15. D. Fitsios, C. Vagionas, G.T. Kanellos, A. Miliou, N. Pleros, Memory speed analysis of an optical flip-flop employing a SOA-MZI and a feedback loop. IEEE J. Quantum Electron. **49**(2), 169–178 (2012)

16. L.Q. Guo, M.J. Connelly, A novel approach to all-optical wavelength conversion by utilizing a reflective semiconductor optical amplifier in a co-propagation scheme. Opt. Commun. **281**(17), 4470–4473 (2008)

17. K. Mukherjee, All optical read only memory with frequency encoded addressing technique. Optik **122**(16), 1437–1440 (2011)

18. S. Kaur, R.S. Kaler, T.S. Kamal, All-optical binary full adder using logic operations based on the nonlinear properties of a semiconductor optical amplifier. J. Opt. Soc. Korea **19**(3), 222–227 (2015)

19. Y.J. Jung, N. Park, Y.M. Jhon, S. Lee, Design of all-optical read-only memory. Appl. Opt. **48**(31), G21–G27 (2009)

20. K. Maji, K. Mukherjee, A. Raja, J.N. Roy, Numerical simulations of an all-optical parity generator and checker utilizing a reflective semiconductor optical amplifier at 200 Gbps. J. Comput. Electron. **19**(2), 800–814 (2020)

21. S. Bosu, B. Bhattacharjee, All-optical dibit-based Feynman gate using reflective semiconductor optical amplifier with frequency encoding scheme. J. Opt. (2022). https://doi.org/10.1007/s12596-022-00875-3

22. A. Kotb, K.E. Zoiros, C. Guo, Performance investigation of 120 Gb/s all-optical logic XOR gate using dual-reflective semiconductor optical amplifier-based scheme. J. Comput. Electron. **17**(4), 1640–1649 (2018)

23. A.S. Das, A.S. Patra, RSOA-based full-duplex WDM-PON for 20 Gbps transmission in two

channels over a long-haul SMF using external modulation scheme. J. Opt. Commun. **36**(3), 231–235 (2015)

24. G.C. Mandal, R. Mukherjee, B. Das, A.S. Patra, A full-duplex WDM hybrid fiber-wired/fiber-wireless/fiber-VLC/fiber-IVLC transmission system based on a self-injection locked quantum dash laser and a RSOA. Opto Commun. **427**, 202–208 (2018)

25. G.C. Mandal, R. Mukherjee, B. Das, A.S. Patra, Bidirectional and simultaneous transmission of baseband and wireless signals over RSOA based WDM radio-over-fiber passive optical network using incoherent light injection technique. AEU Int. J. Electron. Commun. **80**, 193–198 (2017)

26. G.C. Mandal, R. Mukherjee, B. Das, A.S. Patra, Next-generation bidirectional triple-play services using RSOA based WDM radio on free-space optics PON. Opt. Commun. **411**, 138–142 (2018)

27. T. Chattopadhyay, All-optical clocked delay flip-flop using a single terahertz optical asymmetric demultiplexer-based switch: a theoretical study. Appl. Opt. **49**(28), 5226–5235 (2010)

28. Z.V. Rizou, K.E. Zoiros, T. Rampone, A. Sharaiha, Reflective semiconductor optical amplifier direct modulation capability enhancement using birefringent fiber loop. Appl. Sci. **10**, 5328 (2020). https://doi.org/10.3390/app10155328

29. A.S. Das, A.S. Patra, Bidirectional transmission of 10 Gbit/s using RSOA based WDM-PON and optical carrier suppression scheme. J. Opt. Commun. **35**(3), 239–243 (2014)

30. A.S. Das, P.K. Kuiri, A.S. Patra, A RSOA based full-duplex 80 channel CATV signal with 1.25 Gbps data-stream transmission system using optical carrier suppression and injection-locked FPLDs, in *International Conference on Optics and Photonics*, vol. 9654, pp. 356–362 (2015)

31. K. Mallick, R. Mukherjee, B. Das, G.C. Mandal, A.S. Patra, Bidirectional hybrid OFDM based wireless-over-fiber transport system using reflective semiconductor amplifier and polarization multiplexing technique. AEU Int. J. Electron. Commun. **96**, 260–266 (2018)

32. Z.V. Rizou, K.E. Zoiros, M.J. Connelly, Semiconductor optical amplifier pattern effect

suppression using optical notch filtering. J. Eng. Sci. Technol. Rev **9**(4), 198–201 (2016)

33. S. Bosu, B. Bhattacharjee, A novel design of frequency encoded multiplexer and demultiplexer systems using reflected semiconductor optical amplifier with simulative verification. J. Opt. **50**(3), 361–370 (2021)

Author information

Authors and Affiliations

Department of Physics, Bankura Sammilani College, Kenduadihi, Bankura, West Bengal, 722102, India

Surajit Bosu

Department of Physics, Ramananda College, Bishnupur, Bankura, West Bengal, 722122, India

Baibaswata Bhattacharjee

Corresponding author

Correspondence to Baibaswata Bhattacharjee.

Additional information

Publisher's Note

Rights and permissions

About this article

Cite this article

Bosu, S., Bhattacharjee, B. A design of all-optical read-only memory using reflective semiconductor optical amplifier. *J Opt* (2022). https://doi.org/10.1007/s12596-022-00943-8

Received	Accepted	Published
17 April 2022	02 August 2022	29 August 2022

DOI
https://doi.org/10.1007/s12596-022-00943-8

Keywords

Reflective semiconductor optical amplifier

Soliton pulse **Decoder** **Read only memory**

Research Article | Published: 16 May 2022

All-optical dibit-based Feynman gate using reflective semiconductor optical amplifier with frequency encoding scheme

Surajit Bosu & Baibaswata Bhattacharjee

Journal of Optics **52**, 33–41 (2023)

Abstract

In recent years, reversible gates have a great impact on optical nanotechnology, quantum and DNA computing. In the optical field, reversible gates like the Fredkin gate, Feynman gate, Toffoli gate, and Peres gate are very demanding due to their low power consumption. In this article, a novel design of Feynman gate using Add/Drop Multiplexer and Reflective Semiconductor Optical Amplifier (RSOA) is proposed. Frequency encoding scheme and dibit-based logic are incorporated in the proposed design. The Frequency encoding technique decreases the probability of bit error in long-range transmission. Due to the high gain and low noise property of RSOA, the proposed design can perform operations like computation and data processing at ultra-high speed with low noise. To verify the

operation of the proposed design, we have used MATLAB Simulink (R2018a) software.

References

1. S. Dey, P. De, S. Mukhopadhyay, An all-optical implementation of Fredkin gate using kerr effect. Optoelectron. Lett. **15**(4), 317 (2019)

2. J. Zhu, P. Zhou, X. Su, Z. You, Accurate and fast 3D surface MEA- surement with temporal-spatial binary encoding structured illumination. Opt. Express **24**(25), 28549 (2016)

3. S. Dey, S. Mukhopadhyay, All-optical integrated square root of Pauli- Z (SRZ) gates using polarization and phase encoding. J. Opt. **48**(4), 520 (2019)

4. M.N. Sarfaraj, S. Mukhopadhyay, All-optical scheme for implementation of tri-state Pauli-X, Y and Z quantum gates using phase encoding. Optoelectron. Lett. **17**(12), 746 (2021)

5. A. Raja, K. Mukherjee, J. Roy, Analysis of new all optical polarization- encoded dual SOA-based ternary NOT & XOR gate with simulation. Photonic Netw. Commun. **41**(3), 242 (2021)

6. D. Mandal, S. Mandal, M.K. Mandal, S.K. Garai, Alternative approach of developing optical binary adder using reversible Peres gates. Int. J. Opt. (2018). https://doi.org/10.1155/2018/8541371

7. S. Saha, S. Mukhopadhyay, All optical frequency encoded quaternary memory unit using symmetric configuration of MZI-SOA. Opt. Laser Technol. **131**, 106386 (2020)

8. S. Saha, S. Biswas, S. Mukhopadhyay, An alternative approach for binary to decimal conversion of frequency encoded optical data

using MZI-SOA switch. J. Opt. (2021). https://doi.org/10.1007/s12596-021-00786-9

9. S. Bosu, B. Bhattacharjee, A novel design of frequency encoded multiplexer and demultiplexer systems using reflected semiconductor optical amplifier with simulative verification. J. Opt. **50**(3), 361 (2021)

10. S. Bosu, B. Bhattacharjee, All optical frequency encoded dibit-based parity generator using reflected semiconductor optical amplifier with simulative verification. FU Electron. Energy **35**(1), 29 (2022)

11. R. Landauer, Irreversibility and heat generation in the computing process. IBM J. Res. Dev. **5**(3), 183 (1961)

12. S.K. Garai, A novel method of developing all optical frequency encoded Fredkin gates. Opt. Commun. **313**, 441 (2014)

13. S.F. Naz, S. Ahmed, S. Sharma, F. Ahmad, D. Ajitha, Fredkin gate based energy efficient reversible D flip flop design in quantum dot cellular automata. Mater. Today Proc. **46**, 5248–5255 (2021)

14. N. Ghazali, M. Wahid, N.A. Hambali, N. Juhari, M. Shahimin, Characterization of all-optical Feynman and Fredkin gates utilizing optimized SOANOLM. AIP Conf. Proc. **2045**, 020079 (2018)

15. S. Kumar, S.K. Raghuwanshi, Design of optical reversible logic gates using electro-optic effect of lithium niobate based Mach-Zehnder interferometers. Appl. Opt. **55**(21), 5693 (2016)

16. K. Mukherjee, K. Maji, A. Raja, All-optical feynman gate using reflective semiconductor optical amplifiers and binary to gray code converter. Adv. Appl. Math. Sci. **19**(9), 919 (2019)

17. G. K. Maity, S. P. Maity, J. N. Roy, 'TOAD-based Feynman and Toffoli gate', In: 2012 Second International conference on advanced computing & communication technologies, pp. 343–349 (2012)

18. B. Ghosh, S. Hazra, N. Haldar, D. Roy, S.N. Patra, J. Swarnakar, P.P. Sarkar, S. Mukhopadhyay, A novel approach to realize of all optical frequency encoded dibit based XOR and XNOR logic gates using optical switches with simulated verification. Opt. Spectrosc. **124**(3), 337 (2018)

19. P.P. Sarkar, B. Ghosh, S.N. Patra, Simulative study of all optical fre- quency encoded dibit based universal nand and nor logic gates using a reflective semiconductor optical amplifier and an add/drop multiplexer. J. Opt. Technol. **83**(4), 257 (2016)

20. B. Ghosh, S. Biswas, S. Mukhopadhyay, A novel method of all- optical wavelength encoded logic and inhibitor operations with dibit representation technique. Optik **126**(4), 483 (2015)

21. A. Ghosh, A. Jain, N. Singh, S. K. Sarkar, 'Single electron threshold logic based Feynman gate implementation', In: 2016 Second international conference on research in computational intelligence and communication networks (ICRCICN), pp. 266–268 (2016)

22. P.K. Biswas, A.N. Bahar, M.A. Habib, M. Abdullah-Al-Shafi, Efficient design of Feynman and Toffoli gate in quantum dot cellular automata (QCA) with energy dissipation analysis. Nanosci. Nanotechnol. 7(2), 27 (2017)

23. M. H. Khan, 'Single-electron transistor based implementation of NOT, Feynman, and Toffoli

gates, in: 2015 IEEE International symposium on multiple-valued logic, pp. 66–71 (2015)

24. K. Bordoloi, T. Theresal, S. Prince, 'Design of all optical reversible logic gates', in: 2014 International conference on communication and signal processing, pp. 1583–1588 (2014)

25. R.P. Feynman, Quantum mechanical computers. Opt. News **11**(2), 11 (1985)

26. S. Bosu, B. Bhattacharjee, 'All-optical frequency encoded dibit-based half adder using reflective semiconductor optical amplifier with simulative verification', in 2021 Devices for integrated circuit (DevIC), pp. 388–392 (2021)

27. S. Bosu, B. Bhattacharjee, 'A design of frequency encoded dibit-based comparator using reflective semiconductor optical amplifier with simulative verification', in 2021 Devices for integrated circuit (DevIC), pp. 175–179 (2021)

28. K. Mukherjee, K. Majhi, A. Raja, A novel approach to all-optical universal soliton logic gate NAND utilizing reflective semiconductor optical amplifiers. J. Opt. **49**(4), 516 (2020)

29. K. Mukherjee, K. Maji, A. Raja, M.K. Mandal, All-optical soliton based universal logic NOR utilizing a single reflective semiconductor optical amplifier (RSOA). Photonic Netw. Commun. (2021). https://doi.org/10.2298/FUEE2201029B

30. B. Ghosh, S. Hazra, P.P. Sarkar, Simulative study of all-optical frequency encoded dibit-based controlled multiplexer and de-multiplexer using optical switches. J. Opt. **48**(3), 365 (2019)

31. S. Mukhopadhyay, Binary optical data subtraction by using a ternary dibit representation technique in optical arithmetic problems. Appl. Opt. **31**(23), 4622 (1992)

32. S. Bosu, B. Bhattacharjee, 'All-optical frequency encoded dibit-based half subtractor using reflective semiconductor optical amplifier with simulative verification', In Proceedings of the International Conference on Paradigms of Communication, Computing and Data Sciences, ed. by M. Dua, A. K. Jain, A. Yadav, N. K, P. Siarry (Springer, Singapore, 2022), pp. 29–38

33. K. Maji, K. Mukherjee, A. Raja, J.N. Roy, Numerical simulations of an all-optical parity generator and checker utilizing a reflective

semiconductor optical amplifier at 200 Gbps. J. Comput. Electron. **19**(2), 800 (2020)

Acknowledgements

We are thankful to the Department of Physics, Bankura University, Bankura, Pin-722155, West Bengal, India for support to conduct this research work.

Author information

Authors and Affiliations

Department of Physics, Bankura Sammilani College, Kenduadihi, Bankura, West Bengal, 722102, India

Surajit Bosu

Department of Physics, Ramananda College, Bishnupur, Bankura, West Bengal, 722122, India

Baibaswata Bhattacharjee

Corresponding author

Correspondence to Surajit Bosu.

Additional information

Publisher's Note

Rights and permissions

About this article

Cite this article

Bosu, S., Bhattacharjee, B. All-optical dibit-based Feynman gate using reflective semiconductor optical amplifier with frequency encoding scheme. *J Opt* **52**, 33–41 (2023). https://doi.org/10.1007/s12596-022-00875-3

Received	Accepted	Published
20 December 2021	09 April 2022	16 May 2022

Issue Date
March 2023

DOI
https://doi.org/10.1007/s12596-022-00875-3

Keywords

Frequency encoding **Feynman gate** **Dibit-based logic** **RSOA** **ADM**

INDERSCIENCE PUBLISHERS
Linking academia, business and industry through research

Forthcoming and Online First Articles

International Journal of Nanoparticles

Forthcoming articles have been **peer-reviewed** and **accepted for publication** but are pending final changes, are not yet published and may not appear here in their final order of publication until they are assigned to issues. Therefore, the content conforms to our standards but the presentation (e.g. typesetting and proof-reading) is not necessarily up to the Inderscience standard. Additionally, titles, authors, abstracts and keywords **may change before publication**. Articles will not be published until the final proofs are validated by their authors.

Forthcoming articles must be purchased for the purposes of research, teaching and private study only. These articles can be cited using the expression "in press". For example: Smith, J. (*in press*). Article Title. *Journal Title*.

Articles marked with this shopping trolley icon are available for purchase - click on the icon to send an email request to purchase.

Online First articles are published online here, before they appear in a journal issue. Online First articles are fully citeable, complete with a DOI. They can be cited, read, and downloaded. Online First articles are published as Open Access (OA) articles to make the latest research available as early as possible.

Articles marked with this Open Access icon are Online First articles. They are freely available and openly accessible to all without any restriction except the ones stated in their respective CC licenses.

Register for our alerting service, which notifies you by email when new issues are published online.

We also offer Latest issue contents as RSS feed which provide timely updates of tables of contents, newly published articles and calls for papers.

Sign up for new issue alerts
Subscribe/buy articles/issues
View sample articles
Latest issue contents as RSS feed
Forthcoming articles
Journal information in easy print format (PDF)

Keep up-to-date
Our Blog
Follow us on Twitter
Visit us on Facebook
Our Newsletter (subscribe for free)
RSS Feeds
New issue alerts

International Journal of Nanoparticles (2 papers in press)

Regular Issues

- **Synergistic antibacterial effect against S. Aureus in combination with Amoxicillin using fluconazole nanoparticles studied under Atomic Force Microscopy.**

  by Dania Ahmed, Samina Perveen, Raza Shah, Farid Ahmed

  Abstract: COVID-19 patients are increasing day by day. The risk of bacteria-virus co-infection also escalates. Because of the extensive use of antibacterial drugs, the drug resistant bacterial strains are increasing. rnAntibiotic resistance caused by pathogenic bacteria has become a major health challenge these days. The key objective was to examine the antibacterial effects of Fluconazole coated silver nanoparticles (Ful-AgNPs) in combination with amoxicillin against bacteria that show resistance to amoxicillin. Here we are reporting a quick, tranquil, and feasible synthetic procedure for the preparation of Ful-AgNPs. Characterization of nanoparticles was performed by employing Uv-Visible spectroscopy, Fourier-transform infrared spectroscopy, and Atomic force microscopic techniques. The size of Ful-AgNPs was found in the range from 9-18 nm. Ful-AgNPs shows selective recognition capability towards amoxicillin in the presence of other competing drugs without showing any interference. The binding ratio between Ful-AgNPs and amoxicillin was observed 1:1 (Ful-AgNPs: amoxicillin) in Jobs plot study. The sensing capability of Ful-AgNPs was also evaluated in blood plasma and tap water to evaluate the matrix effect, and Ful-AgNPs recognize amoxicillin in both mediums without showing any interferences. Fractional inhibitory concentration index shows synergistic interaction of Ful-AgNPs with amoxicillin. These results demonstrate that the combination of amoxicillin with Ful-AgNPs inhibits the growth of bacterial cells and the MIC value found to be 25-50

  Keywords: *Silver nanoparticles; Antibacterial potential; UV-Visible spectroscopy; Amoxicillin; Synergistic effect; Combinatorial effect; COVID-19.*

- **A combination of carrier erythrocytes and artificial nanoparticles as a promising approach for drug delivery: a review**

  by Nadeesha Athukorala, Sanath Rajapakse, S.D.S.S. Sooriyapathirana

  Abstract: Increased awareness that drug release patterns can affect therapeutic responses, the necessity of safe and efficient drug administration, and the requirement of novel strategies to deliver complex drugs fuelled the drug delivery research. Scientists have understood that novel therapies are possible when a drug is encapsulated within or attached to a carrier. It became clear that the drug carrier systems are essential as the drug itself. Nanotechnology's application in drug delivery is reported to improve therapeutic outcomes. Nevertheless, challenges related to biocompatibility, cytotoxicity, and rapid clearance limited the use of nanomedicine. After extensive research, erythrocyte membrane camouflaged nanoparticles loaded with drugs have become an attractive candidate for drug delivery. The combined strategy has offered an opportunity to unite natural cell membrane properties with artificial nanoparticles. This article reviews the background, development, and importance of the combined strategy, and provides a foundation to stimulate the interests in this novel strategy.

  Keywords: *erythrocytes; nanoparticles; drug delivery; targeted drug delivery.*
  DOI: 10.1504/IJNP.2023.10054751

Return to top

Contact us About Inderscience OAI Repository Privacy and Cookies Statement Terms and Conditions Help Sitemap

Research Article | Published: 02 June 2021

A novel design of frequency encoded multiplexer and demultiplexer systems using reflected semiconductor optical amplifier with simulative verification

Surajit Bosu & Baibaswata Bhattacharjee

Journal of Optics **50**, 361–370 (2021)

Abstract

In this modern era, optical technology is used for high-speed processing because photon carries information instead of an electron. In signal processing, multiplexing and demultiplexing are the most valuable component. In this communication, designs of frequency encoded 2:1 multiplexer and 1:2 demultiplexer with the use of Reflective Semiconductor Optical Amplifier and add/drop multiplexer are devised. These proposed designs work at high-speed due to the high speed switching property of reflective semiconductor optical amplifier. In the multiplexing and demultiplexing system, coded data signals and coded control signals are the most important issues. Here, frequency encoding is opted because

frequency is unaltered after reflection, refraction, absorption, etc., and it gives a very good response for long-distance transmission of processed data. The operation of devised designs has also been verified through MATLAB Simulink (R2018a) software.

References

1. G. Berrettini, A. Simi, A. Malacarne, A. Bogoni, L. Poti, IEEE Phot. Technol. Lett. **18**(8), 917 (2006)

2. S. Bashiri, K. Fasihi, Opt. Quant. Elect. **51**(11), 1 (2019)

3. D. Samanta, S. Mukhopadhyay, J. Opt. **41**(3), 167 (2012)

4. S.K. Chandra, P.P. Sarkar, S. Biswas, S. Mukhopadhyay, Optik **125**(23), 6953 (2014)

5. S.K. Garai, S. Mukhopadhyay, Opt. Laser Technol. **41**(8), 972 (2009)

6. S. Bhattacharya, S. Mukhopadhyay, J. Opt. **48**(2), 199 (2019)

7. S. Dutta, S. Mukhopadhyay, Optik **122**(12), 1088 (2011)

8. K. Mukherjee, Optik **122**(4), 321 (2011)

9. J. Zhu, P. Zhou, X. Su, Z. You, Opt. Express **24**(25), 28549 (2016)

10. S.P. Singh, S. Kar, V. Jain, Fiber Int. Opt. **26**(2), 79 (2007)

11. K. Kaur, K. Bhatia, J. Opt. Commun. **36**(4), 297 (2015)

12. J.K. Rakshit, J.N. Roy, Optica Applicata **44**, 1 (2014)

13. N. Verma, S. Mandal, J. Nonlin. Opt. Phys. Mater. **25**(01), 1650013 (2016)

14. A. Pal, S. Mukhopadhyay, Opt. Laser Technol. **44**(1), 281 (2012)

15. A. Pal, S.K. Pal, S. Mukhopadhyay, Optik **125**(1), 304 (2014)

16. B. Ghosh, S. Hazra, P.P. Sarkar, J. Opt. **48**(3), 365 (2019)

17. N.K. Dutta, Q. Wang, *Semiconductor Optical Amplifiers* (World scientific, Singapore, 2013)

18. R. Kaler, R. Kaler, Optik **122**(15), 1399 (2011)

19. M. Kumar, S. Goel, P.K. Nahata, N. Nair, in *2019 6th International Conference on Signal Processing and Integrated Networks (SPIN)* (IEEE, 2019), pp. 900–902

20. R. Katti, S. Prince, *In 2015 IEEE International Conference on Signal Processing* (Communication and Energy Systems (SPICES) (IEEE, Informatics, 2015), pp. 1–4

21. J.K. Rakshit, J.N. Roy, Optica Applicata **46**(4), 517 (2016)

22. K. Mukherjee, J. Opt. **49**(1), 102 (2020)

23. T. Barwicz, H.A. Haus, J. Lightwave Technol. **23**(9), 2719 (2005)

24. P. Sarkar, B. Ghosh, S.S.N. Patra, J. Opt. Technol. **83**(4), 257 (2016)

25. P.P. Sarkar, B. Satpati, S. Mukhopadhyay, J. Opt. **42**(4), 360 (2013)

26. P.P. Sarkar, B. Satpati, S. Mukhopadhyay, Optik **125**(3), 1333 (2014)

27. L. Guo, M. Connelly, Opt. Commun. **281**(17), 4470 (2008)

28. K. Maji, K. Mukherjee, A. Raja, J. Roy, Journal of Computational Electronics pp. 1–15 (2020)

Author information

Authors and Affiliations

Department of Physics, Bankura Sammilani College, Kenduadihi, Bankura, India

Surajit Bosu

Department of Physics, Ramananda College, Bishnupur, Bankura, India

Baibaswata Bhattacharjee

Corresponding author

Correspondence to Surajit Bosu.

Additional information

Publisher's Note

Springer Nature remains neutral with regard to jurisdictional claims in published maps and institutional affiliations.

Rights and permissions

Reprints and Permissions

About this article

Cite this article

Bosu, S., Bhattacharjee, B. A novel design of frequency encoded multiplexer and demultiplexer systems using reflected semiconductor optical amplifier with simulative verification. *J Opt* **50**, 361–370 (2021). https://doi.org/10.1007/s12596-021-00711-0

Received	Accepted	Published
28 August 2020	10 May 2021	02 June 2021

Issue Date

September 2021

DOI

https://doi.org/10.1007/s12596-021-00711-0

Keywords

Multiplexer **Demultiplexer**

Frequency encoding technique

Reflected semiconductor optical amplifier

Add/drop multiplexer

Research Article | Published: 02 June 2021

A novel design of frequency encoded multiplexer and demultiplexer systems using reflected semiconductor optical amplifier with simulative verification

Surajit Bosu & Baibaswata Bhattacharjee

Journal of Optics **50**, 361–370 (2021)

Abstract

In this modern era, optical technology is used for high-speed processing because photon carries information instead of an electron. In signal processing, multiplexing and demultiplexing are the most valuable component. In this communication, designs of frequency encoded 2:1 multiplexer and 1:2 demultiplexer with the use of Reflective Semiconductor Optical Amplifier and add/drop multiplexer are devised. These proposed designs work at high-speed due to the high speed switching property of reflective semiconductor optical amplifier. In the multiplexing and demultiplexing system, coded data signals and coded control signals are the most important issues. Here, frequency encoding is opted because

frequency is unaltered after reflection, refraction, absorption, etc., and it gives a very good response for long-distance transmission of processed data. The operation of devised designs has also been verified through MATLAB Simulink (R2018a) software.

References

1. G. Berrettini, A. Simi, A. Malacarne, A. Bogoni, L. Poti, IEEE Phot. Technol. Lett. **18**(8), 917 (2006)

2. S. Bashiri, K. Fasihi, Opt. Quant. Elect. **51**(11), 1 (2019)

3. D. Samanta, S. Mukhopadhyay, J. Opt. **41**(3), 167 (2012)

4. S.K. Chandra, P.P. Sarkar, S. Biswas, S. Mukhopadhyay, Optik **125**(23), 6953 (2014)

5. S.K. Garai, S. Mukhopadhyay, Opt. Laser Technol. **41**(8), 972 (2009)

6. S. Bhattacharya, S. Mukhopadhyay, J. Opt. **48**(2), 199 (2019)

7. S. Dutta, S. Mukhopadhyay, Optik **122**(12), 1088 (2011)

8. K. Mukherjee, Optik **122**(4), 321 (2011)

9. J. Zhu, P. Zhou, X. Su, Z. You, Opt. Express **24**(25), 28549 (2016)

10. S.P. Singh, S. Kar, V. Jain, Fiber Int. Opt. **26**(2), 79 (2007)

11. K. Kaur, K. Bhatia, J. Opt. Commun. **36**(4), 297 (2015)

12. J.K. Rakshit, J.N. Roy, Optica Applicata **44**, 1 (2014)

13. N. Verma, S. Mandal, J. Nonlin. Opt. Phys. Mater. **25**(01), 1650013 (2016)

14. A. Pal, S. Mukhopadhyay, Opt. Laser Technol. **44**(1), 281 (2012)

15. A. Pal, S.K. Pal, S. Mukhopadhyay, Optik **125**(1), 304 (2014)

16. B. Ghosh, S. Hazra, P.P. Sarkar, J. Opt. **48**(3), 365 (2019)

17. N.K. Dutta, Q. Wang, *Semiconductor Optical Amplifiers* (World scientific, Singapore, 2013)

18. R. Kaler, R. Kaler, Optik **122**(15), 1399 (2011)

19. M. Kumar, S. Goel, P.K. Nahata, N. Nair, in *2019 6th International Conference on Signal Processing and Integrated Networks (SPIN)* (IEEE, 2019), pp. 900–902

20. R. Katti, S. Prince, *In 2015 IEEE International Conference on Signal Processing* (Communication and Energy Systems (SPICES) (IEEE, Informatics, 2015), pp. 1–4

21. J.K. Rakshit, J.N. Roy, Optica Applicata **46**(4), 517 (2016)

22. K. Mukherjee, J. Opt. **49**(1), 102 (2020)

23. T. Barwicz, H.A. Haus, J. Lightwave Technol. **23**(9), 2719 (2005)

24. P. Sarkar, B. Ghosh, S.S.N. Patra, J. Opt. Technol. **83**(4), 257 (2016)

25. P.P. Sarkar, B. Satpati, S. Mukhopadhyay, J. Opt. **42**(4), 360 (2013)

26. P.P. Sarkar, B. Satpati, S. Mukhopadhyay, Optik **125**(3), 1333 (2014)

27. L. Guo, M. Connelly, Opt. Commun. **281**(17), 4470 (2008)

28. K. Maji, K. Mukherjee, A. Raja, J. Roy, Journal of Computational Electronics pp. 1–15 (2020)

Author information

Authors and Affiliations

Department of Physics, Bankura Sammilani College, Kenduadihi, Bankura, India

Surajit Bosu

Department of Physics, Ramananda College, Bishnupur, Bankura, India

Baibaswata Bhattacharjee

Corresponding author

Correspondence to Surajit Bosu.

Additional information

Publisher's Note

Rights and permissions

About this article

Cite this article

Bosu, S., Bhattacharjee, B. A novel design of frequency encoded multiplexer and demultiplexer systems using reflected semiconductor optical amplifier with simulative verification. *J Opt* **50**, 361–370 (2021). https://doi.org/10.1007/s12596-021-00711-0

Received	Accepted	Published
28 August 2020	10 May 2021	02 June 2021

Issue Date

September 2021

DOI

https://doi.org/10.1007/s12596-021-00711-0

Keywords

Multiplexer **Demultiplexer**

Frequency encoding technique

Reflected semiconductor optical amplifier

Add/drop multiplexer

Dr. Amit Dey

Localization and delocalization in networks with varied connectivity

Tamoghna Ray, Amit Dey, and Manas Kulkarni
Phys. Rev. A **106**, 042610 – Published 17 October 2022

ABSTRACT

We study the phenomenon of localization and delocalization in a circuit-QED network with connectivity varying from finite-range coupling to all-to-all coupling. We find a fascinating interplay between interactions and connectivity. In particular, we consider (i) harmonic, (ii) Jaynes-Cummings, and (iii) Bose-Hubbard networks. We start with the initial condition where one of the nodes in the network is populated and then let it evolve in time. The time dynamics and steady state characterize the features of localization (self-trapping) in these large-scale networks. For the case of harmonic networks, exact analytical results are obtained, and we demonstrate that all-to-all connection shows self-trapping whereas the finite-ranged connectivity shows delocalization. The interacting cases (Jaynes-Cummings and Bose-Hubbard networks) are investigated both via exact quantum dynamics and via a semiclassical approach. We obtain an interesting phase diagram when one varies the range of connectivity and the strength of the interaction. We investigate the consequence of imperfections in the cavity or qubit and the role of inevitable disorder. Our results are relevant especially given recent experimental progress in engineering systems with long-range connectivity.

4 More

Received 6 April 2022 Accepted 26 September 2022

DOI: https://doi.org/10.1103/PhysRevA.106.042610

Physics Subject Headings (PhySH)

Research Areas

Cavity quantum electrodynamics (/search/results?clauses=%5B%7B%22field%22%3A%22physh%22%2C%22value%22%3A%22%7B%5C%22facetid%5C%22%3Anull%2C%5C%22conceptid%
c24fba575e45%5C%22%2C%5C%22label%5C%22%3A%5C%22Cavity%20quantum%20electrodynamics%5C%22%2C%5C%22facetlabel%5C%22%3A%5C%22%5C%22%7D%22%2C%22c

Circuit quantum electrodynamics (/search/results?clauses=%5B%7B%22field%22%3A%22physh%22%2C%22value%22%3A%22%7B%5C%22facetid%5C%22%3Anull%2C%5C%22conceptid
508852ef3d9d%5C%22%2C%5C%22label%5C%22%3A%5C%22Circuit%20quantum%20electrodynamics%5C%22%2C%5C%22facetlabel%5C%22%3A%5C%22%5C%22%7D%22%2C%22c

Localization (/search/results?clauses=%5B%7B%22field%22%3A%22physh%22%2C%22value%22%3A%22%7B%5C%22facetid%5C%22%3Anull%2C%5C%22conceptid%5C%22%3A%5C%
9fa7-
86088b7df853%5C%22%2C%5C%22label%5C%22%3A%5C%22Localization%5C%22%2C%5C%22facetlabel%5C%22%3A%5C%22%5C%22%7D%22%2C%22operator%22%3A%22AND%

**Quantum networks (/search/results?clauses=%5B%7B%22field%22%3A%22physh%22%2C%22value%22%3A%22%7B%5C%22facetid%5C%22%3Anull%2C%5C%22conceptid%5C%
b63a-
535195a24901%5C%22%2C%5C%22label%5C%22%3A%5C%22Quantum%20networks%5C%22%2C%5C%22facetlabel%5C%22%3A%5C%22%5C%22%7D%22%2C%22operator%22%**

Quantum optics (/search/results?clauses=%5B%7B%22field%22%3A%22physh%22%2C%22value%22%3A%22%7B%5C%22facetid%5C%22%3Anull%2C%5C%22conceptid%5C%22%3A%5
b24729a93d8d%5C%22%2C%5C%22label%5C%22%3A%5C%22Quantum%20optics%5C%22%2C%5C%22facetlabel%5C%22%3A%5C%22%5C%22%7D%22%2C%22operator%22%3A%2

Atomic, Molecular & Optical

AUTHORS & AFFILIATIONS

Tamoghna Ray (/search/field/author/Tamoghna%20Ray)[1,*], Amit Dey (/search/field/author/Amit%20Dey)[2,1,†], and Manas Kulkarni (/search/field/author/Manas%20Kulkarni)[1,‡]

[1]International Centre for Theoretical Sciences, Tata Institute of Fundamental Research, Bengaluru 560089, India
[2]Ramananda College, Bankura University, Bankura 722122, India

[*]tamoghna.ray@icts.res.in
[†]amit.dey.85@gmail.com
[‡]manas.kulkarni@icts.res.in

ARTICLE TEXT (SUBSCRIPTION REQUIRED)

CLICK TO EXPAND

REFERENCES (SUBSCRIPTION REQUIRED)

CLICK TO EXPAND

Issue

Vol. 106, Iss. 4 — October 2022 (/pra/issues/106/4)

ISSN 2469-9934 (online), 2469-9926 (print).

(https://librarians.aps.org/sitelicense.pdf).

DR. Saibal Mitra

General and Applied Physics | Published: 03 January 2022

An Analytical Approach for Implementing an All-Optical NOR Operation Using Amplitude Squeezed Light

Saibal Mitra

Brazilian Journal of Physics **52**, Article number: 28 (2022)

Abstract

Squeezed states of light can be a promising candidate in optical communication and measurement for its highly noise-reducing nature. Noise level produced by amplitude squeezed light is below the shot noise level which is called quantum limit of noise. So, if the encoding is done by amplitude squeezed states of light, then one can overcome the limitation significantly. In this paper, the author has proposed an analytical approach of all-optical scheme of NOR operation using amplitude squeezed light with the help of photon fluctuation calculation for ultra-fast noise-reducing communication.

References

1. R. Slusher, L. Hollberg, B. Yurke et al., Phys. Rev. Lett. **55**, 2409 (1985)

2. E.S. Polzik, J. Carri, H.J. Kimble, Phys. Rev. Lett. **68**, 3020 (1992)

3. G. Breitenbach, S. Schiller, J. Mlynek, Nature **387**, 471 (1997)

4. P. K. Lam, T. C. Ralph, B. C. Buchler et al., J. Opt. B. Quantum and Semiclass. Opt. **1**, 469 (1999)

5. A. Sizmann, R. Horowicz, G. Wagner, G. Leuchs, Opt. Communications **80**, 138 (1990)

6. P. Kurz, R. Paschotta, K. Fiedler, A. Sizmann, G. Leuchs, J. Mlynek, Appl. Physics B **55**, 216 (1992)

7. K. Schneider, M. Lang, J. Mlynek, S. Schiller, Opt. Exp. **2**, 59 (1998)

8. S. Suzuki, H. Yonezawa, F. Kannari et al., Appl. Phys. Lett. **89**, 061116 (2006)

9. Y. Takeno, M. Yukawa, H. Yonezawa, A. Furusawa, Opt. Exp. **15**, 4321 (2007)

10. H. Vahlbruch, M. Mehmet, S. Chelkowski et al., Phys. Rev. Lett. **100**, 033602 (2008)

11. T. Eberle, S. Steinlechner, J. Bauchrowitz et al., Phys. Rev. Lett. **104**, 251102 (2010)

12. M. Mehmet, S. Ast, T. Eberle et al., Opt. Exp. **19**, 25763 (2011)

13. M. S. Stefszky, C. M. Mow-Lowry et al., Classical and Quantum Gravity **16**, 145051(2012)

14. H. Yuen, J. Shapiro, IEEE Trans. Inf. Theory **24**, 657 (1978)

15. J. Shapiro, H. Yuen, A. Mata, IEEE Trans. Inf. Theory **25**, 179 (1979)

16. M. Xiao, W. Ling-An, H.J. Kimble, Phys. Rev. Lett. **59**, 278 (1987)

17. P. Grangier, R.E. Slusher, B. Yurke, A. La Porta, Phys. Rev. Lett. **59**, 2153–2156 (1987)

18. E.S. Polzik et al., Phys. Rev. Lett. **68**, 3020–3023 (1992)

19. N. C. Menicucci, P. Van Loock, M. Gu et al., Phys. Rev. Lett. **97**, 110501 (2006)

20. M. Kolobov, C. Fabre, Phys. Rev. Lett. **85**, 3789 (2000)

21. S. L. Braunstein H. Kimble, Phys. l Rev. Lett. **80**, 869 (1998)

22. M. Hillery, Quantum cryptography with squeezed states, Phys. Rev. A **61**, 022309 (2000)

23. S. Lorenz, C. Silberhorn, N. Korolkova et al., Appl. Phys. B **73**, 855–859 (2001)

24. J. Qin, J. Cheng, S. Liang et al., Appl. Sci. **9**, 2397 (2019)

25. J. Aasi, J. Abadie, B. Abbott et al., Nat. Photon. **7**, 613 (2013)

26. S. Mitra S. Mukhopadhyay, Chin. Opt. Lett. **13**, 012702 (2015)

27. S.K. Pal, S. Mukhopadhyay, Optik **122**(5), 411–414 (2011)

28. S.K. Pal, S. Mukhopadhyay, Optik **122**(21), 1943–1946 (2011)

29. S. Mitra, S. Mukhopadhyay, J nonlinear opt phys **24**, 1550048 (2015)

30. S. Mitra, S. Mukhopadhyay, J. Opt. **48**, 220–223 (2019)

31. M.C. Teich, B.E.A. Saleh, Quant. Opt. **1**, 153–191 (1989)

32. M. Fox, Oxford University Press, New York (2006)

33. D. Levandovsky, M. Vasilyev, P. Kumar, Opt. Lett. **24**, 984–986 (1999)

34. D. Krylov, K. Bergman, Opt. Lett. **23**, 1390–1392 (1992)

35. S. Machida, Y. Yamamoto, Y. Itaya, Phys. Rev. Lett. **58**, 1000 (1987)

36. S. Schmitt, J. Ficker et al., Phys. Rev. Lett. **81**, 2446 (1998)

37. R. Paschotta, M. Collett et al., Phys. Rev. Lett. **72**, 3807 (1994)

38. S. Mitra, S. Mukhopadhyay, Optik **124**, 4586–4589 (2013)

Author information

Authors and Affiliations

Department of Physics, Ramananda College, Bishnupur, Bankura, West Bengal, India, 722122

Saibal Mitra

Corresponding author

Correspondence to Saibal Mitra.

Ethics declarations

Competing Interests

The authors declare no competing interests.

Additional information

Publisher's Note

Springer Nature remains neutral with regard to jurisdictional claims in published maps and institutional affiliations.

Rights and permissions

Reprints and Permissions

About this article

Cite this article

Mitra, S. An Analytical Approach for Implementing an All-Optical NOR Operation Using Amplitude Squeezed Light. *Braz J Phys* **52**, 28 (2022). https://doi.org/10.1007/s13538-021-01034-y

Received	Accepted	Published
18 February 2021	14 December 2021	03 January 2022

DOI
https://doi.org/10.1007/s13538-021-01034-y

Keywords

Amplitude squeezed light **Photon fluctuation** **NOR logic**